Electronic Coulomb Correlations in Transition Metal Pnictides

Ambroise van Roekeghem

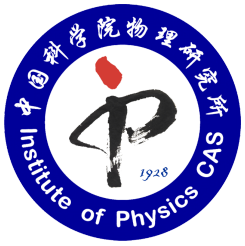

Electronic Coulomb Correlations in Transition Metal Pnictides

Ambroise van Roekeghem

2014

This thesis has been defended on the 23rd of October 2014 at the Institute of Physics, Chinese Academy of Sciences, before the jury composed of:

Hong Jiang	Peking University, Beijing (China)	(Chairman)
Véronique Brouet	Université Paris-Sud, Orsay (France)	(Referee)
Massimo Capone	SISSA, Trieste (Italy)	(Referee)
Pierre Richard	Institute of Physics (CAS), Beijing (China)	(Referee)
Silke Biermann	Ecole Polytechnique, Palaiseau (France)	(Advisor)
Hong Ding	Institute of Physics (CAS), Beijing (China)	(Advisor)
Xi Dai	Institute of Physics (CAS), Beijing (China)	
Shuheng Pan	University of Houston, Texas (USA)	

Electronic Coulomb Correlations in Transition Metal Pnictides

Les Corrélations Electroniques dans les Pnictures de Métaux de Transition

Ambroise van Roekeghem

2014

CENTRE DE PHYSIQUE THÉORIQUE
ECOLE POLYTECHNIQUE
FRANCE

BEIJING NATIONAL LABORATORY
FOR CONDENSED MATTER PHYSICS
INSTITUTE OF PHYSICS
CHINESE ACADEMY OF SCIENCES
PEOPLE'S REPUBLIC OF CHINA

Abstract for the general public

In some materials, for instance those containing transition metals such as iron or cobalt, electrons sometimes display collective behaviors. These collective behaviors result in exotic properties, such as superconductivity but also the transformation of metals into insulators. Hence, they are the manifestation at a human scale of quantum effects, caused for example by the strong electric repulsion between close electrons.

In this thesis, we study the role of these phenomena in the non-superconducting state of iron and cobalt pnictides – compounds containing arsenic. These materials belong to a new family of high-temperature superconductors discovered in 2008. To this aim, we compare the results of the numerical computation techniques we have developed with data from spectroscopic experiments. We show that the strength of collective effects is very sensitive to the number of electrons on the metallic atom, to the frequency-dependence of the repulsion, and to the nonlocal exchange.

Résumé grand public

Dans certains matériaux, notamment ceux contenant des métaux de transition tels que le fer ou le cobalt, il arrive que les électrons se comportent de manière collective. Ces comportements collectifs produisent des propriétés étonnantes, telles que la supraconductivité mais aussi la transformation de matériaux métalliques en isolants. Ils sont ainsi la manifestation à l'échelle humaine de phénomènes quantiques, liés par exemple à la forte répulsion électrique lorsque deux électrons sont proches.

Dans cette thèse, nous étudions l'importance de ces effets dans l'état non-supraconducteur des pnictures (des composés à base d'arsenic) de fer et de cobalt. Ces matériaux appartiennent à une nouvelle famille de supraconducteurs à haute température découverte en 2008. Pour ce faire, nous avons développé des techniques de calcul numérique, dont nous comparons les résultats avec des expériences de spectroscopie. Nous montrons que le nombre d'électrons sur l'atome de métal est un paramètre clef.

Abstract

In this thesis, we discuss the role of electronic Coulomb correlations in the spectral properties of iron and cobalt pnictides in the paramagnetic state. These materials belong to a new family of high-temperature superconductors discovered in 2008, with a maximum critical temperature of 56 K at present. The superconducting state emerges from the paramagnetic state, in which the electrons display many-body effects due to the importance of Hund's coupling. This leads to middle-range renormalizations of the quasiparticle dispersion with an enhancement of the effective mass by a factor of 2 to 5, a finite quasiparticle lifetime, and a bad-metal behavior.

Our work is based on the comparison between experimental data from angle-resolved photoemission spectroscopy (ARPES) and numerical calculations combining density functional theory (DFT) with dynamical mean-field theory (DMFT). Our theoretical technique is fully *ab-initio*, in the sense that all quantities are obtained from the experimental crystal structure of the material under consideration. In particular, we compute the value of the on-site Coulomb interaction by constrained-random phase approximation (cRPA) and take into account its frequency dependence. Furthermore, we go beyond the local density approximation (LDA) by including the effects of nonlocal screened exchange created by the Fock term of a Yukawa potential.

We apply these techniques to the study of the electronic properties of transition-metal pnictides. We focus on three compounds: $BaCo_2As_2$, $CaFe_2As_2$ and $Ba_2Ti_2Fe_2As_4O$. We calculate the spectral functions for all three materials and compare them directly to photoemission measurements, that we have taken in the case of $CaFe_2As_2$. We demonstrate that the electron count in the metallic $3d$ correlated orbital is a key parameter for the strength of correlations and the coherence properties. In particular, we find a hole self-doping effect induced by the Ti_2As_2O layer that places the iron electrons of $Ba_2Ti_2Fe_2As_4O$ in an incoherent state at 150 K, close to the physics of optimally-doped $Ba_{0.6}K_{0.4}Fe_2As_2$. In contrast, we show that $BaCo_2As_2$ displays good Fermi-liquid behavior, which allows photoemission to capture a well-defined quasiparticle dispersion. We take advantage of this property to evaluate the antagonistic effects of the nonlocal screened exchange and of the frequency dependence of the dynamical Coulomb interaction. We find that neglecting both of them leads to an error cancellation which may produce a correct overall bandwidth. Conversely, one needs to take those effects into account for an accurate description of the Fermi surface and low-energy excitations, which are key to assessing the physics of $BaCo_2As_2$ and of pnictides in general.

Résumé

Dans cette thèse, nous examinons l'impact des corrélations électroniques sur les propriétés spectrales des pnictures de fer et de cobalt dans la phase paramagnétique. Ces matériaux appartiennent à une nouvelle famille de supraconducteurs à haute température découverte en 2008, dont la température critique maximale relevée à ce jour est de 56 K. La phase supraconductrice se développe à partir de la phase paramagnétique, au sein de laquelle les effets de la formation d'un état à plusieurs corps par les électrons sont importants, du fait de la valeur élevée du couplage de Hund. Cela conduit à des renormalisations de la dispersion des quasiparticules (avec une masse effective multipliée par un facteur 2 à 5), à un temps de vie fini des quasiparticules, ainsi qu'à un comportement de type mauvais métal.

Notre travail se fonde sur la comparaison entre des données expérimentales de photoémission résolue en angle (ARPES) et des calculs numériques combinant les calculs de structure électronique avec la théorie du champ moyen dynamique (DMFT). Nos calculs théoriques sont dits *ab-initio*, car toutes les quantités physiques sont déterminées uniquement à partir de la structure cristalline expérimentale du matériau étudié. Notamment, la technique de l'approximation de la phase aléatoire avec polarisation contrainte (constrained-RPA) nous permet d'obtenir la valeur de l'interaction de Coulomb sur site, dont nous prenons en compte la dépendance en fréquence. De plus, nous allons plus loin que l'approximation de la densité locale (LDA) en incluant les effets non-locaux du terme d'échange écranté dérivé à partir d'un potentiel de Yukawa.

Nous appliquons ces techniques à l'étude des propriétés électroniques des pnictures de métaux de transition. Nous examinons trois composés: $BaCo_2As_2$, $CaFe_2As_2$ et $Ba_2Ti_2Fe_2As_4O$. Pour chacun, nous calculons la fonction spectrale et la comparons avec les données de photoémission, que nous avons mesurées dans le cas de $CaFe_2As_2$. Nous montrons que le nombre d'électrons dans l'orbitale $3d$ métallique corrélée est un paramètre clef qui contrôle la force des corrélations et la cohérence électronique du matériau. En particulier, nous trouvons un effet d'auto-dopage en trous induit par la couche Ti_2As_2O qui entraîne les électrons fer du $Ba_2Ti_2Fe_2As_4O$ dans un état incohérent à 150 K, comparable à la physique du $Ba_{0.6}K_{0.4}Fe_2As_2$ dans son dopage optimal. A contrario, nous établissons que les électrons du $BaCo_2As_2$ sont à cette même température dans un état de type liquide de Fermi, ce qui permet à la photoémission d'obtenir la dispersion des quasiparticules de manière précise. Nous utilisons cette propriété pour évaluer les effets antagonistes de la non-localité du potentiel d'échange écranté et de la dépendance en fréquence de l'interaction de Coulomb dynamique. Nous montrons que l'approximation consistant à négliger ces deux effets peut produire une largeur de bande raisonnable, car les deux erreurs se compensent. En revanche, il est nécessaire de les prendre en compte afin de décrire correctement la surface de Fermi et les excitations de basse énergie, qui sont indispensables à la compréhension de la physique du $BaCo_2As_2$ et des pnictures en général.

摘要

铁基超导体是于 2008 年发现的新型高温超导材料，其最高转变温度达到了 56K。由于铁基超导材料中洪特耦合所起的重要作用，该材料的顺磁态展现出了很强的多体效应。正是由于这种多体效应导致了铁基超导材料中准粒子有效质量 2～5 倍的中等强度的重整化、有限的准粒子寿命及坏金属行为。在本论文中，我们将讨论顺磁状态下的铁和钴砷化物的能谱中的电子库仑相互作用。

我们的工作基于实验数据和理论模拟的结合：实验方面我们利用角分辨光电子能谱，理论模拟方面则是利用结合了动力学平均场的密度泛函理论。我们的理论方法是第一性的，因为我们的参数都是直接源于实验所得的晶格参数，同位库仑相互作用的大小是由考虑了频率依赖的受限无规相近似的方法得到的。我们甚至在局域态密度近似的基础上更进一步，考虑了汤川势中福克项所产生的非局域屏蔽交换效应。

我们利用上述方法研究了铁基超导体的电子结构，并且着重分析了：$BaCo_2As_2$，$CaFe_2As_2$和 $Ba_2Ti_2Fe_2As_4O$ 这三种化合物。我们计算了这三种材料的谱函数并直接与实验上 ARPES 测得的数据进行了比较。我们证明了 3d 轨道上的电子数是调控上述材料相互作用及相干性的核心参数。特别地，我们指出 $Ba_2Ti_2Fe_2As_4O$ 中 150K 地非相干态是由 Ti_2As_2O 层地自掺杂效应所导致的，其物理机制类似于最佳掺杂 $Ba_{0.6}K_{0.4}Fe_2As_2$。与之相反地 $BaCo_2As_2$ 则显示良好的费米液体行为，从而可以使得 ARPES 测得很好地电子色散。利用 $BaCo_2As_2$ 这一良好地性质，我们评估了非局域屏蔽交换效应和频率依赖地动力学库仑相互作用这一对竞争地效应。我们发现同时忽略这两种效应虽然可以得到正确地能带宽度，但是却无法精确地描述费米面和低能激发。只有考虑以上两种敌对地相互作用才可以准确地描述重要物理量。

Contents

List of Figures

List of Tables

Part I

Introduction

Chapter 1

Iron pnictides

1.1 Superconductivity in iron pnictides

1.1.1 Discovery of superconductivity

The discovery of superconductivity in iron pnictides dates back to 2006, when a critical temperature (T_c) of 5 K was found in $LaFePO_{1-x}F_x$ [Kamihara *et al.* (2006)]. Amusingly, these compounds had already been studied several decades ago [Ban and Sikirica(1965), Rieger and Parthé(1969), Marchand and Jeitschko(1978), Mewis(1980), Rózsa and Schuster(1981), Hoffmann and Zheng(1985)] but this property had gone unnoticed. It is really in 2008, when a higher T_c of 28 K was measured in $LaFeAsO_{1-x}F_x$ by [Kamihara *et al.* (2008)] that the potential of the iron pnictides family as high-temperature superconductors was realized. Since then, over 5000 articles referring to this paper have been published, showing both the excitement and the tremendous effort of the scientific community to understand the underlying physics of these compounds. Indeed, 20 years after the discovery of unconventional high-temperature superconductivity in the cuprates [Bednorz and Müller(1986)] and about one century after superconductivity was first measured below 4.2 K in metallic mercury by Kamerlingh-Onnes in 1911 [Kamerlingh Onnes(1911a), Kamerlingh Onnes(1911b)], this new breakthrough in the domain was expected to shed light on still controversial but fundamental questions such as the pairing mechanism in high-T_c superconductors.

Very quickly, many other representatives of this class have been synthesized. Figure 1.1.1 shows an overview of the diversity of the iron pnictides possible stoechiometries and critical temperatures. In the sole year 2008, more than 30 compounds were already synthesized, providing experimentalists and theoreticians with a large playground to track the origin of superconductivity. The common point in the whole family is the presence of a typical layer formed of a square lattice of iron with a nominal valence close to d^6 and of a pnictogen – most of the time, arsenic – forming another nested square lattice but in which the positions of the atoms alternate between above and below the iron plane. Between those layers, many different atoms can be intercalated and potentially modify the charge or the crystal structure of the layers. Compounds are classified and denominated from their stoechiometry. The principal families are the 1111 (e.g. LaFeAsO) [Kamihara *et al.* (2008), Ren *et al.* (2008), Chen *et al.* (2008a), Wen *et al.* (2008), Chen *et al.* (2008b)] with the primitive tetragonal ZrCuSiAs-type crystal structure (*P4/nmm* space group), the 111 (e.g. LiFeAs) [Tapp *et al.* (2008), Wang *et al.* (2008b), Pitcher *et al.* (2008)], the 11 (e.g. FeSe) [Yeh *et al.* (2008), Hsu *et al.* (2008)] in which the pnictogen

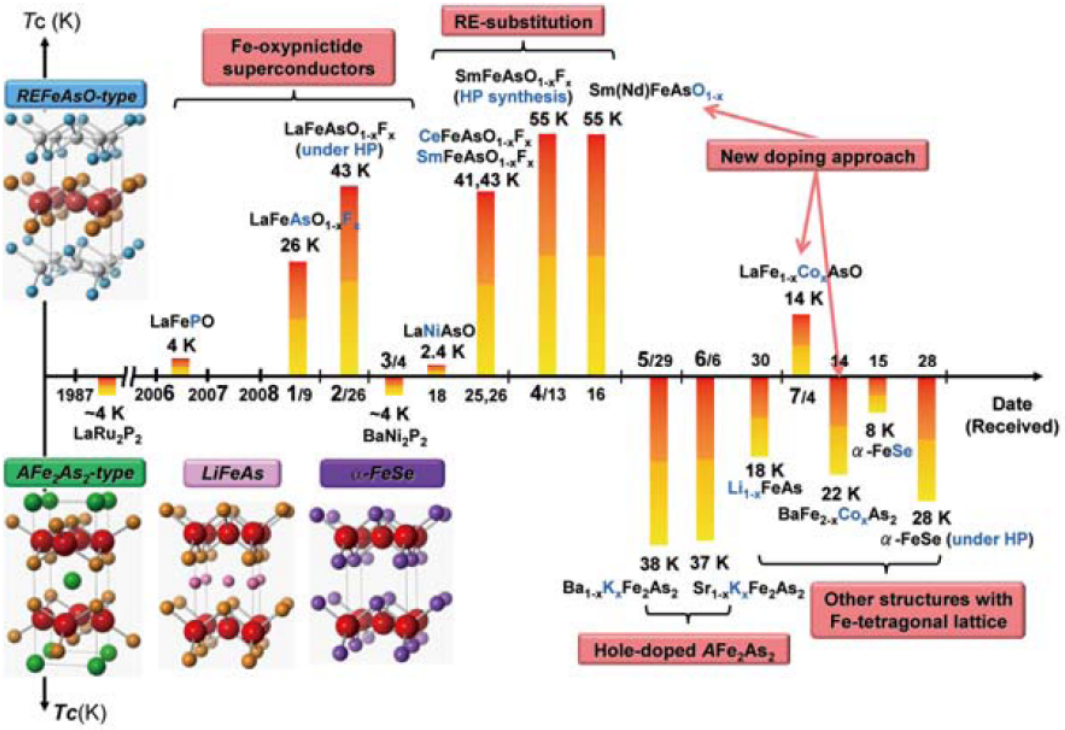

Figure 1.1.1: The fast discovery of new iron pnictides superconductors (from [Hosono(2008)]).

atom is replaced by a chalcogen in order to keep the same nominal valence for the iron atoms, and the 122 (e.g. $BaFe_2As_2$) [Rotter *et al.* (2008b), Sefat *et al.* (2008a), Sharma *et al.* (2010)] with the body-centered tetragonal $ThCr_2Si_2$-type crystal structure (*I4/mmm*) and on which this thesis will mainly focus. The crystal structures of those families are displayed on Figure 1.1.2. More exotic compounds with larger intercalated layers have also been synthesized, such as $(Sr_4Sc_2O_6)Fe_2P_2$ [Ogino *et al.* (2009)], Sr_2VO_3FeAs [Zhu *et al.* (2009)], or $Ba_2Ti_2Fe_2As_4O$ [Sun *et al.* (2013)] – a case we will discuss in Section 11. The highest critical temperature so far (56 K) has been recorded in $Gd_{0.8}Th_{0.2}FeAsO$ of the 1111 family [Wang *et al.* (2008a)]. In the 122 compounds, the highest T_c (38 K) has been measured in $Ba_{0.6}K_{0.4}Fe_2As_2$ [Rotter *et al.* (2008b)].

As for potential applications, iron pnictides are considered to display intermediate properties between the conventional superconductors and the high-T_c cuprates [Putti *et al.* (2010)]. Indeed,

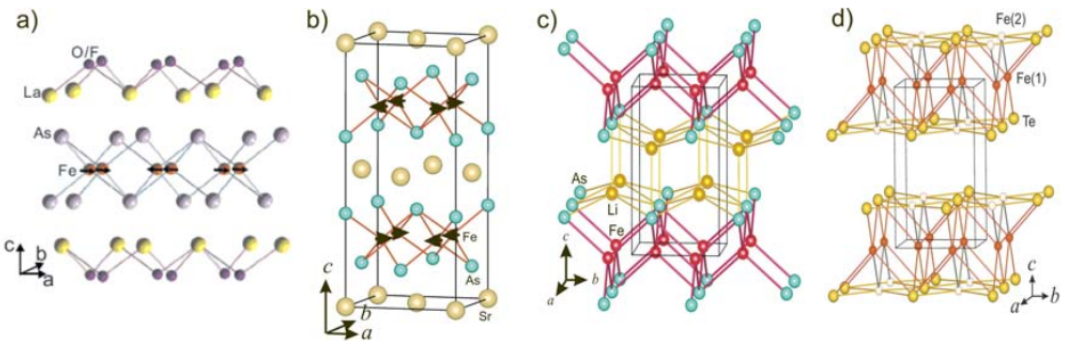

Figure 1.1.2: Crystal structure of (a) $LaFeAsO_{1-x}F_x$ (1111), (b) $SrFe_2As_2$ (122), (c) LiFeAs (111) and (d) $Fe_{1+x}Te$ (11) (from [Lynn and Dai(2009)]). The arrows correspond to the ordered magnetic moments at low temperature.

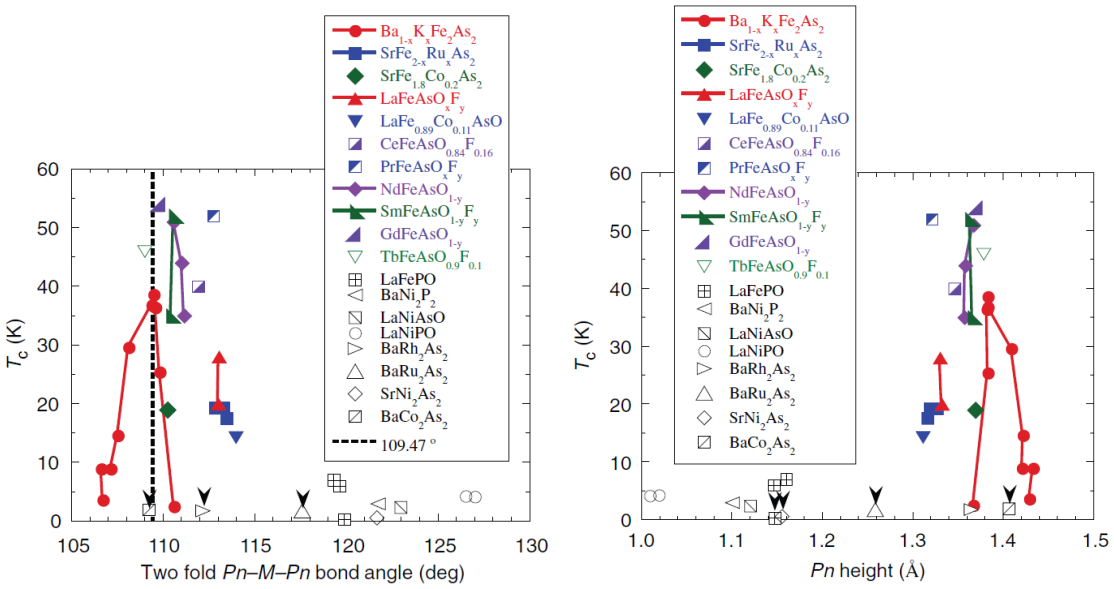

Figure 1.1.3: Correlations between the pnictogen (Pn) position and the critical temperature in iron pnictides (from [Johnston(2010)]).

though the critical temperature is not as high as in the cuprates, the upper critical field is high with values of $\mu_0 H_{c2}$ of the order of 60 T at low temperature and displays a small (< 2) anisotropy for the 122 systems like electron or hole-doped $BaFe_2As_2$ [Yuan *et al.* (2009), Yamamoto *et al.* (2009)]. The critical current density is high in single crystals, with values for J_c of the order of 10^5 – 10^6 A cm^{-2} at low temperature [Zhigadlo *et al.* (2008), Yang *et al.* (2008), Prozorov *et al.* (2008), Taen *et al.* (2009)]. The main limitation for the fabrication of superconducting wires and tapes remains in the radical decrease of J_c in polycrystals because of the grain boundaries (for a review, see [Putti *et al.* (2010)]), although in that respect the iron pnictides may have advantages over the cuprates [Katase *et al.* (2011)]. Finally, the thermoelectric properties of iron pnictides around 80 K may also be interesting for applications [Pinsard-Gaudart *et al.* (2008), Pinsard-Gaudart and Dragoe(2008), Sefat *et al.* (2008b), Kihou *et al.* (2010)].

1.1.2 Structural properties

Attempts to make relations between the structural and superconducting properties of iron pnictides have put forward the role of the position of the arsenic ligand. In particular, there seems to be a correlation between the As-Fe-As angle – with the two As atoms on the same side of the Fe layer – and the magnitude of the critical temperature [Lee *et al.* (2008), Zhao *et al.* (2008a), Kimber *et al.* (2009), Horigane *et al.* (2009)]. The left panel of Figure 1.1.3 shows that the ideal tetrahedral angle generally provides the highest T_c within one series of compounds. Another possible correlation is between the maximum observed critical temperature and the arsenic distance to the layer – the arsenic height (see right panel) [Mizuguchi *et al.* (2010), Okabe *et al.* (2010), Kuroki *et al.* (2009), Huang *et al.* (2010)]. Still, there are exceptions to those rules and a general statement remains difficult though the envelopes of the curves seem to testify in favor of these puzzling correlations. Moreover, the magnitude of the iron spin is also correlated with the As position, according to density functional theory calculations of the ferromagnetic state [Yildirim(2009b)] that show an enhancement of the magnitude of the ordered spin when the Fe-As distance increases.

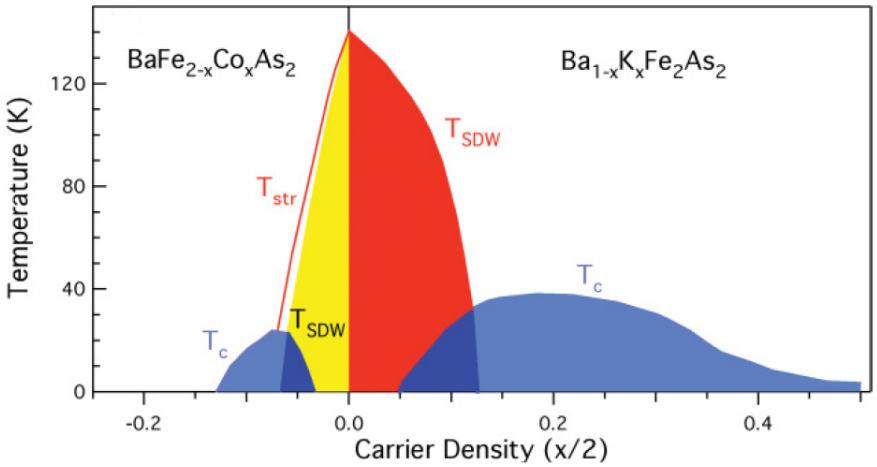

Figure 1.1.4: Phase diagram of the hole and electron-doped Ba122 systems taken from [Rotter *et al.* (2008a)] and [Pratt *et al.* (2009)] respectively. T_c, T_{SDW} and T_{str} refer to the superconducting, spin-density wave and the tetragonal to orthorhombic transition temperatures, respectively (from [Neupane *et al.* (2011)]).

1.1.3 Phase diagram

Figure 1.1.4 displays the phase diagram of hole and electron-doped $BaFe_2As_2$. At low temperature, two superconducting domes can be observed, separated by a magnetic phase. The magnetic phase displays a different crystal symmetry than the paramagnetic one, going from tetragonal to orthorhombic or monoclinic symmetry. Indeed, in this case in the 1111, 111 and the 122 families the iron spins in the plane adopt an antiferromagnetic collinear stripe configuration [Huang *et al.* (2008b), Goldman *et al.* (2008), Huang *et al.* (2008a), Wilson *et al.* (2009), Kitagawa *et al.* (2008), de La Cruz *et al.* (2008), Kitagawa *et al.* (2009), Nomura *et al.* (2008), Rotter *et al.* (2008c), Lynn and Dai(2009)], ordering ferromagnetically along one axis of the square lattice and antiferromagnetically along the other (see Figure 1.1.2). The symmetry breaking between those two axes is coupled to the magnetic order (for reviews of the relation between magnetic and structural order from a Density Functional Theory perspective, see e.g. [Yildirim(2008), Singh(2009), Yildirim(2009a)]). The fact that the structural transition appears before the onset of magnetism may be due to spin fluctuations close to the transition. It is widely believed that the magnetic phase is in competition with superconductivity, which explains the double dome structure. Surprisingly, it has been found that both phases can also coexist microscopically (e.g. in $Ba(Fe_{1-x}Co_x)_2As_2$ [Lester *et al.* (2009), Christianson *et al.* (2009), Pratt *et al.* (2009), Chauvière *et al.* (2010)]), showing that though these phases are in competition the onset of magnetism does not automatically destroy superconductivity [Chubukov *et al.* (2008), Vorontsov *et al.* (2009), Drew *et al.* (2009), Takeshita and Kadono(2009), Shermadini *et al.* (2011)]. Conversely, the magnetic and superconducting phases can also be clearly separated, as in $CeFeAsO_{1-x}F_x$ [Zhao *et al.* (2008a)].

1.2 Spectral properties

Angle-resolved photoemission spectroscopy (ARPES, see Chapter 2 for an introduction) is a powerful tool to probe the electronic properties of materials. It allows for a direct visualization of

the momentum-resolved spectral function, which provides us with crucial information such as the Fermi surface, the quasi-particle dispersions, or even the momentum-resolved magnitude of the superconducting gap (for measurements of the latter in iron pnictides, see e.g. [Ding *et al.* (2008), Zhao *et al.* (2008b), Kondo *et al.* (2008), Nakayama *et al.* (2010), Borisenko *et al.* (2010), Liu *et al.* (2011)] and experiments to which we have participated [Wang *et al.* (2012b), Xu *et al.* (2013a), Xu *et al.* (2013c), Shi *et al.* (2014)]). It can also give insights into the orbital characters of the electronic states with the use of polarized light, core and plasmon excitations, and some clues about the lifetime of quasiparticles – though the latter point is more problematic since the measurements can be influenced by the sample quality or other sources of imprecision. In the following, we will focus on measurements of the paramagnetic, non-superconducting state, for its comprehension is a primordial step to understanding the emergence of superconductivity.

1.2.1 Bandwidth and comparison to local density approximation

In the whole pnictide family, photoemission measurements are able to identify band dispersions and a Fermi surface. At first glance, bandstructures calculated from density functional theory in the local density approximation (LDA) roughly correspond to the measured quasiparticles, except that they have to be renormalized by a factor of about 2 to 5 depending on the material [Richard *et al.* (2011), Yamasaki *et al.* (2010)]. This shows that the iron pnictides and chalcogenides are indeed metals constituted of itinerant quasiparticles with an enhanced effective mass produced by intermediate correlations. We will focus on materials without or with limited surface effects. Indeed, ARPES usually probes the surface in the photon energy considered, and these effects can create big discrepancies with the bulk band structure, for instance in LaFeAsO [Yang *et al.* (2010)] but also in $SrFe_2As_2$ [Hsieh *et al.* (2008)] and in 1111 in general due to the polar cleavage surface [Richard *et al.* (2011), Lu *et al.* (2009), Liu *et al.* (2009)]. Assessing the strength of the bandstructure renormalization allows us to extract general tendencies. Within a same family, and if the crystal structure is not modified by the introduction of impurities, hole-doping increases the band renormalization while electron-doping reduces it. This is most easily seen in the $BaFe_2As_2$ family in the paramagnetic state: for instance in the same study [Yi *et al.* (2009)] found a factor of 2.7 for the hole-doped $Ba_{0.6}K_{0.4}Fe_2As_2$, of 1.5 for the undoped $BaFe_2As_2$ and of 1.4 for the electron-doped $BaFe_{0.88}Co_{0.12}As_2$. The 11 family displays the highest renormalization, with factors found in the literature higher than 3.5 [Yamasaki *et al.* (2010), Yoshida *et al.* (2009), Tamai *et al.* (2010)]. The 111 are an intermediate case with a renormalization factor of 3 – 4 in LiFeAs and NaFeAs [Borisenko *et al.* (2010), He *et al.* (2010), Cui *et al.* (2012)]. Finally, substituting Fe by Ru in $BaFe_2As_2$ substantially reduces these effects, due to the less localized 4*d* shell [Brouet *et al.* (2010), Xu *et al.* (2012)].

1.2.2 Beyond renormalized local density approximation bands

In the above section, we have refrained from discussing extensively the numerous studies of e.g. the $BaFe_2As_2$ family [Fink *et al.* (2009), Malaeb *et al.* (2008), Zhang *et al.* (2011b), Ding *et al.* (2011), Brouet *et al.* (2009), Vilmercati *et al.* (2009), Liu *et al.* (2009), Sato *et al.* (2009), Xu *et al.* (2013b), Dhaka *et al.* (2013), Thirupathaiah *et al.* (2010)]. The reason for this is that the magnitude of the renormalization factors found by different ARPES groups shows an impressive discrepancy. If we compare again with the numbers found by [Yi *et al.* (2009)], for electron-doped $BaFe_{0.84}Co_{0.16}As_2$ [Brouet *et al.* (2011)] found a much higher value of 3.3, while for $Ba_{0.6}K_{0.4}Fe_2As_2$ [Ding *et al.* (2011)] found an overall factor of 2. This reflects the

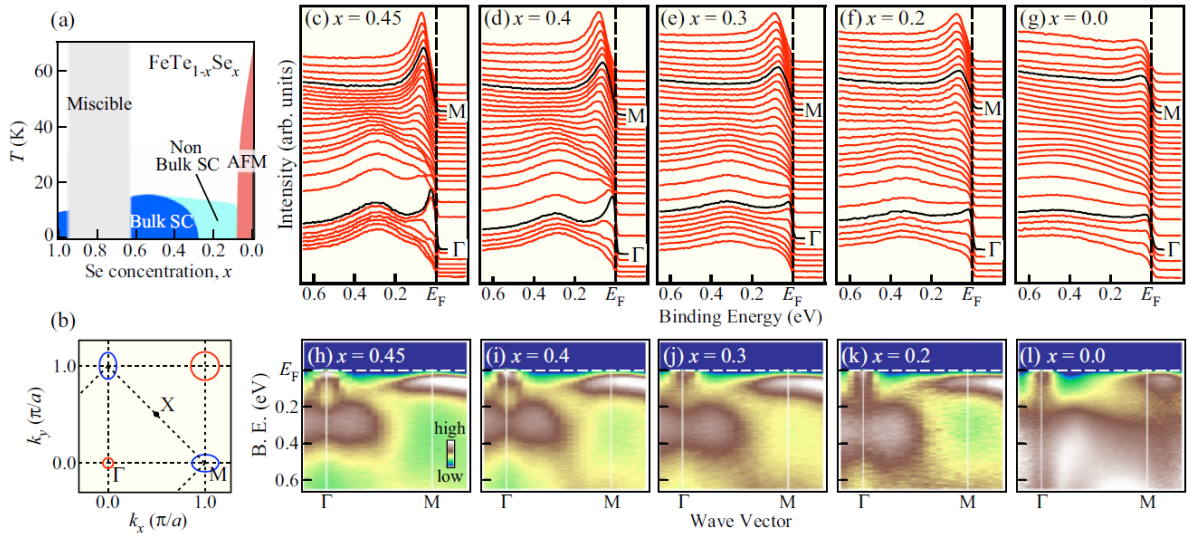

Figure 1.2.1: Coherence-incoherence crossover in $FeTe_{1-x}Se_x$ (from [Ieki *et al.* (2014)]):
(a) Schematic phase diagram of $FeTe_{1-x}Se_x$ derived from [Fang *et al.* (2008), Liu *et al.* (2010), Mizuguchi and Takano(2010)]. SC and AFM denote superconductivity and antiferromagnetism, respectively. The miscible region exists at high Se concentrations due to the difficulty in growing single-phase samples.
(b) One-Fe/unit-cell Brillouin zone of $FeTe_{1-x}Se_x$ used in this study together with the schematic hole and electron Fermi surfaces at the and M points, respectively.
(c)–(g) Se-concentration dependence of normal-state ARPES spectra along the -M line in a wide energy region for $FeTe_{1-x}Se_x$ (T = 25 K for x = 0.45–0.2 and 80 K for x = 0.0) measured with the He-Iα resonance line ($h\nu$ = 21.218 eV).
(h)–(l) Corresponding ARPES intensity plotted as a function of binding energy and wave vector.

fact that the Kohn-Sham bandstructure of DFT does not actually account for the precise and more complicated effects of correlations taking place in iron pnictides, even at the level of the quasiparticle dispersion [Aichhorn *et al.* (2010)]. It has been noted by most ARPES authors, who signal additional momentum-dependent or orbital-dependent shifts of the bandstructure [Yi *et al.* (2009), Brouet *et al.* (2010), Ding *et al.* (2011), Borisenko *et al.* (2010), Fink *et al.* (2009)] or orbital-dependent renormalizations [Lu *et al.* (2008), Ding *et al.* (2011), Sato *et al.* (2009), Yi *et al.* (2013), Brouet *et al.* (2013), Tamai *et al.* (2010), Zhang *et al.* (2011b)]. It is worth noting that the binding energy of itinerant As-4*p* states is also underestimated by LDA in 1111 [Lu *et al.* (2008), Lu *et al.* (2009)], however because of the possible polar surface in these compounds it would be interesting to have similarly precise measurements for other families.

Even more exotic behaviors have been investigated. [Ding *et al.* (2011)] noted energy-dependent renormalizations of the band structure, with an enhanced factor near the Fermi level. This means that the electronic structure of such compounds cannot be interpreted in a Fermi-liquid picture with a single measurable renormalization factor Z, at least for the temperature of measurement. In addition, in the most correlated 11 family [Yoshida *et al.* (2009), Yamasaki *et al.* (2010)] have revealed the existence of a broad feature of Fe-*d* character around -2 eV in the photoemission spectrum, which was interpreted as a Hubbard band [Aichhorn *et al.* (2010)]. In the same vein and very recently, the existence of a coherence-incoherence crossover as a function of the isovalent Te-Se substitution has also been investigated in [Ieki *et al.* (2014)] (see Figure 1.2.1), who found much shorter quasiparticle lifetimes in fully substituted FeTe and a

probable relationship with the development of antiferromagnetism. In the parent compound $Fe_{1.06}Te$, a pseudogap was found in the paramagnetic phase, progressively closing when the temperature is reduced in the antiferromagnetic phase [Lin *et al.* (2013)]. A pseudogap was also measured in underdoped $Ba_{1-x}K_xFe_2As_2$ [Xu *et al.* (2011)], and the relation between those two experiments remains to be understood. Finally, temperature-dependent measurements reveal other surprising effects: [Brouet *et al.* (2013)] found an evolution of the number of carriers via k-dependent shifts on the Fermi surface, while [Yi *et al.* (2013)] investigated an orbital-selective coherence-incoherence crossover. Those subtle changes are technically challenging to analyze, but very enlightening about the physics of iron pnictides, and more experimental evidence would be welcome.

1.2.3 Strength of correlations from theoretical calculations

Much theoretical work has been carried out to explore the role of electronic correlations in the description of the paramagnetic, magnetic and superconducting phases of iron pnictides. In the following, we will mostly focus on results obtained within dynamical mean-field theory (DMFT) [Georges *et al.* (1996)] and its combination with electronic structure methods (LDA + DMFT [Anisimov *et al.* (1997b), Lichtenstein and Katsnelson(1998), Kotliar *et al.* (2006)], see Chapter 3 for an introduction). Early on, the strength of the electronic Coulomb interactions has appeared to be an important issue but also a source of controversy. Soon after the discovery of its superconducting properties under doping, LaFeAsO was described either as a strongly correlated metal close to the Mott metal-insulator transition [Haule and Kotliar(2009), Haule *et al.* (2008)], or as a weakly correlated metal [Anisimov *et al.* (2009), Shorikov *et al.* (2009), Anisimov *et al.* (2008)].

In [Aichhorn *et al.* (2009)], it was demonstrated that the inconsistency between these results was due to the significant differences in the construction of the low-energy Hamiltonian, including the values of the Hubbard interaction parameters U and the different degrees of localization of the Fe 3*d* Wannier orbitals constructed. Their approach was based on an *ab-initio* treatment in the following sense: as proposed earlier in [Miyake *et al.* (2008)], they considered a Hubbard Hamiltonian that incorporated both Fe 3*d* and ligand As and O *p* states as degrees of freedom for LaFeAsO, but with a Coulomb energy cost on Fe 3*d* orbitals only. The many-body Hamiltonian was then solved within LDA+DMFT. The effective interactions for this specific low-energy model were calculated within the constrained random phase approximation (cRPA) [Aryasetiawan *et al.* (2004)] – an approach for deriving from first-principles the interacting Hamiltonian within a target subspace that is appropriate for the description of the low-energy many-body properties. Within this scheme, LaFeAsO was described as a metal with moderate strength of the electronic correlations [Aichhorn *et al.* (2009)], whereas the largest effects were found for α-FeSe (see [Aichhorn *et al.* (2010)] in which a Hubbard band was correctly predicted), with LiFeAs as an intermediate case [Ferber *et al.* (2012)].

1.2.4 The role of Hund's coupling

A fundamental difference with the cuprates lies in the multi-orbital character of iron pnictides. Indeed, a study of a three-band orbital model [Werner *et al.* (2008)] has revealed the existence in multiorbital systems of a "spin-freezing" phase characterized by a power-law behavior of the imaginary part of the self-energy in Matsubara frequencies, in which the electrons are in

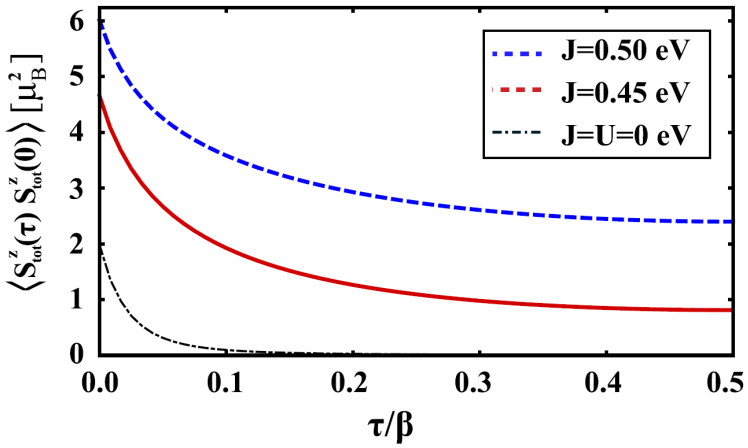

Figure 1.2.2: Total spin-spin correlation function for LaFeAsO at two different values of the Hund's coupling J and β =25 eV^{-1}, compared to the noninteracting $U = J = 0$ case. The calculations were performed within LDA+DMFT using a static U and J in a low-energy model including four orbitals. The short-time ($\tau = 0$) local moment for $J = 0.45$ eV is $m_{loc} = 2.16\mu_B$, comparably large as in LSDA; whereas the long-time moment is screened to only $m \approx 0.7\mu_B$ at T = 50 K (from [Hansmann *et al.* (2010)]).

an incoherent metallic phase with frozen moments. In addition, the Hund's rule coupling J_H appeared to play a fundamental role in the physics of electronic correlations in iron pnictides. In [Haule and Kotliar(2009)], a coherence-incoherence crossover in the electronic properties of LaFeAsO was identified. At present, there is a large consensus over the fact that iron pnictides display intermediate correlations properties – stronger in the 11 family and chalcogenides, weaker in the 1111 and phosphorides in general [Yin *et al.* (2011)] – driven by the physics of strong Hund's coupling in multiorbital systems [de' Medici *et al.* (2011), Georges *et al.* (2013)]. The consequence is that these materials tend to display a bad-metal behavior, in which the effective mass and the coherence properties are very sensitive to the effective number of electrons in the correlated shell [Werner *et al.* (2012), Xu *et al.* (2013b)], which can be tuned by small details of the electronic structure, notably the hybridization between the metal and the pnictogen [Wang *et al.* (2010)]. In that context, it has been proposed that iron pnictides exhibit both weakly and strongly correlated electrons and are in the proximity of an orbital-selective Mott transition [de' Medici *et al.* (2009), de' Medici(2011), Lanatà *et al.* (2013), de' Medici *et al.* (2014)].

One of the most visible consequences is the diversity of the measured magnetic moments in the different pnictides families. Experimentally, LaFeAsO exhibits an antiferromagnetic local moment around $0.3-0.6\mu_B$ below $T \sim 130$ K [Ishida *et al.* (2009), Qureshi *et al.* (2010)]. This is much smaller than the magnetic moment around $2\mu_B$ that is calculated within density functional theory in the local spin density approximation (DFT-LSDA) [Mazin *et al.* (2008a), Subedi *et al.* (2008)]. The discrepancy with the local moment from the high spin configuration is surprising at first glance, since the values of Hund's rule coupling, commonly found in the literature, are larger than the crystal and ligand field splitting and would thus be in favor of a high-spin configuration within a local picture. This anomaly was interpreted by [Sawatzky *et al.* (2009)] as a solvation effect due to the extremely large polarisability of the arsenic ligands, which leads to a strong reduction of the Hubbard interaction on the Fe *d* manifold. In the 122 and 11 families, on the other hand, larger magnetic moments were determined: around $0.9\mu_B$ for $BaFe_2As_2$ [Huang *et al.* (2008a)] and $2.2\mu_B$ for FeTe [Li *et al.* (2009)]. These discrepancies

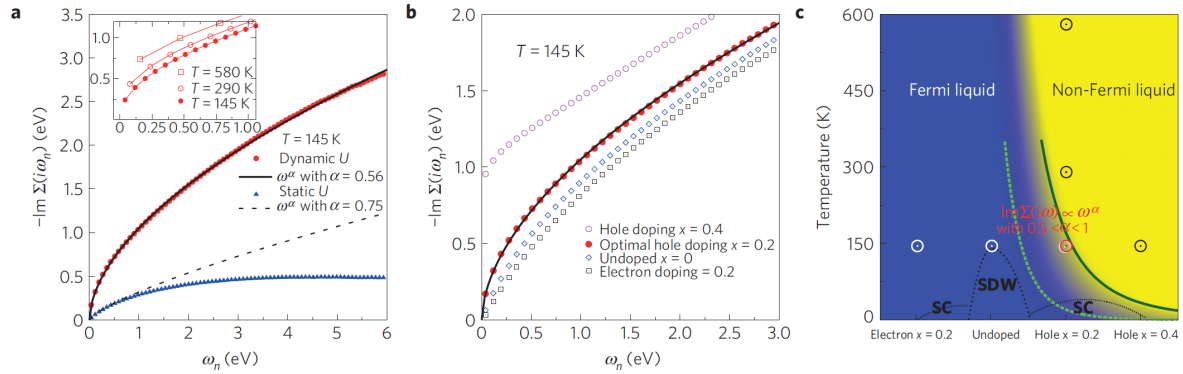

Figure 1.2.3: Fractional power-law behavior of the self-energy in $Ba_{1-x}K_xFe_2As_2$ (from [Werner *et al.* (2012)]).
(a) Imaginary part of the self-energy (orbital average) on the Matsubara axis for optimal hole-doping (x=0.2 per Fe). Calculations were performed within LDA+DMFT, using either the full frequency-dependence of the dynamical interaction $U(\omega)$ (red circles) or a static $U(\omega = 0)$ (blue triangles). Solid and dashed lines are fits of the low-frequency behavior of the function $-\mathrm{Im}\Sigma(i\omega_n) = A(\omega_n)^\alpha$. The inset shows the low-frequency behavior of the dynamic-U result for different temperatures. As the temperature is raised, the extrapolation $\omega_n \longrightarrow 0$ yields a non-zero intercept, which indicates that even excitations at the Fermi level exhibit a finite lifetime.
(b) Low-energy behavior of the self-energy as a function of doping. Fermi-liquid behavior is found in the undoped and electron-doped compounds, whereas a non-zero intercept appears in the overdoped case.
(c) Sketch of the phase diagram in the space of temperature and doping. The blue region indicates Fermi-liquid behavior, whereas yellow indicates a frequency dependence of the self-energy that is not compatible with Fermi-liquid theory. The light green dashed line marks the boundary of the crossover region, where the exponent α starts to deviate from 1. The dark green solid line corresponds to $\alpha = 0.5$, which marks the "spin-freezing" transition. To the right of this line, an incoherent metal phase with a non-zero intercept of $\mathrm{Im}\Sigma$ is found. The experimentally measured phase diagram with superconducting (SC) and spin-density wave (SDW) ordered phases is indicated by black dotted lines. Full substitution (KFe_2As_2) corresponds to x=0.5.

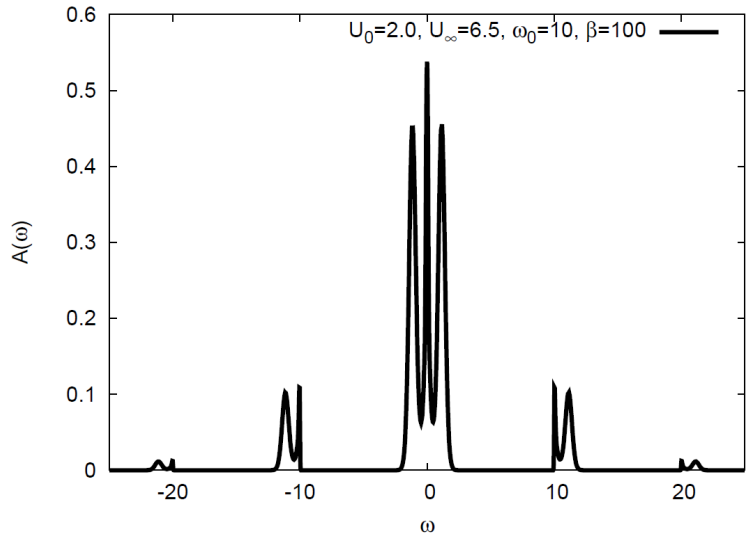

Figure 1.2.4: Spectral representation of the Green's function for a Holstein-Hubbard model with a plasmon frequency $\omega_0 = 10$, a screened Hubbard interaction $U_0 = 2$, an unscreened Hubbard interaction $U_\infty = 6.5$ and an inverse temperature $\beta = 100$. The analytic continuation has been assisted by the dynamic atomic limit approximation (DALA) Bose factor, which allows one to describe accurately the plasmon satellites centered around frequencies multiple of ω_0 (from [Casula *et al.* (2012a)]).

have been clarified by calculations of the two-particle correlation functions within LDA+DMFT that have put forward the role of quantum fluctuations leading to a dichotomy between large local and small ordered magnetic moments [Hansmann *et al.* (2010), Toschi *et al.* (2012)]. As shown on Figure 1.2.2, they found a large instantaneous local moment which is quickly screened, depending strongly on the value of Hund's coupling. As a result, the magnitude of the spin measured within neutron experiments was reconciled with theoretical calculations.

1.2.5 Frequency-dependent Coulomb interactions

Finally, the impact of the energy-dependence of the Hubbard interactions – $U(\omega)$ as calculated within constrained-RPA – on the low-energy properties and the coupling between electronic and plasmonic excitations in the many-body calculations, has been first investigated in prototypical models [Casula *et al.* (2012a)] and then applied to $BaFe_2As_2$ [Werner *et al.* (2012)] in a study revealing the spin-freezing phase in the hole-doped side of the phase diagram (see Figure 1.2.3). Moreover, the inclusion of energy-dependent Hubbard interactions within a dynamical version of LDA+DMFT [Casula *et al.* (2012a), Werner *et al.* (2012)], leads to a reduction of the quasi-particle weight at the Fermi energy, compared to the standard LDA+DMFT with a static interaction. The spectral weight is shifted to additional satellites at larger energies corresponding to plasmon excitations (see Figure 1.2.4 for an illustration of this effect in a model case). An effective model introducing a bosonic renormalization factor to account for the high-frequency tail of $U(\omega)$ was introduced in [Casula *et al.* (2012b)] (see Section 4.4). The values of such coefficient are between 0.59 and 0.63 for LaFeAsO, FeSe and $BaFe_2As_2$ [Casula *et al.* (2012b)], which suggests a further enhancement of the effective masses computed by static LDA+DMFT by a factor of at least 1.6 – 1.7 in iron pnictides and raises again the controversy about the precise strength of correlations. One of the aims of this thesis is to explore the impact of this

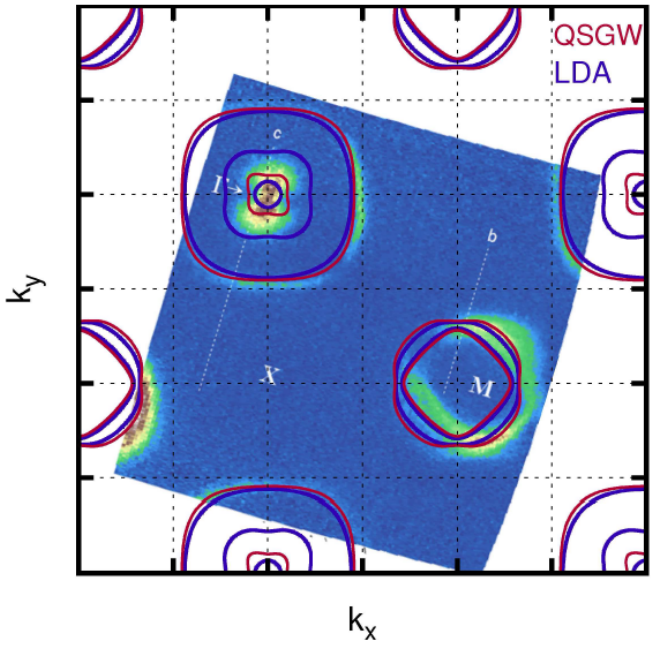

Figure 1.2.5: Fermi surface of LiFeAs from QSGW and LDA compared to the experimental ARPES spectrum from [Borisenko *et al.* (2010)]. $k_z = 0$ plane in the Brillouin zone for 2 Fe atoms. One of the hole pockets at Γ sinks below the Fermi level in GW, and another shrinks drastically, in agreement with photoemission. (From [Tomczak *et al.* (2012b)].)

frequency-dependence of the interaction and to test the validity of this approach in the prediction of the spectral properties of iron pnictides.

1.2.6 Calculations of the Fermi surface

The determination of the Fermi surfaces and low-energy excitations of transition metal pnictides is believed to be a key issue for the understanding of the phase diagram. ARPES has been used to systematically map out quasi-particle dispersions, and to identify electron and hole pockets potentially relevant for low-energy instabilities [Ding *et al.* (2008), Liu *et al.* (2008), Brouet *et al.* (2009), Shimojima *et al.* (2010), de Jong *et al.* (2009), Fink *et al.* (2009), Malaeb *et al.* (2009)]. Density functional theory (DFT) calculations have complemented the picture, yielding information about orbital characters [Singh(2009)], or the dependence of the topology of the Fermi surface on structural parameters or element substitution [Vildosola *et al.* (2008), Mazin *et al.* (2008b)]. DFT within the local density approximation (LDA) or generalized gradient schemes has also served as a starting point for refined many-body calculations addressing band renormalizations and quasi-particle dispersions directly from a theoretical perspective (see e.g. [Haule *et al.* (2008), Aichhorn *et al.* (2009), Aichhorn *et al.* (2010), Ferber *et al.* (2012), Hansmann *et al.* (2010), Anisimov *et al.* (2009), Werner *et al.* (2012), Wang *et al.* (2010)]), and its combination with dynamical mean field theory (LDA+DMFT) is nowadays the state-of-the-art ab initio many-body approach to low-energy properties of transition metal pnictides.

Despite tremendous successes, however, limitations have also been pointed out, e.g. in $Ba(Fe,Co)_2As_2$, where ARPES has evidenced persisting discrepancies in comparison with DFT and DFT+DMFT calculations [Brouet *et al.* (2013)]. In $BaFe_2As_2$, the d_{xy} band is found to form

a third hole pocket in calculations with the experimental structure while a maximum around -150 meV below the Fermi level is captured by photoemission [Liu *et al.* (2009), Vilmercati *et al.* (2009)][1]. This discrepancy was also revealed in hole-doped $Ba_{0.6}K_{0.4}Fe_2As_2$, where the band-top of the inner hole pocket, detected from high-temperature measurements, was found lower than in LDA calculations [Ding *et al.* (2011)].

Interestingly, many-body perturbation theory approximating the self-energy by its first order term in the screened Coulomb interaction W (so-called "GW approximation") results in a substantially improved description: quasi-particle self-consistent (QS)GW [van Schilfgaarde *et al.* (2006)] calculations pinpointed momentum-dependent corrections to the LDA Fermi surfaces (not captured in LDA+DMFT) [Tomczak *et al.* (2012b)]. In LiFeAs for example, the Fermi surface within QSGW shows only two hole pockets around the center of the Brillouin zone [Tomczak *et al.* (2012b)] compared to three in LDA or LDA+DMFT [Singh(2008), Ferber *et al.* (2012), Lee *et al.* (2012)]. The precise topology of the Fermi surface is difficult to know with certainty since one of the bands at the Γ point practically touches the Fermi level [Borisenko *et al.* (2010), Kordyuk *et al.* (2011), Borisenko *et al.* (2012), Lee *et al.* (2012)], so that there is a controversy in the ARPES results as to the possible existence of a very small third hole pocket at Γ. Still, the overall size of the pockets predicted by GW is in better agreement with photoemission measurements than the LDA Fermi surface (see Figure 1.2.5). This is why the combination of advantages offered by GW such as the calculation of non-local exchange and of the non-perturbative computation of correlations effects from DMFT is desirable, which is another objective of this thesis.

1.3 Structure of the thesis

After this snapshot of the current state of research, we describe in a second part the techniques that we use in this manuscript. We present the basics of Angle-Resolved Photoemission Spectroscopy (ARPES), focusing on issues specific to iron pnictides such as the Brillouin zone notations or the matrix elements. We then introduce the *ab-initio* calculation scheme we use, based on Density Functional Theory (DFT) and its combination with Dynamical Mean Field Theory (DMFT), as well as the constrained-random phase approximation (cRPA) approach to the computation of the Hubbard interactions. In a third part, a particular attention is given to the treatment of the frequency-dependence of these interactions. Our contribution to this scheme has consisted in generalizing its combination with Density Functional Theory to dynamical interactions, and to benchmark it on realistic materials. Notably, we have proposed a new expression for the double-counting term, and participated in the development of an effective model which allows to take into account in an approximate way the intershell interaction between the atoms of ligand and metal – a procedure we call "shell-folding". Finally, we present a new method including the Fock-like static screened exchange created by a Yukawa potential in a DFT+DMFT calculation, while getting rid of the LDA exchange and correlation potential. We call this method "SEX+DMFT", inspired by the so-called COHSEX approximation [Hedin(1965), Hedin(1999)] in which the self-energy is interpreted as a Coulomb hole plus screened exchange. This COHSEX self-energy

[1] It is interesting to note that if the arsenic height is moved away from the experimental crystal structure in order to minimize the LDA energy, the position of the d_{xy} band at the Γ point can be dramatically modified [Vildosola *et al.* (2008), Singh(2009), Mazin *et al.* (2008a)]. In some cases, the bandstructure then found can be closer to the ARPES measurements. In particular, in $BaFe_2As_2$ the maximum around -150 meV captured by photoemission is reproduced [Liu *et al.* (2009)]. Within DFT+DMFT, the optimized arsenic height is much closer to the experimental structure [Aichhorn *et al.* (2011), Lee *et al.* (2012)].

is actually a static approximation to the GW self-energy, which itself corresponds to a first-order perturbation theory in the screened Coulomb interaction W. Thus, our SEX+DMFT method can also be understood as a simplified and extremely efficient version of the combined GW+DMFT method [Biermann *et al.* (2003)]. The aim is to combine the nonlocal screened-exchange self-energy with the local self-energy from DMFT with dynamical interaction.

The fourth and fifth parts are devoted to the presentation of our results. We begin by the application of the shell-folding procedure to the frequency-dependent Hubbard interactions of typical members of the iron pnictides families. We compare the zero-frequency values, evaluate the quality of a parametrization by Slater integrals for the full interaction matrix, and study the relative importance of the screening channels. The high-frequency tail is analyzed and compared to the free-electron plasma plasma frequencies. Finally, we focus on the spectral properties of three different iron (or cobalt) pnictides: $BaCo_2As_2$, $CaFe_2As_2$ and $Ba_2Ti_2Fe_2As_4O$. We calculate the spectral functions for all three materials and compare them directly to photoemission measurements – that we have taken in the case of $CaFe_2As_2$. We discuss the reduction of electronic correlations in $BaCo_2As_2$ compared to $BaFe_2As_2$ due to an increased number of electrons. This compound is also an ideal case to assess our SEX+DMFT scheme, and discuss the antagonistic actions of the nonlocal exchange and of the frequency-dependence of the Hubbard interaction on the electronic structure. We then study the tetragonal/collapsed tetragonal phase transition in $CaFe_2As_2$ and show that the discrepancies between the two compounds are driven by the intralayer structure. Finally, in $Ba_2Ti_2Fe_2As_4O$, we find an electron transfer from the Fe_2As_2 layer to the Ti_2As_2O layer induced by correlations, resulting in an effective hole-doping in the Fe 3*d* atomic shell.

We finish by drawing general conclusions on the methodological developments and the effects of correlations in iron pnictides.

Part II

Experimental and theoretical tools for spectroscopy

Chapter 2

Angle-resolved photoemission spectroscopy of iron pnictides

2.1 Angle-resolved photoemission spectroscopy

Photoemission spectroscopy, also called photoelectron spectroscopy, is a technique based on the photoelectric effect [Hertz(1887)]. A light source is used to produce photons of a given energy, which are sent on a sample with a chosen incidence. An electron of the sample can then absorb a photon of the incident beam and escape with a maximum energy $E = \hbar\omega - \phi$ with ϕ the workfunction of the material. By collecting those electrons and analyzing their energies and wavevectors, one can get much information about the electronic structure of a material, such as a direct visualization of the quasiparticle dispersions and of the Fermi surface (for a comprehensive book, see e.g. [Hüfner(2003)], for an introduction, see e.g. [Damascelli(2004)]).

The photoemission process can be understood within the three-step model (see Figure 2.1.3), in which the electron is excited from an initial state to a final state, then travels to the surface, and finally escapes from the solid. But fundamentally, the analysis of the photoemission spectrum is a many-body problem, for the escape of an electron leaves the solid in an excited state that may involve several electrons. This is the one-step model (see Figure 2.1.3), in which the photoemission process is described as an optical transition between a ground-state many-body wavefunction involving N electrons and an excited wavefunction involving N-1 electrons and an escaping planewave. A thorough derivation using the one-step model gives an expression for the photocurrent related to the spectral function $A(k, \omega)$:

$$I(k, \omega) = I_0(k, \nu, \overrightarrow{A}) A(k, \omega) f(\omega) * R(k, \omega) \tag{2.1.1}$$

R being the resolution function of our ARPES experiment, f the Fermi function, and I_0 depending on one-electron matrix elements. The spectral function is a quantity we calculate directly from first principles using Dynamical Mean Field Theory (DMFT, see Section 3.2 for more details). Hence, those two techniques are an ideal match to compare experimental and theoretical results. However, due to the small mean free path of electrons at the kinetic energies we consider [Seah and Dench(1979)] (see Figure 2.1.1), ARPES is a surface probe. This can further complicate the interpretation of the results if the surface electronic structure is different from the bulk (for a discussion in the context of pnictides superconductors, see [Richard

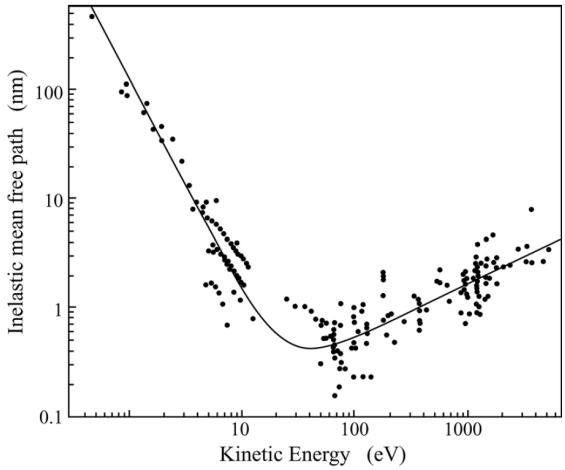

Figure 2.1.1: Inelastic mean free path of electrons inside a solid as a function of kinetic energy (from [Seah and Dench(1979)]).

et al. (2011)]). Furthermore, the component of the wavevector perpendicular to the plane is not conserved during the photoemission process, only the in-plane component is (see Figure 2.1.2).

Photoemission results can be more easily interpreted within an independent particle picture, the sudden approximation and the three-step model (see Figure 2.1.3). Under those assumptions, one can directly study the momentum-resolved band-structure of the solid. It also allows to estimate the perpendicular component of the wave-vector: using a nearly-free electron model for the final state, one has the dispersion:

$$k_\perp = \frac{\sqrt{2m}}{\hbar}\sqrt{E_{kin}cos^2\theta + V_0} \tag{2.1.2}$$

with $V_0 = |E_0| + \phi$ the inner potential, which depends on the material considered, and θ the polar angle as in Figure 2.1.2. In practice, to estimate V_0 one can vary the photon energy – which is possible using synchrotron light – and observe a periodic dispersion of the bandstructure.

2.2 Conventions and notations

All iron pnictides considered in this thesis are from the 122 family, with the body-centered tetragonal $ThCr_2Si_2$-type crystal structure (*I4/mmm* spacegroup), in which the two arsenic atoms of different layers are on top of each other – the layers are translated before they are stacked on top of each other. The three-dimensional Brillouin zone of this family is represented on Figure 2.2.1, with the crystallographic notations for the high-symmetry points. The iron pnictides literature can be ambiguous because high-symmetry points are often denominated differently, due to the different spacegroups and authors considering so-called "one-Fe" or "two-Fe" unit cells. In particular, the crystallographic X point is often named M in the "one-Fe" notation.

In our case and for practical purposes, we will define our points as in Figure 2.2.2, which shows a cut of the Brillouin zone at $k_z = 0$. One can see that our X point is actually not a symmetry point along the ΓXZ direction – where there is no symmetry point a priori. On the other hand, M is a well defined symmetry point on both ΓMΓ and ZMZ directions.

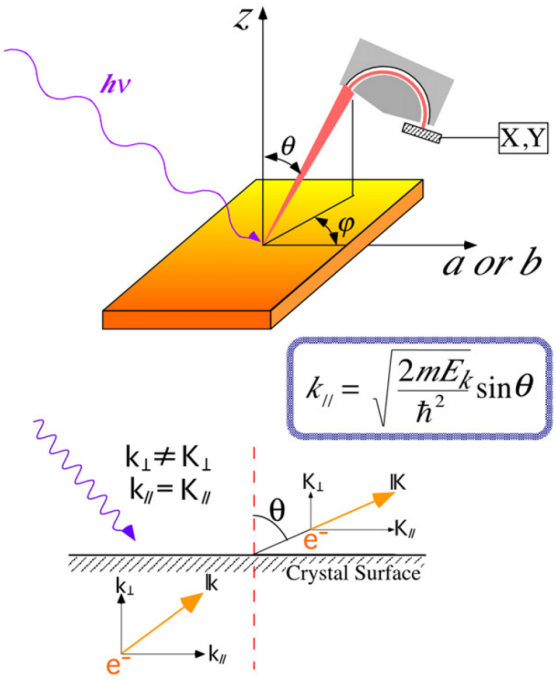

Figure 2.1.2: Principles of an angle-resolved photoemission experiment (from [Richard *et al.* (2011)]).

2.3 Orbital characters and matrix elements

A common procedure in ARPES to obtain information about the orbital characters of electronic states consists in using different light polarizations to highlight or filter certain symmetries (see Figure 2.3.1 for a simple case). The matrix element $I_0(k, \nu, \overrightarrow{A})$ is proportional to:

$$I_0(k, \nu, \overrightarrow{A}) \propto | < \psi_k^f | \overrightarrow{\epsilon} \cdot \overrightarrow{x} | \psi_k^i > |^2 \tag{2.3.1}$$

with $|\psi_k^f >$ and $|\psi_k^i >$ the final and initial states respectively and $\overrightarrow{\epsilon}$ a unit vector along the direction of the polarization of the vector potential $\overrightarrow{A}$. The principle is then to find a mirror plane in which we detect the photoelectrons, for this allows us to classify states into even or odd symmetry with respect to this plane. In that geometry, the final state has to be even to be detected, and so does $\overrightarrow{\epsilon} \cdot \overrightarrow{x} | \psi_k^i >$ in order that the matrix element is not zero. Finally, if $\overrightarrow{\epsilon}$ is in the mirror plane (p polarization) we obtain that $|\psi_k^i >$ has to be even, and if $\overrightarrow{\epsilon}$ is perpendicular to the plane (s polarization) $|\psi_k^i >$ has to be odd.

However, in iron pnictides the problem is more complicated. Due to the fact that the arsenic position is alternating above and below the iron plane, creating a 2-Fe unit cell, there is no such mirror plane containing the ΓM direction as in Figure 2.3.1. Still, a possibility to attribute symmetries to the electronic states is to consider this alternating position of As as a small perturbation potential breaking translation-symmetry and to analyze the bandstructure as a superposition of a "main" in-phase bandstructure in the sense of the 1-Fe unit cell and of the corresponding out-of-phase folded bandstructure [Lin *et al.* (2011), Brouet *et al.* (2012)]. The symmetry of electronic states is found to be different due to the alternating arsenic position. Furthermore, a second effect appears, due to the fact that the final state – close to a free-electron state – is not sensitive to the translation-symmetry breaking potential. As a consequence, the spectral weight is different in the first and second Brillouin zones, such that the bands originating

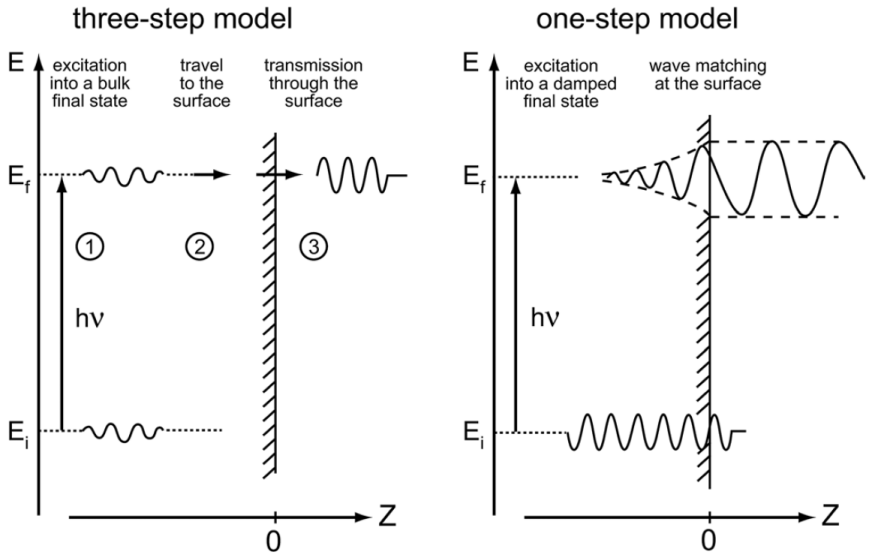

Figure 2.1.3: Three-step and one-step models (from [Hüfner(2003)]).

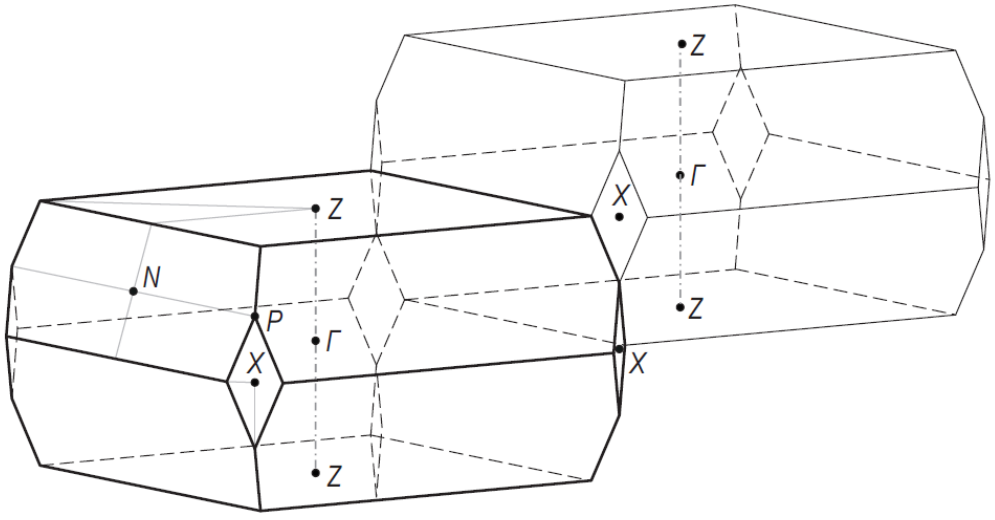

Figure 2.2.1: Body-centered tetragonal first and second Brillouin zone (from [Andersen and Boeri(2011)]).

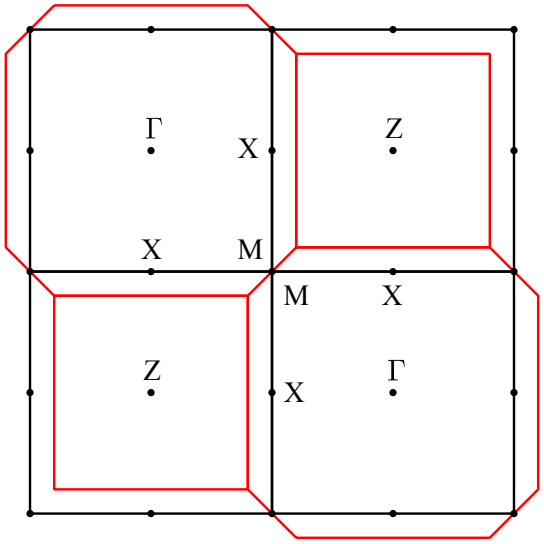

Figure 2.2.2: Cut of the body-centered tetragonal Brillouin zones in the $k_z = 0$ plane (red) along with our choice of notations for the high-symmetry points (black).

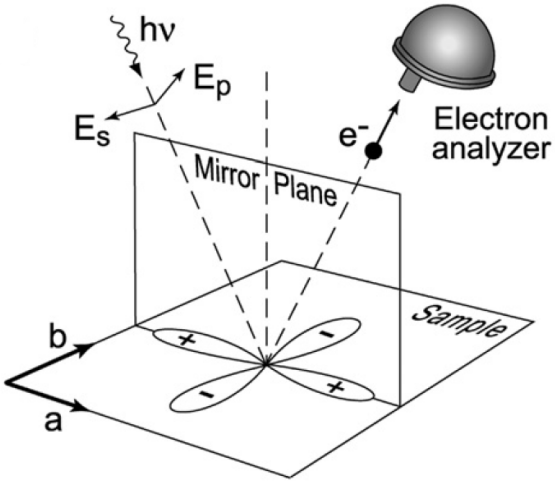

Figure 2.3.1: Example of an ARPES experimental geometry in which the mirror plane is on a $d_{x^2-y^2}$ orbital and the analyzer is aligned with the plane. In p polarization, photoelectrons from this orbital are detected while in s polarization the matrix element is zero. (From [Damascelli(2004)].)

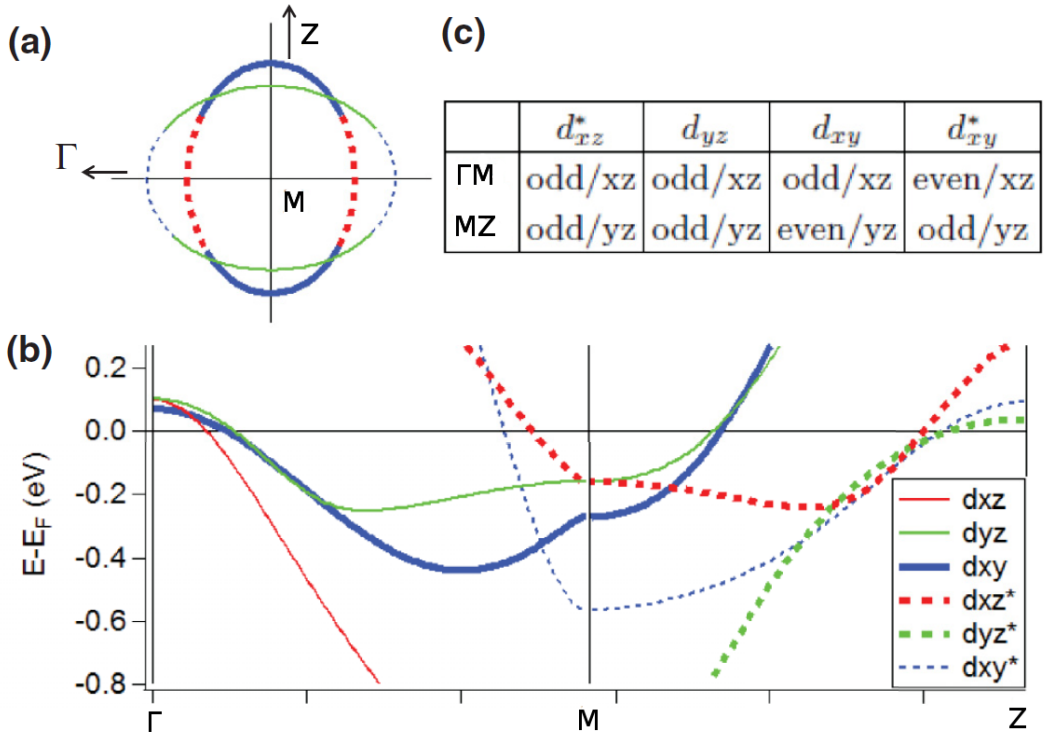

	$d^{\star}_{xz}$	d_{yz}	d_{xy}	$d^{\star}_{xy}$
ΓM	odd/xz	odd/xz	odd/xz	even/xz
MZ	odd/yz	odd/yz	even/yz	odd/yz

Figure 2.3.2: Effect of the 2-Fe unit cell on matrix elements
(a) Sketch of the bands forming the electron pockets. Solid and dotted lines represent the in-phase and out-of-phase orbitals. Colors indicate the main orbital character.
(b) Sketch of the dispersion of the different bands along the path ΓMZ (in the $k_z = 0$ plane). The color sketches the main orbital character, although there may be hybridization with other orbitals.
(c) Symmetries of the different bands forming the electron pockets at M.
(Adapted from [Brouet *et al.* (2012)] using the notations of Figure 2.2.2)

mainly from folding have a small spectral weight in the first Brillouin zone. Those results are summarized in Figure 2.3.2, in particular for the electron pockets around the M point which are the most impacted.

Chapter 3

Electronic structure of materials from *ab-initio* calculations

In this chapter, we introduce the basics of our ab-initio *scheme based on the combination of density functional theory (DFT) with dynamical mean-field theory (DMFT). The idea of this approach is to use DFT as a good approximation for the high-energy states of the system, while the electronic correlations in the low-energy degrees of freedom are treated by the construction of a Hubbard model that will be solved within DMFT. This low-energy model is based on localized orbitals built from the DFT eigenfunctions, and the value of the Coulomb repulsion between them is evaluated by constrained random phase approximation (cRPA). The underlying motivation for such a scheme is to eliminate possible biases by calculating all parameters from first principles.*

3.1 Density Functional Theory

The difficulty and diversity of solid state physics is mainly due to the many-body physics of electrons in a crystal. While for very small systems such as an atom or small molecule one can write and solve the full Schrödinger equation, thus obtaining the eigenvalues and eigenfunctions of the system, the exponential growth of degrees of freedom with the size of the system definitely leads to the failure of such an approach, for even the physical storage of these information would quickly become impossible.

The success of density functional theory is based on replacing this inextricable problem with a much simpler – but still difficult – one: finding the ground-state density of the system. From this ground-state density one can then calculate other properties of the system.

3.1.1 The Hohenberg-Kohn theorem

The Hohenberg-Kohn theorem [Hohenberg and Kohn(1964)] is at the heart of density functional theory. It establishes that:

- There is a one-to-one correspondence between any external potential $v^{ext}(r)$ acting on a system of interacting electrons and the ground state density $\rho_0(r)$ of this system.

- All ground-state expectation values of physical observables are determined by the ground state density $\rho_0(r)$.
- For a given external potential, there exists a universal functional of the density $F[\rho(r)]$ – in the sense that it is independent of the external potential – leading to the energy $E[\rho(r)]$ of the system with a density $\rho(r)$:

$$E[\rho(r)] = F[\rho(r)] + \int v^{ext}(r)\rho(r)d^3r \tag{3.1.1}$$

The ground-state density of the system then corresponds to the minimum $E_0[\rho_0(r)]$ of this functional. This dramatically simplifies the many-body problem, though it only leads to the ground-state properties of the system, and it does not explain how to calculate the functional $F[\rho(r)]$.

3.1.2 The Kohn-Sham equations

The idea of Kohn and Sham [Kohn and Sham(1965)] was to replace the system of interacting electrons by a fictitious effective model of non-interacting particles but with the same density. This leads to a set of one-particle Schrödinger equations:

$$\left[-\frac{\hbar^2}{2m_0}\nabla^2 + v^{KS}[\rho](r)\right]\psi_{n,k}(r) = \epsilon_{n,k}\psi_{n,k}(r) \tag{3.1.2}$$

where $v^{KS}[\rho]$ is chosen such that the ground-state density of this non-interacting problem is equal to ρ_0. In other words, all interacting effects are cast into the Kohn-Sham potential acting on non-interacting particles. Because at the energy minimum the density is stationary, it is then self-consistently determined as:

$$\rho(r) = \sum_{\epsilon_{n,k}\leq\epsilon_F} |\psi_{n,k}(r)|^2 \tag{3.1.3}$$

We stress that formally, the Kohn-Sham eigenvalues and eigenfunctions have no constraint on their resemblance to the electronic states of the original interacting system, only the ground-state density does. Moreover, one still has to find an expression for v^{KS}. Yet, in practice the Kohn-Sham states astonishingly lead to very good approximations for many properties of different systems, which is why DFT is now so popular.

3.1.3 The local density approximation for the exchange-correlation potential

The Kohn-Sham potential is usually decomposed between an external potential created by the positive ions, a Hartree potential describing the mean Coulomb interaction between electrons and an exchange-correlation potential containing all the rest:

$$v^{KS}(r) = v^{ext}(r) + v^{Hartree}(r) + v^{xc}[\rho](r) \tag{3.1.4}$$

with $v^{ext}(r)$ the external potential, $v^{Hartree}(r) = \int \frac{\rho(r')}{|r-r'|} d^3r'$ the Hartree potential, and $v^{xc}[\rho](r)$ the exchange-correlation potential defined as:

$$v^{xc}[\rho](r) = \frac{\delta E^{xc}[\rho]}{\delta \rho(r)} \tag{3.1.5}$$

where $E^{xc}[\rho]$ is the exchange-correlation energy of the non-interacting system, defined from the functional $F[\rho]$ of the original system and the kinetic and Hartree energy of non-interacting system (respectively T_{ni} and $E^{Hartree}$):

$$E^{xc}[\rho] = F[\rho] - T_{ni}[\rho] - E^{Hartree}[\rho] \tag{3.1.6}$$

Until now, the scheme is still exact and would allow the calculation of all ground-state properties. The problem is that there is no known expression for $F[\rho]$. Thus, approximations have to be made for the exchange-correlation potential v^{xc}. One of the most popular is the local density approximation (LDA) in which:

$$E^{xc}_{LDA}[\rho] = \int d^3r \rho(r) \epsilon^{xc}_{LDA}(\rho(r)) \tag{3.1.7}$$

where $\epsilon^{xc}_{LDA}(\rho)$ is the energy density of an homogeneous electron gas with a uniform density ρ. It means that the exchange-correlation potential at each point r, $v^{xc}[\rho](r)$, is replaced by $\epsilon^{xc}_{LDA}(\rho(r))$, hence approximating locally the system as an homogeneous electron gas with uniform density $\rho(r)$. This function is not known analytically, but interpolation formulas based on Quantum Monte Carlo calculations are available [Ceperley and Alder(1980)].

The LDA is not well controlled and, when combined with DMFT, leads to double-counting problems (see Section 3.3). However, it is one of the most simple and widely used approximations, which is why we will use it throughout this thesis.

3.1.4 The Hartree-Fock method

The Hartree-Fock assumption consists in writing the wavefunction of the system as a Slater determinant of single-particle states $\psi_{i,\sigma}(r)$, in order to fulfill the Pauli principle. The variational principle then allows us to decouple the full Schrödinger equation into a set of single-particle equations, similar to the above sections if we replace the Kohn-Sham potential by the Hartree-Fock potential:

$$v^{HF}_{i,\sigma}(r) = v^{ext}(r) + v^{Hartree}(r) + v^{x}_{i,\sigma}(r) \tag{3.1.8}$$

$$v^{x}_{i,\sigma}(r) = -\sum_{j=1}^{N_e} \int dr' \psi^*_{j,\sigma}(r') \psi_{i,\sigma}(r') \frac{1}{|r-r'|} \frac{\psi_{j,\sigma}(r)}{\psi_{i,\sigma}(r)} \tag{3.1.9}$$

$v^{x}_{i,\sigma}(r)$ is the exchange potential, also called the Fock term, and accounts for the lowered repulsion between electrons of same spin because the spatial part of their wavefunctions is antisymmetric. It is a static and non-local potential, in the sense that it depends on the electronic wavefunctions in the whole Brillouin zone, and not only at point r.

Hartree-Fock theory usually does not work well for solids, in which it severely overestimates the gap of insulators and the bandwidth of metals. Indeed, as the screening of the Coulomb potential is not taken into account the magnitude of exchange is overestimated. In Chapter 5, we propose to use a screened Yukawa potential for an approximation of the exchange term in the solid, that we combine with the correlation term obtained by DMFT.

3.2 Combination of Density Functional Theory with Dynamical Mean Field Theory (DFT+DMFT)

In the study of electronic properties of materials, theories based on the view of a single electron in an effective periodic potential have already produced outstanding results. In particular, Density Functional Theory has been able to produce ab-initio quantitative predictions for many chemical and physical systems [Kohn(1999)]. However, that particular view has proved unable to explain more exotic comportment, such as the Mott insulator or superconductivity, which are intrinsically due to many-body effects and correlations between electrons. Furthermore, many physical properties such as the photoemission spectrum are linked to excitations of the system, which are fundamentally out of reach from DFT.

More generally, many compounds with partially filled $3d$ or $4f$ shells and not necessarily very strongly correlated do not display a single-particle-like spectral function, nor solely Hubbard bands that could be obtained via simpler formalism such as LDA+U [Anisimov *et al.* (1993), Anisimov *et al.* (1997a), Petukhov *et al.* (2003)], but a renormalized quasi-particle peak associated with incoherent excitations. As discussed in Chapter 1, iron pnictides are the typical intermediate case in which it is necessary to use a theory able to probe both strongly and weakly correlated regimes, such as Dynamical Mean Field Theory (DMFT).

Over the last decades, DMFT has obtained many success in providing qualitative understanding but also quantitative spectral functions directly comparable to experiments. We present below a summary of DMFT basic principles (for extensive reviews, see [Georges *et al.* (1996), Georges(2004), Kotliar *et al.* (2006), Bulla(2006)]).

3.2.1 Model for correlated electrons

Let us consider a given crystal, and take a simple model with only one atomic level per site, which can harbor a maximum of two electrons with opposite spin. If we add an electron to the crystal, it is more energetically favorable for it to access an unoccupied site than an occupied one, because of the additional repulsion created by the already-present electron. This is probably the main modification introduced by correlations on a single-electron model, but it is quite opposed to the usual delocalized point of view of Bloch states. In the limit where this local repulsion is large, the most adapted point of view is to consider the electrons as localized in space.

To take into account the competition between the delocalization of electrons and these local effects, a simple model – but containing a very rich physics – was introduced by Hubbard [Hubbard(1963), Hubbard(1964)]. The idea is to include correlations in the original Hamiltonian by adding a Coulomb repulsion when two electrons are on the same atomic site. We consider only a single orbital which can contain a maximum of two electrons. This means that there are three possible energy values for one atomic level depending on its occupation number:

- unoccupied, eigenvector $|0>$ with energy 0
- a single electron, eigenvectors $|\uparrow>$or $|\downarrow>$ with energy ϵ_0
- two electrons, eigenvector $|\uparrow\downarrow>$ with energy $2\epsilon_0 + U$

where U is such that, with χ the wavefunction associated to the considered atomic level on the site R:

$$U \sim \int dr dr' |\chi_R(r)|^2 W^r(r - r') |\chi_R(r')|^2$$

with W^r the partially screened interaction between electrons (see Section 3.4 for more details on the calculation of U).

We also consider the transition probabilities between two nearest-neighbors sites R, R' which give birth to the hopping terms $t_{R,R'}$. Using the second quantization formalism, the Hamiltonian of this Hubbard model is then written:

$$H = - \sum_{R,R',\sigma} t_{R,R'} c^\dagger_{R,\sigma} c_{R',\sigma} + \epsilon_0 \sum_{R,\sigma} n_{R,\sigma} + U \sum_R n_{R,\uparrow} n_{R,\downarrow}$$

This reflects the competition between two phenomena: the electronic correlations introduced by U which tends to localize electrons and the kinetic delocalization characterized by the hopping terms. Depending on the ratio U/W, with W the bandwidth (related to the $t_{R,R'}$), we can qualify our system as strongly or weakly correlated.

For simplicity we will limit our description to the above single orbital model, which can be easily generalized to multiorbital systems.

3.2.2 Objective

The aim is to determine the Green's function of a correlated system. From this Green's function, one is able to compute different physical quantities, including response functions, the self-energy and the spectral density function. An introduction to Green's functions in Matsubara frequencies and the expression of response functions is given in Appendix A. The problem is that the Hubbard model introduced above cannot be solved analytically. Dynamical Mean Field Theory is at present one of the most successful methods to solve it numerically, although with some approximations. The interesting point, and the reason why this theory is called "dynamical", is the time-dependence of the Weiss field describing the bath to which the impurity is coupled, which delivers information about the evolution of the system after an excitation.

3.2.3 Principles of Dynamical Mean Field Theory

In a few words, DMFT consists in replacing the N-site lattice problem by a model of one site coupled to a bath, thus having to make a spatial local approximation (Mean Field, which makes us lose the momentum-dependency of the self-energy) but saving the dynamical quantum fluctuations (Dynamical). We can also remark that the principle is similar to the classical Ising

spins mean-field resolution, except that we have quantum fluctuations: the states of the single site and of the bath evolve when they interact with each other.

In practice, it works on the basis of two self-consistent equations, that constitute the "DMFT loop".

The Anderson impurity model

Let us begin by introducing the model used to replace our lattice. Different impurity models can be used (one site of the lattice being identified to an impurity by opposition to the bath), but we will focus on the Anderson impurity model. Here, the impurity is still affected by the effects of correlations, through U, and is coupled to the non-interacting bath states l (of energy ϵ_l) by transition terms V_l. The creation and annihilation operators on the impurity are written $c^\dagger$ and c respectively, while the corresponding operators for the bath are written $a^\dagger$ and a. $n = c^\dagger c$ is the number of electrons on the impurity. We can decompose the Hamiltonian into three parts. One is related to the bath, another to the impurity, and the third one to the coupling between the bath and the impurity:

$$H_{AIM} = H_{bath} + H_{atom} + H_{coupling} \tag{3.2.1}$$

with

$$H_{atom} = U n_\uparrow n_\downarrow + (\epsilon_0 - \mu)(n_\uparrow + n_\downarrow)$$

$$H_{coupling} = \sum_{l,\sigma} V_l (a^\dagger_{l,\sigma} c_\sigma + c^\dagger_\sigma a_{l,\sigma})$$

$$H_{bath} = \sum_{l,\sigma} \epsilon_l a^\dagger_{l,\sigma} a_{l,\sigma}$$

Back to the lattice

The condition to simulate the lattice problem by the impurity model is that the local Green's function of the lattice, defined as the sum over the momentum k of the momentum-resolved Green's functions, is equal to the Green's function of the model.

Actually, this Green's function of the impurity model only depends on a hybridization function Δ which integrates all the degrees of freedom of the bath:

$$\Delta(i\omega_n) = \sum_l \frac{V_l^2}{i\omega_n - \epsilon_l}$$

through the formalism of an effective action S_{eff}:

$$S_{eff} = -\int_0^\beta d\tau \int_0^\beta d\tau' \sum_\sigma c^\dagger_\sigma(\tau) \mathcal{G}_0^{-1}(\tau - \tau') c_\sigma(\tau') + U \int_0^\beta d\tau n_\uparrow(\tau) n_\downarrow(\tau)$$

in which the Weiss dynamical mean field $\mathcal{G}_0$ is defined as:

$$\mathcal{G}_0^{-1}(i\omega_n) = i\omega_n + \mu - \epsilon_0 - \Delta(i\omega_n)$$

This means that the impurity model is fully described by the effective field $\mathcal{G}_0$ and the Hubbard U.

If we assume that we can solve the model and find the associated Green's function G_{imp}, we then get access to the impurity model self energy:

$$\Sigma_{imp}(i\omega_n) \equiv \mathcal{G}_0^{-1}(i\omega_n) - G_{imp}^{-1}(i\omega_n)$$

We now make the DMFT approximation: identifying the impurity model self-energy with the lattice self-energy,

$$\Sigma(k, i\omega_n) \simeq \Sigma_{imp}(i\omega_n) \tag{3.2.2}$$

In so doing, we lose all the non-local components of the self-energy (there is no momentum dependence of the self-energy any more) and approximate the local component by that of the model.

Consequently, the lattice local Green's function G_{local} is computed as:

$$G_{local}(i\omega_n) = \int dk G_{local}(k, i\omega_n) = \int d\epsilon \frac{D(\epsilon)}{i\omega_n + \mu - \Sigma_{imp}(i\omega_n) - \epsilon} \tag{3.2.3}$$

with $D(\epsilon)$ the non-interacting density of states of the lattice.

We have our first equation: from $\mathcal{G}_0$ we have obtained the local Green's function of the lattice.

Self-consistency condition

The self-consistency condition (the correspondence between the lattice and the model) provides us with the second equation: we must have $G_{local} = G_{imp}$. It can be expressed as:

$$\mathcal{G}_0^{-1} = G_{local}^{-1} + \Sigma$$

This means that the Green's function of an electron in the bath is self-consistently determined, such that the impurity's Green's function is exactly equal to the local Green's function of the lattice – within the DMFT approximation $\Sigma(k, i\omega_n) \simeq \Sigma(i\omega_n)$.

DMFT loop

In practice, this system is solved in an iterative way (the loop), until convergence. The whole process is summarized in Figure 3.2.1.

The technical challenge is the resolution of the impurity model, which is computationally demanding but at present is relatively accessible, notably thanks to the implementation of a toolbox open to the scientific community [Ferrero and Parcollet(2011)]. Furthermore, another

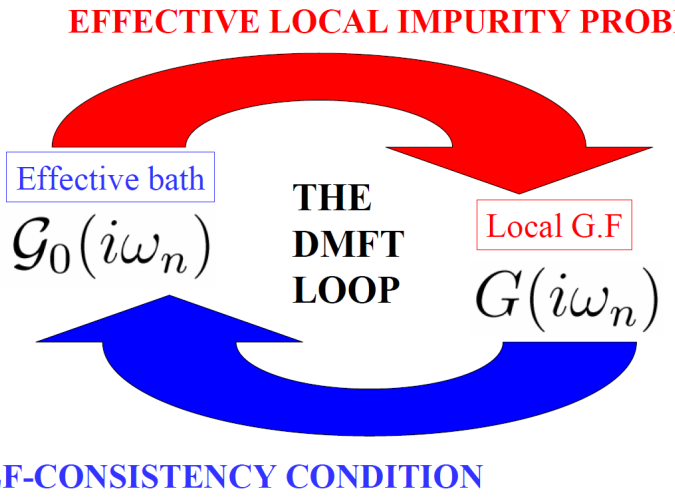

Figure 3.2.1: The DMFT iterative loop. The following procedure is generally used in practice: starting from an initial guess for $\mathcal{G}_0$, the impurity Green's function G_{imp} is calculated by using an appropriate solver for the impurity model (top arrow). The impurity self-energy is also calculated from $\Sigma_{imp} = \mathcal{G}_0^{-1}(i\omega_n) - G_{imp}^{-1}(i\omega_n)$. This is used in order to obtain the on-site Green's function of the lattice model by performing a k-summation (or integration over the free density of states): $G_{loc} = \sum_k \left[i\omega_n + \mu - \epsilon_k - \Sigma_{imp}(i\omega_n)\right]^{-1}$. An updated Weiss function is then obtained as $\mathcal{G}_{0,new}^{-1} = G_{loc}^{-1} + \Sigma_{imp}$, which is injected again into the impurity solver (bottom arrow). The procedure is iterated until convergence is reached. (From [Georges(2004)])

technical limit to the applications of DMFT is the analytic prolongation of the self-energy to real frequencies, which requires very precise and low-energy data and hence increases the necessity for huge computational resources.

3.2.4 Combination of DFT and DMFT

In realistic calculations, all electrons cannot be treated within DMFT since the computation would be too heavy and the local picture might not be useful for delocalized electrons such as those in *s* and *p* orbitals. Moreover, it is interesting to benefit from long-range and momentum-dependent effects better described in DFT. The idea is thus to combine the one-particle Hamiltonian from DFT with an improved description of the correlated states within DMFT [Anisimov *et al.* (1997b), Lichtenstein and Katsnelson(1998)]. To do so, we construct a low-energy model adapted to the material under study by choosing a set of localized orbitals which are described by a Hubbard model, solved within DMFT. The full DFT+DMFT Hamiltonian is then written as:

$$H^{DFT+DMFT} = H^{DFT} + H^{int} + H^{DC} \tag{3.2.4}$$

In which H^{DFT} corresponds to the one-particle Hamiltonian obtained by Density Functional Theory:

$$H^{DFT} = \sum_{i,j,\sigma,m} h^{ij}_{m_1 m_2} c^{\dagger}_{im_1\sigma} c_{jm_2\sigma} \tag{3.2.5}$$

where $c^{\dagger}$ and c are creation and annihilation operators, i and j different sites of the crystal, m represent different orbitals, σ is the spin and h is the Hamiltonian.

H^{int} corresponds to the interaction Hamiltonian within the low-energy model. For instance, we can choose an on-site static Hubbard Hamiltonian with density-density interactions:

$$H^{int} = \frac{1}{2}\sum_i U \sum_{(m_1\in C,\sigma)\neq(m_2\in C,\sigma')} n_{im_1\sigma}n_{im_2\sigma'} \tag{3.2.6}$$

where C is the subspace of correlated orbitals.

Finally, H^{DC} is the double-counting Hamiltonian due to effects taken into account both in H^{DFT} and H^{int}. It will be discussed in more details in Section 3.3.

3.2.5 Basis-set and localized Wannier-like orbitals

The scheme combining DFT and DMFT that we use is based on the Wien2k electronic structure code [Blaha *et al.* (2001)], which develops the wavefunctions on a linearized augmented plane waves (LAPW) basis set. In short, the unit cell is divided into muffin-tin spheres around the atoms, and interstitial regions between the spheres (we will ignore the technical details introduced by the local orbitals part in the LAPW+lo basis). The eigenfunctions $\psi^{\sigma}_{n,k}(r)$ of the Kohn-Sham Hamiltonian are then expanded into the LAPW basis $\psi^{K,\sigma}_{k}(r)$ (with K a reciprocal lattice vector), basically consisting in a plane-wave expansion in the interstitial region and an atomic-like orbitals expansion in the muffin-tin spheres S^{α}_{MT}:

$$\psi^{\sigma}_{n,k}(r) = \sum_{K}^{K_{max}} c^{n,\sigma}_{K}(k)\psi^{K,\sigma}_{k}(r)$$

$$\psi^{K,\sigma}_{k}(r) = \begin{cases} \frac{1}{\sqrt{\Omega}}e^{i(k+K)r} & \textit{outside spheres} \\ \sum_{l,m}[A^{\alpha,\sigma}_{l,m}(k+K)u^{\alpha,\sigma}_{l}(r,E^{\alpha}_{l}) & \\ +B^{\alpha,\sigma}_{l,m}(k+K)\dot{u}^{\alpha,\sigma}_{l}(r,E^{\alpha}_{l})]Y_{l,m}(\theta,\phi) & \textit{inside sphere } S^{\alpha}_{MT} \end{cases} \tag{3.2.7}$$

in which $Y_{l,m}(\theta,\phi)$ are the spherical harmonics, r in each sphere is defined with respect to the center of the sphere, Ω is the volume of the unit cell and $u^{\alpha,\sigma}_{l}(r,E^{\alpha}_{l})$ is the solution of the radial Schrödinger equation for the free atom α at the energy ϵ in the potential inside the sphere $V(r)$:

$$\left[\frac{-d}{dr^2} + \frac{l(l+1)}{r^2} + V(r) - E^{\alpha}_{l}\right] r u^{\alpha,\sigma}_{l}(r,E^{\alpha}_{l}) = 0 \tag{3.2.8}$$

normalized within the muffin-tin sphere:

$$\int_0^{R^{\alpha}_{MT}} r^2 \left|u^{\alpha,\sigma}_{l}(r,\epsilon)\right|^2 dr = 1$$

The coefficients $A^{\alpha,\sigma}_{l,m}(k+K)$ and $B^{\alpha,\sigma}_{l,m}(k+K)$ are obtained by requiring the continuity of the wavefunction in value and slope at the muffin-tin radius, and E^{α}_{l} is a well chosen linearization energy close to the center of the band.

Expanding the $\psi^{\sigma}_{n,k}(r)$ in this basis allows us to attribute orbital characters l, m to bands as a function of their coefficients $A^{n,\alpha,\sigma}_{l,m}(k) = \sum_K c^{n,\sigma}_K(k) A^{\alpha,\sigma}_{l,m}(k+K)$, which would be equal to 1 in the case of a free atom with a purely atomic orbital of l, m character. Such statement naturally leads to the construction of localized Wannier-like orbitals $\chi^{\alpha,\sigma}_{l,m}$ as in [Aichhorn *et al.* (2009)] and of associated projectors $P^{\alpha,\sigma}_{l,m,n}(k)$:

$$P^{\alpha,\sigma}_{l,m,n}(k) \quad = \quad < \chi^{\alpha,\sigma}_{k,l,m} | \psi^{\sigma}_{n,k} > \tag{3.2.9}$$

We construct these orbitals within a limited energy window $\mathbb{W}$ corresponding to our low-energy model, such that:

$$|\chi^{\alpha,\sigma}_{k,l,m} >= \sum_{n \in \mathbb{W}} P^{\alpha,\sigma *}_{l,m,n}(k) |\psi^{\sigma}_{n,k} > \tag{3.2.10}$$

and in real space:

$$|\chi^{\alpha,\sigma}_{R,l,m} >= \frac{1}{\sqrt{N}} \sum_k e^{-ikR} |\chi^{\alpha,\sigma}_{k,l,m} > \tag{3.2.11}$$

In practice, this means that we first define temporary projectors $\tilde{P}^{\alpha,\sigma}_{l,m,n}(k)$ and Wannier orbitals $\tilde{\chi}^{\alpha,\sigma}_{k,l,m}$ as:

$$\tilde{P}^{\alpha,\sigma}_{l,m,n}(k) = A^{n,\alpha,\sigma}_{l,m}(k)$$

and the temporary Wannier orbitals $\tilde{\chi}^{\alpha,\sigma}_{k,l,m}$ are orthonormalized[1] to obtain $\chi^{\alpha,\sigma}_{k,l,m}$. Those Wannier functions are the localized orbitals on which we construct our Hubbard model.

3.3 Double-Counting correction for the DFT+DMFT combination

3.3.1 The Double-Counting problem

The aim of combining Density Functional Theory and Dynamical Mean Field Theory is to describe more precisely the electronic correlations in the correlated shell caused by the Coulomb repulsion. However, the effects of the Coulomb repulsion are already partially taken into account in DFT via the Hartree term and the exchange-correlation potential. This leads to a redundancy with the introduced Hubbard model, that one needs to sort out. This issue was historically already identified in the framework of LDA+U [Anisimov *et al.* (1991), Anisimov *et al.* (1993)].

The underlying problem of this double-counting term is that DFT is based on the total density of the system, while the many-body part only deals with a limited number of orbitals [Petukhov *et al.* (2003)]. As a result, the correlations applied to the chosen set of orbitals in DFT are caused by all the electrons in the solid, while DMFT only considers the low-energy screened interaction between correlated electrons. Moreover, approximations have to be made for the exchange-correlation potential (for instance the LDA), which do not have a controlled diagrammatic expression that could be substracted later. The cohabitation of these two incompatible frameworks has lead to several propositions for the double-counting. Two popular expressions that we will describe below are the Fully Localized Limit [Anisimov

[1] Indeed, due to the truncation of the LAPW basis the temporary Wannier orbitals are not orthonormal.

et al. (1993)] and the Around Mean Field [Anisimov *et al.* (1991)], but other possibilities have been considered [Lichtenstein *et al.* (2001), Held(2007)].

The best choice, when there is one, usually depends on the considered material and on how the assumptions upon which the double-counting expression is based on are adapted. Benchmarks between FLL and AMF double-counting in the LDA+U scheme have been done in [Czyżyk and Sawatzky(1994), Ylvisaker *et al.* (2009)]. For LDA+DMFT, a systematic study has been conducted in the case of NiO [Karolak *et al.* (2010)]. In all these studies the choice of the double-counting has been shown to have important impact on the calculated physical properties of the system. A comparison between FLL and AMF double counting terms calculated using the impurity density has also been made in the case of LaFeAsO [Aichhorn *et al.* (2011)]. Notably, it has been shown that the charge self-consistency loop of LDA+DMFT reduces efficiently the discrepancies of the spectral properties between the two schemes that show up in the case of a one-shot calculation. Another interesting result was the proximity of the spectral properties of the one-shot calculation with FLL to the charge-converged final result. On the other hand, the AMF formula gives better results for the equilibrium position of the arsenic atom. An around mean field formulation seems indeed more adapted in the context of LaFeAsO, a metallic compound with weak correlations and high Hund's coupling which tends to balance the electrons between all orbitals.

3.3.2 Fully localized limit

For a Hubbard hamiltonian $H = Un_\uparrow n_\downarrow$, the fully localized limit consists in making the assumption that each electron is perfectly localized on one single orbital. If there is only 0 or 1 electron on the atom, then the interaction energy is equal to 0. If two electrons are present, this energy has a value U.

For a multiorbital system with orbitals i, the Hamiltonian generalizes to

$$H^{Hubbard} = \frac{1}{2}U \sum_{i,\sigma \neq j,\sigma'} n_{i,\sigma} n_{j,\sigma'}$$

thus giving birth to an energy term in the fully localized limit:

$$E^{DC} = \frac{1}{2}Un(n-1)$$

with n the total number of electrons on the atom. The associated potential is:

$$V(n) = \frac{\partial E^{DC}}{\partial n} = U(n - \frac{1}{2})$$

This is what is usually taken for the double-counting correction. When dealing with a crystal with non-integer mean number of electrons on one atom, this is not rigorous but since the fully localized double counting is already an assumption in itself, it is not so crucial. The idea behind is that LDA correctly estimates the energy of the system. Thus, if we add a Hubbard Hamiltonian we should substract the total energy created by this term. In the case of strongly correlated, localized electrons, then the atomic limit is supposed to be a good estimation for this energy.

The generalization of double counting to multiorbital system with Hubbard parameter U and Hund's coupling parameter J has been treated in the same spirit [Czyżyk and Sawatzky(1994)] and can be written:

$$H_{DC-UJ} = \frac{1}{2}Un(n-1) - \frac{1}{2}J\left(n_\uparrow(n_\uparrow - 1) + n_\downarrow(n_\downarrow - 1)\right)$$

3.3.3 Around mean-field limit

The idea behind the AMF double-counting is that Density-Functional Theory is a mean-field theory, in the sense that it describes the mean value of the Hubbard Hamiltonian, without the quantum fluctuations.

We can write:

$$\begin{aligned} H^{Hubbard} &= \sum_{i\sigma \neq j\sigma'} \frac{1}{2}U(i\sigma, j\sigma')(n_{i\sigma} - < n_{i,\sigma} > + < n_{i\sigma} >)(n_{j\sigma'} - < n_{j,\sigma'} > + < n_{j\sigma'} >) \\ &= \sum_{i\sigma \neq j\sigma'} \frac{1}{2}U(i\sigma, j\sigma')(\delta_{i\sigma} + < n_{i\sigma} >)(\delta_{j\sigma'} + < n_{j\sigma'} >) \\ &= \sum_{i\sigma \neq j\sigma'} \frac{1}{2}U(i\sigma, j\sigma')\left[\delta_{i\sigma}\delta_{j\sigma'} + < n_{i\sigma} > \delta_{j\sigma'} + < n_{j\sigma'} > \delta_{i\sigma} + < n_{i\sigma} >< n_{j\sigma'} >\right] \end{aligned}$$

In a mean field theory the $\delta_{i\sigma}\delta_{j\sigma'}$ is ignored and we have the final result:

$$H^{DC} = \sum_{i\sigma \neq j\sigma'} \frac{1}{2}U(i\sigma, j\sigma')\left[< n_{j\sigma'} > n_{i,\sigma} + < n_{i,\sigma} > n_{j,\sigma'} - < n_{i,\sigma} >< n_{j,\sigma'} >\right]$$

$$V_{i,\sigma}^{DC} = \frac{\partial H^{DC}}{\partial n_{i,\sigma}} = \sum_{j,\sigma' \neq i,\sigma} U(i\sigma, j\sigma') < n_{j\sigma'} > \tag{3.3.1}$$

Most of the time, this expression is considered in the case where all orbitals have the same electronic density:

$$\forall(i,\sigma) \ < n_{i\sigma} >= \frac{N_\sigma}{n_{orb}} \tag{3.3.2}$$

Where N is the total number of electrons in the correlated shell. With this constraint and for a Slater-parametrized Hubbard Hamiltonian (see Section 3.4), noting $U = F^0$ and $J = \left(F^2 + F^4\right)/14$ for *d* orbitals, the AMF double-counting reduces to:

$$V_{AMF}^{DC-UJ} = U\left(N - \frac{N_\sigma}{n_{orb}}\right) - J\left(N_\sigma - \frac{N_\sigma}{n_{orb}}\right) \tag{3.3.3}$$

While in Section 3.3.2 the estimation of the energy is made in the case of fully localized electrons, here it is supposed that the mean field limit close to DFT is still a good starting point. The best choice for the DC term ultimately depends on the system we consider.

3.3.4 Why should we have an orbital-dependent DC?

It is clear that most of the time, because of crystal field, the orbital occupancies can be different. This naturally makes the shift in equation 3.3.1 orbital-dependent. However, if we go back to history, early band calculations used a "muffin-tin" approximation in which the charge density in the sphere was averaged. This used to fix the value of the LDA Hartree and exchange-correlation potentials within the sphere, since they were calculated from this average density. As a consequence, the idea was basically that the DC term should be computed in a similar way than the LDA Hartree and exchange-correlation potentials, and thus had to keep the same orbital-independency [Anisimov *et al.* (1991), Lichtenstein *et al.* (1995)]. This means that the orbital densities were averaged, such as in equations 3.3.2 and 3.3.3.

However, as we are now using a full-potential method, this is not true anymore [Blaha *et al.* (2001)], for the LAPW (APW+lo) method expands the potential in the following form:

$$V(r) = \begin{cases} \sum_{LM} V_{LM}(r) Y_{LM}(\mathbf{r}) & \textit{inside sphere} \\ \sum_{\mathbf{K}} V_{\mathbf{K}} e^{i\mathbf{K}\cdot\mathbf{r}} & \textit{outside sphere} \end{cases}$$

and the charge densities analogously. Thus no shape approximations are made, which is exactly the meaning of the term "full potential". The "muffin-tin" approximation used in early band calculations corresponds to retaining only the l = 0 component inside the sphere (which exactly means that the density is averaged) and only the K = 0 component outside. This is why we choose to use an orbital-dependent DC term. Indeed, while at each point of the space the potentials are orbital-independent since they only depend on the total density, we suppose that the different spatial distribution of electrons in the local orbitals can potentially allow for an orbital-dependent value of the average potential they feel.

3.3.5 Multi-orbital AMF double-counting: another point of view

Density Functional Theory mimics the real density of the system by the density of a system of independent particles. It is theoretically exact: if one had an exact expression for the exchange-correlation potential V_{xc} the density and energy would be correctly described. Still, the Kohn-Sham wavefunctions should not correspond to the real system wavefunctions, and many-body theory would be necessary to describe the physics of the system in the case of correlated compounds.

However, let us examine the case where the Kohn-Sham one-particle Hamiltonian is a good approximation to the quasiparticles of the system, as it surprisingly happens in many compounds, for instance the nickel pnictide $SrNi_2P_2$ ([Zeng *et al.* (2014)], in preparation). We construct the same DFT+DMFT framework as in the previous sections by adding a Hubbard Hamiltonian to the DFT part. The total Hamiltonian is:

$$H = H^{DFT} + \left(H^{Hubbard} - H^{DC}\right) \tag{3.3.4}$$

Where H^{DC} is the double-counting Hamiltonian we have to substract because both H^{DFT} and $H^{Hubbard}$ contain derived effects of the Coulomb repulsion potential between electrons. We choose to express H^{DC} as an orbitally-resolved shift of the chemical potential:

$$H^{DC} = \sum_{i,\sigma} V^{DC}_{i,\sigma} n_{i,\sigma} \tag{3.3.5}$$

The problem of H^{DC} is usually that H^{DFT} is not orbitally resolved since it relies on the full density of the system, while $H^{Hubbard}$ considers low-energy degrees of freedom of a reduced number of orbitals. Still, in this ideal case, our aim is not to substract an orbitally-resolved H^{DC} to H^{DFT}. On the other hand, since H^{DFT} is supposed to describe well the physics of the system, we just want that $H^{Hubbard}$ and H^{DC} do not impact the ground state. For a system of independent particles $H^{Hubbard}$ can be decoupled into a Hartree term acting on each orbital:

$$H_{i,\sigma}^{Hubbard} = V_{i,\sigma} n_{i,\sigma} \tag{3.3.6}$$

Where

$$V_{i,\sigma} = \sum_{j,\sigma' \neq i,\sigma} U(i\sigma, j\sigma') < n_{j,\sigma'} > \tag{3.3.7}$$

As we want H^{DC} and $H^{Hubbard}$ to cancel for the ground state density, we then choose to fix the value of the double-counting potential to the value of the Hartree potential at the ground state:

$$V_{i,\sigma}^{DC} = V_{i,\sigma}\left(\rho_0^{DFT}\right) = \sum_{j,\sigma' \neq i,\sigma} U\left(i\sigma, j\sigma'\right) < n_{j,\sigma'} >_{\rho_0^{DFT}} \tag{3.3.8}$$

In this framework, the original DFT density is still a fixed point of our new total Hamiltonian, and the double-counting term is coherent with the system of independent particles we consider. Moreover, there is no limitation on the form of the U matrix, and it can be simply considered as a multi-orbital generalization of the Around Mean Field Double Counting form.

Now that an acceptable form for the double-counting Hamiltonian is identified for a system of independent particles, we can also relax this constraint and examine the final Hamiltonian in a different angle:

$$H = \left(H^{DFT} - H^{DC}\right) + H^{Hubbard} \tag{3.3.9}$$

Here we interpret naively H^{DC} as the part of the Hartree term contained in the Hubbard Hamiltonian but as it would be calculated within DFT, that is to say for a system of independent particles with the DFT ground-state density. This means that in a correlated system where the orbital polarizations change compared to DFT, the value of the Hartree term is allowed to be corrected by the Hubbard Hamiltonian. One of the approximations made in that case is that the change in correlated orbital polarizations will not affect the Hartree term issued from interactions with other non-correlated orbitals. This might be questioned especially when the total number of correlated electrons is dramatically changed between DFT and DFT+DMFT. Since the Hartree repulsion between non-correlated, itinerant electrons is much lower than for localized electrons, this approximation seems reasonable for moderate changes of the repartition of electrons between localized and itinerant orbitals.

Updating the Around Mean Field DC term with the density from every DMFT loop would be the inverse approach: one considers that the Hartree term from DFT is globally correct and that the modification of electrons repartition should not change the value of it. The problem in this last approach is that it is not likely that two electrons in itinerant orbitals create the same Hartree energy than two electrons in localized orbitals. Moreover, it would cancel the orbital levels shifts induced by the reorganization of orbital polarization inside the correlated shell. On the other hand, one has to be aware that in the case of ideal, exact DFT the expression of Hartree energy, exchange-correlation energy and total density might be exact while the orbital-resolved

densities calculated from the Kohn-Sham wavefunctions might be wrong. In that case it sounds better to consider that the Hartree energy from DFT should be saved and the DC term should be calculated with the impurity model orbital densities. Still, both the calculation of the U-matrix, the Wannier functions and the hopping terms used in the impurity model are based on the Kohn-Sham wavefunctions from DFT, such that one can doubt that the final result would be correct.

For moderately correlated systems like iron pnictides, we consider the multi-orbital AMF double-counting calculated with DFT orbital densities, described in equations 3.3.5 and 3.3.8, as a good starting point, and we will use it throughout this thesis. It is shown in Chapter 11 that it provides results closer to experiment than the other double-counting possibilities.

However, we stress that we have only addressed the question of Hartree double-counting, while the correlations double-counting problem has not been treated. Chapter 9 will provide some insight into this problem, and we will see that the Local Density Approximation to the exchange-correlation potential seems to essentially accounts for the plasmonic renormalization of bands.

3.4 Calculating the Hubbard interactions

3.4.1 General framework

The constrained random phase approximation (cRPA) [Aryasetiawan *et al.* (2004)] allows to construct from first-principles low-energy Hamiltonians with specific "target" degrees of freedom. The main idea consists in expanding a partially screened interaction W^r onto a subset of localized Wannier orbitals $\{|\phi_m\rangle\}$, with m an orbital quantum number. This partially screened interaction W^r corresponds to the bare Coulomb interaction but within the target low-energy subspace generated by $\{|\phi_m\rangle\}$, which means that it has been screened by higher energy degrees of freedom.

The partially screened interaction W^r is calculated by constraining the polarization such that the screening processes involving the target states included in the low-energy Hamiltonian are not double counted in a further many-body calculation. The random phase approximation simplifies the expression of the polarization, P, in terms of transitions between occupied and empty states. Within such an assumption, it is possible to calculate the constrained polarization $P^r = P - P^{sub}$ which leads to W^r, where P^{sub} is the polarization within the target low-energy subspace only [Vaugier *et al.* (2012b)]. It is energy-dependent since screening is a dynamical process. The additional screening taking place in the low-energy subspace then allows us to recover the fully screened interaction W:

$$\begin{aligned} W &= \left[1 - vP\right]^{-1} v = \left[1 - vP^r - vP^{sub}\right] v \\ &= \frac{v/\left[1 - vP^r\right]}{1 - \left[v/\left[1 - P^r v\right]\right] P^{sub}} \\ &= \left[1 - W^r P^{sub}\right]^{-1} W^r \end{aligned} \tag{3.4.1}$$

3.4.2 Interaction matrices

The value of the partially screened interaction W^r between local orbitals is expressed in terms of the four-index interaction matrix $U^{(\mathcal{S})}_{m_1m_2m_3m_4}$:

$$\begin{aligned} U^{(\mathcal{S})}_{m_1m_2m_3m_4}(\omega) &\equiv \langle \phi_{m_1}\phi_{m_2}|W^r(\omega)|\phi_{m_3}\phi_{m_4}\rangle \\ &= \iint d^3r d^3r' \phi^*_{m_1}(r)\phi_{m_3}(r)W^r(r,r';\omega)\phi^*_{m_2}(r')\phi_{m_4}(r') \end{aligned} \quad (3.4.2)$$

where the superscript $\mathcal{S}$ is added for specifying the angular symmetry of the localized orbitals considered.

Most matrix elements are of the order of 0.1 eV or less, except for two-index reduced interaction matrices, $U^{\sigma\sigma}_{mm'}|_{\text{cRPA}}$, $U^{\sigma\bar{\sigma}}_{mm'}|_{\text{cRPA}}$ and $J^{\text{cubic}}_{mm'}$ which can be extracted from the calculation. Cubic angular harmonics are considered in our case as an approximation to the crystal field in the iron-based pnictides and chalcogenides:

$$U^{\sigma\bar{\sigma}}_{mm'}|_{\text{cRPA}} \equiv U^{\text{cubic}}_{mm'mm'} = \langle \phi_m\phi_{m'}|W^r(0)|\phi_m\phi_{m'}\rangle \quad (3.4.3)$$

$$U^{\sigma\sigma}_{mm'}|_{\text{cRPA}} \equiv U^{\text{cubic}}_{mm'mm'} - U^{\text{cubic}}_{mm'm'm} \quad (3.4.4)$$

where m runs over the d orbital subspace and σ refers to the spin degree of freedom.

As two atoms of Fe are found in the conventional unit-cell of the iron-based pnictides and chalcogenides, one has access to the nearest-neighbor interaction between Fe-3d orbitals within equation 3.4.2 (see [Vaugier *et al.* (2012b)] for a more general expression of the non-local interactions). One can also calculate the interaction between Fe-3d and As-4p orbitals in the same way.

3.4.3 Slater parametrization

Replacing the four-index interaction matrix $U_{m_1m_2m_3m_4}$ by a small subset of fitting parameters is usually done in the literature of many-body calculations, e.g. LDA+U or LDA+DMFT, in order to avoid double-counting issues. However, the errors induced by considering such an approximated interacting Hamiltonian in many-body calculations have not been investigated yet (see Part IV for a further discussion). For isolated atoms, the development into a finite number of Legendre polynomials of the matrix elements of the Coulomb potential with spherical harmonics is exact [Judd(1998), Slater(1960), Sugano *et al.* (1970)]. It involves only three radial integrals – or Slater integrals – for d states, whereas the angular part is determined with well defined Racah-Wigner coefficients, α_k:

$$\alpha_k(m_1,m_2,m_3,m_4) = \frac{4\pi}{2k+1}\sum_{q=-k}^{k}\langle Y_{lm_1}|Y_{kq}Y_{lm_3}\rangle\langle Y_{lm_2}Y_{kq}|Y_{lm_4}\rangle \quad (3.4.5)$$

where Y_{lm} are spherical harmonics and $\langle Y_{l_1m_1}|Y_{l_2m_2}Y_{l_3m_3}\rangle$ refer to the Gaunt coefficients. It is the sphericity of the isolated atom – and of the spherical harmonics used – that sets the finite number of the Slater integrals to $l+1$ where l is the orbital quantum number.

Assuming that i) the localized Wannier orbitals, $\{|\phi_{m,-2\leq m\leq 2}\rangle\}$, to which the Hamiltonian is downfolded at low-energy, still retain the sphericity of the isolated atom although they are

embedded in the solid, and ii) screening does not induce strong orbital anisotropy, allows to define Slater integrals for correlated orbitals in materials as follows [Vaugier *et al.* (2012b)]:

$$F^k(\omega) = \mathcal{C}_{l,k} \sum_{m_1,m_2,m_3,m_4} (-1)^{m_1+m_4} U^{\text{(spheric)}}_{m_1 m_2 m_3 m_4}(\omega) \times \begin{pmatrix} l & k & l \\ -m_1 & m_1 - m_3 & m_3 \end{pmatrix} \begin{pmatrix} l & k & l \\ -m_2 & m_2 - m_4 & m_4 \end{pmatrix} \tag{3.4.6}$$

where the parentheses correspond to the Wigner 3j-symbols and the coefficients $\mathcal{C}_{l,k}$ are defined as follows:

$$\mathcal{C}_{l,k} = \frac{2k+1}{(2l+1)^2 \begin{pmatrix} l & k & l \\ 0 & 0 & 0 \end{pmatrix}^2}. \tag{3.4.7}$$

The superscript "spheric" indicates that Wannier orbitals with spherical angular harmonics are employed. In addition, it follows the usual definition of the Hubbard $U = F^0$ and Hund's exchange $J = (F^2 + F^4)/14$. Analogously, we define the bare parameters, v and J_{bare} when considering the Slater integrals that parametrize the bare interaction matrix elements.

The Slater integrals can be used for calculating the Slater-symmetrized interaction matrix, $\bar{U}^{(\mathcal{S})}_{m_1 m_2 m_3 m_4}$, with the symmetry $\mathcal{S}$ of the crystal field:

$$U^{(\mathcal{S})}_{m_1 m_2 m_3 m_4}(\omega) = \sum_{m'_1 m'_2 m'_3 m'_4} \mathcal{S}_{m_1 m'_1} \mathcal{S}_{m_2 m'_2} \times \left\{ \sum_{k=0}^{2l} \alpha_k(m'_1, m'_2, m'_3, m'_4) F^k(\omega) \right\} \mathcal{S}^{-1}_{m'_3 m_3} \mathcal{S}^{-1}_{m'_4 m_4} \tag{3.4.8}$$

Choosing $\mathcal{S}$ as the transformation from spherical to cubic harmonics leads to the Slater-symmetrized reduced interaction matrices with cubic symmetry:

$$\bar{U}^{\sigma\bar{\sigma}}_{mm'}|_{\text{Slater}} \equiv \bar{U}^{\text{cubic}}_{mm'mm'} \tag{3.4.9}$$

$$\bar{U}^{\sigma\sigma}_{mm'}|_{\text{Slater}} \equiv \bar{U}^{\text{cubic}}_{mm'mm'} - \bar{U}^{\text{cubic}}_{mm'm'm}. \tag{3.4.10}$$

We stress that within this method (introduced in [Vaugier(2011)]), three independent Slater integrals are deduced for *d* Hubbard interaction matrices. This is in contrast to previous Slater parametrizations [Anisimov *et al.* (1997a)] that provided only two independent integrals and therefore required as a third relation, to set the ratio F^4/F^2 to its empirical atomic value around 0.63. Relations similar to equation 3.4.6 were used in [Kutepov *et al.* (2010)] for $BaFe_2As_2$ but employing a self-consistent GW approximation for calculating the four-index Hubbard interaction matrix.

3.4.4 Frequency dependence

Because of the frequency dependence of the constrained polarization, the partially screened interaction W^r is also frequency dependent. Consequently, the U matrix and the Slater integrals parameterizing it are defined as a function of frequency: $U = U(\omega)$. At infinite frequency, the interaction $W^r(\omega = \infty)$ is equal to the bare, unscreened Coulomb interaction v. The largest

variation is observed on the monopole part F_0, which can be reduced by one order of magnitude at zero frequency compared to the unscreened value, while the multipole terms are proportionally less impacted [Antonides *et al.* (1977), Sawatzky and Allen(1984), van der Marel *et al.* (1984)].

A naive idea to take into account the high-frequency tail would be to increase the static interaction $U(\omega = 0)$ such that it gives a correct description of the physics of the system. However, this is not a good way to proceed since the physics contained in the frequency-dependent interaction is qualitatively different from any renormalized static interaction. For instance, $U(\omega = 0)$ is a good estimation of the gap in a Mott insulator and corresponds to a measurable quantity, so renormalizing it would not be physical. Moreover, the frequency dependence will transfer some spectral weight from low-energy scale to high-energy scales as the excitation of an electron will create at the same time a hole at low energy and a plasmon excitation at higher energy [Casula *et al.* (2012a)]. Rather, it has been shown that the high-frequency tail renormalizes the one-particle part of the Hamiltonian [Casula *et al.* (2012b)]. Indeed, the interaction of electrons and plasmons results in the creation of quasiparticles with a higher effective mass. This will be explained in more detail in Part III.

3.4.5 Shell-folding

At infinite frequency screening is suppressed and the instantaneous intrashell Coulomb interaction in iron pnictides, $U^{dd}(\omega = \infty)$, is around 20 eV. This is about one order of magnitude bigger than the static interaction $U^{dd}(\omega = 0)$. At the same time, the intershell *p*-*d* interaction $U^{dp}(\omega = \infty)$ is of the order of 6 eV, and it seems reasonable to take it into account in the construction of the Hubbard model. We choose to construct an effective model where only the *d* states are considered as correlated, based on the assumption that the total number of electrons in *p* and *d* orbitals is constant (more details and static applications will be published in [Seth *et al.* (2015)]). In a *dp* model the interaction Hamiltonian on one site can be written as:

$$\begin{aligned} H_{int} &= \frac{1}{2} \sum_{\substack{(m,\sigma)\neq(m',\sigma') \\ m,m'\in\{d\}}} U^{dd}_{m\sigma m'\sigma'} n_{m\sigma} n_{m'\sigma'} \\ &+ \frac{1}{2} \sum_{\substack{(m,\sigma)\neq(m',\sigma') \\ m,m'\in\{p\}}} U^{pp}_{m\sigma m'\sigma'} n_{m\sigma} n_{m'\sigma'} \\ &+ \sum_{\sigma,\sigma'} U^{dp} N_{d\sigma} N_{p\sigma'} \end{aligned}$$

which is strictly equal to:

$$\begin{aligned} H_{int} &= \frac{1}{2} \sum_{\substack{(m,\sigma)\neq(m',\sigma') \\ m,m'\in\{d\}}} \tilde{U}^{dd}_{m\sigma m'\sigma'} n_{m\sigma} n_{m'\sigma'} \\ &+ \frac{1}{2} \sum_{\substack{(m,\sigma)\neq(m',\sigma') \\ m,m'\in\{p\}}} \tilde{U}^{pp}_{m\sigma m'\sigma'} n_{m\sigma} n_{m'\sigma'} \\ &+ U^{dp} \frac{N(N-1)}{2} \end{aligned}$$

where $N = \sum_\sigma (N_{d\sigma} + N_{p\sigma})$ is the total number of electrons in *p* and *d* orbitals and $\tilde{U} = U - U^{dp}$. We then neglect the $\tilde{U}^{pp}$ term, since in many compounds U^{pp} is of the order of U^{dp}. In our approximation, the total number of electrons on the local site is considered to be a good quantum number. In that sense, neglecting the influence of the remaining term $U_{dp}N(N-1)/2$ on the physics of the system is a better approximation than neglecting the intershell interaction. Finally, we end up with a Hubbard model where only the *d* subspace is considered as correlated with a renormalized Coulomb interaction $\tilde{U}^{dd} = U^{dd} - U^{dp}$.

Part III

Beyond the combination of density functional theory with dynamical mean field theory (DFT+DMFT)

In this part, we propose and implement a new approach to the spectral properties of correlated electron materials taking into account screened exchange beyond the local density approximation (LDA) and dynamical correlations as described by dynamical mean field theory with frequency-dependent local Hubbard interactions. The approach can be understood as a simplified and extremely efficient version of the combined GW+DMFT method [Biermann et al. (2003)], as a non-perturbative dynamical generalisation of the popular "COulomb-Hole-Screened-EXchange" (COHSEX) scheme [Hedin(1965)], or as a combination of generalized Kohn-Sham schemes [Bylander and Kleinman(1990), Seidl et al. (1996)] with DMFT.

We begin by the implementation of dynamical interactions in the hybridization impurity solver for Dynamical Mean Field Theory originally introduced by [Werner and Millis(2010)]. We explain the practical details of the calculation, derive expressions for key quantities and tackle the subtle issues of double-counting and analytic prolongation. We then focus on a new method including Fock-like static screened exchange created by a Yukawa potential in a DFT+DMFT calculation, while getting rid of the LDA exchange and correlation potential. The aim is to combine the nonlocal screened-exchange self-energy with the local self-energy from DMFT with dynamical interaction. We finally apply this scheme to SrVO3 (see Section 5.6) and BaCo2As2 (see Chapter 9).

Chapter 4

Dynamical screening effects

The treatment of correlated electrons in Dynamical Mean Field Theory is based on the construction of a low-energy model. Because it depends on the screening induced by higher-energy degrees of freedom, which is a dynamical process in general, the effective Coulomb interaction between two electrons is frequency-dependent. This can be captured by methods such as constrained-RPA, as we have seen in Section 3.4.

The importance of this frequency-dependence of the dynamical Hubbard interaction $U(\omega)$ has been demonstrated in the related context of Hubbard-Holstein models [Deppeler and Millis(2002), Takada and Chatterjee(2003), Capone *et al.* (2004), Macridin *et al.* (2004), Koller *et al.* (2004)]. Indeed, as we will show in Sections 4.1 and 4.2, the effect of dynamical screening can be described by a Hubbard-Holstein model accounting for the interaction of electrons with a collection of plasmons. This will lead to the formation of electronic polarons with a screened Coulomb interaction [Sawatzky *et al.* (1975), Antonides *et al.* (1977)]. Based on this statement [Werner and Millis(2007)], the continuous-time quantum Monte Carlo implementation proposed by [Werner and Millis(2010)] has recently given access to the resolution of this model within DMFT at a reasonable computation cost. Another scheme for the weak-coupling algorithm has also been proposed [Casula *et al.* (2012a)]. Still, few calculations for realistic materials have been performed so far [Casula *et al.* (2012a), Werner *et al.* (2012), Sakuma *et al.* (2013), Hansmann *et al.* (2013), Huang and Wang(2012), Tomczak *et al.* (2012a), Tomczak *et al.* (2014)]. We hope that the details provided in this thesis will help to spread this method.

The dynamical CT-HYB impurity solver [Werner *et al.* (2006), Werner and Millis(2010)] has been implemented in the Toolbox for Research on Interacting Quantum Systems (TRIQS) [Ferrero and Parcollet(2011)] by Thomas Ayral, Michel Ferrero, Hartmut Hafermann and Olivier Parcollet. Our contribution to this scheme has consisted in generalizing the combination of Density Functional Theory with DMFT to dynamical interactions, and to benchmark it on realistic materials *ab-initio*, including the calculation of the frequency-dependent interaction using constrained-RPA. In particular, we have worked on the double-counting terms and the analytical continuation, with the help of Michele Casula for this latter point.

We begin by a description of a single band Hubbard-Holstein model as a simple way to understand the effects of the screening of a Hubbard interaction V by a single plasmon mode, which results in a frequency-dependent $U(\omega)$. We then show that any physically reasonable $U(\omega)$ can be described by a Hubbard-Holstein model with a collection of plasmon oscillators. We explain how to solve this model by quantum Monte Carlo, and how it can be approximated by an effective low-energy model combining a bosonic renormalization factor Z_B with a static U.

Finally, we tackle the issues of its combination with Density Functional Theory by calculating the around mean-field orbital-dependent double-counting term and explaining the analytic continuation procedure.

4.1 Hubbard-Holstein model

In order to understand qualitatively the effects of a frequency-dependent $U(\omega)$, we first study the simple case of a one-band Hubbard model in which the bare interaction V between correlated electrons is screened by a single plasmon mode described by bosonic excitations at the frequency ω_0. It corresponds to the following Hubbard-Holstein Hamiltonian:

$$H_{loc} = H_{Hubbard} + H_{coupling} + H_{boson} \tag{4.1.1}$$

$$H_{loc} = V n_\uparrow n_\downarrow + \lambda(n_\uparrow + n_\downarrow)(b^\dagger + b) + \omega_0 \left(b^\dagger b + \frac{1}{2} \right) \tag{4.1.2}$$

Here, $H_{coupling}$ is linking the charge on the atom with the position $x = (b^\dagger + b)/\sqrt{2}$ of the harmonic oscillator describing the plasmon mode. λ is the strength of the electron-plasmon coupling. When there is no electron, $H_{Hubbard} + H_{coupling}$ goes to zero and there is no plasmon excitation in the ground state. To understand the effect of the plasmon at the mean field level when there are electrons on the site, we can introduce the momentum of the harmonic oscillator $p = (b^\dagger - b)/i\sqrt{2}$ and rewrite the plasmonic part of the Hamiltonian:

$$H_B = H_{coupling} + H_{boson} = \lambda\sqrt{2}(n_\uparrow + n_\downarrow)x + \frac{\omega_0}{2}(x^2 + p^2) \tag{4.1.3}$$

If we forget about the fluctuations of $n_\uparrow$ and $n_\downarrow$, we see that the bosons are influenced by an external field $\lambda\sqrt{2}(n_\uparrow + n_\downarrow)$, which gives a new equilibrium position for the bosons:

$$\begin{aligned} \frac{\partial H_B}{\partial x}|_{x=x_0} &= \lambda\sqrt{2}(n_\uparrow + n_\downarrow) + \omega_0 x_0 = 0 \\ x_0 &= -\frac{\lambda\sqrt{2}}{\omega_0}(n_\uparrow + n_\downarrow) \end{aligned} \tag{4.1.4}$$

Let us now go back to the full Hamiltonian H_{loc} of equation 4.1.2. We want to absorb $H_{coupling}$ in the Hubbard Hamiltonian, which is possible by means of a Lang-Firsov transformation [Lang and Firsov(1962), Werner and Millis(2007)]. This will allow us to express the Hamiltonian in terms of decoupled polarons and bosons instead of electrons and bosons with a coupling interaction. We define a transformation matrix S as:

$$S = ipx_0 = \frac{\lambda}{\omega_0}(n_\uparrow + n_\downarrow)(b^\dagger - b)$$

and rewrite the hamiltonian $\tilde{H}_{loc} = e^S H_{loc} e^{-S}$ in terms of new creation and annihilation operators $\tilde{o} = e^S o e^{-S}$ (see Appendix B.1):

$$\tilde{H}_{loc} = (V - 2\frac{\lambda^2}{\omega_0})\tilde{n}_\uparrow\tilde{n}_\downarrow - \frac{\lambda^2}{\omega_0}(\tilde{n}_\uparrow + \tilde{n}_\downarrow) + \omega_0 \left(b^\dagger b + \frac{1}{2} \right) \tag{4.1.5}$$

This means that adding the plasmon interaction has three effects on the bare Hubbard hamiltonian:

- it renormalizes the Coulomb interaction to a value $U = V - 2\lambda^2/\omega_0 < V$
- it induces a shift of the chemical potential of value $(V - U)/2$
- it dresses the fermionic operators with a bosonic term

Physically, the interaction of electrons and plasmons results in the formation of a dressed quasiparticle – an electronic polaron – which has a lower interaction with other quasiparticles, a shifted energy level due to the gain of energy made by forming a quasiparticle, and a higher effective mass because of the potential well that they create around themselves.

4.2 Generalization to several screening modes

We will now tackle the case of a general (physically reasonable) dynamical interaction $U(\omega)$ and show that it can be treated by extending the above Hubbard-Holstein model to several plasmon modes. The many-body physics of the system can be expressed in the form of an action S, such that the grand-canonical partition function $Z = \mathrm{Tr} e^{-\beta H}$ is now written $Z = \int D(c^\star, c) e^{-S}$, where $c^\star$ and c are conjugate anticommuting Grassman fields. Within this formalism, the bare Hubbard model:

$$H_{Hubbard} = V n_\uparrow n_\downarrow$$

corresponds to an action:

$$\begin{aligned} S_{Hubbard}(c^\star, c) &= \int_0^\beta d\tau n_\uparrow(\tau) V n_\downarrow(\tau) && (4.2.1) \\ &= \frac{1}{2}\sum_{\sigma\sigma'} \int_0^\beta d\tau \int_0^\beta d\tau' n_\sigma(\tau) V \delta_{\tau\tau'}(1 - \delta_{\sigma\sigma'}) n_{\sigma'}(\tau') && (4.2.2) \end{aligned}$$

Replacing the bare interaction V with a dynamically screened $U(\omega)$ is simple in this form: in imaginary time this corresponds to replacing the instantaneous interaction $V\delta_\tau(1 - \delta_{\sigma\sigma'})$ by a dynamical interaction $U(\tau) = V\delta_\tau(1 - \delta_{\sigma\sigma'}) + U_{ret}(\tau)$. The action is thus written:

$$S_{loc}(c^\star, c) = \frac{1}{2}\sum_{\sigma\sigma'} \int_0^\beta d\tau \int_0^\beta d\tau' n_\sigma(\tau) U_{\sigma\sigma'}(\tau - \tau') n_{\sigma'}(\tau') \tag{4.2.3}$$

We can show (see Appendix B.2) that in the case of the single plasmon Hubbard-Holstein model, $U_{ret}(\tau)$ is defined as:

$$U_{ret}(\tau) = -\lambda^2 \cosh\left[\left(\tau - \frac{\beta}{2}\right)\omega_0\right] / \sinh\left[\frac{\omega_0\beta}{2}\right] \tag{4.2.4}$$

such that we obtain the expression of U_{ret} in Matsubara frequencies after a Fourier transformation:

$$U_{ret}(i\nu_n) = -2\frac{\lambda^2\omega_0}{\nu_n^2 + \omega_0^2} \tag{4.2.5}$$

And we see that we recover the static value of U as in the previous section:

$$U(i\nu_n = 0) = V - 2\lambda^2/\omega_0$$

The expression of $U_{ret}(i\nu_n)$ 4.2.5 can actually be generalized to any form of the dynamical interaction. To this aim, we now write:

$$U_{ret}(i\nu_n) = \int \frac{d\omega}{\pi} \Im U_{ret}(\omega) \frac{2\omega}{\nu_n^2 + \omega^2} \tag{4.2.6}$$

and consider, instead of a single plasmon, a collection of oscillators defined at each frequency by:

$$\Im U_{ret}(\omega) = -\pi \int_0^\infty \lambda^2_{\omega'} \delta(\omega - \omega') d\omega' \tag{4.2.7}$$

$$\lambda^2_{\omega'} = -\frac{\Im U_{ret}(\omega')}{\pi} \tag{4.2.8}$$

This shows that the generalized action for a dynamical interaction of the form 4.2.6 is equivalent to a Hubbard-Holstein Hamiltonian with a collection of plasmon oscillators. As a consequence, the physical picture drawn in the previous section stays qualitatively valid.

4.3 Solving the polaron system

We now want to find the solution of the impurity model with a dynamical interaction corresponding to the action 4.2.3. This can be done using continuous time quantum Monte Carlo algorithms, for instance in the dynamical CT-HYB impurity solver [Werner *et al.* (2006), Werner and Millis(2010)], as implemented in the Toolbox for Research on Interacting Quantum Systems (TRIQS) [Ferrero and Parcollet(2011)] for density-density interactions. The principle of this algorithm is to decompose the partition function of the system into a sum of contributions of an infinite number of configurations with a certain weight corresponding to the probability of a configuration to occur. The weight is related to the action S of the impurity model:

$$Z = \int D\left[c_i^*, c_i\right] e^{-S}$$

This decomposition allows us to compute the physical quantities of the system – notably, the Green's function – by using a quantum Monte Carlo algorithm which, in the limit of infinite time, will visit all configurations with the correct probability. Basically, going from static to dynamical Coulomb interactions will modify the weight of a configuration by a factor w_{boson} (see equation 4.3.4). As a consequence, using dynamical instead of static interactions simply leads to the calculation of an additional factor for the probability to have a given configuration in the Monte Carlo algorithm. In principle the computational effort will only increase linearly with the number of iterations. However, in practice, it seems that due to the larger energy scales in the dynamical model the spanned configurations are different, which results in a longer computation time.

We will now focus on the calculation of the bosonic weight w_{boson}, which relies on finding a convenient expression for the dynamical Hubbard action. We construct a function $K(\tau)$ for

$0 \leq \tau \leq \beta$ from the values of $U(i\omega)$ obtained by cRPA in order to find $K''(\tau) = U_{ret}(\tau)$, considering that $U(i\omega)$ is an even function:

$$K(\tau) = -\frac{1}{\beta}\sum_{n\neq 0}\frac{U(i\omega_n)-V}{\omega_n^2}\left(e^{i\omega_n\tau}-1\right)+\frac{V-U_0}{2}\left(1-\frac{\tau}{\beta}\right)\tau \tag{4.3.1}$$

Equivalent forms for the expression of $K(\tau)$ are given in Appendix B.3. We can see that $K(\tau) \geq 0$ and $K(0) = K(\beta) = 0$. It is also shown in Appendix B.3 that we can write the action as a function of $K''(\tau)$:

$$\begin{aligned} S_{loc} &= \frac{1}{2}\sum_{\sigma,\sigma'}\int\int d\tau d\tau' n_\sigma(\tau)U_0(1-\delta_{\sigma,\sigma'})\delta(\tau-\tau')n_{\sigma'}(\tau') \\ &+\frac{1}{2}\sum_{\sigma,\sigma'}\int\int d\tau d\tau' n_\sigma(\tau)K''(\tau-\tau')n_{\sigma'}(\tau') - \frac{V-U_0}{2}\int n(\tau)d\tau \end{aligned} \tag{4.3.2}$$

The first term is just the static Hubbard model with a screened Hubbard parameter, while the second accounts for the dressing of the propagators, by analogy with the Hubbard-Holstein model. The last term is a chemical potential shift but, as will be shown in Section 4.5, it will be canceled by the additional term in the double counting. Eventually, we can simply depart from a static Hubbard model with a screened interaction U_0 and add a term:

$$S_{boson} = \frac{1}{2}\sum_{\sigma,\sigma'}\int\int d\tau d\tau' n_\sigma(\tau)K''(\tau-\tau')n_{\sigma'}(\tau') \tag{4.3.3}$$

which does not modify the ground state in a static approximation since $K''(0) = 0$, and thus should not do any double-counting harm.

If we put this action in a CT-HYB impurity solver, the associated weight for a given configuration $\{(s_i, \sigma_i, \tau_i)\}$ with $s = 1$ for a creation operator and $s = -1$ for an annihilation operator is [Werner and Millis(2010), Ayral *et al.* (2013)]:

$$\ln w_{boson} = \sum_{i>j} s_i s_j K(\tilde{\tau}_i - \tilde{\tau}_j) \tag{4.3.4}$$

where $\tilde{\tau}$ means that the τ have been time-ordered.

The interactions between two operators of same spin can be seen as a modification of H_{hyb}, in the sense that they deal with the probability of a particle to go on or away from the impurity. For two given segments with no overlap the factor corresponding to their respective interaction has the value:

$$\ln w_{boson} = K(\tau^\dagger_{\sigma_i} - \tau^\dagger_{\sigma_j}) + K(\tau_{\sigma_i} - \tau_{\sigma_j}) - K(\tau_{\sigma_i} - \tau^\dagger_{\sigma_j}) - K(\tau^\dagger_{\sigma_i} - \tau_{\sigma_j})$$

For two given segments with an overlap, it reads as:

$$\ln w_{boson} = K(\tau^\dagger_{\sigma_i} - \tau^\dagger_{\sigma_j}) + K(\tau_{\sigma_i} - \tau_{\sigma_j}) - K(\tau_{\sigma_i} - \tau^\dagger_{\sigma_j}) - K(\tau_{\sigma_j} - \tau^\dagger_{\sigma_i})$$

If $K(\tau)$ were a constant equal to $K(\beta/2)$ except for $K(\tau = 0) = 0$, then the bosonic weight would always be zero except for the interaction within one single segment:

$$\ln w_{boson} = \sum_{\sigma_i} K(\tau_{\sigma_i} - \tau^\dagger_{\sigma_i}) = \sum_{\sigma_i} K\left(\frac{\beta}{2}\right)$$

The probability of a particle to be on the impurity is equal to the mean total length of segments divided by β. In our simplified case, if we consider only the space of configurations where the total length of segments is equal to this probability, we can see that the bosonic weight favors configuration where the length is divided between as few segments as possible. That means that the probability to hop from the impurity to the bath is reduced by the high-frequency tail.

Without this approximation, we can see that the situation is more complex. Indeed, the system could also favor configurations with many very small segments:

$$\tau_{\sigma_i} - \tau^\dagger_{\sigma_i} \longrightarrow 0$$

in which case both the interaction within one segment and between two different segments will tend to zero. It would be interesting to see how the mean number of segments and the distribution of their length evolves when turning on dynamical interactions and to see if it is the source for the rise of computation time and the larger energy scales.

4.4 Effective low-energy model: the bosonic factor Z_B

The approach described in the previous section allows to solve exactly the impurity problem. However, it is computationally heavy. Another point of view is to go back to the interpretation of the Hubbard-Holstein model in terms of electronic polarons as in equation 4.1.5, and to solve this model approximately. This allows to interpret the effect of the high-frequency tail of the dynamical Hubbard interaction $U(\omega)$ as a renormalization of the bandwidth and hopping probabilities [Casula *et al.* (2012b)]. It is quantified by a bosonic renormalization factor Z_B. The idea is to focus on the low-energy degrees of freedom by projecting the following Hamiltonian on the subspace of zero boson $|0>_B$:

$$H = -\sum_{i,j,\sigma} t_{i,j}\tilde{c}^\dagger_{i,\sigma}\tilde{c}_{j,\sigma} + U\sum \tilde{n}_{i,\uparrow}\tilde{n}_{i,\downarrow} + \omega_0 \sum_i \left(b^\dagger_i b_i + \frac{1}{2}\right) \tag{4.4.1}$$

which is just the full Hamiltonian corresponding to equation 4.1.5 but including hopping between different sites and putting aside the chemical potential shift for now [1]. Using the fact that:

$$\begin{aligned} \tilde{c}_\sigma &= e^{(-\lambda/\omega_0)(b^\dagger - b)} c_\sigma \\ \tilde{c}^\dagger_\sigma &= e^{(\lambda/\omega_0)(b^\dagger - b)} c^\dagger_\sigma \end{aligned}$$

and that ${}_B<0|e^{(-\lambda/\omega_0)(b^\dagger-b)}|0>_B = {}_B<0|e^{(\lambda/\omega_0)(b^\dagger-b)}|0>_B = e^{-\lambda^2/(2\omega_0^2)}$ we get:

$$ {}_B<0|\tilde{c}^\dagger_{i,\sigma}\tilde{c}_{j,\sigma}|0>_B = Z_B c^\dagger_{i,\sigma} c_{j,\sigma} \tag{4.4.2}$$

$$ Z_B = e^{-\lambda^2/\omega_0^2} \tag{4.4.3}$$

If we include non-correlated states we get a factor $\sqrt{Z_B}$ renormalizing every hopping between correlated and non-correlated states. Eventually, if we name p the non-correlated orbitals and d the correlated, the hopping part of the effective Hamiltonian looks like:

$$\begin{bmatrix} p^\dagger & d^\dagger \end{bmatrix} \begin{bmatrix} T_{pp} & \sqrt{Z_B}T_{pd} \\ \sqrt{Z_B}T^\dagger_{pd} & Z_B T_{dd} \end{bmatrix} \begin{bmatrix} p \\ d \end{bmatrix}$$

[1] It will be shown in Section 4.5 that this shift is substracted in the double-counting part.

Another consequence is that the Green's function of the correlated orbitals is also renormalized by Z_B, which means that the spectral weight at low-energy is reduced. Indeed, the rest of the spectral weight is lost in plasmon excitations, which are supposed to happen at higher energies.

In the case of a generalized dynamical interaction with several bosonic oscillators the expression of Z_B becomes, using equation 4.2.8:

$$\ln Z_B = -\int_0^\infty \frac{\Im U_{ret}(\omega)}{\pi\omega^2} d\omega \tag{4.4.4}$$

We will now make links between this effective model and the previous exact derivation for the CT-HYB solver. The value of the function $K(\tau)$ introduced in equation 4.3.1 at $\tau = \beta/2$ can also be written (see Appendix B.3 for the proof):

$$K\left(\tau = \frac{\beta}{2}\right) = \int_0^\infty \frac{\Im U_{ret}(\omega)}{\pi\omega^2} \left[\frac{1-\cosh\left(\frac{\omega\beta}{2}\right)}{\sinh\left(\frac{\omega\beta}{2}\right)}\right] d\omega \tag{4.4.5}$$

If we take the limit for $\beta \to \infty$, which suppresses gradually the higher energy degrees of freedom, we realize that:

$$\ln Z_B = -\int_0^\infty \frac{\Im U_{ret}(\omega)}{\pi\omega^2} d\omega = -\lim_{\beta\to+\infty} K\left(\frac{\beta}{2}\right) \tag{4.4.6}$$

Which means that one could also define a temperature-dependent bosonic factor as

$$Z_B(T) = \exp\left(-K\left(\frac{\beta}{2}\right)\right) \tag{4.4.7}$$

Another approach using slave-rotor has been recently published in [Krivenko and Biermann(2014)], leading to different definitions for a temperature-dependent Z_B, including one expression very close to the combination of equations 4.4.7 and 4.4.5. We would like to point out that our expression gives a physical limit in both cases $\beta \to \infty$ and $\beta \to 0$ – in which case $Z_B \to 1$.

Using equation B.3.6, we obtain a new expression for Z_B:

$$\ln Z_B = \lim_{\beta\to\infty} \frac{4}{\beta} \sum_{n\in\mathbb{N}} \frac{U(i\omega_{2n+1}) - U_0}{\omega_{2n+1}^2}$$

More details about the practical calculation of this factor are given in Appendix B.4.

It is interesting to look at different curves for $K(\tau)$ depending on the temperature. Figure 4.4.1 shows $K(\tau)$ and its derivative $K'(\tau)$ for $SrVO_3$ in the *t2g-t2g* model constructed with a truncation of $V - U(i\omega_n)$ for frequencies $\omega_n > 200$ eV at inverse temperature β = 1, 10, and 30 eV^{-1}. At low temperature we see that most of the time the function has a value $K(\tau) \backsimeq K(\frac{\beta}{2})$. The discrepancy between the effective model and the exact calculation happens because there is a scale where $K(\tau)$ goes from $K(\tau = 0) = 0$ to $K(\frac{\beta}{2})$ and where the retarded interaction between electrons on the impurity has a more complex expression.

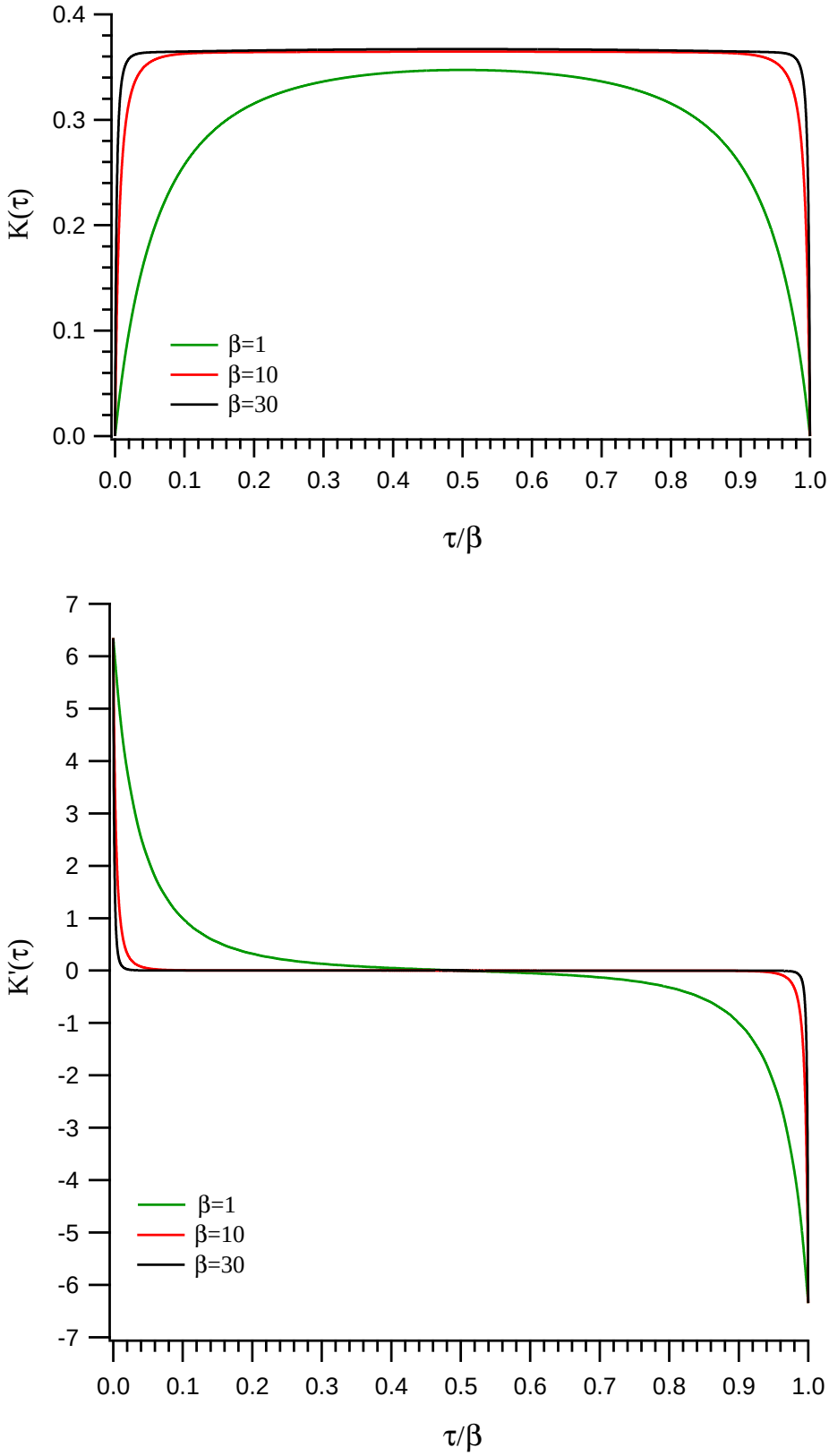

Figure 4.4.1: $K(\tau)$ (top) and $K'(\tau)$ (bottom) for β=1, 10, and 30 eV^{-1} from the interorbital interaction in $SrVO_3$ in a *t2g-t2g* model.

4.5 Double-counting for dynamical interactions

We adopt the point of view of Section 3.3.5, in which we have derived an multi-orbital around mean field double-counting term, but with the dynamical U local Hamiltonian 4.1.5:

$$\tilde{H}_{loc} = (V - 2\frac{\lambda^2}{\omega_0})\tilde{n}_\uparrow\tilde{n}_\downarrow + \frac{\lambda^2}{\omega_0}(\tilde{n}_\uparrow + \tilde{n}_\downarrow) + \omega_0\left(b^\dagger b + \frac{1}{2}\right) - \frac{\lambda^2}{\omega_0} \tag{4.5.1}$$

Here we use the simplified case of correlated electrons in one band interacting with a single plasmon mode (see Section 4.1) but the discussion stays valid in the general case. The last term of the Hamiltonian is a constant, that we can immediately drop since it has no effect on the physics of the system. We also replace $V - 2\frac{\lambda^2}{\omega_0} = U$ and $\frac{\lambda^2}{\omega_0} = \frac{V-U}{2}$. We consider again a system of independent particles, without any bosonic excitation, and a double-counting term of the form 3.3.5. Applying to this Hamiltonian the same idea that lead to equation 3.3.8 – finding the double-counting Hamiltonian such that it cancels with the local Hamiltonian in the DFT ground state – now gives us:

$$V^{DC}_{i,\sigma} = \sum_{j,\sigma' \neq i,\sigma} U\,(i\sigma, j\sigma') < n_{j,\sigma'} >_{\rho_0^{DFT}} - \frac{V-U}{2} \tag{4.5.2}$$

Which means that the chemical potential shift coming from electron-plasmon interaction is compensated by the double-counting term. Eventually, the effect of dynamical interactions compared to a static screened Hubbard model is essentially to dress the fermionic operators with a bosonic propagator. This will further renormalize the quasiparticle weight and energy levels. The physical idea is that the screening of the interaction and the stabilization of the quasiparticle energies created by the plasmons is already well taken into account in the ground state of Density Functional Theory. Taking into account this double-counting term, the picture of the Hamiltonian we apply to our low-energy model is not that of a bare Coulomb interaction which is screened by higher degrees of freedom, but of a screened Couloumb interaction that may be increased when it is not static because the screening is less efficient.

We can see that we recover the same expression by projecting equation 4.1.2 at the boson equilibrium position (before the Lang-Firsov transformation that changes this position), noting that in that case $b^\dagger b = \frac{\lambda^2}{\omega_0}(n_\uparrow + n_\downarrow)^2$:

$$\begin{aligned} H^{eq.}_{loc} &= V n_\uparrow n_\downarrow - 2\frac{\lambda^2}{\omega_0}(n_\uparrow + n_\downarrow)^2 + \frac{\lambda^2}{\omega_0}(n_\uparrow + n_\downarrow)^2 \\ H^{eq.}_{loc} &= \left(V - 2\frac{\lambda^2}{\omega_0}\right) n_\uparrow n_\downarrow - \frac{\lambda^2}{\omega_0}(n_\uparrow + n_\downarrow) \end{aligned} \tag{4.5.3}$$

And the around mean field expression of this Hamiltonian is then:

$$H^{eq.,AMF}_{loc} = U\,(n_\uparrow < n_\downarrow > + n_\downarrow < n_\uparrow > - < \tilde{n}_\uparrow >< \tilde{n}_\downarrow >) - \frac{V-U}{2}(n_\uparrow + n_\downarrow) \tag{4.5.4}$$

which can be decoupled in a one-particle potential:

$$V^{AMF}_\sigma = U < n_{\bar{\sigma}} > - \frac{V-U}{2}$$

At this point, one may wonder if the enhancement of the effective mass from the electron-plasmon interaction is not also taken into account in the approximations for the exchange-correlation potential such as the LDA. Indeed, a simple approximation for the plasmon frequency based on the average electronic density usually gives good agreement with experiment (see for instance [Pines(1964)]), which raises the question of what kind of plasmon effects might be captured by local density potentials. Clearly the effects of finite lifetime and of spectral weight reduction cannot be captured. On the other hand, according to the Hohenberg-Kohn theorem [Hohenberg and Kohn(1964)] the calculation of the total energy is definitely possible. As for the quasiparticle dispersion, the effective model described in Section 4.4 gives us a first hint by showing that the correlations effects contained in the high-frequency tail of $U(\omega)$ can be approximately captured while keeping the one-particle picture of DFT. The strong reduction of the Coulomb interaction through screening is a common feature of all materials, which means that all have a non-negligible bosonic renormalization factor Z_B. For those materials which are correctly described by DFT-LDA, it seems a fair hypothesis to think that the renormalization of the quasiparticle dispersion could be taken into account at the one-particle level, at least partially. More details and results of realistic calculations for pnictides about the link between plasmon frequencies calculated from the electronic density and constrained-RPA screening are discussed in Chapter 8. Finally, a direct comparison of LDA+DMFT calculations with ARPES experiments for $BaCo_2As_2$ is examined in Chapter 9.

One of the advantages of this double-counting form is that it is potentially compatible with any form of the Hubbard interaction matrix and with orbitally-resolved expressions of the screening. This means that we do not need to parametrize the matrix by Slater integrals, which in principle could lead to poor results in some materials, and that we could take into account the dynamical variation of the Hund's coupling. For simplicity reasons and because the screening of the Hund's coupling is expected to be relatively small [Antonides *et al.* (1977), van der Marel *et al.* (1984)], all results presented in Part V only consider the frequency dependence of the monopole term of the interaction and a Slater-symmetrized matrix, though we could technically get rid of these approximations.

4.6 Analytic continuation

The spectral function calculated in the dynamical interactions model presents high-energy features due to the plasmon excitations, that are not easily captured by the usual analytic prolongation schemes based on the maximum entropy algorithm or Pade approximants. For instance in the case of the single plasmon Hubbard-Holstein model, the spectral function displays peaks at multiples of the plasmon frequency ω_0. In that context, it has been proposed [Casula *et al.* (2012a)] to use an Green's function ansatz inspired from the exact solution of the atomic limit [Florens(2003)]. We present below the details of this procedure, that we use for the analytic continuation of our dynamical U calculations. We first define the two Green's functions:

$$\widetilde{G}(i\omega_n) = \frac{1}{i\omega_n - \Sigma(i\omega_n) + C} \tag{4.6.1}$$

$$\widetilde{G}^{aux}(\tau) = \frac{\tilde{G}(\tau)}{B(\tau)} \tag{4.6.2}$$

where the constant C is chosen such that $\tilde{G}^{aux}$ is a Green's function that can be reasonably analytically continued and

$$B(\tau) = e^{-K(\tau)} \tag{4.6.3}$$

Then we get $\widetilde{A}^{aux}(\omega)$ from $\tilde{G}^{aux}(\tau)$ by the maximum entropy algorithm [Jarrell and Gubernatic(1996)]. The next step is to obtain the spectral function $\tilde{A}$ from the convolution of $\tilde{A}^{aux}$ and of the bosonic spectral function ρ_B corresponding to $B(\tau)$:

$$\tilde{A}(\omega) = \int_{-\infty}^{+\infty} \tilde{A}^{aux}(x)\rho_B(\omega - x)\frac{1 + e^{-\beta\omega}}{(1 + e^{-\beta x})(1 - e^{\beta(x-\omega)})}dx \tag{4.6.4}$$

An explanation of this equation and further practical details concerning the analytic prolongation procedure are given in Appendix B.5. By Kramers-Kronig transformation we can then find $\tilde{G}(\omega)$ from $\widetilde{A}(\omega)$. Finally we obtain the self-energy Σ and the spectral function of the system A:

$$\Sigma(\omega) = \omega - \frac{1}{\tilde{G}(\omega)} + C \tag{4.6.5}$$

$$A(k, \omega) = \frac{1}{\pi}\Im\frac{1}{\omega + \mu - \epsilon_k - \Sigma(\omega)} \tag{4.6.6}$$

We note that in theory we could choose any function $B(\tau)$ to do this prolongation. In practice though, we have to make sure that $\tilde{G}^{aux}(\tau)$ is a Green's function and that its high energy features have been absorbed by the bosonic part so that it can be correctly analytically continued. That is why we choose to use the same $K(\tau)$ as in previous sections, since these properties are verified in the atomic limit.

Chapter 5

Screened exchange combined with DMFT (SEX+DMFT)

5.1 Non-local effects and DMFT calculations

In Dynamical Mean Field Theory there is a mean-field approximation in space. This is why it can only capture the local part of the self-energy, without any momentum-dependence. This approximation is exact in the limit of infinite dimensions [Müller-Hartmann(1989), Georges and Kotliar(1992)]. In realistic systems, if the non-local part of the correlation self-energy is small compared to the local part, as seems to be the case in many compounds, DMFT usually describes the correct physics. However, in low dimensions, and especially for systems on the verge of a phase transition which exhibit strong momentum-dependence of their physical properties such as the cuprate superconductors, the accuracy of this approximation is fundamentally challenged.

Several methods have been developed and are still being improved to try to cure this problem by recovering some of the non-local correlations effects. From the atomic point of view of DMFT, a natural prolongation is the cluster DMFT method [Schiller and Ingersent(1995), Lichtenstein and Katsnelson(2000), Kotliar *et al.* (2001), Biermann *et al.* (2001), Biroli and Kotliar(2002), Parcollet *et al.* (2004)] where several sites exchange electrons with the bath in the impurity model instead of only one. It is also possible to consider that the self-energy $\Sigma(k,\omega)$ is a piecewise constant in the Brillouin zone and to derive a cluster method in k-space. This is the Dynamical Cluster Approximation [Hettler *et al.* (1998), Maier *et al.* (2005)]. Those methods require a heavier computational charge, especially for multi-orbital compounds like iron pnictides and are not practical to use in that case.

Another alternative is to include directly a momentum-dependent self-energy $\Sigma(k,\omega)$ that does not interfere with the DMFT local self-energy, as done in the DMFT+Σ_k method [Kuchinskii *et al.* (2005)]. The difficulty then consists in finding an approximate scheme to derive this momentum-dependent part of the self-energy.

Finally, the GW+DMFT method – in which the non-local self-energy calculated at the first order perturbation theory [Hedin(1965)] is combined with the local part from DMFT [Biermann *et al.* (2003)] – also allows to recover some momentum-dependent parts of the self-energy. This technique presents many advantages, but a major drawback is, again, the large computational resources required. Moreover, very few dynamical implementations have been worked out. That is why only a handful of GW+DMFT calculations has been performed so far [Hansmann

et al. (2013), Ayral *et al.* (2013), Tomczak *et al.* (2012a), Tomczak *et al.* (2014)], even within further approximations [Biermann *et al.* (2003), Sakuma *et al.* (2013), Taranto *et al.* (2013)].

We choose to tackle the problem from a similar starting point. It has been shown recently that the self-energy at the GW level can be roughly separated into a non-local static part and a local dynamical part at low-energy in the iron pnictides [Tomczak *et al.* (2012b)] and in the transition metal oxide $SrVO_3$ [Tomczak *et al.* (2014)]. Inspired by this study, we propose to interpret the non-local static part of the GW self-energy as a screened-exchange term, while the non-local part is attributed to correlations:

$$\Sigma(k,\omega) = \Sigma_{sex}(k) + \Sigma_c(\omega) \tag{5.1.1}$$

This corresponds to the application of DMFT on a better starting point than the usual DFT-LDA bandstructure, that is to say another quasiparticle Hamiltonian H_0. We choose to approximate Σ_{sex} by a Hartree-Fock calculation in which the Coulomb potential is replaced by a Yukawa potential defined by the Thomas-Fermi screening length. Σ_c is finally calculated by Dynamical Mean Field Theory, including dynamical interactions $U(\omega)$. We describe below this scheme in further details, as well as the result of a calculation on $SrVO_3$, a usual benchmark compound in the field of strongly correlated materials. The case of transition metal pnictides is presented in Chapter 9.

5.2 The SEX+DMFT method

In the "one-shot" scheme in which there is no self-consistency loop on the charge density, we take the DFT-LDA density as a starting point. Our expectation is that this density is close to the reality, and would even be exact in the case of an exact functional. Basically, our SEX+DMFT method consists in applying DMFT on the result of a Hartree-Fock-like calculation in which the Coulomb potential is screened by the Thomas-Fermi wavelength. Though the Kohn-Sham bands are not physically relevant, the idea is to use them as a basis set to calculate exchange and correlations corrections. Based on the Kohn-Sham wavefunctions, we calculate by constrained-RPA the frequency-dependent Hubbard interactions between the correlated orbitals. This interaction will be used in our Hubbard model for DMFT. The screening length for the Yukawa potential is estimated from the LDA density of states at the Fermi level. Indeed, in the static, long wavelength limit the RPA screened interaction has a Yukawa form:

$$W^{RPA}(q \to 0, \omega = 0) \to -\frac{e^2}{4\pi\epsilon_0}\frac{4\pi}{q^2 + k_{TF}^2}$$

with

$$k_{TF}^2 \equiv -e^2\epsilon_0^{-1}P^0(0,0)$$

The polarization in the homogeneous electron gas at low temperature $k_BT \ll \epsilon_F$ has the limit

$$P^0(0,0) \to -\rho(\epsilon_F)$$

In copper for instance, the Thomas-Fermi wavenumber is of the order of 1 bohr^{-1}. In $BaCo_2As_2$, with a LDA density of 6.94 states/eV/cell we obtain a Thomas-Fermi wavenumber of 1.88 bohr^{-1}. We then calculate the screened Hartree-Fock bandstructure with a Yukawa potential as implemented in the Wien2k code [Tran and Blaha(2011)], based on the LDA density and

wavefunctions. The procedure is the following: first, based on the LDA converged density, we calculate the LDA Kohn-Sham wavefunctions and deduce the matrix elements of the screened-exchange potential $v_{x,\sigma}^{Yukawa}$ in the LAPW basis, using the Thomas-Fermi screening length which defines the Yukawa potential:

$$v^{Yukawa}(r_1, r_2) = \frac{e^2 \exp\left(-k_{TF}|r_1 - r_2|\right)}{|r_1 - r_2|}$$

Then, we calculate the wavefunctions with the LDA exchange potential – that we will only use as a basis set – and we obtain the matrix elements of the perturbation operator:

$$< \psi_{n,k}^{\sigma LDA} | v_{x,\sigma}^{Yukawa} - v_{x,\sigma}^{LDA} | \psi_{n',k}^{\sigma LDA} >$$

by developing the wavefunctions in the LAPW basis. We add the rest of the potential and the matrix is then diagonalized to finally give the screened Hartree-Fock eigenvalues and eigenfunctions. Finally, we construct localized orbitals using the projection scheme on Wannier-type orbitals described in [Aichhorn *et al.* (2009)] and apply Dynamical Mean Field Theory with dynamical interactions $U(\omega)$, as implemented in the TRIQS project [Ferrero and Parcollet(2011)]. It is worth noting that the whole scheme is implemented within the same basis set, based on the Wien2k LAPW code, and fully *ab-initio*.

One could also make the scheme self-consistent, but the computational effort would be one order of magnitude heavier: in that case the density, screening length and partially screened interaction $U(\omega)$ would have to be evaluated after each loop instead of being calculated from LDA. This is shown on Figure 5.2.1.

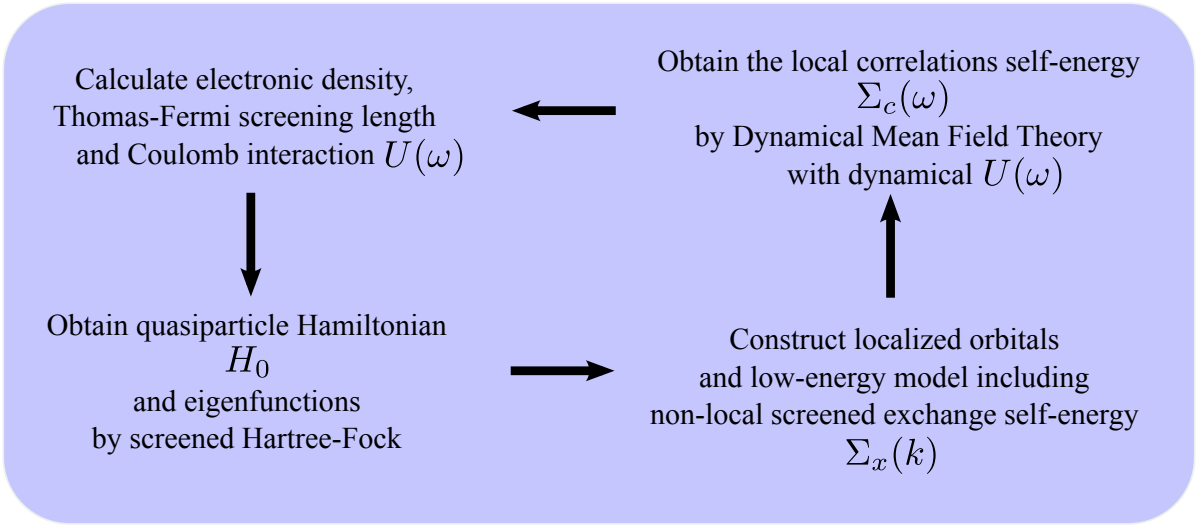

Figure 5.2.1: Screened-Exchange+Dynamical Mean Field Theory with dynamical interactions $U(\omega)$ self-consistent scheme.

5.3 Double counting for SEX+DMFT

Since the screened-exchange term is similar to the Fock exchange, it is interesting to qualitatively understand the double counting term contained in the Hubbard model in the case of a Hartree-Fock approximation. This approximation consists in minimizing the total energy of the ground

state of the solid in the space of single Slater determinant wavefunctions. When decoupling the equations for each particle, the Coulomb interaction part of the full Hamiltonian

$$H = H_{ion} + H_{kin} + H_{Coulomb}$$

then gives birth to the Hartree term and the Fock exchange [Slater(1951)]:

$$\Sigma_x(r_1,r_2) = -\sum_{iocc} \phi_i(r_1)\phi_i^*(r_2)v(r_1,r_2)$$

which is both static and non-local. On the other hand, applying the Hubbard Hamiltonian on a wavefunction of independent particles only provides the same Hartree-like term than obtained in Section 3.3.5 and a potential for each orbital similar to equation 3.3.7:

$$V_{i,\sigma}^{DC} = \sum_{j,\sigma' \neq i,\sigma} U(i\sigma, j\sigma') < n_{j,\sigma'} > \tag{5.3.1}$$

Actually, some local exchange is already included by construction in the Hubbard Hamiltonian via the Hund's coupling. Indeed, the origin of this term, that can be understood as a reduction of Coulomb interaction in the case of electrons with parallel spin, is exactly the on-site exchange. By substracting the double counting 5.3.1 one also substract the part of Fock exchange included in the Hubbard model, which corresponds to its mean value when acting on independent particles. There is no additional double-counting since the long-range part of exchange is totally ignored in the one-site Hubbard model.

For the case of screened-exchange, this result stays valid. The role of the screening length is just to estimate more accurately the static exchange. Indeed, combining Hartree-Fock approximation and one-site Dynamical Mean Field Theory would not be physically correct, since all screening processes acting on the long-range Coulomb potential would be neglected in that case. If one could apply extended DMFT on a sufficient number of sites and atoms, then the screening processes could be recovered, but it is not technically feasible.

5.4 Double-counting for GW+DMFT

Another possibility would be to take the result of a GW calculation as a starting point for DMFT. This has several advantages over DFT-LDA. Part of non-local exchange and correlations is included in the GW result, whereas it is not in LDA. Local correlations are also taken into account partially in GW, but because the approximation is well controlled we can substract them to avoid double-counting problems. At the end, the combination of GW and DMFT has both non-local effects from GW and local correlations from DMFT, and one can avoid the misdefinition of correlations double-counting in LDA [Biermann *et al.* (2003)]. The on-site part of the GW self-energy is defined as:

$$\Sigma_{loc}^{GW}(i\omega_n) = \sum_k \Sigma^{GW}(k, i\omega_n)$$

and decomposed on the orbitals m, m' of the correlated atom α:

$$\left[\Sigma^{GW}_{loc}(i\omega_n)\right]^{\alpha,\sigma}_{m,m'} = \sum_{k,\nu,\nu'} P^{\alpha,\sigma}_{lm,\nu}(k)\left[\Sigma^{GW}(k,i\omega_n)\right]^{\sigma}_{\nu,\nu'}\left[P^{\alpha,\sigma}_{lm',\nu'}(k)\right]^*$$

with P the projector used to construct the Wannier orbitals χ from the Kohn-Sham orbitals ψ:

$$P^{\alpha,\sigma}_{lm,\nu}(k) =< \chi^{\alpha,\sigma}_{lm}|\psi^{\sigma}_{k,\nu} >$$

Here we consider the case of one correlated shell. Finally we can define:

$$\left[V^{DC}_{total}(\sigma,i\omega_n)\right]_{m,m'} = V^{DC}_{Hartree}(m,\sigma)\delta_{m,m'} + \left[\Sigma^{GW}_{loc}(\sigma,i\omega_n)\right]_{m,m'}$$

Where $V^{DC}_{Hartree}$ has the expression of equation 3.3.8. We stress that the GW self-energy used to construct the double-counting should be only the correlation part, as pointed out in Section 5.3.

5.5 SEX+DMFT compared to GW+DMFT: limitations and benefits

To draw a larger picture and make links with the GW+DMFT method, we can understand the SEX+DMFT approach as the combination of the COulomb Hole and Screened EXchange approximation (COHSEX) [Hedin(1965)] with Dynamical Mean Field Theory. In the COHSEX approximation, the self-energy is static and divided between a non-local screened-exchange term

$$\Sigma_{SEX}(r_1,r_2) = -\sum_{iocc}\phi_i(r_1)\phi^*_i(r_2)W(r_1,r_2,\omega=0)$$

and a local Coulomb hole

$$\Sigma_{COH}(r_1,r_2) = \frac{1}{2}\delta(r_1-r_2)\left(W(r_1,r_2,0)-v(r_1,r_2)\right)$$

Combining this self-energy with the impurity self-energy from DMFT implies a double-counting of correlations as in GW+DMFT, but in that case it is exactly equal to the Coulomb hole. Eventually, we recover the SEX+DMFT equations.

Compared to GW+DMFT, the differences in SEX+DMFT are that:

- non-local dynamical correlations are not taken into account
- the screened exchange is in our case calculated differently

We point out that the question of what method is more adapted to calculate the screened exchange is difficult to answer. Using a Yukawa potential with a single Thomas-Fermi screening length might be a problem because it is independent of the atom considered and the most adapted way of calculating its value is an open question[1]. Still, it is not clear that the Random Phase Approximation used to calculate the screened Coulomb interaction W is more accurate, though it

[1]This will be discussed in more details in Chapter 9 but one of the main questions is whether the screening length should be calculated self-consistently or not. However, we stress that this question of self-consistency is also controversial in the GW context [Holm and von Barth(1998), Caruso *et al.* (2013)].

at least reproduces the Friedel oscillations in the dielectric function while the Thomas-Fermi does not [Mahan(1990)][2]. On the other hand, the GW approximation presents the clear advantage of including correlations for all states, and not only a low-energy subspace, which is important for the description of higher energy states and their hybridization with the correlated orbitals. In addition, the screening of the Coulomb potential used to calculate the exchange term is a full matrix. Eventually, the SEX+DMFT method should be understood as a cheaper way to include non-local exchange and get free of LDA double-counting problems, but probably not as accurate as GW+DMFT would be.

Finally, we want to point out that the main question one should think about before applying the SEX+DMFT method for a given material is exactly that of neglecting non-local correlations, as in equation 5.1.1. If the non-local part of self-energy is mainly static in the low-energy subspace considered, it will be equal to a Fock-like exchange term, in which all higher-energy degrees of freedom have been integrated in the screening of the Coulomb potential and the renormalization of the quasiparticles energies, that is to say screened exchange. This question can be addressed already within the GW approximation, and it has been answered positively at least in the case of iron pnictides [Tomczak *et al.* (2012b)] and of $SrVO_3$ [Tomczak *et al.* (2014)].

5.6 Application to $SrVO_3$

$SrVO_3$ is a moderately correlated transition-metal oxide. A review of its electronic properties can be found in [Tomczak *et al.* (2014)]. Because of its simple electronic structure, it has become a benchmark compound for DMFT-based methods. In this section, we present the results of calculations using our SEX+DMFT approach.

The density of states of $SrVO_3$ at the Fermi level is purely composed of *t2g* states. DFT-LDA predicts a value of 1.6 states/eV/cell for a volume of the cell of 56.71 $Å^3$, which corresponds to a Thomas-Fermi screening wavenumber of 1.2 $bohr^{-1}$. We remind the interorbital dynamical interaction $U(\omega)$ in a *t2g-t2g* model and show the corresponding bosonic spectral function ρ_B for $\beta = 30$ on Figure 5.6.1. The main feature of the dynamical screening is an important plasmon peak around 15 eV, but there is also a smaller one around 4 eV corresponding to the onset of occupied oxygen *2p* to empty vanadium *eg* transitions. The value of the corresponding bosonic factor is $Z_B = 0.69$.

We choose to use an Around Mean Field double-counting, which is equivalent to the orbital-dependent AMF since the *t2g* orbitals are degenerate. The calculation of the screened-exchange matrix elements is performed over 150 bands on a 6x6x6 grid and the matrix is then diagonalized for each kpoint on a 12x12x12 grid.

A comparison of the spectral function from SEX+DMFT with dynamical interactions $U(\omega)$ at inverse temperature $\beta = 30$ with the bandstructures calculated from LDA and screened-Hartree Fock is displayed on Figure 5.6.2. While the non-local screened exchange self-energy increases the bandwidth of the *t2g* states by about 22% compared to LDA, the combination of exchange and correlation self-energies finally reduces the LDA bandwidth by about 50%, in excellent agreement with the ARPES data of [Yoshida *et al.* (2005), Eguchi *et al.* (2006), Yoshida

[2] We also note that in some GW codes the self-energy matrix is considered diagonal in the space of Kohn-Sham orbitals which in general does not even correctly mimic the quasiparticle states, especially for the empty bands. In the implemented SEX scheme one can choose if the matrix is diagonalized or not and we can see that the difference is important for the precision we want to achieve.

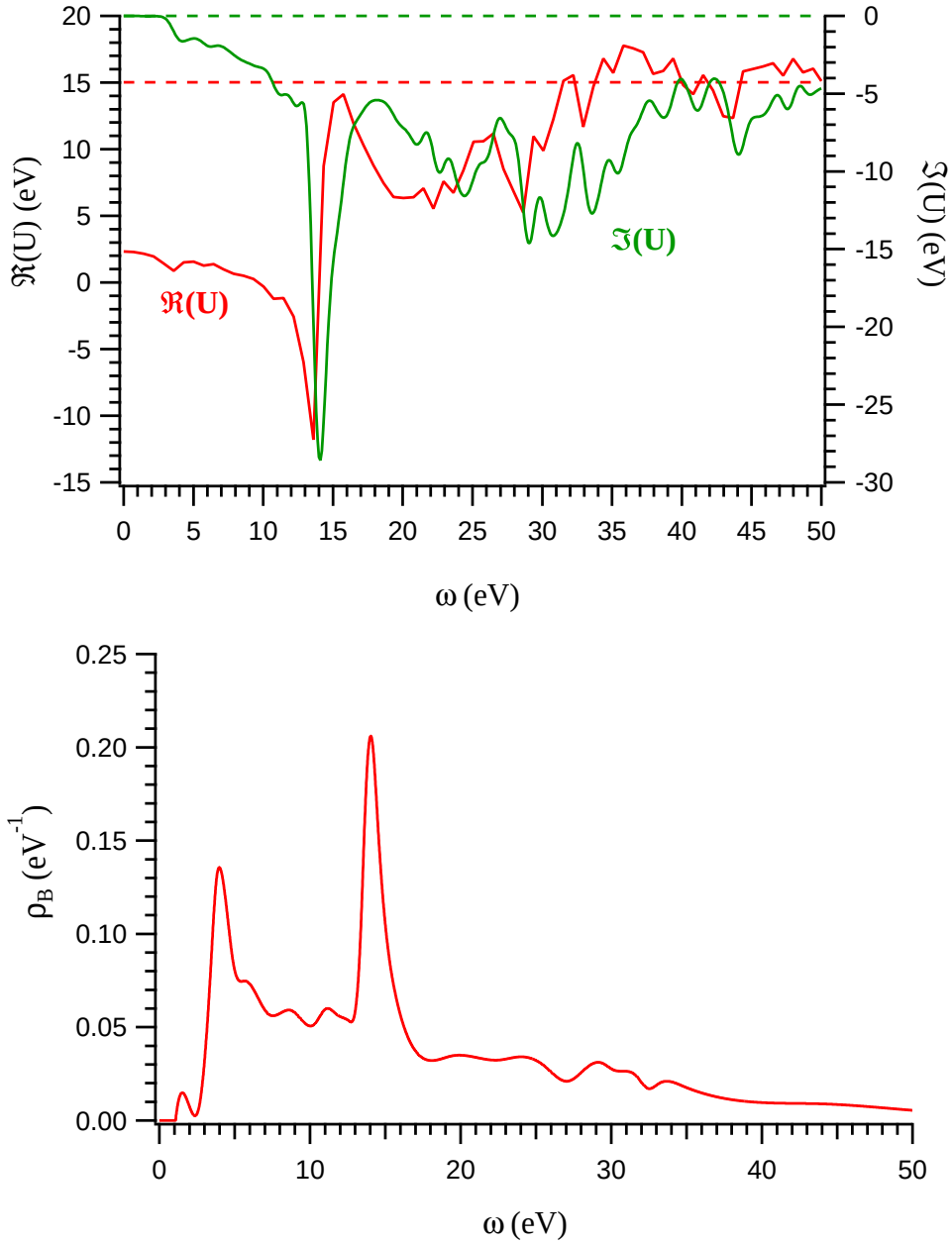

Figure 5.6.1: Frequency-dependent interorbital Coulomb interaction $U(\omega)$ in the $SrVO_3$ *t2g* shell (top) and corresponding bosonic spectral function $\rho_B(\omega)$ (bottom).

et al. (2010)]. Indeed we find a renormalization factor Z equal to 0.49, and since the LDA and SEX bandstructures are very close on the occupied part this corresponds to an effective mass of about $2m_{LDA}$.

The Hubbard bands can be well identified around -1.2 eV and 2 eV. The photoemission measurements of [Sekiyama *et al.* (2004), Morikawa *et al.* (1995)] find a slightly deeper lower Hubbard band, around -1.5 eV. This is related to the static value of the monopole interaction found by our constrained-RPA code, $F^0 = 3.2$ eV, which is lower than the value of 3.5 eV to 4 eV used in the literature that reproduce the exact position of the lower Hubbard band [Casula *et al.* (2012a), Huang and Wang(2012), Tomczak *et al.* (2012a), Tomczak *et al.* (2014)]. The density of states from LDA is compared to the density of states from SEX and the integrated

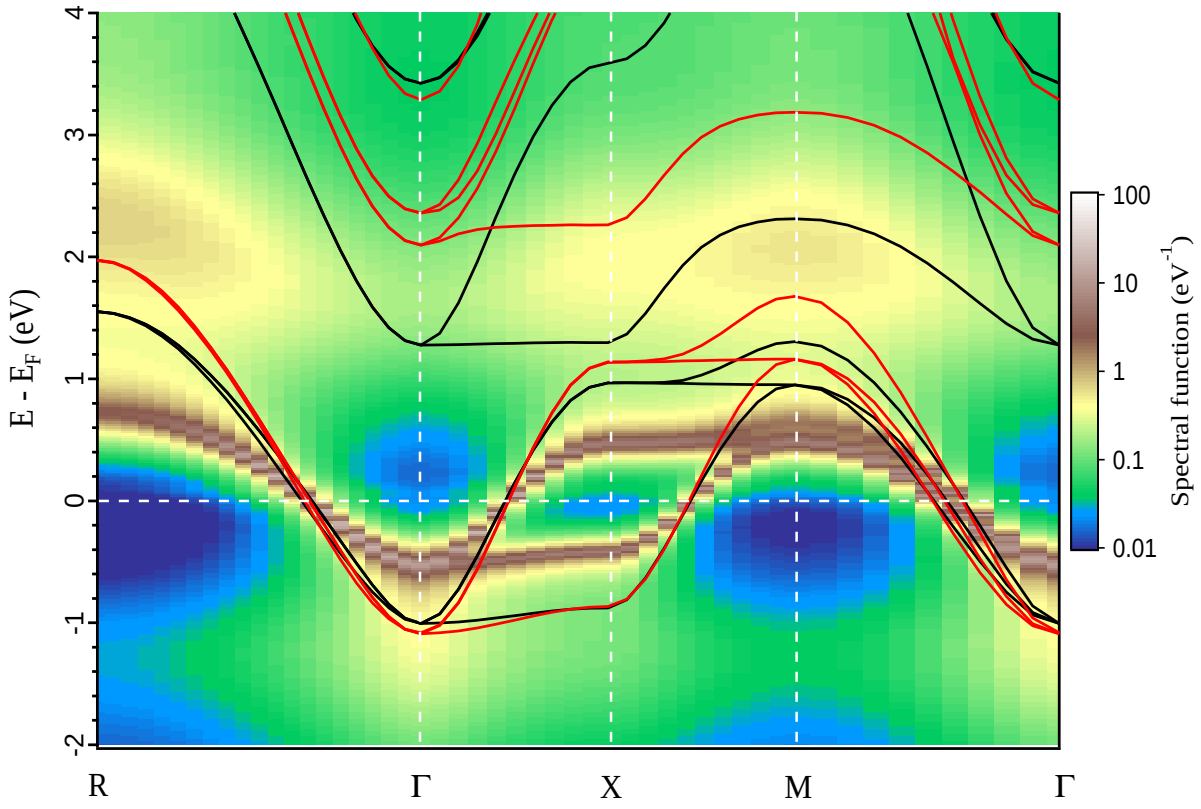

Figure 5.6.2: Bandstructure from Local Density Approximation (black) and Screened EXchange with $k_{TF} = 1.2$ bohr^{-1} (red) for $SrVO_3$ superimposed on the spectral function from SEX+DMFT with dynamical interactions $U(\omega)$.

spectral function from SEX+DMFT with dynamical interactions on Figure 5.6.3, and the spectral function is replotted on a larger scale on Figure 5.6.4 (sum over momentum space) and Figure 5.6.5 (momentum-resolved spectral function). We point out the transfer of spectral weight to plasmon excitations around 14-15 eV that can be clearly identified.

The effect of the broadening induced by the screened exchange is stronger on the unoccupied part of the spectrum than on the occupied one. This has also been pointed out in [Tomczak *et al.* (2014)], though quantitatively the expansion of the bandwidth induced by non-local effects within the Quasiparticle Self-consistent GW approximation has been found twice stronger, increasing the LDA bandwidth by about 44%. This might be an indication that using the LDA density of states to calculate the screening length leads to an underestimation of screened exchange. Indeed, since the Fock exchange expands the bandwidth it will most of the time reduce the density of states at the Fermi level. After DMFT in our case the Luttinger theorem implies that the integrated spectral function at the Fermi level stays equal to this reduced value of the DOS. Depending on the material and the chosen model, the real part of the self-energy and double-counting might induce some small changes[3]. Yet, we can understand that in general correlations included at the LDA level reduce the bandwidth compared to our screened Hartree-Fock but do not take into account the corresponding quasiparticle weight, thus overestimating the density of states at the Fermi level. This effect is taken into account at the QSGW level in

[3] It is not the case in $SrVO_3$ because all orbitals included in the low-energy model are degenerate but can happen in multiorbital systems like iron pnictides.

the previously mentioned calculation, and it may be one of the reasons why the broadening of the bandwidth due to the non-local GW self-energy is found to be stronger.

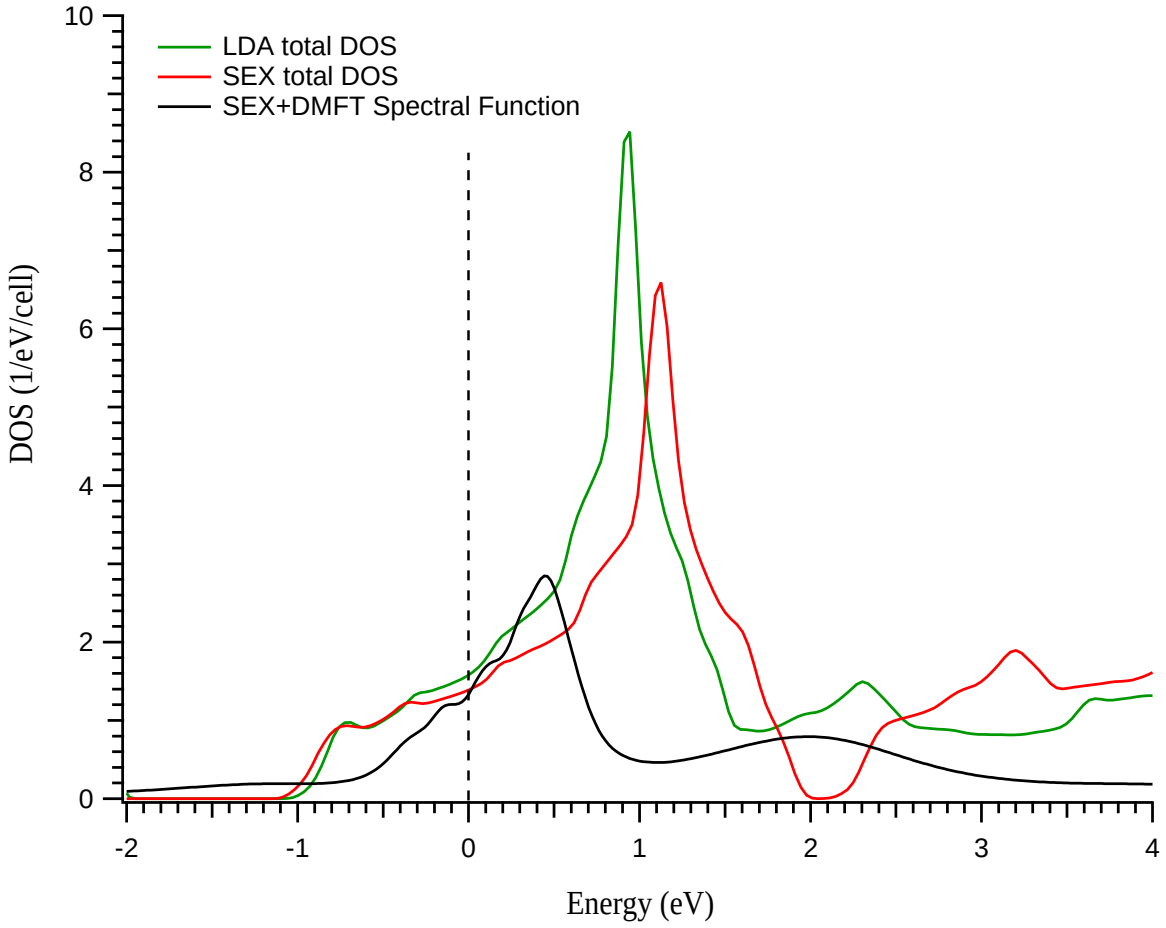

Figure 5.6.3: Density of states of $SrVO_3$ from Local Density Approximation (green), Screened EXchange (red) and integrated spectral function from SEX+DMFT with dynamical interactions $U(\omega)$ for the *t2g* states (black).

A first solution to cure this problem would be to self-consistently calculate the screening length, as shown in Figure 5.2.1. In $SrVO_3$, because we consider that there are only *t2g* states in our model and at the Fermi level, and because those *t2g* orbitals are degenerate and are thus all shifted by the same real part of the self-energy, the Luttinger theorem implies that the value of the density of states at the Fermi level in SEX is equal to the value of the spectral function from SEX+DMFT (see Figure 5.6.3 for an illustration). As a consequence, we can find the self-consistent value for the Thomas-Fermi screening length only from the result of the SEX density of states, which is much cheaper than performing dynamical DMFT for each try. We find that the screening wavenumber from the SEX+DMFT spectral function at the Fermi level is self-consistent for a value of 1.1 $bohr^{-1}$ – corresponding to 1.4 states/eV/cell. Such a small variation with the LDA Thomas-Fermi screening length does not impact much the spectral function of Figure 5.6.2, and does not explain the difference of renormalization between our Screened exchange bandstructure and the non-local QSGW one. These results and an application to weakly electron-doped $SrTiO_3$ can be found in [van Roekeghem and Biermann(2014)].

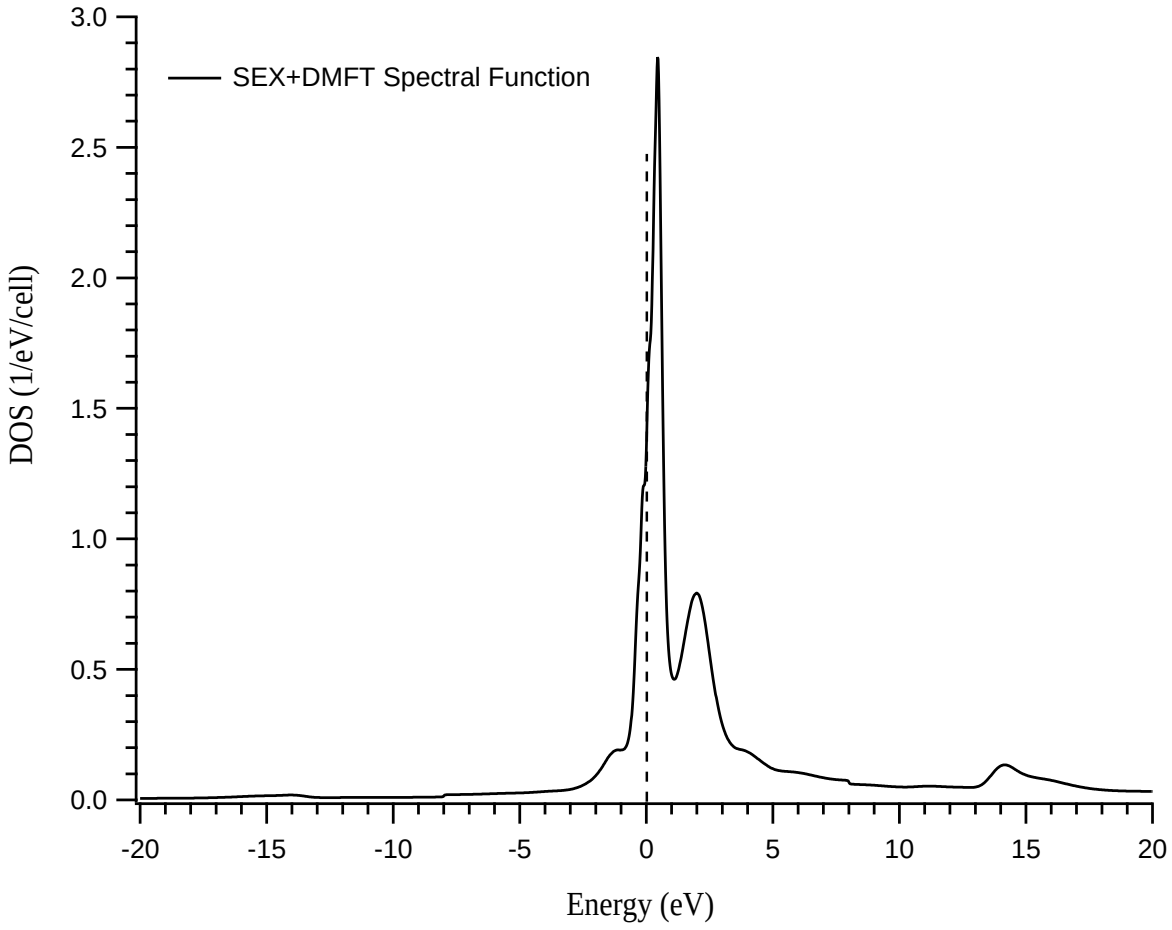

Figure 5.6.4: Integrated spectral function from SEX+DMFT with dynamical interactions $U(\omega)$ for the *t2g* states on a larger scale.

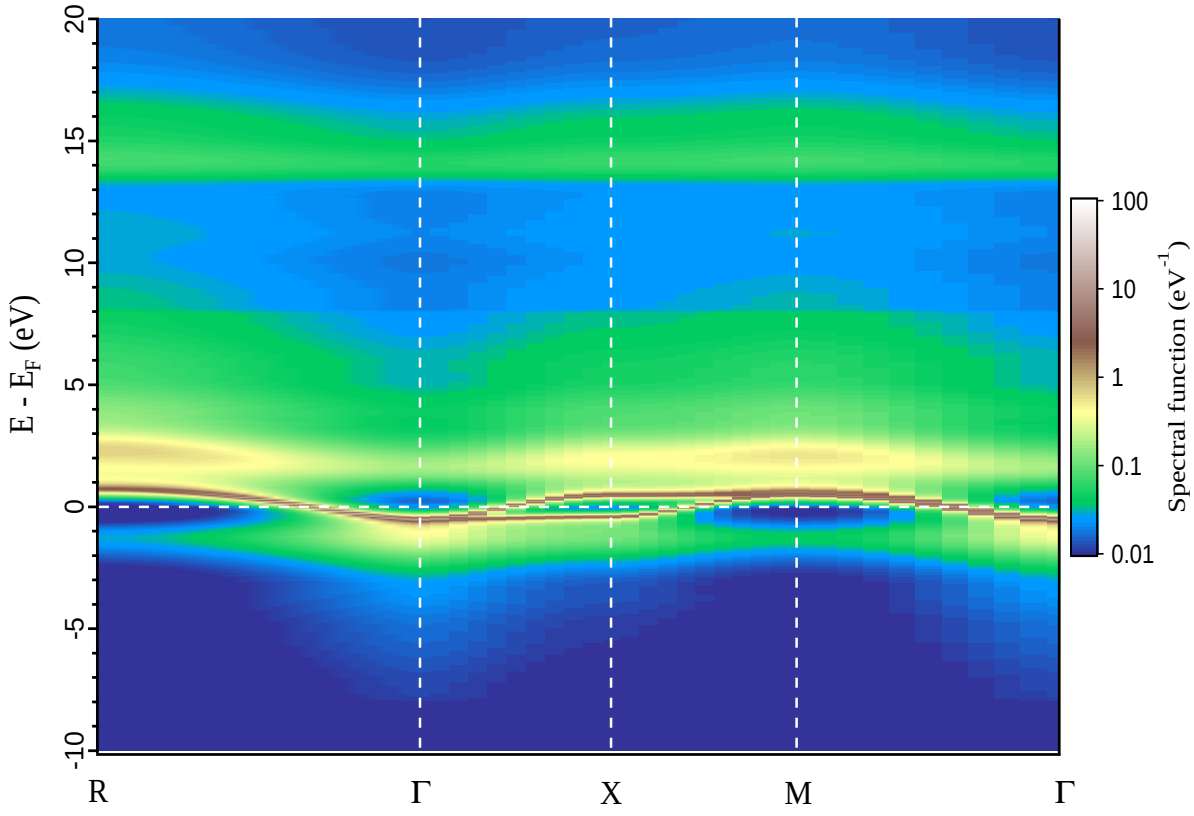

Figure 5.6.5: Momentum-resolved spectral function from SEX+DMFT with dynamical interactions $U(\omega)$ on a larger scale.

Part IV

Dynamical Hubbard interactions in iron pnictides

In this part, in collaboration with Loïg Vaugier, Hong Jiang and Silke Biermann, the strength of the frequency-dependent on-site electronic interactions in the iron-based pnictide (LaFeAsO, $BaFe_2As_2$ and $BaRu_2As_2$, LiFeAs) and chalcogenide (FeSe) families is calculated from first-principles within the constrained random phase approximation as described in Section 3.4. We use the recent implementation of [Vaugier et al. (2012b)], based on the electronic structure code Wien2k [Blaha et al. (2001)]. Both Fe d and ligand As (and O in oxypnictides) p degrees of freedom are considered in the construction of the resulting parameter-free low-energy "dp-dp" *Hamiltonian. An effective* "d-dp" *Hamiltonian where only the occupation on Fe-*d *orbitals is affected by the Coulomb repulsion can then be constructed via a "shell-folding" procedure (see Section 3.4.5). Our results for the static value of the interaction parameter are similar to the calculations performed in [Vaugier(2011)] in a* d-dp *model in which only the transitions from and to the bands with a majority of* d*-orbital character were cut within constrained-RPA and U_{dp} was neglected. On the other hand, the infinite frequency value is reduced by about 30%. In agreement with widespread ideas, we show that the effective Coulomb interactions for Fe-3*d *shells, are larger in "11" chalcogenides than in "122" and "1111" pnictides, while the "111" are an intermediate case.*

The accuracy of an atomic-like parametrization of the two-index density-density interaction matrices within the "dp-dp" *low-energy Hamiltonian is then discussed. It is based on the calculation of an optimal set of three independent Slater integrals, assuming that the angular part of the Fe-d localized orbitals can be described within spherical harmonics as for isolated Fe atoms (see Section 3.4.3). Similarly to what was demonstrated for the* d-dp *model in [Vaugier(2011)], we find that this accuracy depends on the ligand-metal bonding character rather than on the dimensionality of the lattice: it is excellent for ionic-like Fe-Se (FeSe) chalcogenides and not as good for more covalent Fe-As (LaFeAsO, $BaFe_2As_2$) pnictides. This illustrates the differences in the sphericity of the Fe-3*d *Wannier orbitals and in the anisotropy of the screening.*

In a second chapter, we investigate the relative importance of screening channels which reduce the on-site bare interaction to the fully screened one. We show that the screening channels are analogously structured in the pnictide and chalcogenide families, while this structure is very different in a benchmark oxide $SrVO_3$. The ligand channel does not appear to be responsible for the dominant screening mechanism in iron pnictides.

Finally, we analyze the frequency dependence of the interaction and its relation with the values of the free-electrons plasmon frequencies. We show that it cannot be simply modeled with a single plasmon, and that the effective model has a critical influence on the high-frequency tail and the resulting bosonic renormalization of quasiparticle dispersions.

Chapter 6

Hubbard interactions and Slater parametrization in chalcogenides and pnictides

In this chapter, we calculate the on-site electronic interactions in the iron-based pnictide (LaFeAsO, $BaFe_2As_2$ and $BaRu_2As_2$, LiFeAs) and chalcogenide (FeSe) families from first-principles within the constrained random phase approximation as described in Section 3.4. We use the recent implementation of [Vaugier et al. (2012b)], based on the electronic structure code Wien2k [Blaha et al. (2001)]. Both Fe d and ligand As (and O in oxypnictides) p degrees of freedom are considered in the construction of the resulting parameter-free low-energy "dp-dp" *Hamiltonian. An effective* "d-dp" *Hamiltonian where only the occupation on Fe-d orbitals is affected by the Coulomb repulsion can then be constructed via a "shell-folding" procedure (see Section 3.4.5). We compare the strength of the static and bare interactions within these families. We then discuss the accuracy of an atomic-like parametrization of the two-index density-density interaction matrices based on the calculation of an optimal set of three independent Slater integrals. Our results are very similar to the calculations performed in [Vaugier(2011)] in a* d-dp *model in which only the transitions from and to the* d*-like bands were cut within constrained-RPA, except for the infinite frequency value of the interaction, which is reduced by about 30%.*

6.1 General trends

We calculate the four-index Coulomb interaction matrices $U_{m_1m_2m_3m_4}$ from first-principles for a *dp-dp* Hamiltonian. Most matrix elements are of the order of 0.1 eV or less, except for two-index reduced interaction matrices, $U^{\sigma\sigma}_{mm'}|_{\text{cRPA}}$, $U^{\sigma\bar{\sigma}}_{mm'}|_{\text{cRPA}}$ and $J^{\text{cubic}}_{mm'}$ which can be extracted from the calculation. We then apply the shell-folding procedure described in Section 3.4.5. The values for the Hubbard U and Hund's exchange J for the effective *d-dp* low-energy Hamiltonian are reported in Table 6.1.2. Here U is defined as the mean value of the full $U^{\sigma\bar{\sigma}}_{mm'}$ matrix while J is defined such that $U-J$ is the mean value of $U^{\sigma\sigma}_{mm'}$. 4x4x3, 5x5x2, 4x4x2 and 4x4x4 meshes were used for the Brillouin zone integration for FeSe, LaFeAsO, LiFeAs and $BaFe_2As_2$ and $BaRu_2As_2$, respectively. The localized orbitals for Fe-3*d* and Ru-4*d* are constructed out of the Kohn-Sham states within the energy window $\mathcal{W}_{dp}$ (Table 6.1.1), following the implementation of [Aichhorn *et al.* (2009)].

Table 6.1.1: Lattice parameters used for the iron pnictides and chalcogenides and energy windows $\mathbb{W}_{dp}$ (in eV) for the *d-dp* low-energy Hamiltonians. *d* localized orbitals are constructed out of the Kohn-Sham states included in $\mathbb{W}_{dp}$.

	a(Å)	c(Å)	z_{As}	$\mathbb{W}_{dp}$(eV)
FeSe	3.77	5.50	0.267	[-6.5,2.4]
LiFeAs	3.79	6.36	0.2635	[-6.0,2.8]
$BaFe_2As_2$	3.96	13.02	0.3545	[-6.5,2.7]
LaFeAsO	4.03	8.74	0.349	[-5.5,2.5]
$BaRu_2As_2$	4.15	12.25	0.353	[-6.5,3.6]

Table 6.1.2: Hubbard $U_{eff}(\equiv F^0 - U_{dp})$, Hund's exchange $J(\equiv (F^2+F^4)/14)$ and screened ratio F^4/F^2 for effective (shell-folded) *d-dp* Hamiltonians. Both static ($\omega = 0$) and infinite frequency values are shown, as well as the unscreened (bare) interaction $v \equiv F^0(\omega = +\infty)$. The mean value of the intershell interaction $U_{dp}(0)$ and $U_{dp}(+\infty) = v_{dp}$ is also reported. Values in parentheses (see also [Miyake *et al.* (2010)]) are indicated for comparison with cRPA calculations using maximally localized Wannier functions to represent the *d* local orbitals.

(eV)	$U_{eff}(\omega=0)$	$J(\omega=0)$	F^4/F^2	$U_{dp}(\omega=0)$
FeSe	3.90	0.92	0.699	2.11
	(4.0 [Aichhorn *et al.* (2010)])	(0.9 [Aichhorn *et al.* (2010)])		
LiFeAs	3.06	0.86	0.704	1.85
$BaFe_2As_2$	2.30	0.81	0.725	1.33
	(2.7 [Werner *et al.* (2012)])			
LaFeAsO	1.97	0.77	0.732	1.17
	(2.7 [Aichhorn *et al.* (2009)])	(0.7 [Aichhorn *et al.* (2009)])		
$BaRu_2As_2$	1.80	0.58	0.804	1.40

(eV)	$U_{eff}(+\infty)$	v	$J(+\infty)$	$F^4/F^2(+\infty)$	$U_{dp}(+\infty)$
FeSe	14.32	20.36	1.03	0.623	6.04
LiFeAs	13.77	19.51	0.97	0.624	5.74
$BaFe_2As_2$	13.73	19.31	0.96	0.620	5.58
LaFeAsO	13.23	18.74	0.92	0.622	5.51
$BaRu_2As_2$	7.78	13.13	0.72	0.669	5.35

FeSe is the material that exhibits the largest Hubbard $U = 3.9$ eV and Hund's exchange $J = 0.9$ eV. We obtain similar values within a direct calculation of a non-shell-folded *d-dp* model where only transitions from *d* to *d* bands are cut (see [Vaugier(2011)]), which was expected since there is negligible hybridization between Fe-*d* orbitals and Se-*p* orbitals. The values agree with the ones calculated within an other implementation of cRPA, employing maximally localized Wannier orbitals as Fe-3*d* local orbitals [Miyake *et al.* (2010), Aichhorn *et al.* (2010)]. The large values of U and J lead to the identification of a lower Hubbard band within LDA+DMFT [Aichhorn *et al.* (2010)], in agreement with photoemission experiments on $FeSe_{0.42}Te_{0.58}$ [Tamai *et al.* (2010)].

The Hubbard U within the *d-dp* low-energy Hamiltonian in the iron-based pnictides LaFeAsO and $BaFe_2As_2$ is about 1.5 eV smaller than in the chalcogenide FeSe (see Table 6.1.2). The screened ratios of the Slater integrals, F^4/F^2, are on the other hand more deviated from the empirical atomic value for 3*d* shells.

In comparison, the values for the Hubbard U and Hund's coupling J for $BaRu_2As_2$ are lower than for $BaFe_2As_2$. Because the bandwidth of the Ru-4*d* bands is almost 2 eV larger than Fe-3*d*, the kinetic energy on the Ru-4*d* orbitals is much larger. This suggests that a band theory is appropriate to describe the electronic properties in $BaRu_2As_2$, in agreement with photoemission experiments [Brouet *et al.* (2010)].

Finally, LiFeAs can be considered as an intermediate case, where the Coulomb interactions are higher than the two other studied iron pnictides. This can be linked to the longer Fe-As distance of 2.42 Å in this compound, compared to 2.40 Å in the others, making the iron Wannier functions closer to atomicity.

6.2 Accuracy of the Slater parametrization

We now display the interaction matrices for FeSe, LiFeAs, $BaFe_2As_2$ and $BaRu_2As_2$ and discuss the accuracy of the Slater parametrization introduced in Section 3.4.3.

6.2.1 FeSe

The reduced interaction matrices (in eV) from a direct cRPA calculation with cubic symmetry in a *dp-dp* model read as (see equations 3.4.3 and 3.4.4):

$$U^{\sigma\sigma}_{mm'}|_{\text{cRPA}} = \begin{pmatrix} 0 & 2.56 & 2.53 & 3.44 & 3.44 \\ 2.56 & 0 & 3.65 & 2.85 & 2.85 \\ 2.53 & 3.65 & 0 & 2.81 & 2.81 \\ 3.44 & 2.85 & 2.81 & 0 & 2.87 \\ 3.44 & 2.85 & 2.81 & 2.87 & 0 \end{pmatrix}$$

$$U^{\sigma\bar{\sigma}}_{mm'}|_{\text{cRPA}} = \begin{pmatrix} 4.97 & 3.36 & 3.33 & 3.95 & 3.95 \\ 3.36 & 4.94 & 4.06 & 3.55 & 3.55 \\ 3.33 & 4.06 & 4.85 & 3.52 & 3.52 \\ 3.95 & 3.55 & 3.52 & 4.99 & 3.56 \\ 3.95 & 3.55 & 3.52 & 3.56 & 4.99 \end{pmatrix}.$$

Here we have already applied the shell-folding procedure, with the calculated intershell interaction $U_{dp} = 2.11$ eV. The ordering of the orbitals in those matrices is $d_{3z^2-r^2}$,$d_{x^2-y^2}$,d_{xy},d_{xz},d_{yz}. There is a small orbital dependence of the intra-orbital interactions, through the diagonal of $U^{\sigma\bar{\sigma}}_{mm'}|_{\text{cRPA}}$, since the cubic symmetry is an approximation for the crystal field in FeSe. The deviation is around 0.14 eV and the average intra-orbital interaction (before shell-folding) calculated with cubic symmetry is $U_m = 7.06$ eV.

This deviation does not increase when elongating the crystal structure through the c-direction, perpendicular to the Fe-Se tetrahedra, although the dimensionality is reduced. It shows that the chemical environment of Fe is the main actor for the accuracy of the atomic-like Slater parametrization.

For the *Slater symmetrized* reduced interaction matrices (in eV), we get from equations 3.4.9 and 3.4.10:

$$\bar{U}^{\sigma\sigma}_{mm'}|_{\text{Slater}} = \begin{pmatrix} 0 & 2.55 & 2.55 & 3.40 & 3.40 \\ 2.55 & 0 & 3.69 & 2.84 & 2.84 \\ 2.55 & 3.69 & 0 & 2.84 & 2.84 \\ 3.40 & 2.84 & 2.84 & 0 & 2.84 \\ 3.40 & 2.84 & 2.84 & 2.84 & 0 \end{pmatrix}$$

$$\bar{U}^{\sigma\bar{\sigma}}_{mm'}|_{\text{Slater}} = \begin{pmatrix} 4.95 & 3.35 & 3.35 & 3.92 & 3.92 \\ 3.35 & 4.95 & 4.11 & 3.54 & 3.54 \\ 3.35 & 4.11 & 4.95 & 3.54 & 3.54 \\ 3.92 & 3.54 & 3.54 & 4.95 & 3.54 \\ 3.92 & 3.54 & 3.54 & 3.54 & 4.95 \end{pmatrix}.$$

The deviation from the directly calculated values is of the order of 0.10 eV with a relative error around 2%. It is a property of the atomic parametrization to set an orbital-independent intra-orbital interaction with cubic symmetry.

Considering the higher-order Slater integrals, $F^2 = 7.57$ eV and $F^4 = 5.30$ eV, it appears that the screened ratio $F^4/F^2 = 0.70$ is deviated from the atomic empirical value around 0.63 (see Table 6.1.2). Such deviation does not imply that the localized orbitals for Fe in FeSe display orbital anisotropies since the atomic parametrization appears to be well justified, as shown above. We stress that for the bare (unscreened) ratio $F^4/F^2|_{\text{bare}}$ we recover the atomic value.

6.2.2 LaFeAsO

The reduced interaction matrices (in eV) calculated with cubic symmetry read as:

$$U^{\sigma\sigma}_{mm'}|_{\text{cRPA}} = \begin{pmatrix} 0 & 0.94 & 0.85 & 1.53 & 1.53 \\ 0.94 & 0 & 1.82 & 1.12 & 1.12 \\ 0.85 & 1.82 & 0 & 1.00 & 1.00 \\ 1.53 & 1.12 & 1.00 & 0 & 1.00 \\ 1.53 & 1.12 & 1.00 & 1.00 & 0 \end{pmatrix}$$

$$U^{\sigma\bar{\sigma}}_{mm'}|_{\text{cRPA}} = \begin{pmatrix} 3.04 & 1.66 & 1.51 & 1.97 & 1.97 \\ 1.66 & 3.23 & 2.19 & 1.73 & 1.73 \\ 1.51 & 2.19 & 2.65 & 1.57 & 1.57 \\ 1.97 & 1.73 & 1.57 & 2.68 & 1.55 \\ 1.97 & 1.73 & 1.57 & 1.55 & 2.68 \end{pmatrix},$$

where the order of the orbital in these matrices is $d_{3z^2-r^2}$,$d_{x^2-y^2}$,d_{xy},d_{xz},d_{yz}. The interactions have been shell-folded with $U_{dp} = 1.17$ eV.

The intra-orbital repulsions are larger on $d_{3z^2-r^2}$ and $d_{x^2-y^2}$ orbitals. It is due to the smaller orbital spreads of these orbitals that do not point toward the As ligands [Vildosola *et al.* (2008)]. The deviations for the orbitally-resolved intra-orbital interactions are larger than in FeSe. In particular, the deviation yields 0.58 eV between the intra-orbital interactions on $d_{x^2-y^2}$ and d_{xy} orbitals, against 0.14 eV for FeSe.

Within the Slater parametrization, the symmetrized reduced interaction matrices read as:

$$\bar{U}^{\sigma\sigma}_{mm'}|_{\text{Slater}} = \begin{pmatrix} 0 & 0.87 & 0.87 & 1.55 & 1.55 \\ 0.87 & 0 & 1.77 & 1.10 & 1.10 \\ 0.87 & 1.77 & 0 & 1.10 & 1.10 \\ 1.55 & 1.10 & 1.10 & 0 & 1.10 \\ 1.55 & 1.10 & 1.10 & 1.10 & 0 \end{pmatrix}$$

$$\bar{U}^{\sigma\bar{\sigma}}_{mm'}|_{\text{Slater}} = \begin{pmatrix} 2.85 & 1.53 & 1.53 & 1.98 & 1.98 \\ 1.53 & 2.85 & 2.13 & 1.68 & 1.68 \\ 1.53 & 2.13 & 2.85 & 1.68 & 1.68 \\ 1.98 & 1.68 & 1.68 & 2.85 & 1.68 \\ 1.98 & 1.68 & 1.68 & 1.68 & 2.85 \end{pmatrix}.$$

The largest discrepancy with the direct calculation, around 0.38 eV, is obtained for $d_{x^2-y^2}$. It is the hybridization with the As ligands and the covalent character of the As-Fe bonding that induce larger deviations of the atomic sphericity than in FeSe. Se atoms have a Pauling electronegativity around 2.55 that is larger than As (2.18) and Fe (1.83). The more ionic character of the Fe-Se bonding makes the localized Fe-3*d* orbitals more atomic-like, and hence the Slater parametrization more accurate.

6.2.3 $BaFe_2As_2$ and $BaRu_2As_2$

Similar arguments can be employed for understanding the Slater parametrization for $BaFe_2As_2$. The reduced interaction matrices calculated with cubic symmetry read as

$$U^{\sigma\sigma}_{mm'}|_{\text{cRPA}} = \begin{pmatrix} 0 & 1.22 & 1.15 & 1.84 & 1.86 \\ 1.22 & 0 & 2.15 & 1.36 & 1.37 \\ 1.15 & 2.15 & 0 & 1.29 & 1.30 \\ 1.84 & 1.36 & 1.29 & 0 & 1.27 \\ 1.86 & 1.37 & 1.30 & 1.27 & 0 \end{pmatrix}$$

$$U^{\sigma\bar{\sigma}}_{mm'}|_{\text{cRPA}} = \begin{pmatrix} 3.47 & 1.96 & 1.86 & 2.31 & 2.33 \\ 1.96 & 3.47 & 2.53 & 1.99 & 2.00 \\ 1.86 & 2.53 & 3.11 & 1.89 & 1.90 \\ 2.31 & 1.99 & 1.89 & 3.04 & 1.85 \\ 2.33 & 2.00 & 1.90 & 1.85 & 3.07 \end{pmatrix}.$$

whereas it follows for the *Slater symmetrized* interaction matrices:

$$\bar{U}^{\sigma\sigma}_{mm'}|_{\text{Slater}} = \begin{pmatrix} 0 & 1.12 & 1.12 & 1.85 & 1.85 \\ 1.12 & 0 & 2.09 & 1.36 & 1.36 \\ 1.12 & 2.09 & 0 & 1.36 & 1.36 \\ 1.85 & 1.36 & 1.36 & 0 & 1.36 \\ 1.85 & 1.36 & 1.36 & 1.36 & 0 \end{pmatrix}$$

$$\bar{U}^{\sigma\bar{\sigma}}_{mm'}|_{\text{Slater}} = \begin{pmatrix} 3.22 & 1.82 & 1.82 & 2.30 & 2.30 \\ 1.82 & 3.22 & 2.47 & 1.98 & 1.98 \\ 1.82 & 2.47 & 3.22 & 1.98 & 1.98 \\ 2.30 & 1.98 & 1.98 & 3.22 & 1.98 \\ 2.30 & 1.98 & 1.98 & 1.98 & 3.22 \end{pmatrix}.$$

The order of the orbitals is still $d_{3z^2-r^2}$,$d_{x^2-y^2}$,d_{xy},d_{xz},d_{yz}. The interactions have been shell-folded with $U_{dp} = 1.33$ eV. The largest discrepancy with the direct calculation yields around 0.25 eV and is obtained for $d_{3z^2-r^2}$ that points toward the interlayer Ba planes and for $d_{x^2-y^2}$.

The larger hybridization of Ru 4*d* states with the As ligands also makes the atomic-like Slater parametrization less accurate. We note that the largest value of the screened ratio F^4/F^2 is obtained for this compound.

6.2.4 LiFeAs

The same procedure is applied to LiFeAs, where we find $U_{dp} = 1.85$ eV. Of all studied pnictides compounds, LiFeAs is the closest to FeSe with higher Coulomb interactions and lower screened ratio F^4/F^2. We obtain for the reduced interactions matrices with cubic symmetry, after shell-folding:

$$U^{\sigma\sigma}_{mm'}|_{\text{cRPA}} = \begin{pmatrix} 0 & 1.84 & 1.82 & 2.64 & 2.64 \\ 1.84 & 0 & 2.84 & 2.05 & 2.05 \\ 1.82 & 2.84 & 0 & 2.02 & 2.03 \\ 2.64 & 2.05 & 2.02 & 0 & 2.05 \\ 2.64 & 2.05 & 2.03 & 2.05 & 0 \end{pmatrix}$$

$$U^{\sigma\bar{\sigma}}_{mm'}|_{\text{cRPA}} = \begin{pmatrix} 4.19 & 2.60 & 2.57 & 3.12 & 3.12 \\ 2.60 & 4.07 & 3.23 & 2.71 & 2.71 \\ 2.57 & 3.23 & 3.95 & 2.68 & 2.69 \\ 3.12 & 2.71 & 2.68 & 3.99 & 2.68 \\ 3.12 & 2.71 & 2.69 & 2.68 & 3.99 \end{pmatrix}.$$

whereas for the *Slater symmetrized* interaction matrices:

$$\bar{U}^{\sigma\sigma}_{mm'}|_{\text{Slater}} = \begin{pmatrix} 0 & 1.81 & 1.81 & 2.60 & 2.60 \\ 1.81 & 0 & 2.86 & 2.07 & 2.07 \\ 1.81 & 2.86 & 0 & 2.07 & 2.07 \\ 2.60 & 2.07 & 2.07 & 0 & 2.07 \\ 2.60 & 2.07 & 2.07 & 2.07 & 0 \end{pmatrix}$$

$$\bar{U}^{\sigma\bar{\sigma}}_{mm'}|_{\text{Slater}} = \begin{pmatrix} 4.04 & 2.55 & 2.55 & 3.08 & 3.08 \\ 2.55 & 4.04 & 3.25 & 2.73 & 2.73 \\ 2.55 & 3.25 & 4.04 & 2.73 & 2.73 \\ 3.08 & 2.73 & 2.73 & 4.04 & 2.73 \\ 3.08 & 2.73 & 2.73 & 2.73 & 4.04 \end{pmatrix}.$$

The parametrization is better than for other pnictides: the maximum discrepancy between the parametrized and the directly calculated matrices is only 0.15 eV. This, again, is the sign of more atomic-like Wannier functions, due to the larger Fe-As distance.

6.3 Conclusion

In conclusion, we have studied the strength of static and instantaneous Hubbard interactions and the accuracy of the Slater parametrization in the iron pnictides family for a shell-folded *dp-dp* model. In agreement to what was demonstrated in [Vaugier(2011)] for the *d-dp* model, we find that the effective Coulomb interactions for Fe-3*d* shells, are larger in 11 than in 122 and 1111 pnictides, while the 111 are an intermediate case, and that the accuracy of the Slater parametrization depends on the ligand-metal bonding character rather than on the dimensionality of the lattice: it is excellent for ionic-like Fe-Se (FeSe) chalcogenides and not as good for more covalent Fe-As (LaFeAsO, $BaFe_2As_2$) pnictides. The main effect of the shell-folding procedure is to reduce the value of the instantaneous Coulomb interaction by about 30%.

Chapter 7

Screening channels

In addition to the Hubbard interaction, other partially screened interactions can be deduced, depending on the particle-hole transitions that are removed from the RPA polarization. One can then examine the relative importance of specific transitions in the screening, or screening channels. These channels are not additive, hence the interpretation is not straightforward. In this chapter, we calculate different quantities at zero frequency in the iron pnictides and chalcogenide family and in $SrVO_3$. A detailed comparison allows us to understand the global trend and to contrast the relative importance of the screening contributions from the ligand p *and from the metallic* d *orbitals.*

7.1 Global trends through the pnictides and chalcogenide series

For each compound, we calculate seven different quantities at zero frequency, which are shown on Figure 7.1.1. The bare values on the local d orbitals vary less than 10% (except for the case of $BaRu_2As_2$ because of the larger extension of the $4d$ orbitals), as well as the fully screened values. Thus one can directly compare the values of the intra-orbital interactions obtained when considering specific occupied to empty transitions. While $SrVO_3$ stands out, the structure of the screening in all calculated pnictides and chalcogenide is remarkably similar.

If we look at the relative importance of the channels, one main difference is visible: the relative magnitude of the interaction in case (4) where all the transitions involving occupied p and all $d \rightarrow d$ transitions have been cut, and in case (6) where only the transitions from all occupied states (except d) to empty d states are considered. On top of common screening channels, it is equivalent to comparing the screening of all occupied except p and d to all empty states except d (case (4)) with the screening of $p \rightarrow d$ (case (6)). In FeSe where there is no interlayer atom and LiFeAs where Li electrons are deep core states, the number of channels of case (4) is reduced compared to the cases of $BaFe_2As_2$, LaFeAsO and $BaRu_2As_2$ where the interlayer atoms provide more screening channels. That is why the interaction in case (4) becomes bigger than in case (6) in FeSe and LiFeAs, while it is the opposite for other compounds.

For the same reason, the values of partially screened interactions are globally enhanced in FeSe and LiFeAs, because there are less possibilities of transitions. That is also why LaFeAsO displays lower values of the interaction. Eventually, the differences in screening within the pnictides and chalcogenides family happen to be mostly due to the interlayer structure.

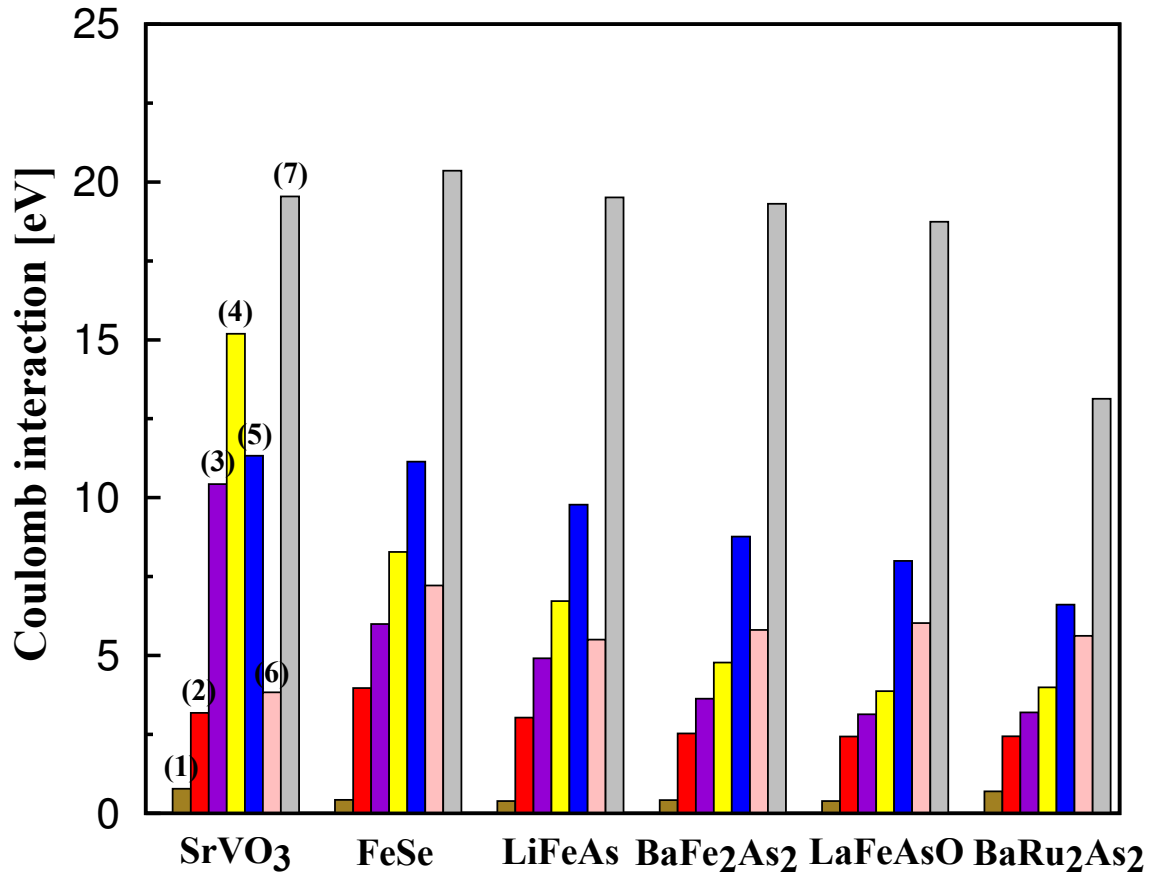

Figure 7.1.1: Strength of the screening channels in the comparison of an early transition metal oxide ($SrVO_3$) with iron-based pnictides. The bar charts show the static values of the monopole part of partially screened interactions for the 3*d* local orbitals within the *dp* low-energy Hamiltonians when removing specific "occupied to empty" transitions from the total RPA polarization. Cases (1) (brown) and (7) (gray) respectively correspond to the fully screened and unscreened cases. Case (2) (red) is the value of the static average intra-orbital interaction when removing $d \rightarrow d$ transitions only (corresponding to the *d-dp* Hamiltonian). Case (3) (purple) corresponds to the average intra-orbital interaction within the *dp* Hamiltonian, i.e. removing all the transitions within the energy window $\mathbb{W}_{dp}$, whereas in Case (4) (yellow), all the transitions involving *p* as well as $d \rightarrow d$ are removed. In Case (5) (blue), all the transitions involving *d* states are removed, whereas in Case (6) (salmon), only the transitions involving empty *d* states are considered.

7.2 Screening contributions from the ligands p orbitals

The ligands (arsenic or selenium in the pnictides/chalcogenide family, oxygen in $SrVO_3$) influence is analyzed through the prism of two different quantities: screening involving occupied ligand *p* to empty metallic *d* states, and screening involving occupied ligand *p* to other states. The ligand influence is not reduced to the screening arising from its *p* orbitals, but the screening from these orbitals is dominant since they are closer to the Fermi level.

7.2.1 Ligand *p* to metallic *d* transitions

To analyze these transitions we compare the values of cases (2) and (3) of Figure 7.1.1. The only difference between those two cases is precisely that ligand *p* to metallic *d* transitions have been cut. In $SrVO_3$ the reduction of the Coulomb interaction due to this channel is remarkable, about 63%. Moreover, by comparing to the bare value and to the fully screened value, we see that these $d \rightarrow p$ transitions account for about 40% of the total screening. On the other hand, in pnictides and chalcogenides this reduction lies between 20% (LaFeAsO and $BaRu_2As_2$) and 33% (LiFeAs), two to three times less, and the $d \rightarrow p$ transitions account for only 10% of the total screening. This could be expected given the large number of ligands surrounding the metal in $SrVO_3$ and their ionic character. In the pnictides, the As-Fe electronegativity difference is smaller, thus the bonding is more covalent and the electrons are less free to rearrange their density to screen the charge.

7.2.2 Ligand p to other empty states

Now we compare cases (3) and (4). In case (4) all transitions from p states to other states than metallic *d* have been further suppressed. Again we can see that while in $SrVO_3$ these transitions give a reduction of 29% of the Coulomb interaction, in the pnictides and chalcogenide it is only a reduction of 17% to 23 %. The transitions from ligand *p* to other states are not as important as the transitions to metallic *d* states, which could be expected since the *d* states are closer to the Fermi level.

7.3 Screening contributions from metallic d orbitals

Let us examine cases (5) and (6). In case (5) all transitions involving *d* states have been removed, while in case (6) only transitions to empty *d* states are considered. The difference can tell us how important is the metallic *d* orbitals contribution to the screening in the materials.

7.3.1 $SrVO_3$

In $SrVO_3$ we see that the transitions to empty *d* states are nearly enough to recover the full *d-dp* value. Added to the conclusion of the previous section, we see that in this oxide the main channels are related to the empty *d* states, and the $p \rightarrow d$ channel is especially predominant. Still, suppressing all these channels allows to screen about 60% of the bare value.

7.3.2 Pnictides and chalcogenides

In iron pnictides and chalcogenides the difference is not as impressive as in $SrVO_3$. In the extreme case of $BaRu_2As_2$, cases (5) and (6) nearly give the same result, showing that the empty *d* states are not as important. For 3*d* orbitals compounds, these transitions recover some predominance, and for FeSe and LiFeAs we can see that they account for a large part of the screening of the *d-dp* model. This importance is reduced in materials with interlayer screening atoms, as is also shown by the reduction of the value of case (5). Finally, we see that in pnictides and chalcogenides the main channels are also linked to metallic *d* states. Also, this family is characterized by a very similar FeAs layer and the ligand *p* states are not dominant in the screening. This is why we attribute the small differences in the screening of the Coulomb interactions within the iron pnictides family to the interlayer structure. Indeed, the atoms between layers can participate to the screening by adding possibilities of transitions with the *d* states, and the efficiency of these transitions would depend on the material. We can also see this effect from an atomic point of view and presume that the higher polarizability of a large Ba ion will be more efficient to screen the monopole interaction as in $BaFe_2As_2$ than a more localized Li ion as in LiFeAs.

7.4 Conclusion

We have discussed the relative importance of screening channels which reduce the on-site bare interaction to the fully screened one. We have shown that the screening channels are analogously structured in the pnictides and chalcogenides family, while this structure is very different in a benchmark oxide $SrVO_3$. The ligand channel does not appear to be responsible for the dominant screening mechanism in iron pnictides.

Chapter 8

Frequency dependence

In this chapter, we discuss the frequency-dependence of the Hubbard interactions in the iron pnictides and chalcogenides family and in $SrVO_3$. We display the frequency-dependent intrashell and intershell interactions in the dp-dp *Hamiltonian in which both Fe-*d *and As-*p *orbitals are taken into account. The structure of the high-frequency tail is compared with the free-electrons like plasmon frequencies obtained for selected numbers of electrons. We then calculate the strength of the bosonic renormalization factor and the impact of the shell-folding procedure on this quantity. Finally, we discuss the screening of the multipole Slater integrals.*

8.1 High-frequency tail of the monopole interaction

We calculate the real part of Slater integrals as a function of real frequency in pnictides and chalcogenides. The same method is also applied for SrVO3 to use this compound as a benchmark. A complete view of the *dp-dp* Hamiltonian (before shell folding) is shown on Figure 8.1.1.

For non-entangled systems where the hybridization between the correlated atom and the ligand is small, the *d* bands can be clearly defined and separated from the ligand bands. As a consequence, calculating the strength of the static Coulomb interaction by shell folding of a *dp-dp* Hamiltonian or using a *d-dp* scheme where only transitions from and to bands with a majority of *d*-orbital character are cut and U_{dp} is neglected will give about the same result. That is the case in most iron pnictides because the entanglement is still relatively small and the *d* bands can be reasonably defined.

This is not true anymore if we look at the bare value. Indeed, the bare repulsion is essentially related to the spread of the Wannier function of the correlated orbital since no screening processes happen. So before shell-folding the strength of the Coulomb interaction within the *d*-shell is the same for both *dp-dp* and *d-dp* calculations. However there is a big difference in the treatment of the intershell interaction U_{dp}. While in a *dp-dp* model we see that the bare value of U_{dp} is much larger than the static value, it is just ignored in a *d-dp* "entangled" calculation.

This motivates the application of frequency-dependent shell-folding. The results for all studied pnictides and chalcogenide are displayed on Figure 8.2.1, and compared to an "entangled" *d-dp* calculation where only transitions from and to bands with a majority of *d*-orbital character are cut.

For all compounds, at first sight the main correction introduced by the effective model is on the high-frequency tail, while the static part stays essentially the same. The infinite frequency

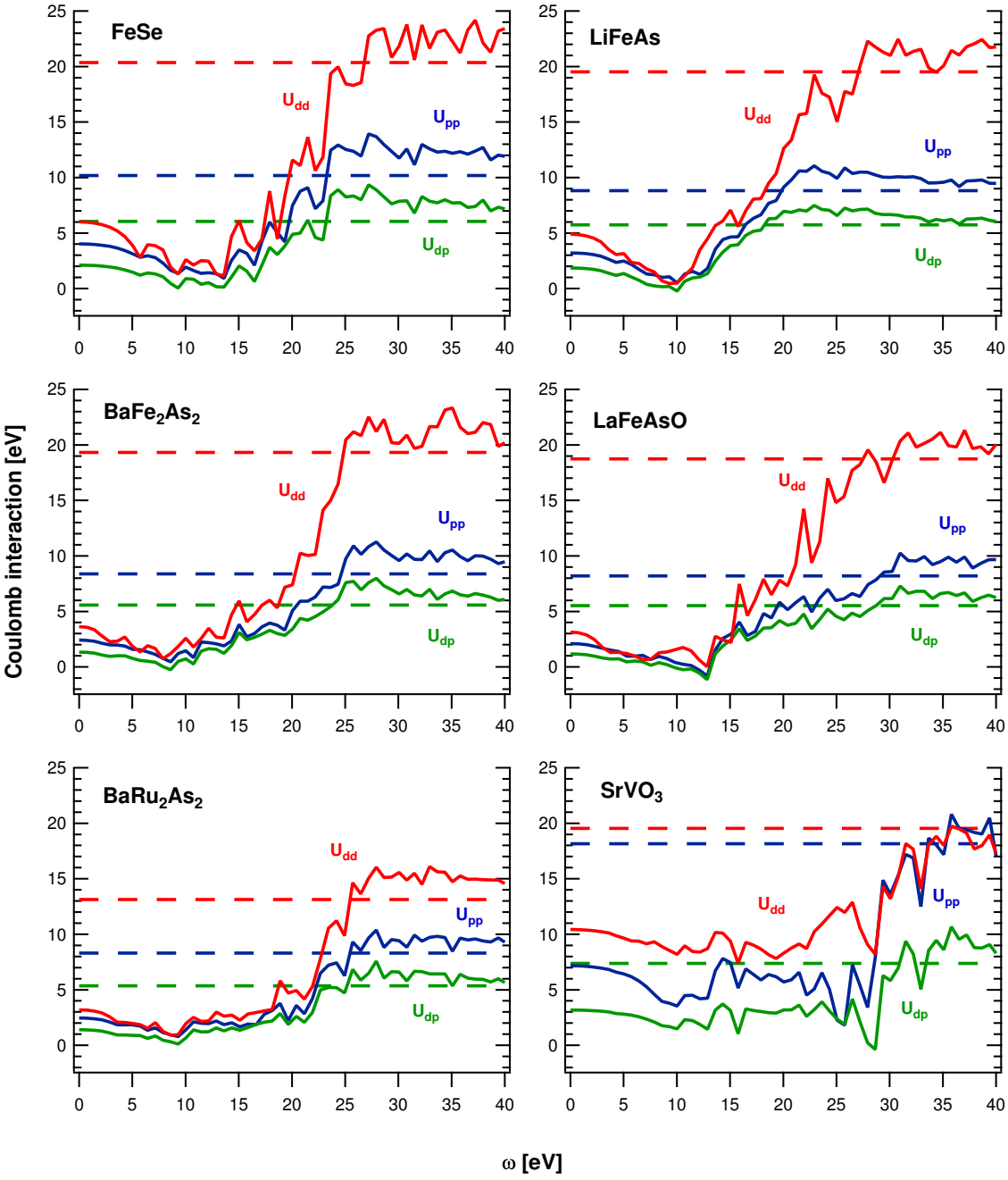

Figure 8.1.1: Frequency dependence of the different Hubbard interactions in the *dp* Hamiltonian before any shell-folding. Here $U_{dd} = F^0$ and U_{pp} should be understood as the monopole part of the partially screened interaction between p orbitals. Dashed lines are the values at infinite frequency.

value is lowered by about 30%. On the other hand, the frequency dependence of both models looks similar, with peaks around the same values of ω. Those peaks are less sharp in the effective model. Indeed F_0 and U_{dp} also share the same frequency dependence so $U_{eff} = F_0 - U_{dp}$ is smoothed compared to F_0.

Interestingly, the case of $SrVO_3$ is much different from the pnictides, since both $U(0)$ and the high frequency tail are greatly modified when we take U_{dp} into consideration. Moreover, while in pnictides taking the *p-d* interactions into account leaves $U(0)$ stable or reduces it, in $SrVO_3$ $U(0)$ is increased. The correction of this value induced by the effective model is in agreement with values used in a *d* model DMFT calculation to reproduce the experimental results [Seth *et al.* (2015)].

8.2 Plasmons and interband transitions

The dynamical structure of the Coulomb interaction is directly linked to the variations of the constrained polarization P^r. These variations are influenced principally by interband transitions and collective excitations. Indeed, in iron pnictides, ion-core polarization can be neglected, as shown by calculations of the constrained macroscopic dielectric function where all transitions from and to the valence electron bands have been cut. We calculate the main plasmon mode with the free-electrons formula for the plasma frequency:

$$\omega_p = \sqrt{\frac{ne^2}{m\epsilon_0}} \tag{8.2.1}$$

To calculate the density we take into account all valence electrons, which corresponds to all bands down to -20 eV: the Fe 3*d* electrons, As or Se 4*p* and 4*s* electrons, Ba 4*p* in $BaFe_2As_2$ and $BaRu_2As_2$, and La 5*p*, O 2*p* and 2*s* in LaFeAsO. The binding energies of those electrons are still lower than the obtained plasma frequency (between 20 and 25 eV), so it is reasonable to think that they will enter the collective resonance. For $SrVO_3$ we take into account V 3*d*, O 2*p*, Sr 4*p* and O 2*s* electrons. The plasmon frequency is then compared to the imaginary part of the monopole interaction in a *dp* model (see the highest number of electrons for each compound on Figure 8.2.1). We can see that the main peak of $\Im(F^0)$ agrees very well with the calculated plasmon frequency and corresponds to a cutoff frequency where the Coulomb interaction increases sharply from the static value to the infinite frequency value.

We also show that some of the other peaks could be assigned to partial plasmon resonances. The first partial resonance would correspond to the number of Fe 3*d* (or V 3*d*) electrons. For the second one, we add the As or Se 4*p* electrons (or the O 2*p* in the case of $SrVO_3$). We also show a third partial resonance in LaFeAsO, corresponding to the addition of the O 2*p* electrons. However, it is difficult to make a one-to-one correspondence with certainty because of the entanglement of the plasmons with the interband transitions that creates a continuum of screening modes. This effect has been documented in transition metals, where the interband transitions from the *d* bands to higher bands act to shift and broaden the plasmons composed of *s* and *p* electrons [Pines(1964)]. It also happens in the pnictides and chalcogenides since there are possibilities of transitions at frequencies close to the value of the free-electrons plasmon. As an illustration, we can see in the case of $SrVO_3$ that the agreement between a partial resonance of O 2*p* and V 3*d* electrons with the plasmon around 15 eV is really bad. However, the free-electrons plasma frequency of about 21.5 eV is likely to be modified by a combination of

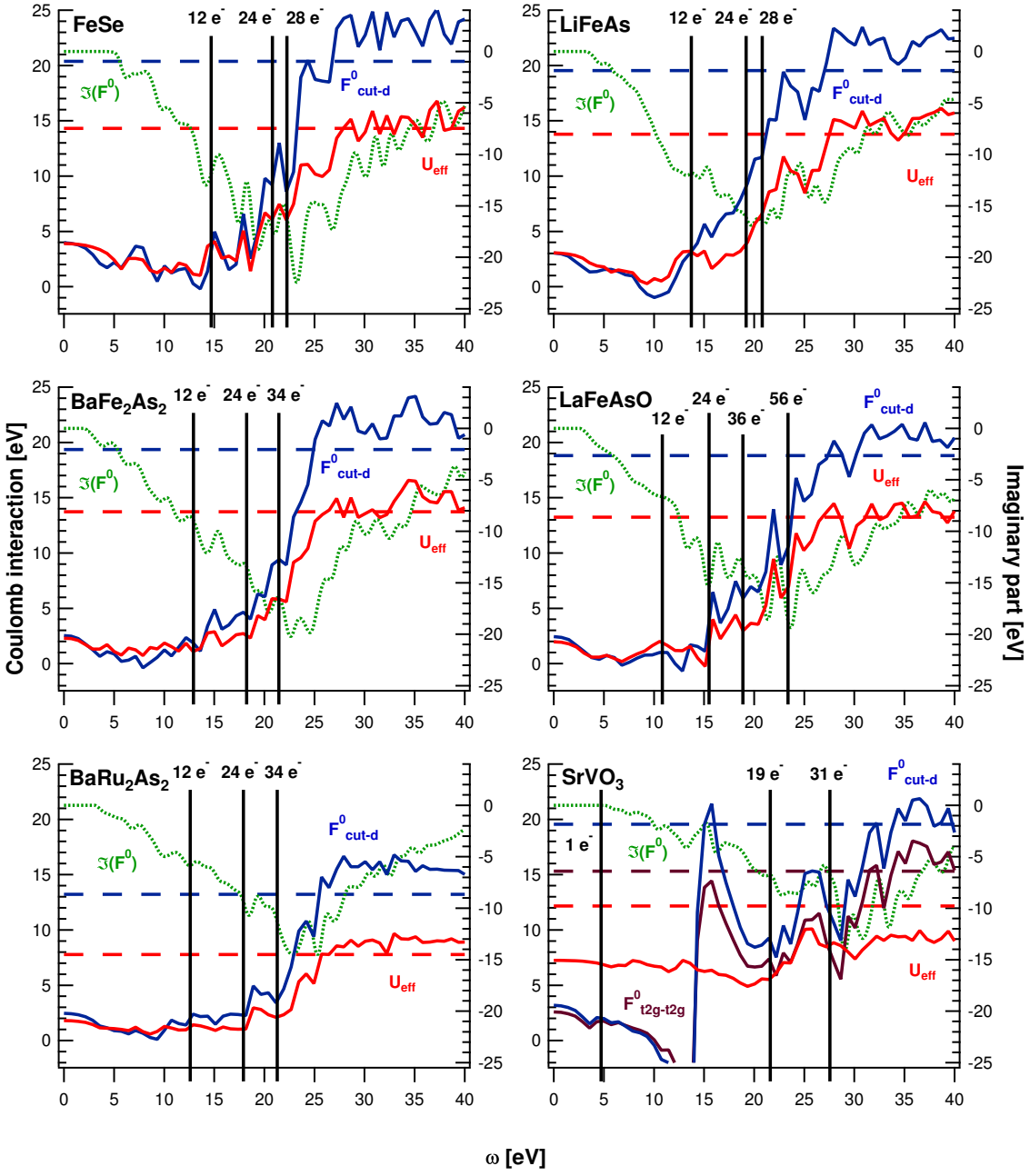

Figure 8.2.1: Frequency dependence of the monopole part of the partially screened Coulomb interaction within the *d*-shell. $U_{eff}(\omega)$ refers to $F^0(\omega) - U_{dp}(\omega)$ calculated in the *dp-dp* model. F^0_{cut-d} is the monopole part of the interaction calculated in an "entangled" *d-dp* model where only $d \rightarrow d$ transitions are removed. Dashed lines are the values at infinite frequency. The dotted line corresponds to the imaginary part of $F^0(\omega)$ and is compared to a free-electron calculation of the plasma frequency at partial resonances (vertical bars).

possible interband transitions in this frequency range and background polarization provided by lower-lying states. Indeed, the calculation of the constrained macroscopic dielectric function where transitions from *dp* bands to all empty states have been removed gives a value of about 1.4 at $\omega = 16$ eV. Simply taking this background macroscopic dielectric function into account would already reduce the plasma frequency to around 18 eV. Further adding the contribution of the possible interband transitions could easily shift the value of the plasma frequency to 15 eV.

8.3 Density of screening modes

We can now examine the impact of taking into account the *d-p* interaction on $\Im(U(\omega))/\omega^2$, which can be physically understood as the density of screening modes and determines Z_B (see Figure 8.3.1). Though the global structure is conserved, a strong renormalization is induced.

Two effects are successively involved. First, we cut more transitions in the cRPA calculation in the *dp-dp* model. This will have an impact at low frequency, especially if the first transitions happening in the *d-dp* model were from occupied *p* to empty *d*. In that case the gap of the screening modes, that is to say the energy needed for the first transition between occupied and empty bands, will increase. At higher frequencies, the difference is largely negligible. Indeed, most of the screening processes do not involve *p*→*d* transitions, as shown in Chapter 7. The second effect is due to the shell-folding procedure. Due to the fact that U_{dd} and U_{dp} share variations in frequency, the frequency dependence of the effective interaction is flattened. Eventually, most of the dynamical structure of the screening stays unchanged when we suppress *p*→*d* transitions, and the main effect of shell-folding is a reduction of the density of screening modes.

One could wonder about the validity of the different models depending on the frequency. At very low frequency (below the gap of the *d-dp* model), the *d-dp* model result is adapted for the pnictides, because the entanglement is not too strong and the bands can be relatively well separated. However, as soon as the frequency becomes larger than the gap, this low-energy model is not valid anymore in the sense of the renormalization group. For higher frequencies, it is all the more true since the Coulomb interaction between *d* and *p* orbitals is even higher and cannot be neglected.

8.4 Bosonic renormalization factor Z_B

We focus on the impact of the shell-folding procedure on the bosonic renormalization factor Z_B introduced in Section 4.4. The smaller density of screening modes in the effective model lowers the value of Z_B through

$$\ln(Z_B) = -\int_0^{+\infty} \frac{\Im U_{ret}(\omega)}{\pi\omega^2} d\omega \tag{8.4.1}$$

We compare the values obtained for a *d-dp* model with and without shell-folding on Table 8.4.1.

At low frequency, the weight enhancement factor for the quasiparticles is $Z_{eff} \times Z_B$ where Z_{eff} is the renormalization obtained in a static Hubbard model [Casula *et al.* (2012b)]. Z_{eff} depends on $U(0)$/D with D the bandwidth. In the pnictides case, $U(0)$ is nearly the same in the two calculations. Qualitatively, Z_{eff} will be a little bigger in the effective model since both $U(0)$ is slightly smaller and the bandwidth is larger due to a higher Z_B. So the discrepancies

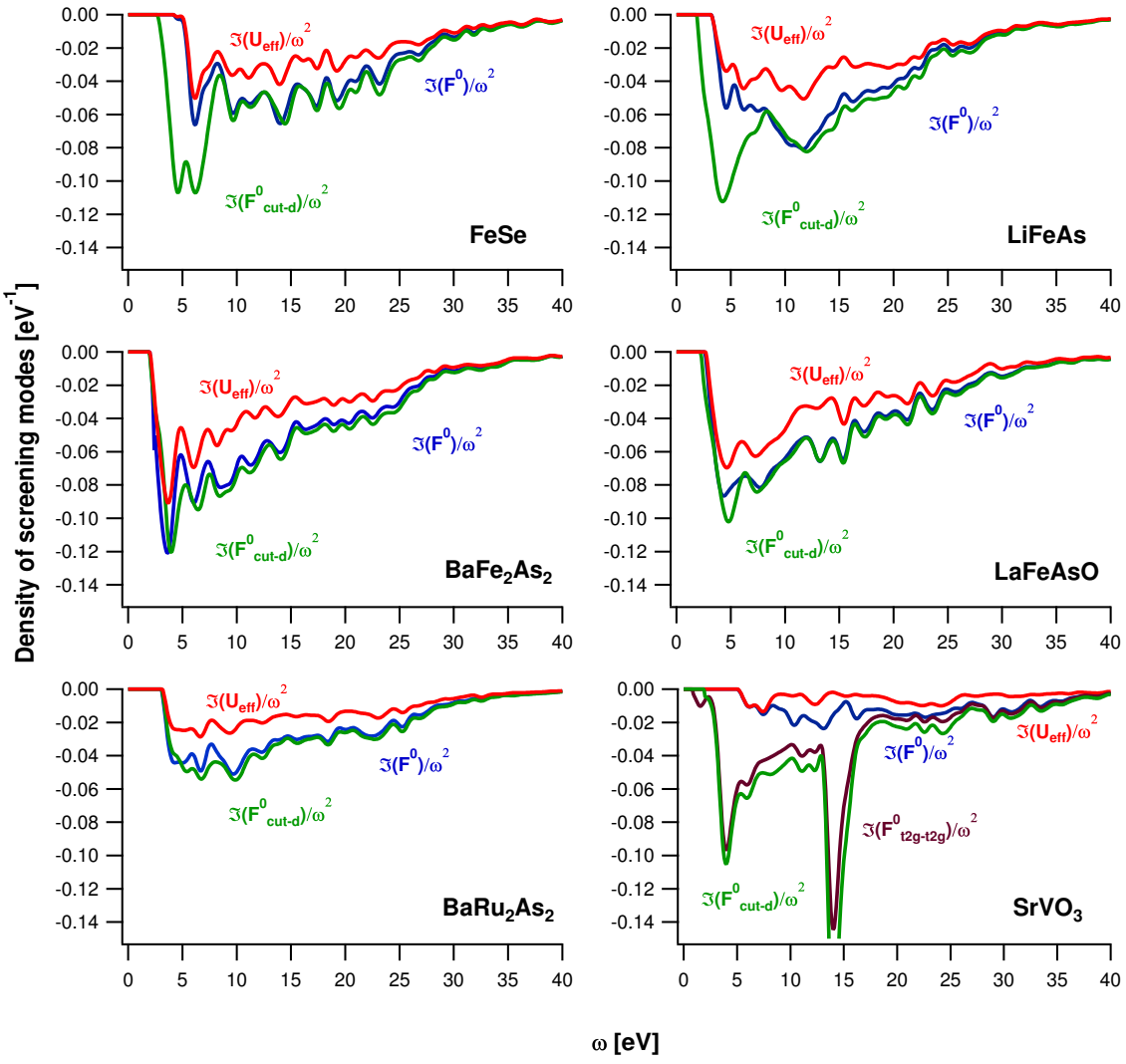

Figure 8.3.1: Density of screening modes in iron pnictides and chalcogenides before and after shell folding of a *dp-dp* model compared to an entangled *d-dp* model. $SrVO_3$ is also shown for comparison.

Table 8.4.1: Values of Z_B extracted from the monopole part of the interaction within the *d*-shell. Results for the shell-folded *dp-dp* model and for the directly calculated *d-dp* model are displayed.

	FeSe	LiFeAs	$BaFe_2As_2$	LaFeAsO	$BaRu_2As_2$
Z_B (effective)	0.78	0.76	0.71	0.73	0.85
Z_B (entangled)	0.63	0.60	0.59	0.62	0.74

between the two models as to the physical properties of the system will be largely dependent on the bosonic renormalization factor Z_B. Eventually, the renormalization is greatly changed when we take into account the *p-d* interactions. In Chapter 9, we discuss the effect of the shell-folding procedure on the calculated spectral function of a real material ($BaCo_2As_2$). If one does not take into account the *d-p* interactions, the obtained renormalization is stronger.

As for $SrVO_3$, the bosonic renormalization factor Z_B in the effective model is equal to 0.93, which should be compared to a value of 0.70 in a t_{2g}-t_{2g} model (0.64 when cutting only the transitions from and to the *d*-like bands). We see that in this compound U_{eff} is very close to being static, while in the pnictides there is still a large frequency dependence even in the effective model. Indeed, U_{eff} is less screened in $SrVO_3$: the infinite frequency value is reduced by 40%, while in the pnictides the reduction is much higher, from 70% in FeSe to 85% in LaFeAsO. This indicates a low coupling to the plasmon. The reason is that the main plasmon around 15 eV in $SrVO_3$ is due to transitions from occupied O-*p* to empty Fe-*eg* states (see Figures 8.3.1 and 7.1.1), which are suppressed in a *dp-dp* model. The shell-folding procedure allows us to take into account the intershell *p-d* interaction that was ignored in an entangled *d-dp* model. However, when we project our *dp-dp* model into an effective *d-dp* model we lose the possibility to reintroduce the screening from p$\longrightarrow$d transitions – which might also necessitate a more refined model including long-range interactions. This shows that the choice of the appropriate model must be done carefully, since the effects contained within the different models are not the same.

8.5 Dynamical J

We will now focus on the full Hund's coupling matrix

$$J_{mm'} = U_{mm'm'm,m\neq m'} \tag{8.5.1}$$

In a cubic basis we can define

$$J \equiv \frac{5}{7}\frac{F^2 + F^4}{14} \tag{8.5.2}$$

which physically corresponds to an arithmetic mean of all elements $J_{mm'}$. This quantity is frequency dependent and differs by a factor 5/7 from the definition of Chapter 6 (which is more adapted to the case of a model defined only by U and J, while here we are considering the full orbital-dependent matrix). In $BaFe_2As_2$, it will vary by about 17%, from 0.58 eV at zero frequency to 0.68 eV at infinite frequency. However, if one looks at the full J matrix at zero

frequency, we find:

$$J_{mm'}|_{\text{cRPA}} = \begin{pmatrix} 0 & 0.74 & 0.71 & 0.47 & 0.47 \\ 0.74 & 0 & 0.38 & 0.63 & 0.63 \\ 0.71 & 0.38 & 0 & 0.60 & 0.60 \\ 0.47 & 0.63 & 0.60 & 0 & 0.58 \\ 0.47 & 0.63 & 0.60 & 0.58 & 0 \end{pmatrix}.$$

where the order of the orbitals is $d_{3z^2-r^2}$,$d_{x^2-y^2}$,d_{xy},d_{xz},d_{yz}. The spread of this matrix is really large: for instance, the $d_{z^2} \longleftrightarrow d_{x^2-y^2}$ element is about two times the $d_{x^2-y^2} \longleftrightarrow d_{xy}$ element. Consequently, J is not a good quantity to focus on, and it is better to look at the frequency dependence of the Slater integrals F^2 and F^4. This is shown on Figure 8.5.1. While F^4 shows very little variation with ω, F^2 exhibits a minimum at an intermediate frequency which corresponds to the onset of interband transitions. It is also a minimum of J and a maximum of F^4/F^2.

In a DMFT calculation, one can wonder how to deal with this non-monopole frequency dependence. We suggest several answers. Using the bare value for F^2 and F^4 is satisfying from a model point of view. At infinite frequency the Slater parametrization of the Coulomb interaction matrix is excellent because the system is atomic like. Then one can presume that the plasmon is only screening the monopole part of the interaction. On the other hand, the low-energy properties of the system are more influenced by the static part of the interaction. In this view, the best would be to parametrize the Coulomb interaction matrix at low frequency as well as possible, and then to ignore again the effects of the plasmons on the non-monopole terms. Finally, one could also consider a fully frequency-dependent matrix and derive the usual algorithm for a multi-orbital system.

8.6 Conclusion

We have calculated the full-frequency dependence of the Hubbard interaction in the 11, 111, 122 and 1111 families of iron pnictides and compared it to $SrVO_3$ in the *dp-dp* model, including both Fe-*d* and As-*p* degrees of freedom. We have calculated the free-electrons plasmon frequencies corresponding to different numbers of electrons involved in the resonance, and we have shown that the screening modes could not be approximated by a single plasmon as in $SrVO_3$. Finally, we have studied the effect of the shell-folding procedure and compared the so-constructed effective *d-dp* model to a *d-dp* model where only transitions from and to bands with a majority of *d*-orbital character are cut and U_{dp} is neglected. We find an important reduction of the high-frequency tail which results in a bosonic renormalization factor Z_B closer to one.

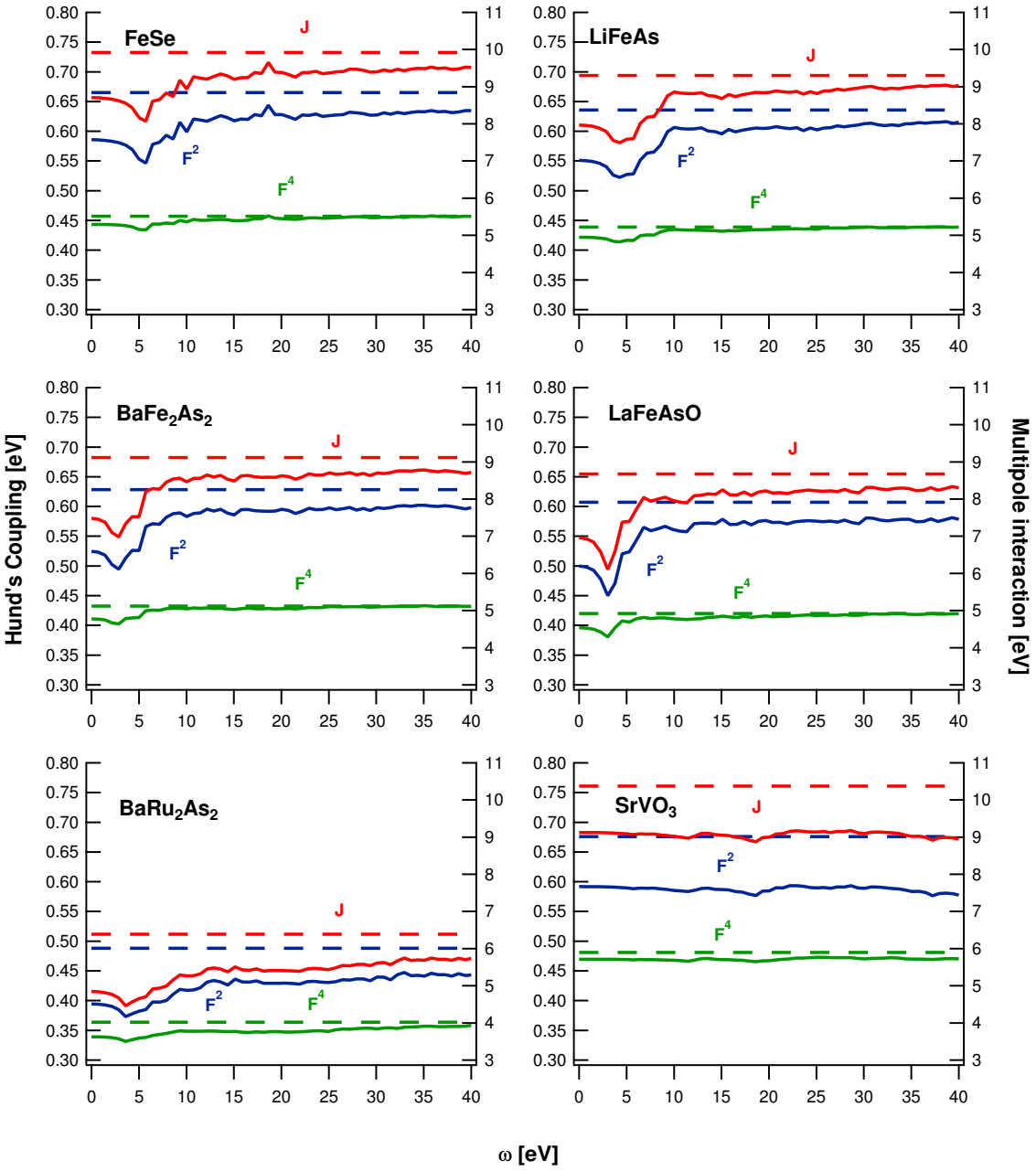

Figure 8.5.1: Frequency dependence of F^2, F^4 and $J\left(\equiv \frac{5}{7}\frac{F^2+F^4}{14}\right)$ calculated in a *dp-dp* model. Dashed lines are the values at infinite frequency.

Part V

Spectral properties of iron pnictides

In this part, we show applications of many-body techniques and angle-resolved photoemission spectroscopy to study and predict the physical properties of iron pnictides. We focus on three compounds, all of the so-called 122 family, whose prototype member is $BaFe_2As_2$: $BaCo_2As_2$, $CaFe_2As_2$ and $Ba_2Ti_2Fe_2As_4O$. We calculate the spectral functions for all three materials and compare them directly to photoemission measurements, that we have taken in the case of $CaFe_2As_2$. This also allows us to test-proof the technical improvements presented in Parts II and III, in particular the effect of the multi-orbital double-counting, of the non-local screened exchange and of the frequency-dependence of the Hubbard interaction.

We begin by observing the effect of an increased number of carriers on the strength of correlations of d *electrons, with the substitution of Fe by Co. It is shown that compared to $BaFe_2As_2$, $BaCo_2As_2$ has a higher coherence energy scale and a lower effective mass, and that this difference is largely due to the Hund's coupling.*

We continue with the study of the tetragonal/collapsed tetragonal phase transition in $CaFe_2As_2$. This structural modification while keeping the same symmetry is impacting both the interlayer As-As bonding, which is the source of the collapse, and the intralayer Fe-As distance. We show that, from the point of view of electronic correlations, the discrepancies between the two compounds are driven by the intralayer structure.

*Finally, we focus on a "heterostructure" of $BaFe_2As_2$ and $BaTi_2As_2O$: $Ba_2Ti_2Fe_2As_4O$. In contrast to $CaFe_2As_2$, it is shown that the buffer layer Ti_2As_2O importantly modifies the physics of the compound by hole-doping the Fe_2As_2 layer. In the same fashion as $BaFe_2As_2$ compared to $BaCo_2As_2$, the electronic correlations in $Ba_2Ti_2Fe_2As_4O$ are then stronger than in $BaFe_2As_2$. Eventually, the Fe-*d *electron count in the Fe_2As_2 layer of $Ba_2Ti_2Fe_2As_4O$ is similar to optimally-doped $Ba_{0.6}K_{0.4}Fe_2As_2$.*

Chapter 9

Reduced correlations and antagonistic effects of static exchange and dynamical correlations in $BaCo_2As_2$

In this chapter, we demonstrate the validity of our new approach to the spectral properties of correlated electron materials taking into account screened exchange beyond the local density approximation (LDA) and dynamical correlations as described by dynamical mean field theory with frequency-dependent local Hubbard interactions (see Part III for technical details). To this aim, we benchmark the calculated spectral function of $BaCo_2As_2$, for which we dispose of detailed ARPES results [Xu et al. (2013b), Dhaka et al. (2013)]. Our work sheds new light on the physical justifications of combined density functional dynamical mean field electronic structure techniques, by revealing a subtle error cancelation between non-local exchange interactions and dynamical screening effects, both neglected in standard methods.

In a second time, we compare the strength of correlations between $BaCo_2As_2$, with a d^7 filling, and optimally doped $Ba_{0.6}K_{0.4}Fe_2As_2$, with a nominal filling of $d^{6.8}$. We use the simpler LDA+DMFT with static interaction $U(\omega = 0)$ scheme since it will be shown that it describes very well the spectral function in this compound.

This work has been conducted in collaboration with the authors of [Xu et al. (2013b)] and [van Roekeghem et al. (2014)]. In particular, Nan Xu, Peng Zhang, Hu Miao and Pierre Richard recorded the angle-resolved photoemission spectra and Nan Xu analyzed the data, while Jan M. Tomczak performed the GW calculations.

9.1 The puzzle of cobalt pnictides magnetic properties

Our target compound, $BaCo_2As_2$, is isostructural to the prototypical parent compound of the so-called 122 iron-based superconductors, $BaFe_2As_2$. Replacing Fe by Co, however, increases the filling to a nominal d^7 configuration of the $3d$ states, with drastic consequences: effective masses and quasiparticle lifetime broadenings are reduced and Fermi liquid coherence temperature is increased compared to its Fe counterpart [Werner *et al.* (2012)], and ARPES identifies clearly defined quasi-particle bands with relatively weak mass renormalizations and long lifetimes [Xu *et al.* (2013b)].

Nevertheless, the electronic structure of this compound raises puzzling questions concerning its paramagnetic behavior. Indeed, standard electronic structure calculations predict a huge density of states at the Fermi level, which, given the large Stoner parameter of Co, would be expected to trigger an instability towards a ferromagnetic state [Sefat *et al.* (2009)]. The density of states of the isoelectronic compound $SrCo_2As_2$ presents the same features, but the maximum appears to be just below the Fermi level [Pandey *et al.* (2013)]. Still, in $SrCo_2As_2$ – also a paramagnet – important antiferromagnetic fluctuations have been measured, possibly competing with ferromagnetic order [Pandey *et al.* (2013), Jayasekara *et al.* (2013)]. $CaCo_2As_2$, $Ca_{0.9}Sr_{0.1}Co2As2$ and $CaCo_{1.86}As2$ exhibit magnetic phases with in-plane ferromagnetism at low temperatures [Cheng *et al.* (2012), Ying *et al.* (2012), Anand *et al.* (2014)].

ARPES data of $BaCo_2As_2$ show that there is indeed a flat band (dominantly of $d_{x^2-y^2}$ character) very close to the Fermi surface, albeit less filled than predicted by LDA calculations [Xu *et al.* (2013b), Dhaka *et al.* (2013)], suggesting $BaCo_2As_2$ to be on the verge of a transition. Indeed, a presentation of the ARPES spectra in a second derivative plot of the intensities reveals the presence of a flat band just above the Fermi level [Xu *et al.* (2013b)], as pointed out in [Dhaka *et al.* (2013)]. These properties make the compound an ideal benchmark system, on which to test new theoretical approaches.

9.2 LDA as a starting point for many-body calculations

We start our analysis by comparing results for the spectral function calculated within different state-of-the-art electronic structure techniques to the ARPES spectral function of [Xu *et al.* (2013b)] that we replot in a color representation (Figure 9.2.3). Specifically, we analyze the Kohn-Sham band structure of DFT-LDA and the spectral functions of standard LDA+DMFT and LDA+DMFT with frequency-dependent local Hubbard interactions $U(\omega)$. The latter scheme will be abbreviated in the following as "LDA+DDMFT" to stress the doubly dynamical nature of the theory, which determines a frequency-dependent self-energy in the DMFT spirit but does so extending DMFT to frequency-dependent interactions. Details of the scheme can be found in [Casula *et al.* (2012a), Werner *et al.* (2012)] and Part III. The momentum values in the experimental spectra are labeled with respect to the 1 Fe unit-cell Brillouin zone, and we use $c' = c/2$ as the distance between two Fe planes.

9.2.1 Fermi surface

In Figures 9.2.1(a) and 9.2.1(b), we display cuts of the Fermi surface calculated using the local density approximation at $k_z = 0$ and $k_z = \pi$, respectively. The corresponding photoemission data, obtained by integrating the ARPES intensity within 10 meV of the Fermi level, are shown in Figures 9.2.1(d) and 9.2.1(e), respectively. The Fermi surface topology of $BaCo_2As_2$ is quite different from that of the Fe pnictides. For example, the more or less circular hole Fermi surface pockets at the point of superconducting $Ba_{0.6}K_{0.4}Fe_2As_2$ [Ding *et al.* (2011)] are replaced by star-shaped electron Fermi surface pockets in $BaCo_2As_2$, thus removing all possibility for electron-hole quasinesting scattering in this system. In Figure 9.2.1(f), we show the k_z dispersion at E_F approximated by scanning the photon energy over a wide range, and we display the corresponding LDA calculation in Figure 9.2.1(c). The computed and measured Fermi surfaces show a good qualitative agreement overall, yet quantitatively speaking we can

see for instance that the electron pocket around the Γ point is too large in LDA, and we expect that including non-local exchange will produce a better agreement.

Although the Fermi surface of $BaCo_2As_2$ differs substantially from that of the 122 ferropnictides, Nan Xu and coauthors find that the constant energy maps recorded at 470 meV below E_F for the $k_z = 0$ and $k_z = \pi$ planes, which are, respectively, displayed in Figures 9.2.1(g) and 9.2.1(h), are quite similar to the Fermi surfaces of $Ba_{0.6}K_{0.4}Fe_2As_2$. To illustrate this resemblance, they overlap on these Figures the Fermi surfaces obtained for $Ba_{0.6}K_{0.4}Fe_2As_2$ in [Ding *et al.* (2011)]. In a similar fashion, the k_xk_z map at 470 meV binding energy displayed in Figure 9.2.1(i) could easily be mistaken for the k_z dispersion at the Fermi level of some typical 122 ferropnictides [Malaeb *et al.* (2008), Xu *et al.* (2012)]. At least qualitatively, the simplest explanation for this behavior is to assume an approximately 470-meV upward shift of the chemical potential following a 3*d*-shell filling from $3d^6$ in $BaFe_2As_2$ to $3d^7$ in $BaCo_2As_2$. As can be seen in Figure 9.2.3, all the bands in $BaCo_2As_2$ below a binding energy of 470 meV find their near E_F equivalent in the 122 ferropnictides. This shows that $BaCo_2As_2$ is the natural extension of $BaFe_2As_2$ in the electron-doped range.

9.2.2 Hubbard interactions

The interactions are determined from the constrained random phase approximation (cRPA) in the implementation of [Vaugier *et al.* (2012a)]. In the zero-frequency limit, we obtain the Slater integrals $F^0(0) = 2.9$ eV, $F^2(0) = 6.9$ eV and $F^4(0) = 5.1$ eV calculated on a grid of 4x4x4 k-points, which we use to determine the orbital-dependent coefficients $U_{mm'}$ of density-density interactions, including Hund's exchange $J_{mm'}$, in a standard Slater parametrisation [Vaugier(2011)]. We find $J = 0.86$ and the interaction matrices in the cubic basis d_{z^2}, $d_{x^2-y^2}$, d_{xy}, d_{xz}, d_{yz} at $\omega = 0$:

$$\bar{U}^{\sigma\sigma}_{mm'}|_{\text{Slater}} = \begin{pmatrix} 0 & 1.66 & 1.66 & 2.41 & 2.41 \\ 1.66 & 0 & 2.66 & 1.91 & 1.91 \\ 1.66 & 2.66 & 0 & 1.91 & 1.91 \\ 2.41 & 1.91 & 1.91 & 0 & 1.91 \\ 2.41 & 1.91 & 1.91 & 1.91 & 0 \end{pmatrix}$$

$$\bar{U}^{\sigma\bar{\sigma}}_{mm'}|_{\text{Slater}} = \begin{pmatrix} 3.87 & 2.40 & 2.40 & 2.90 & 2.90 \\ 2.40 & 3.87 & 3.06 & 2.56 & 2.56 \\ 2.40 & 3.06 & 3.87 & 2.73 & 2.56 \\ 2.90 & 2.56 & 2.56 & 3.87 & 2.56 \\ 2.90 & 2.56 & 2.56 & 2.56 & 3.87 \end{pmatrix}.$$

The full frequency-dependent monopole integral $F^0(\omega)$ is displayed on Figure 9.2.2, along with the corresponding bosonic spectral function $\rho_B(\omega)$. The imaginary part of F^0 has a minimum around 22 eV, which corresponds to the main plasmon. At this frequency the real part of F^0 is multiplied by 4, going from a low-frequency regime to a high-frequency regime. Still, a non-trivial frequency dependence persists at lower frequencies, and that is why the spectrum of ρ_B shows many features and a broad distribution of the spectral weight. Under these conditions, it is not clear that approximating the effect of the plasmons by a single bosonic renormalization factor Z_B (=0.59 here) would be a good choice. For LDA+DDMFT, the full frequency-dependence of the monopole term, $F_0(\omega)$ is retained in the calculation. The effective

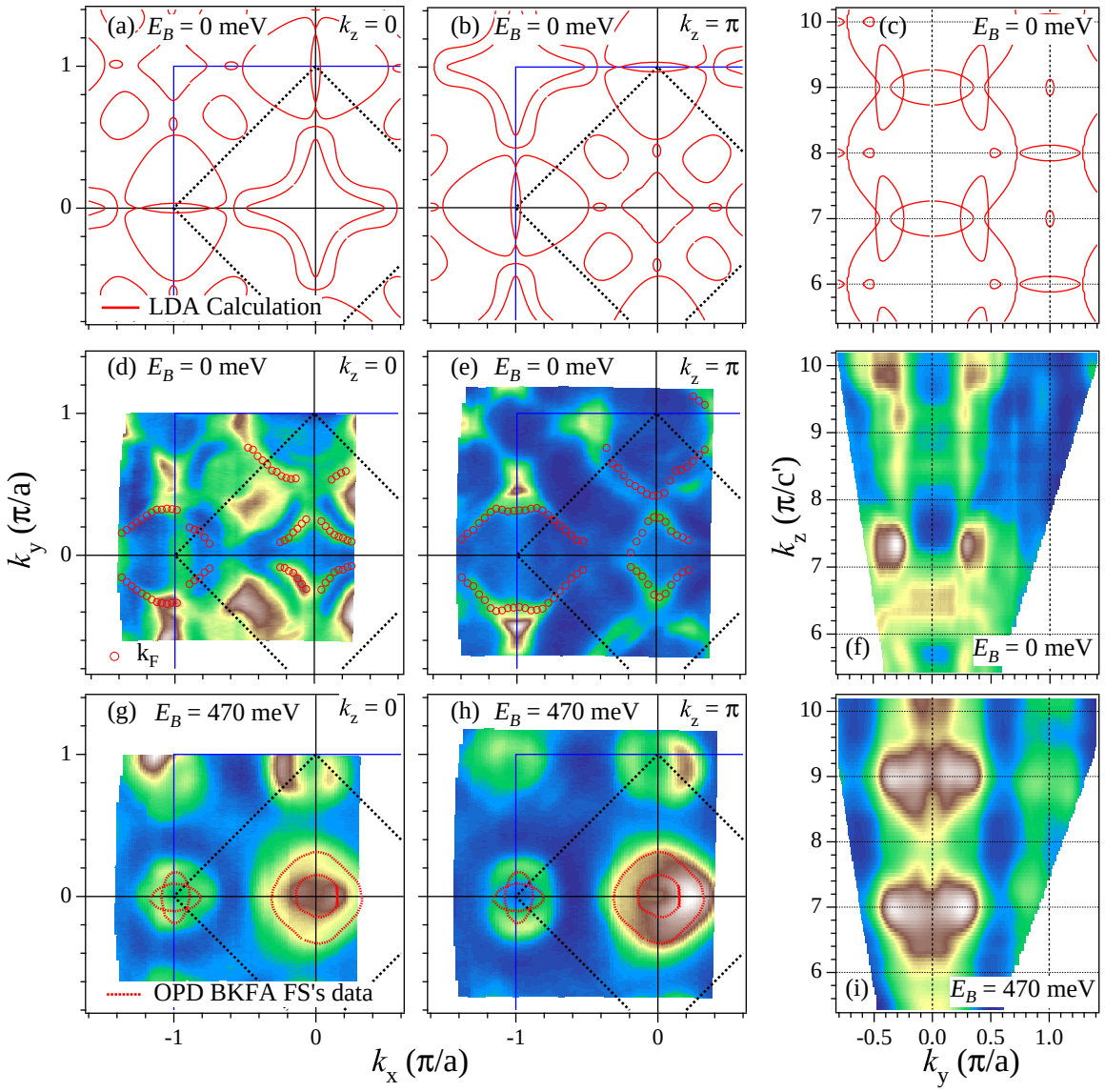

Figure 9.2.1: (a),(b) Cuts of the Fermi surface calculated from local density approximation (LDA) at $k_z = 0$ and $k_z = \pi$, respectively. (c) LDA Fermi surface in the plane defined by $k_y = 0$. (d)–(f) Experimental Fermi surface mappings corresponding to the cases described in panels (a)–(c). The open symbols represent extracted Fermi surface data. (g)–(i) Same as (d)–(f) but for ARPES data recorded 470 meV below the Fermi level. The ARPES Fermi surface data from [Ding *et al.* (2011)] for $Ba_{0.6}K_{0.4}Fe_2As_2$ (red dashed lines) are plotted in (g),(h) for comparison.

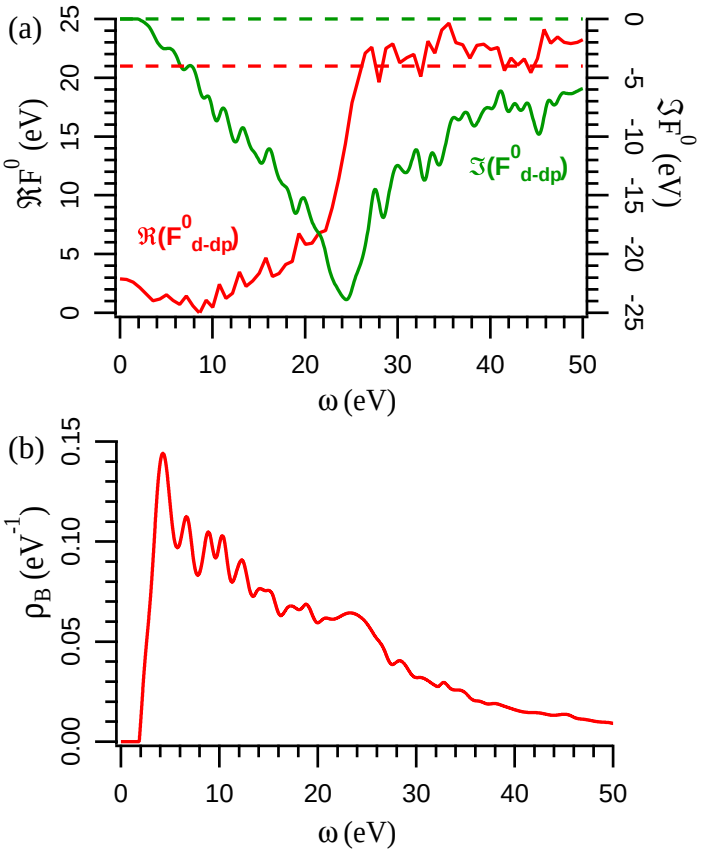

Figure 9.2.2: (a): Frequency-dependent real and imaginary parts of the monopole screened Coulomb interaction $F^0_{d-dp}(\omega)$; (b): corresponding bosonic spectral function $\rho_B(\omega)$.

local problem with dynamical $\mathcal{U}$ is solved self-consistently by means of a continuous-time Monte Carlo algorithm [Werner and Millis(2010)] as implemented within the TRIQS toolbox [Ferrero and Parcollet(2011)].

9.2.3 Spectral functions and bandwidth renormalizations

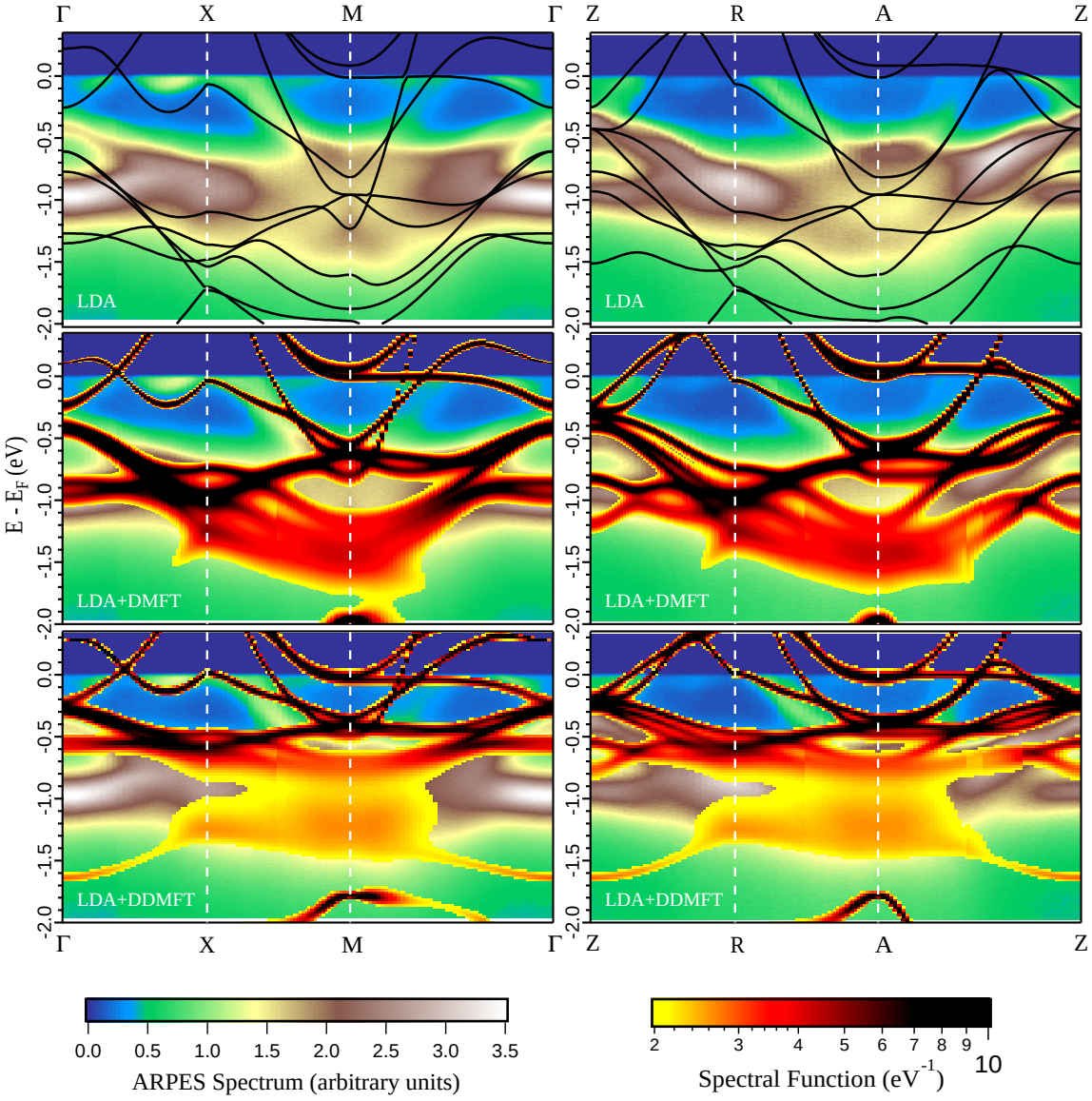

Figure 9.2.3: $BaCo_2As_2$ photoemission spectra, replotted from [Xu *et al.* (2013b)]. Superimposed are (top) the Kohn-Sham band structure of DFT-LDA (middle) those parts of the spectral function of standard LDA+DMFT with $U(\omega = 0)$ that show intensities beyond 2 states/eV, roughly corresponding to the maxima of the spectra (bottom) those parts of the spectral function of LDA+DDMFT with $U(\omega)$ that show intensities beyond 2 states/eV.

Electronic bands in the energy window between the Fermi level and -2 eV binding energy are states of predominant Co-3*d* character, and undergo – even in this quite moderately correlated compound – a non-negligible band renormalization, as compared to the LDA band

structure (Figure 9.2.3 (top)). Standard LDA+DMFT (Figure 9.2.3 (middle)) captures this effect, leading to a reduced bandwidth in good agreement with the ARPES results. When dynamical screening effects are taken into account (Figure 9.2.3 (bottom)), additional renormalizations occur, corresponding to the electronic polaron effect discussed in [Casula *et al.* (2012b)], and the overall bandwidth reduction appears to be overestimated. We will, however, argue below that one should not conclude from this analysis that dynamical screening effects are absent. Rather, non-local exchange – routinely neglected in DFT-based techniques – reshapes and widens the quasi-particle band structure, and the apparent success of LDA+DMFT in obtaining the correct quasi-particle bandwidth relies on an error cancelation when both dynamical screening and nonlocal exchange are neglected in the calculation of the spectral function.

9.3 Combining static screened-exchange and dynamical correlations

9.3.1 One particle-level

We will now substantiate this claim by explicitly including screened exchange, and performing a DMFT calculation with fully dynamical Hubbard interactions based on the following one-particle Hamiltonian:

$$H_0 = H_{Hartree} + H_{SEX} \tag{9.3.1}$$

where the first term denotes the Hamiltonian of the system at the Hartree mean-field level, evaluated at the self-consistent DFT-LDA density. H_{SEX} is a screened Fock exchange term, calculated from a Yukawa potential

$$\frac{e^2 exp(-k|r-r'|)}{|r-r'|} \tag{9.3.2}$$

with screening wavenumber k. This scheme can be understood as the next generation after the recent LDA+DDMFT scheme, by replacing the local Kohn-Sham exchange-correlation potential of DFT by a nonlocal screened Fock exchange correction. We note that in SEX+DDMFT non-local and dynamical renormalizations are by construction separated on the self-energy/hamiltonian level. This separability was recently justified for iron pnictides [Tomczak *et al.* (2012b)] and found to hold also for metallic transition metal oxide [Tomczak *et al.* (2014)]. More technical details can be found in Chapter 5.

The problem of calculating the screened exchange term therefore boils down to determining the effective screening length. In $BaCo_2As_2$ the LDA density of 6.94 states/eV/cell at the Fermi level corresponds to a Thomas-Fermi wavenumber of 1.88 bohr^{-1}. However, as argued above, one of the main consequences of the electronic exchange and correlations effects is precisely the rearrangement of the electronic states in the immediate proximity of the Fermi level, and a concomitant reduction of the density of states, as already discussed in Chapter 5 for the case of $SrVO_3$. Indeed, a SEX+DDMFT calculation with the LDA screening length results in a reduction of states at the Fermi level, given by a zero-frequency spectral function of 4.66 states/eV/unit cell, corresponding to a screening wavenumber of 1.54 bohr^{-1}. It thus becomes clear that the true challenge consists in a *self-consistent* determination of the effective screening length. For computational reasons, however, and since the precise value of the DOS on the Fermi level is – for the same reasons as the subtle Fermi surface modifications discussed above

– a quantity very hard to converge, we mimic convergence by choosing an ad hoc screening wavenumber of 1.33 bohr^{-1}, corresponding to half the LDA-DOS. Since this is approximately the value we eventually find for the value of the spectral function on the Fermi level (4.26 states/eV/cell – which corresponds to about 1.47 bohr^{-1}), this choice can be considered as a poor man's self-consistency.

For the screened Hartree-Fock calculation performed using Wien2k [Blaha *et al.* (2001),Tran and Blaha(2011)], we calculate the matrix-elements for the second variational procedure on 150 bands, on a grid of 7x7x7 kpoints. We choose the parameters gmax=6 and lmaxe=5 for the expansion of the product of two orbitals and of the generated potential (magnitude of the largest G vector in the interstitial and maximum value of the angular momentum for the expansion in spherical harmonics in the atomic sphere, respectively); and lmaxv=4 for the expansion of the orbitals used in the product (maximum value of the angular momentum for the expansion in spherical harmonics in the atomic sphere).

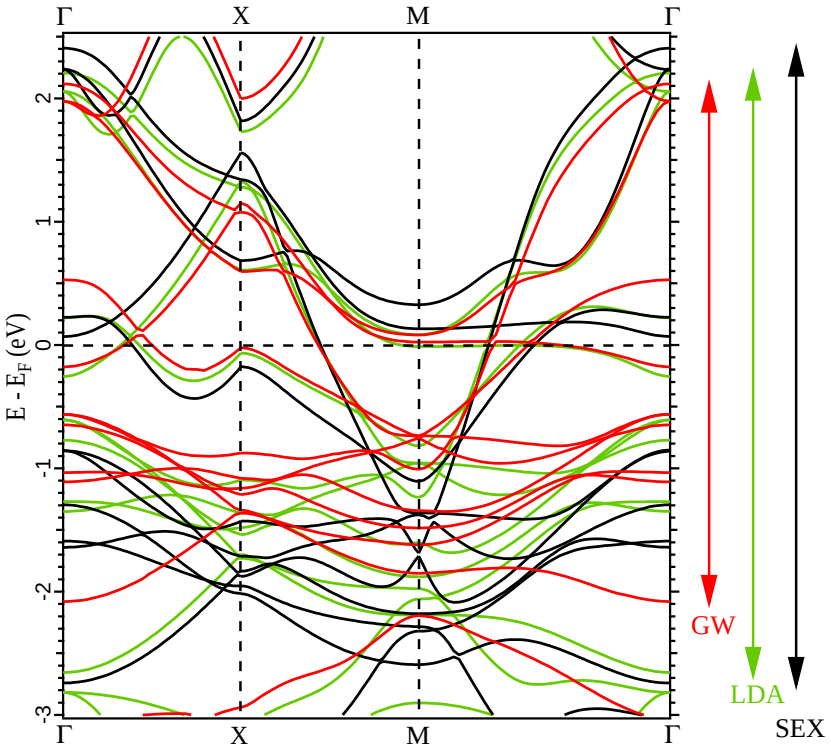

Figure 9.3.1: Comparison of bandstructures of $BaCo_2As_2$ in the $k_z = 0$ plane calculated with Quasiparticle Self-consistent GW approximation (red), Local Density Approximation (green) and Screened-EXchange (black).

We first analyze the band structure corresponding to the single-particle part of the Hamiltonian, that is, H_0 alone, in comparison to the LDA band structure and the quasi-particle band structure obtained from many-body perturbation theory within Hedin's GW approximation [Hedin(1965)] in the quasi-particle self-consistent implementation of [Kotani *et al.* (2007)] (see Figure 9.3.1). As expected, the inclusion of nonlocal exchange increases the delocalization of electrons, particularly for the bands crossing the Fermi level, and thus widens the bands as compared to the LDA electronic structure. In QSGW, this effect is overruled by correlation-induced band-narrowing, and the bandwidth of Cobalt *d*-like bands is about 15% smaller than the LDA bandwidth. These comparisons highlight the fact that – taking the screened exchange

band structure as a reference – the effect of the effective exchange-correlation potential of DFT incorporates not only exchange (in a local fashion), but also mimics band renormalizations due to correlations (albeit without keeping track of the corresponding spectral weight transfers). In addition, one observes interesting modifications of the low-energy band structure; we will come back to this point below.

9.3.2 Momentum-resolved spectral function and orbital polarization

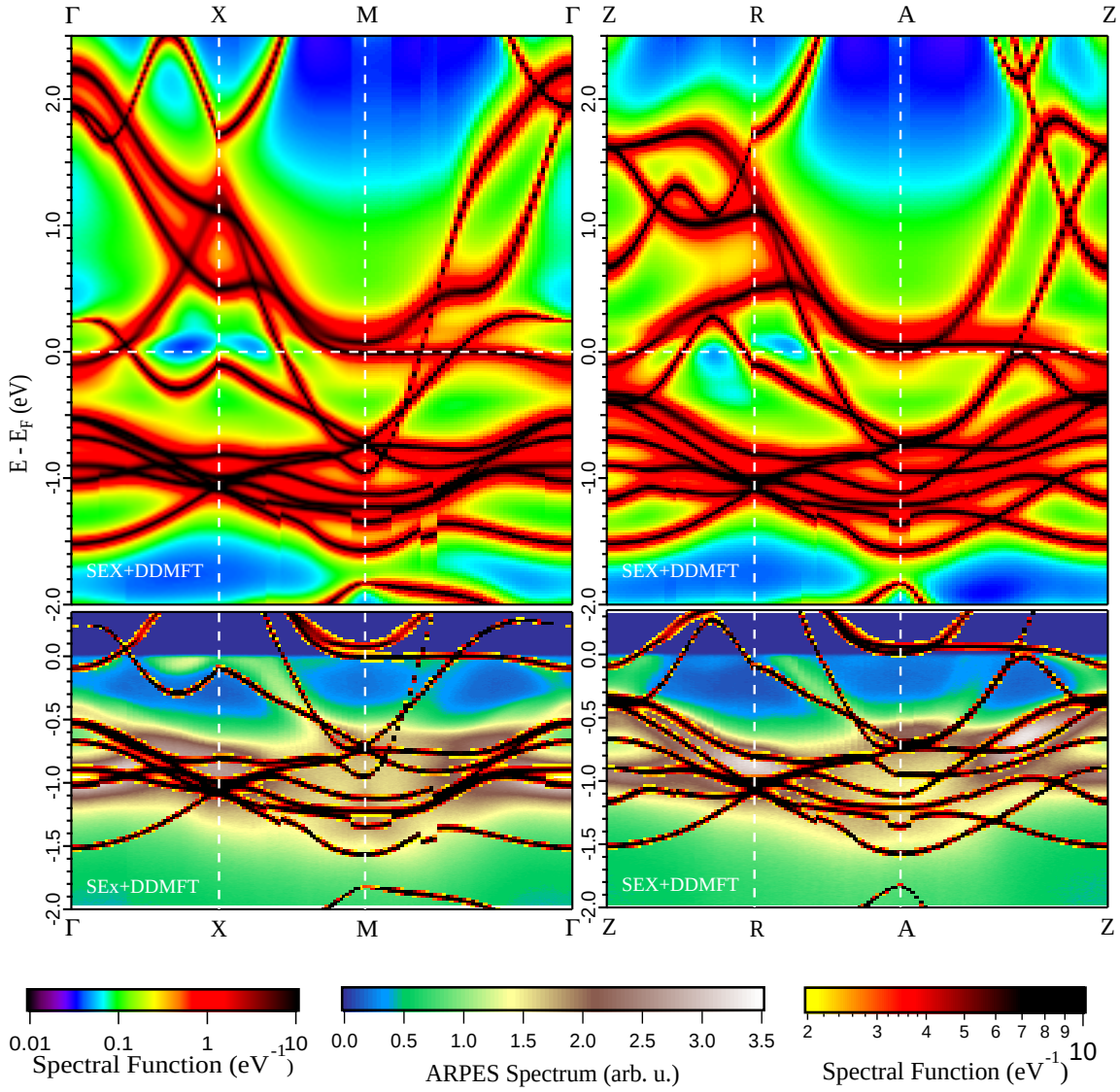

Figure 9.3.2: (top) $BaCo_2As_2$ spectral function obtained by Screened EXchange+Dynamical Mean Field Theory with dynamical interaction $U(\omega)$ along the ΓXMΓ and ZRAZ momentum path; (bottom) Bands extracted from the maxima of the spectral function of SEX+DDMFT with $U(\omega)$ superimposed on ARPES data as in Figure 9.2.3.

We finally turn to the results of our new scheme: Figure 9.3.2 displays the spectral function within combined screened exchange (SEX) plus dynamical mean field theory with $U(\omega)$ (SEX+DDMFT). The bottom panels display again the ARPES data, but this time the maxima

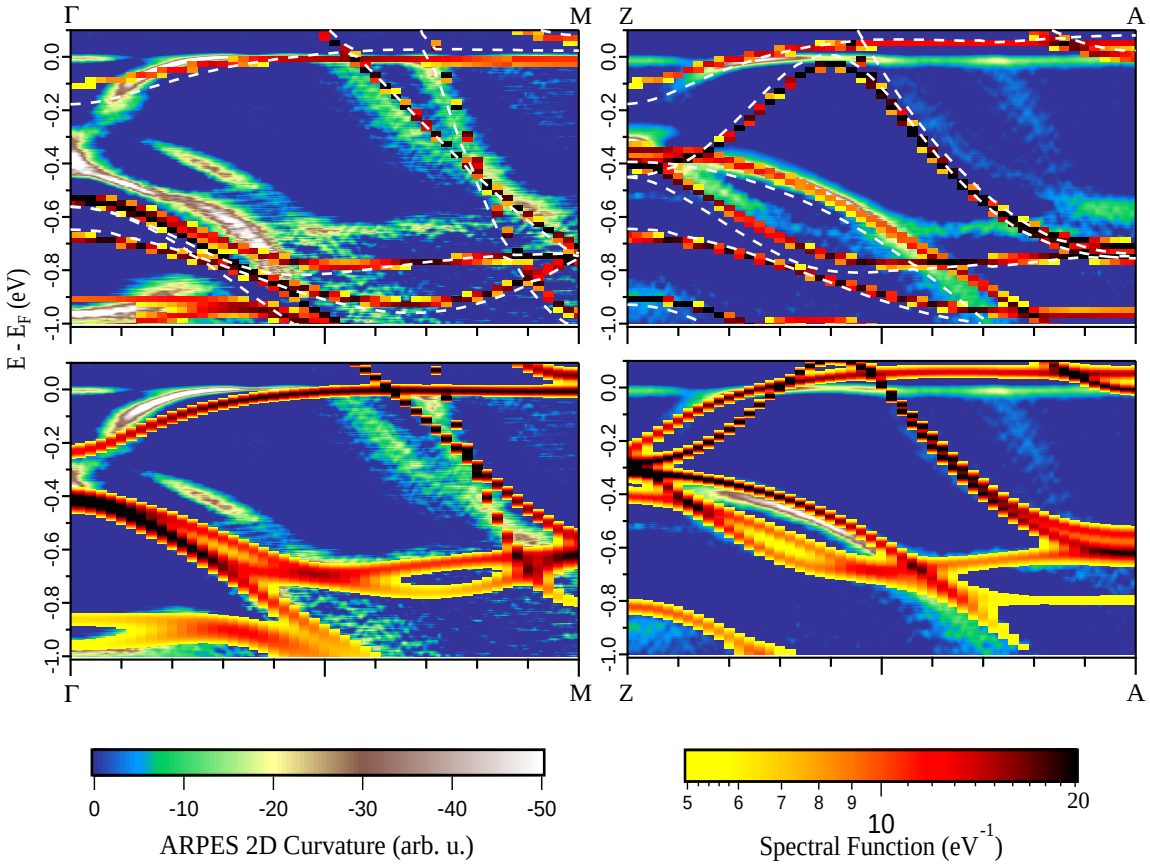

Figure 9.3.3: Bands along the ΓM and ZA directions, extracted from the spectral function calculated by (top) SEX+DDMFT with U(ω) and (bottom) LDA+DMFT with $U(0)$ superimposed on ARPES data from [Xu *et al.* (2013b)]. The ARPES data are represented as a second derivative of the photoemission intensity, on a colour scale ranging from blue to white. Also given is the QSGW band structure (white dashed lines).

of SEX+DDMFT spectral function are superimposed to the color spectrum. The overall spectrum from SEX+DDMFT is very close to the experiment: bandwidth, Fermi surface and band renormalizations close to the Fermi level are correctly predicted. The main discrepancy between the photoemission data and the theoretical spectral function – both within LDA+DMFT or SEX+DDMFT – can be seen around the A point, where the position of one electron pocket is very different (for more details, see Figure 9.3.3 right panel). We suspect that this strong disagreement could be due to the approximation of using a constant photon energy along the whole momentum path, while in the free electron final state approximation the variation of $k_{\parallel}$ at a constant photon and binding energy implies a modification of $k_{\perp} = k_z$ according to (see e.g. [Damascelli(2004)]):

$$k_{\parallel}^2 + k_{\perp}^2 = constant \tag{9.3.3}$$

In our case the "$k_z = 0$" cut actually corresponds to $8\pi/c'$ and the "$k_z = \pi$" to $9\pi/c'$, where c' is the distance between two CoAs planes. That means that the k_z at the M point is actually lower by about $0.32\pi/c'$ compared to the Γ point and at the X point it is about $0.16\pi/c'$ lower. For the "$k_z = \pi$" cut we obtain that the k_z at the A point is about $0.29\pi/c'$ lower than at the Z point, and the R point about $0.14\pi/c'$ lower. Given the precision of our comparison, we consider that we might be within the error bars.

Figure 9.3.4 shows the spectral function obtained by SEX+DDMFT with dynamical $U(\omega)$, projected on Co-*d* and As-*p* orbital characters. We can see that the As-*p* states are more hybridized with the empty or near-Fermi level Co-*d* states than with the filled Co-*d* states. Still, since in our SEX+DDMFT calculations of $BaCo_2As_2$ the imaginary part of self-energy stays weak at low frequency. That is why this difference in hybridization does not cause an obviously visible change in the coherence of the filled and empty Co-*d* states, which can bee seen in [Werner *et al.* (2012)]. The highest "band" shown, between 2 and 3 eV, is very coherent. It is actually Ba-*d* states, which hybridizes both with Co and As states.

The results of photoemission with p polarization are displayed on Figure 9.3.5 – all data displayed before were taken in s polarization. Around the M point, the two electrons pockets are visible under s polarization while only the outer one is under p polarization. Going back to our calculations of the orbital-resolved spectral function, we can see on Figure 9.3.4 that both electron pockets around M display some d_{xy} character, and only the outer pocket has $d_{xz} + d_{yz}$ character. This would be in good agreement with the photoemission observation, all the more since the use of p polarization adds a k_z component to the polarization that usually highlights the $d_{xz} + d_{yz}$ bands, while the in-plane d_{xy} orbital matrix element is always reduced due to the analyzer angle [Brouet *et al.* (2012), Wang *et al.* (2012a)]. However, the s-polarization spectra have been taken with the slit along the ΓM direction, while the p-polarization spectra have been taken with the slit perpendicular to that direction – which in theory should actually correspond to the MZ direction, though the dispersions look similar. When we take into account the effects of the 2-Fe unit cell [Brouet *et al.* (2012)] we see that we obtain the opposite assignment of the orbital characters. We do not understand the reason for this discrepancy at present, but we tend to favor the attribution of orbital characters as in Figure 9.3.4. This would suggest an interpretation of the symmetry of the electronic states as in a naive 1-Fe unit cell view.

The orbital-resolved electron count obtained with SEX+DDMFT is displayed in Table 9.3.1 and compared to the LDA, SEX, LDA+DMFT and LDA+DDMFT electron count. The orbital polarization from LDA is reduced by correlations, and nearly suppressed within LDA+DDMFT. On the other hand, screened exchange increases the orbital polarization, and the final SEX+DDMFT result still displays stronger orbital polarization than LDA. This trend can be directly related to

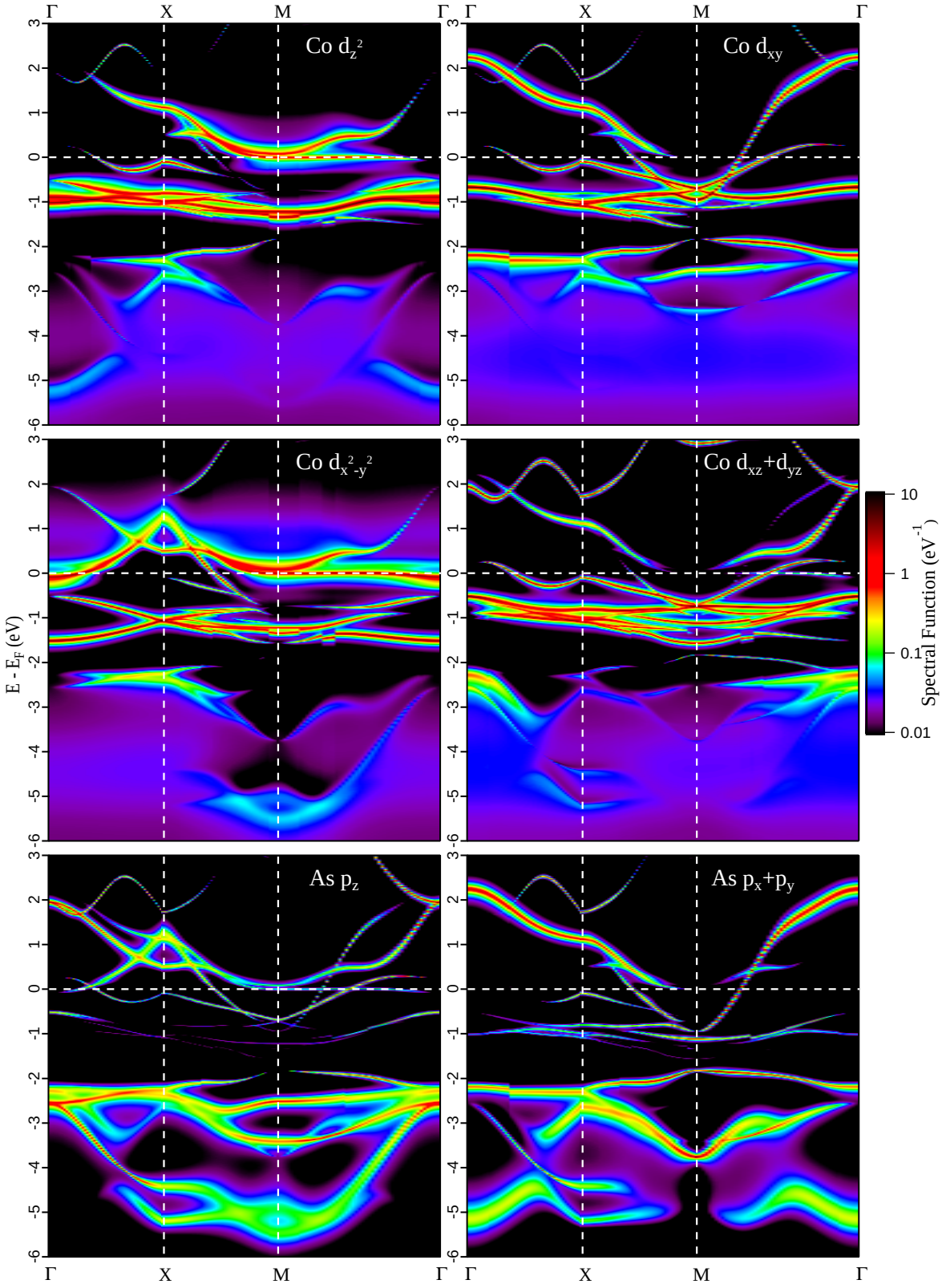

Figure 9.3.4: $BaCo_2As_2$ spectral function obtained by Screened EXchange+Dynamical Mean Field Theory with dynamical interaction $U(\omega)$ on the momentum path ΓXMΓ, projected on Co-*d* and As-*p* orbital characters

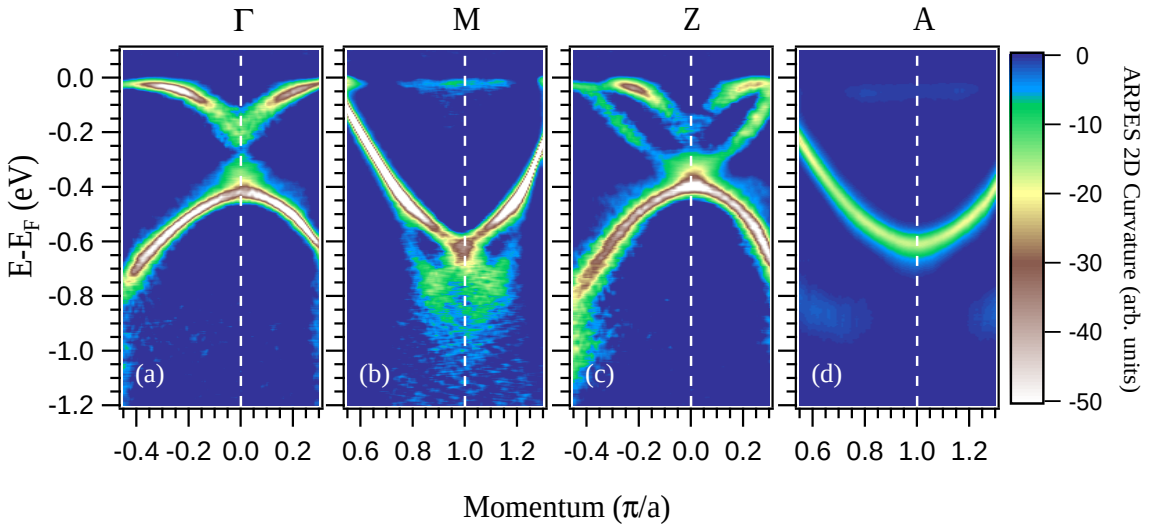

Figure 9.3.5: Photoemission spectra taken with p polarization on the ΓM direction.

Table 9.3.1: Number of electrons in Cobalt-*d* Wannier functions within the DFT-Local Density Approximation, Screened Exchange approximation, SEX+DDMFT with dynamical $U(\omega)$, LDA+DMFT with static U and LDA+DDMFT with dynamical $U(\omega)$.

	n^{e-}_{LDA}	n^{e-}_{SEx}	$n^{e-}_{\text{SEx+DDMFT}}$	$n^{e-}_{\text{LDA+DMFT}}$	$n^{e-}_{\text{LDA+DDMFT}}$
d_{z^2}	1.64	1.66	1.63	1.61	1.62
$d_{x^2-y^2}$	1.49	1.27	1.37	1.53	1.59
d_{xy}	1.74	1.78	1.72	1.67	1.63
d_{xz+yz}	1.69	1.73	1.68	1.64	1.62
total	8.24	8.16	8.08	8.09	8.09

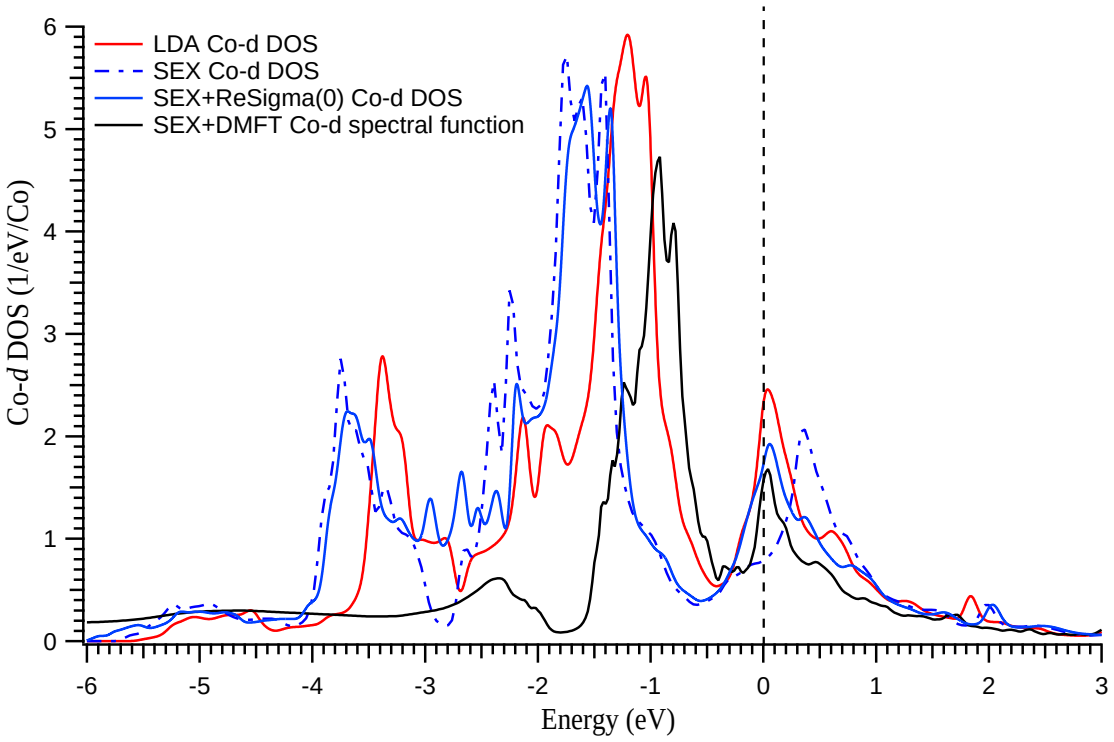

Figure 9.3.6: Cobalt-*d* shell density of states for one Cobalt atom. Red: LDA DOS; black: SEX+DDMFT spectral function, blue (solid line): SEX+$Re\Sigma(0)$ DOS, blue (dotted line): SEX DOS

the weakly dispersive $d_{x^2-y^2}$ states discussed above: as in the SEX band dispersion of Figure 9.3.1, the effect of screened exchange is to push the flat $d_{x^2-y^2}$-like band away from the Fermi level, to the point of suppressing the electron pocket at the Γ point. This does not correspond to the experimental spectrum, and indeed it is corrected by the onset of correlations. Figure 9.3.3 displays the low-energy spectra along the ΓM direction comparing SEX+DDMFT and LDA+DMFT overlaid to the second derivative of the ARPES data [Zhang *et al.* (2011a)], together with the QSGW band dispersion. The electron pocket at Γ is recovered in SEX+DDMFT, and the proportion of $d_{x^2-y^2}$ electrons increases. Within LDA, the flat band is nearly filled along the ΓM direction (at variance with the ARPES results), and it is even worse when we put correlations. From ARPES, this flat band should be filled only in a small electron pocket at Γ, containing about 0.18 e^-. This result is consistent with the absence of ferromagnetism in this compound. Indeed, this flat band lying on the Fermi surface would imply a high density of states at the Fermi level that could trigger a Stoner instability.

9.3.3 Density of states and Stoner instability

We have performed LDA+DMFT calculations with static interactions at lower temperatures in search for this potential Stoner instability. We take a LDA paramagnetic calculation as starting point, and let a DMFT calculation converge without imposing any spin symmetry. For $\beta > 150$ eV^{-1}, we find that both paramagnetic or ferromagnetic solutions can be stable, depending on whether we manually break or conserve the paramagnetic symmetry on the first DMFT iteration. For higher temperatures, only the paramagnetic solution is found to be stable. This shows that already at the LDA+DMFT level $BaCo_2As_2$ is on the verge of the ferromagnetic transition,

and reducing the density of states at the Fermi level is likely to push the compound on the paramagnetic side of the phase diagram. Yet, at such low temperatures the computation time is still a barrier for the inclusion of dynamical interactions, though we have also constated the stability of the paramagnetic phase only for $\beta = 30$ in SEX+DDMFT.

We calculated the density of states at the Fermi level projected on Cobalt atoms by correcting the SEX DOS by the shifts induced by the real part of $\Sigma(\omega = 0)$, the double-counting and the chemical potential, obtaining 0.97 states/eV/Co/spin. Assuming a Stoner parameter of ~ 0.9 eV this leaves us slightly below the onset of Stoner ferromagnetism. However, slight electron doping would bring us close to the maximum value of 1.04 states/eV/Co/spin that we find at $\omega = 44$meV, corresponding to the peak of the Co $d_{x^2-y^2}$ DOS, and a ferromagnetic instability might then appear. Interestingly, the QSGW scheme also provides an overall very good description, including of the $d_{x^2-y^2}$ flat band for which the Fermi wavevector of the electron pocket is well predicted and the rest of the band is left empty. Taking non-local exchange into account is thus necessary to capture this physics, and our SEX+DDMFT scheme performs well for these subtle effects.

Figure 9.3.6 compares the density of Cobalt-*d* states obtained from LDA to the SEX+DDMFT spectral function and the SEX and SEX+$Re\Sigma(0)$ DOS (all broadened by 40 meV). Because of the quasiparticle weight, the area under the curve is reduced and the spectrum is renormalized towards the Fermi level. The LDA DOS has higher peaks than the SEX and SEX+$Re\Sigma(0)$ DOS. However, we point out that some correlations effects, and notably the interaction with the plasmons, are already included in the LDA dispersion, thus reducing the bandwidth and enhancing the DOS. The non-interacting density of states might be better defined by the SEX+$Re\Sigma(0)$ result, which falls below the Stoner criterion at the Fermi level. The value of the SEX+$Re\Sigma(0)$ DOS should be equal to the spectral function obtained by SEX+DDMFT at the Fermi level. We consider the agreement satisfactory within our numerical precision.

Figure 9.3.7 finally compares the photoemission spectrum with the LDA density of states, the SEX+DDMFT spectral function and the QSGW DOS (multiplied by a factor of 0.6 to simulate the effect of the imaginary part of the self-energy at low frequency). The LDA DOS is clearly under-renormalized. As for QSGW and SEX+DDMFT, the agreement with experiment for the position of the highest peak at -0.9 eV is excellent. The main difference between the two theoretical calculations is on the position of the As-*p* states, and of the most binded Co-*d* band. The gap between the Co-*d* and As-*p* states is the same, but it is situated 0.5 eV closer to the Fermi level in SEX+DDMFT. LDA+DMFT with a static $U(0)$ gives a position of the gap similar to QSGW. Unfortunately, the last Co-*d* band is not well detected by ARPES (see Figure 9.2.3), and neither is the position of the As-*p* peaks. We remind that the Yukawa potential has been designed in order to provide a good approximation at low-energy. There is no reason for the effective screening length to be the same for all energies and atomic species, which would explain why we have a good agreement between the two methods for the Co states but not for the As states.

9.3.4 Double counting

The values of the multi-orbital double counting and of the effective masses are displayed on Table 9.3.2. In comparison to a monopole double-counting, we can see that the shifts induced by the multiorbital double counting encourage the orbital polarization reduction.

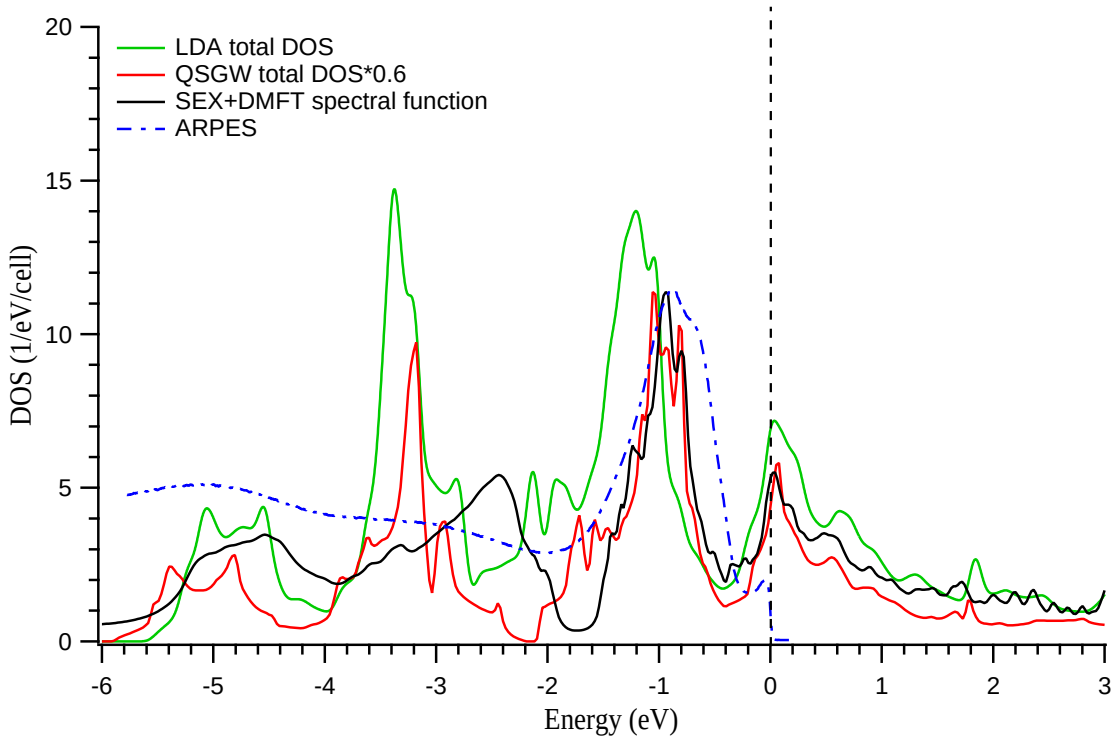

Figure 9.3.7: Cobalt-*d* shell density of states for one Cobalt atom. Red: LDA DOS; black: SEX+DDMFT spectral function, blue (solid line): SEX+$Re\Sigma(0)$ DOS, blue (dotted line): SEX DOS

Table 9.3.2: Orbital-resolved value of double-counting for LDA and Screened Exchange, and effective mass of Cobalt-*d* Wannier functions in SEX+DDMFT with dynamical $U(\omega)$, LDA+DMFT with static U and LDA+DDMFT with dynamical $U(\omega)$.

	DC_{LDA}	DC_{SEX}	$m^*_{SEX+DDMFT}$	$m^*_{LDA+DMFT}$	$m^*_{LDA+DDMFT}$
d_{z^2}	18.665	18.552	1.74	1.26	1.95
$d_{x^2-y^2}$	18.493	18.159	1.86	1.27	1.90
d_{xy}	18.719	18.628	1.68	1.25	1.94
d_{xz+yz}	18.599	18.415	1.68	1.24	1.90

9.3.5 Self-consistency for the Thomas-Fermi screening length and shell-folding

Motivated by the fact that both calculations starting from a screening wavenumber of 1.88 bohr^{-1} and 1.33 bohr^{-1} gave a final density of states corresponding to a new screening wavenumber of about 1.5 bohr^{-1}, we have guessed that this latter value corresponds to self-consistency. Figure 9.3.8 displays the spectral functions obtained from SEX+DDMFT within the previously used *d-dp* model and within a *dp-dp* model which has been shell-folded into an effective *d-dp* model as described in Section 3.4.5 – it will be referred as "shell-folded model". Because the screening of the exchange potential is now larger, the SEX bandstructure has a smaller bandwidth and the *d-dp* model spectral function has a too strong renormalization. In contrast, the shell-folded model describes very well the measured dispersion. The results of this more refined scheme taking into account self-consistency and *p-d* Coulomb interaction are very similar to those discussed above. The most striking discrepancy is in the lifetime of the quasiparticles. Indeed, while in Figure 9.3.2 the quasiparticles are very well defined with nearly no broadening from the imaginary part of the self-energy, the picture is now different: we observe a clear broadening beginning from -0.5 eV. In particular, the lowest $d_{x^2-y^2}$ band is so broadened that it is difficult to identify in the spectral function. Interestingly, also in the ARPES data this band is not visible. Moreover, we can also see that this spectral function is much closer to the one obtained from LDA+DMFT with static U (see Figure 9.2.3). Finally, we obtain a density of 4.76 states/eV/cell at the Fermi level, which corresponds to a screening wavenumber of about 1.55 bohr^{-1}. Since, especially for this compound, the density of states at the Fermi level is very sensitive to small details of the calculation, we consider it as self-consistent within our limit of precision.

9.4 How can LDA+DMFT with static interactions give reasonable results?

Finally, we come back to the computational scheme designed in this work. The spectral function from SEX+DDMFT bears much resemblance with the one from LDA+DMFT, giving a pragmatic *a posteriori* explanation for the correct predictions of LDA+DMFT calculations with static interactions. For total energy calculations within DFT, it is well-known that there are subtle error cancelation effects between the exchange and correlation contributions in approximate density functionals. Here, we evidence a similar effect for spectral properties. The effect of dynamical screening as incorporated in the high-energy tail of the dynamical Hubbard interaction $U(\omega)$ can roughly be understood by a band narrowing by a factor

$$Z_B = \exp\left(-\int_0^\infty d\omega \Im U(\omega)/(\pi\omega^2)\right)$$

In the anti-adiabatic limit, where the characteristic frequency of variations in $U(\omega)$ is larger than the other energy scales of the system, this statement can be made rigorous by means of a Lang-Firsov transformation, as demonstrated in [Casula *et al.* (2012b)]. For $BaCo_2As_2$, we find dynamical screening to be a non-negligible effect, with $Z_B \sim 0.6$. On the other hand, when starting from the LDA, the bandwidth has already been decreased by correlation effects hidden in the effective exchange-correlation potential of DFT, with respect to the Hartree-Fock or SEX bandstructure, and LDA+DDMFT doublecounts this narrowing effect. Starting a many-body calculation from LDA, thus raises not only the usual well-known double counting questions

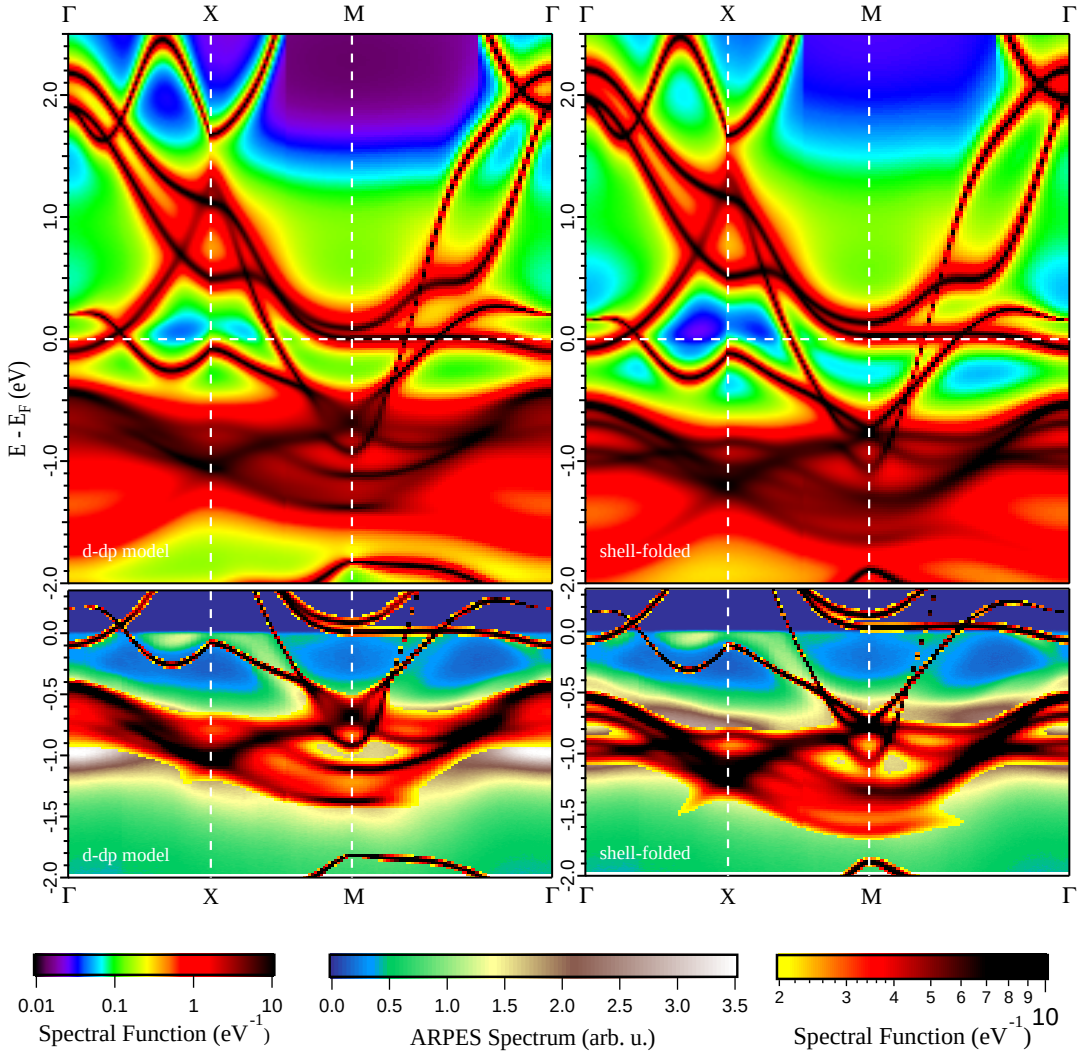

Figure 9.3.8: (Top): SEX+DDMFT spectral functions for $BaCo_2As_2$ with $k_{TF} = 1.5$ bohr^{-1}along the ΓXMΓ momentum path within (left) a *d-dp* model and (right) a shell-folded effective model. (Bottom) Bands extracted from the maxima of the spectral function of SEX+DDMFT superimposed on ARPES data as in Figure 9.2.3.

related to the energetic position of correlated states with respect to itinerant ones, but even more serious ones related to the double counting of screening processes. Our SEX+DDMFT scheme avoids these, providing a more solid foundation for the investigation of dynamical screening effects. On a more pragmatic level, the similarity of the LDA+DMFT and SEX+DDMFT spectral functions also suggests that error cancelations between the neglect of dynamical screening and non-local exchange in LDA+DMFT make this scheme suitable at least for questions concerning the overall bandwidth reduction of correlated electron systems. Finer details related to the very low energy behavior or Fermi surface topologies, on the other hand, might require explicit exchange corrections as introduced in the present work.

9.5 Electronic correlations and the importance of Hund's coupling

Hund's-rule coupling has been identified as an efficient tuning parameter for electronic correlations in iron pnictides [Haule and Kotliar(2009), Aichhorn *et al.* (2010), Liebsch and Ishida(2010), Ishida and Liebsch(2010)], indicating the importance of local moments in the physics of these materials. Very recently [Werner *et al.* (2012)], a study of hole-doped $BaFe_2As_2$ evidenced an unusual non-Fermi-liquid behavior with frozen moments in the paramagnetic phase. The doping-temperature phase diagram of these materials exhibits exotic fractional power-law behavior of the many-body self-energies consistent with the phase diagram of the ''spin-freezing'' scenario [Werner *et al.* (2008)], where fractional behaviors occur in some temperature range at fillings close to half-filling. (For a review, see [Georges *et al.* (2013)].) Following this logic, one would expect the strength of the electronic correlations to vary significantly when the electronic structure is tuned away from the d^{6-x} filling of hole-doped $Ba_{1-2x}K_{2x}Fe_2As_2$, with reduced correlation effects when the d^7 filling is reached.

In this section, we compare the strength of correlations between $BaCo_2As_2$, with a d^7 filling, and optimally doped $Ba_{0.6}K_{0.4}Fe_2As_2$, with a nominal filling of $d^{6.8}$. We use the simpler LDA+DMFT with static interaction $U(\omega = 0)$ scheme since we have seen in the previous section that it describes very well the spectral function in this compound. To quantify the strength of the electronic correlations, let us first compare the overall bandwidth found experimentally with the one predicted by our local-density approximation (LDA) calculations. For $BaCo_2As_2$ the LDA bands are renormalized by about 1.25 compared to experiment (see Table 9.3.2) near the Fermi level, indicating much weaker correlation effects than in its cousin $BaFe_2As_2$, for which a renormalization factor between 2 and 3 was reported [Richard *et al.* (2010), Ding *et al.* (2011)].

We go beyond this analysis by comparing the imaginary part of self-energies obtained by LDA+DMFT calculations and the dynamically screened local moments, which is a signature of correlations in iron pnictides [Hansmann *et al.* (2010)]. Our results indicate that the weaker correlation effects in $BaCo_2As_2$ as compared to those of the ferropnictides are mainly a consequence of the larger band filling in the Co compound. These findings support previous theoretical results by confirming the crucial role played by the Hund's-rule coupling in the ferropnictide materials [Haule and Kotliar(2009), Aichhorn *et al.* (2010), Liebsch and Ishida(2010), Ishida and Liebsch(2010)]. In addition, they also provide an explicit confirmation of the theoretical prediction [Werner *et al.* (2012)] of the filling of the d band being an efficient tuning parameter for the strength of electronic correlations in the larger family of ferro- and non-ferropnictides in the presence of Hund's-rule coupling.

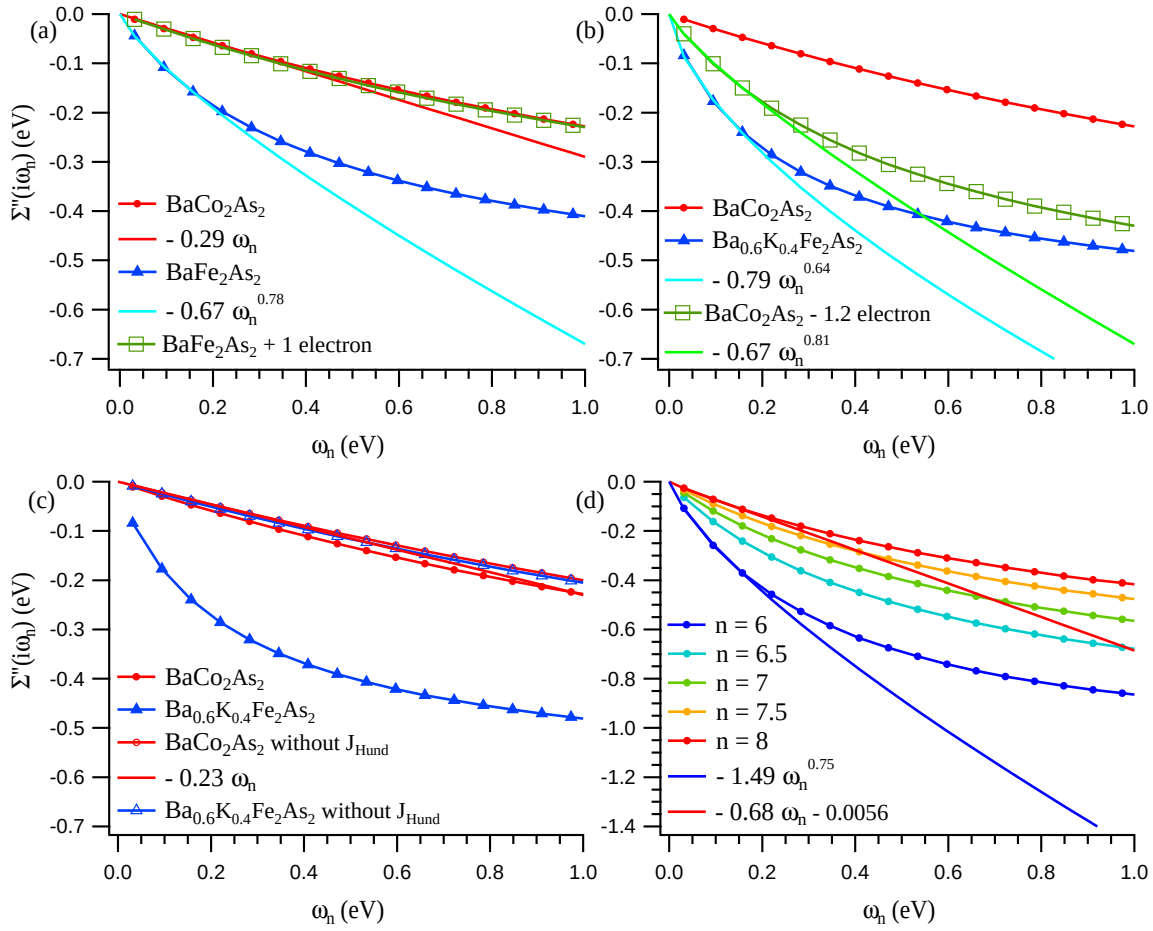

Figure 9.5.1: (a) and (b): Effect of doping on the low-energy imaginary part of the self-energy as a function of Matsubara frequencies $\Sigma''(i\omega_n)$ of the d_{xy} orbital in $BaCo_2As_2$ and $BaFe_2As_2$, calculated at T = 120 K. (c): Impact of the suppression of the Hund's coupling on $\Sigma''(i\omega_n)$ of the d_{xy} orbital in $BaCo_2As_2$ and $Ba_{0.6}K_{0.4}Fe_2As_2$. (d) Imaginary part of the self-energy for a model calculation of five degenerate bands with a half-bandwidth of 1.5 eV and the same value of U and J than in $BaCo_2As_2$.

As observed in $Ba(Fe_{1-x}Ru_x)_2As_2$ [Xu *et al.* (2012), Brouet *et al.* (2010)], a large decrease in the electronic correlations is expected as 3*d* electrons are substituted by 4*d* electrons. The situation is quite different in $Ba(Fe_{1-x}Co_x)_2As_2$, where the conducting properties of both Fe^{2+} and Co^{2+} derive from 3*d* electron orbitals with similar spatial extension. To investigate the nature of this unexpected decrease of the electronic correlations in $BaCo_2As_2$, we have performed LDA+DMFT calculations on this material and on paramagnetic $BaFe_2As_2$ using the experimental crystal parameters. We furthermore vary the doping, the temperature, and the strength of Hund's coupling.

In Figure 9.5.1(a), we plot the imaginary part of the self-energy $\Sigma''(i\omega_n)$ of both $BaCo_2As_2$ and paramagnetic $BaFe_2As_2$ as a function of the Matsubara frequencies, for the d_{xy} orbital. $\Sigma''(i\omega_n)$ varies linearly at low frequency in $BaCo_2As_2$, indicating coherent Fermi-liquid behavior already at the temperature of the calculation (T = 120 K). In $BaFe_2As_2$ we can already see that this linear behavior is not valid. If we still try to extract an effective mass from the first two values in order to approximate the dispersion of the electronic states, even if they are not Fermi-liquid like quasiparticles, we find about $2m_{LDA}$. This is in good agreement with [Brouet *et al.* (2013)]

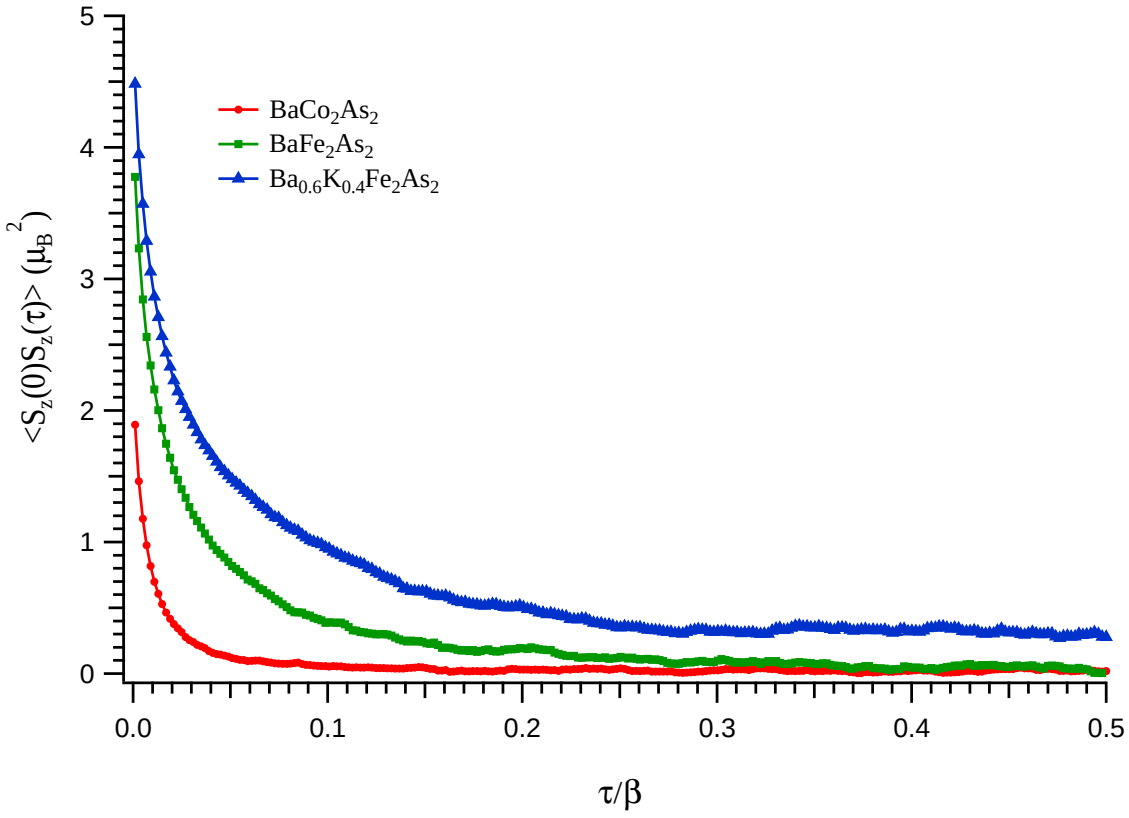

Figure 9.5.2: DMFT calculation of the spin-spin correlation function of $BaCo_2As_2$, $BaFe_2As_2$ and $Ba_{0.6}K_{0.4}Fe_2As_2$ at T=120 K.

and is probably not totally absurd because we are close to the coherence temperature (see Figure 9.5.3). In comparison, we find an effective mass of about $1.3m_{LDA}$ for the quasiparticles in $BaCo_2As_2$. Paramagnetic $Ba_{0.6}K_{0.4}Fe_2As_2$ is also simulated by artificially removing 0.2 electron per Fe in $BaFe_2As_2$ to mimic the effect of substitution, while maintaining the LDA Hamiltonian of this compound. Interestingly, $\Sigma''(i\omega_n)$ then follows a nearly square-root behavior characteristic of the "spin-freezing" regime in $Ba_{0.6}K_{0.4}Fe_2As_2$ (see Figure 9.5.1(b)). At 120 K we can only extract a minimum of $2.5m_{LDA}$ for the effective mass, that increases to $3m_{LDA}$ when we lower the temperature to 40 K – where we nearly recover the Fermi liquid behavior – in good agreement with [Ding *et al.* (2011)].

To investigate further the origin of these phenomena, we have artificially added 1 electron per Fe in $BaFe_2As_2$. Surprisingly, the self-energy of this hypothetical crystal can hardly be distinguished from that of $BaCo_2As_2$, as shown in Figure 9.5.1(a). This result strongly suggests that the decrease in the electronic correlations in $BaCo_2As_2$ is mainly due to the less drastic effects of Hund's exchange in the Co compound whose d^7 filling is further away from the case of a half-filled shell.

Indeed, this huge change in the level of correlations cannot be linked to a variation of the Coulomb parameter U. In both cases, we find $U = F_0$ around 2.6 – 2.9 eV by constrained-RPA and the Hund's coupling $J_H = (F_2 + F_4)/14$ around 0.85 eV, with even a small increase of U in the Co case. Furthermore, we have performed additional calculations in which we artificially set J_H to 0 (see Figure 9.5.1(c)). In this case, we see a sudden drop of the renormalization and the suppression of the non-Fermi-liquid behavior in $Ba_{0.6}K_{0.4}Fe_2As_2$. However, $BaCo_2As_2$ becomes only slightly less correlated.

An analogous effect has recently been studied in a three-orbital Hubbard model [Werner *et al.* (2008)], where Hund's exchange was found to induce an exotic "spin-freezing" regime at finite temperatures for incommensurate fillings close to the half-filled case. This explanation rules out any significant influence from structural variations. We caution though that structural variations are actually important around a doping level of 6 electrons, especially near the crossover between Fermi liquid and non-Fermi liquid. For instance, trying to hole-dope the $BaCo_2As_2$ compound gives a different picture with a power-law at low-frequency closer to 1 (see Figure 9.5.1(b)), indicating that this compound has not yet fully entered the spin-freezing phase – or equivalently that his coherence temperature is closer to the temperature of the calculation. We stress that this effect is not primarily due to the density of states. Indeed, a calculation with five degenerate bands gives qualitatively the same conclusion (see Figure 9.5.1(d)), and the reduction of orbital polarization by Hund's coupling is likely to push the compound close to that model case.

The fact that the spin-freezing scenario is realized at fillings close (but not equal) to half-filling is consistent with the unified view of the pnictide and cuprate superconductors put forward for example in [Ishida and Liebsch(2010), Misawa *et al.* (2012), de' Medici *et al.* (2014)], where the proximity to Mottness, that is, to the d^5 filling of the Mott insulator, is considered as the decisive parameter to tune electronic correlations. Indeed, also in the pnictide family, d^5 compounds (such as LaMnPO [Simonson *et al.* (2012)] or $BaMn_2As_2$ [Satya *et al.* (2011)]) have been synthesized and characterized as good insulators. Our findings demonstrate that the evolution – as a function of filling – of the d^5 manganite insulators into the strongly correlated and badly metallic d^6 ferropnictides can be further extended into a weakly correlated regime for the higher fillings of the d shell in the cobaltates.

Early experimental results suggested the presence of large unscreened local moments in some ferropnictide materials [Bondino *et al.* (2008)]. Our results emphasize further the

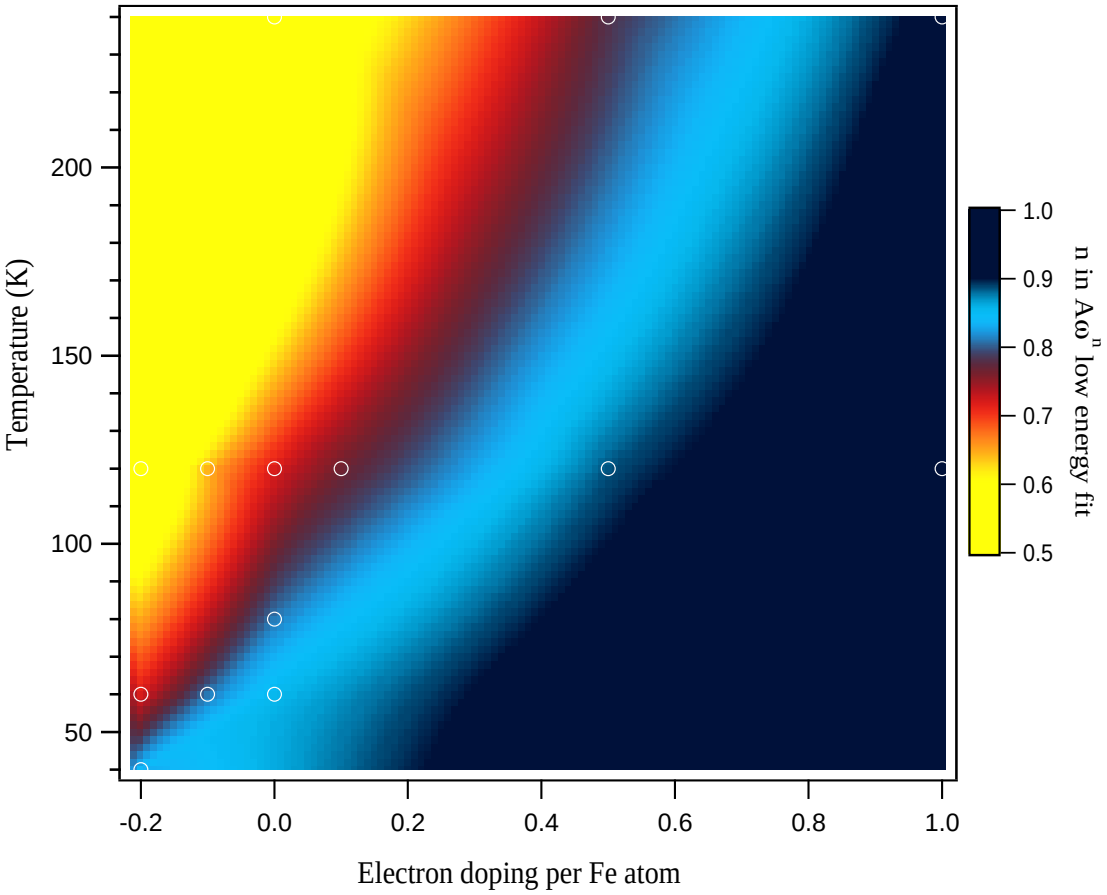

Figure 9.5.3: Spin-freezing transition in doped $BaFe_2As_2$ in a static-U model.

importance of these moments. In the spin-freezing regime, these unscreened local moments have a long lifetime, and spin-spin correlation functions do not decay anymore [Werner *et al.* (2008)]. As shown by our DMFT calculations of the spin-spin correlations plotted in Figure 9.5.2, this situation corresponds to hole-doped $Ba_{0.6}K_{0.4}Fe_2As_2$ at the temperature of the calculations. In contrast, the spin-spin correlations in $BaCo_2As_2$ decay rapidly and become vanishingly small in the long-time limit. The apparent strength of the electronic correlations increases with the local moments.

Thus, correlations in the ferropnictides can be interpreted as the interaction of local moments with itinerant electrons, as in the Kondo problem. In the present study, we have compared two compounds with small orbital polarization (due to the strength of Hund's coupling): $BaFe_2As_2$, with six electrons in five bands, and $BaCo_2As_2$, with seven electrons in five bands. In the former case, Hund's exchange drastically reduces the available channels for Kondo screening, thus enhancing the consequences of electronic correlations, while in the latter, screening is quite efficient and reestablishes a largely uncorrelated picture. We finally plot a rough phase diagram of the spin-freezing transition in Figure 9.5.3 from the power-law behavior shown by the imaginary part of the self-energy. We can see that the spin-freezing crossover happens in the hole-doped side. However, we caution that the low-energy behavior of the self-energy is typically a quantity very sensitive to taking into account the dynamical interactions. Still, it is interesting to see that our diagram is similar to the one found in [Werner *et al.* (2012)], which took into account this high-frequency tail.

9.6 Conclusions

In summary, we have shown that screened exchange combined with dynamical correlations provides an excellent description of the low-energy physics in $BaCo_2As_2$. In contrast to perturbative schemes, it can be expected that our non-perturbative method can be extended to regimes with arbitrarily strong correlations, making it a promising tool for probing the normal state of iron pnictides and chalcogenides superconductors.

For $BaCo_2As_2$, we have shown that the $d_{x^2-y^2}$-states that form a flat band in immediate vicinity of the Fermi level are extremely sensitive to an accurate treatment of screened exchange, which reduces the occupation of these states and enhances the orbital polarization. It would be useful to perform pump-probe photoemission probing the exact location of the flat band and possibly finding new ways to tailor its exact energetic position, thus directly playing on possible Fermi surface instabilities.

Finally, our study indicates that $BaCo_2As_2$ is significantly less correlated than $BaFe_2As_2$ at equal Hund's coupling, due to the larger filling of the d electron shell. Our results reveal the importance of local moments in the physics of the Fe-based superconductors, as predicted theoretically in [Werner *et al.* (2012)], and establish the d-shell filling as the most important tuning parameter for electronic correlations in the series of Mn, Fe, or Co pnictides.

Chapter 10

The structural collapse of $CaFe_2As_2$

In this chapter, we present preliminary results on the tetragonal to collapsed tetragonal transition in $CaFe_2As_2$. We have performed ARPES experiments and LDA+DMFT calculations on both phases to explore a possible link with a spin-freezing transition, in collaboration with Pierre Richard, Xun Shi, Wu Shangfei, Tian Qian, Hong Ding and Silke Biermann.

10.1 Introduction to the collapse transition

$CaFe_2As_2$ at ambient pressure and temperature is in a paramagnetic tetragonal phase. When temperature is lowered under 170 K it becomes magnetic and orthorhombic [Ronning *et al.* (2008), Ni *et al.* (2008), Diallo *et al.* (2009)]. When put under pressure, this orthorhombic phase can be suppressed, and replaced by a non-magnetic collapsed tetragonal phase in which the distance between two FeAs layers is strongly reduced due to the formation of covalent bonds between As atoms from two different layers (see Figure 10.1.1). Superconductivity can also develop from this collapsed phase [Torikachvili *et al.* (2008), Kreyssig *et al.* (2008)]. Recently, it has been found that a quench of the annealing phase during the synthesis of the crystal can produce samples presenting similar properties as $CaFe_2As_2$ under pressure [Ran *et al.* (2011), Saparov *et al.* (2014)]. At ambient temperature and pressure, they are in the tetragonal phase, and when temperature is lowered there is a transition into a collapsed tetragonal phase, around 90 K in our samples synthesized by authors of [Saparov *et al.* (2014)]. There are also other ways to induce a collapse transition at ambient pressure, such as isovalent substitution of As by P [Coldea *et al.* (2009)], electron-doping by Rh at the Fe site [Danura *et al.* (2011)] or electron doping by rare-earth on the Ca site [Saha *et al.* (2012)]. However, while $CaFe_2As_2$ in the collapsed tetragonal phase can become superconductor under pressure[1] or with rare-earth doping [Torikachvili *et al.* (2008), Saha *et al.* (2012)], it is not the case in these quenched crystals.

During the collapse, the c axis of the unit cell is strongly reduced by about 10%, while the a axis is enlarged by about 2%. This modification of the crystal structure is at the origin of a reorganization of the Fermi surface and electronic structure of the compound [Coldea *et al.* (2009), Danura *et al.* (2011), Tsubota *et al.* (2013), Dhaka *et al.* (2014), Gofryk *et al.* (2014)], which has been studied within DFT [Yildirim(2009b), Tomić *et al.* (2012), Coldea *et al.* (2009), Dhaka *et al.* (2013)] and very recently within DFT+DMFT [Mandal *et al.* (2014), Diehl *et al.* (2014)].

[1] Superconductivity can also occur in a non-collapsed phase, e.g. in $Ca_{1-x}La_xFe_2As_2$ [Saha *et al.* (2012)] or for low-doping values in $CaFe_2As_{2-x}P_x$ [Kasahara *et al.* (2011)].

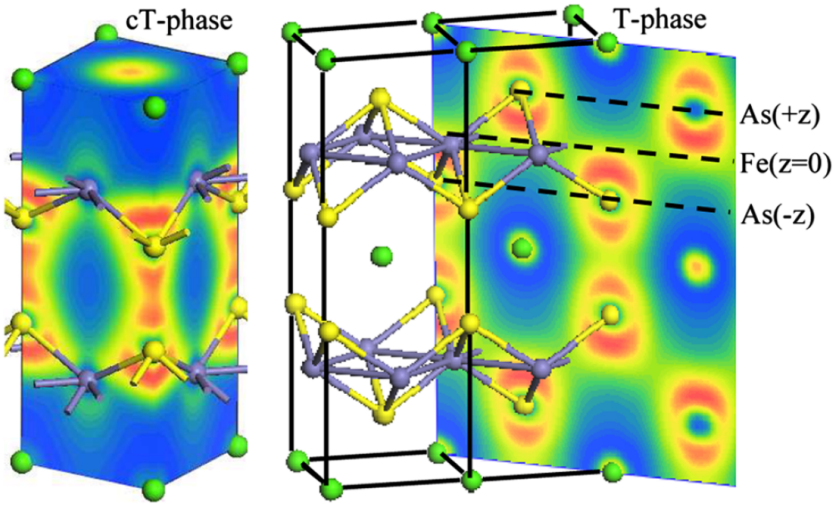

Figure 10.1.1: Contour plot of the As p_z orbital in the collapsed tetragonal (cT) phase (left) and the tetragonal (T) phase (right) of $CaFe_2As_2$, respectively. Note that the As-As hybridization present in both phases is much more significant in the cT-phase. There is also clear hybridization between intra-As atoms below and above the Fe-plane in the T-phase (right). (From [Yildirim(2009b)].)

Interestingly, the resistivity at the transition changes its low-energy behavior from $\rho \propto T$ or $\rho \propto T^{1.5}$ in the tetragonal phase to $\rho \propto T^2$ – as in a good Fermi liquid – in the collapsed tetragonal phase [Kasahara *et al.* (2011), Danura *et al.* (2011), Saparov *et al.* (2014)]. Rare-earth electron-doped $Ca_{1-x}RE_xFe_2As_2$ also exhibits a Fermi-liquid like resistivity, but including in the non-collapsed tetragonal phase of $Ca_{1-x}La_xFe_2As_2$ [Saha *et al.* (2012)]. Recent Nuclear Magnetic Resonance data further find a suppression of antiferromagnetic spin fluctuations in the collapsed tetragonal phase [Furukawa *et al.* (2014)]. Motivated by these intriguing results, we have performed LDA+DMFT calculations and ARPES experiments on the tetragonal and collapsed-tetragonal phase of $CaFe_2As_2$ to explore a possible link with a spin-freezing transition, in collaboration with Pierre Richard, Xun Shi, Wu Shangfei, Tian Qian, Hong Ding and Silke Biermann.

10.2 Modification of electronic properties through the collapse transition

We have performed angle-resolved photoemission measurements on samples grown by the self-flux method that are quenched to air at 960°C (marked as as-grown "p1" samples in [Saparov *et al.* (2014)]). Experiments were conducted at the CASSIOPEE beamline of the SOLEIL synchrotron (France) and at the Institute of Physics, Chinese Academy of Sciences (China). Both systems are equipped with VG-Scienta R400 electron analyzers. All samples were cleaved *in situ* at temperatures higher than 200 K and measured in a working vacuum between 5×10^{-10} and 1×10^{-9} torr at SOLEIL, and better than 5×10^{-11} torr at the Institute of Physics. The photon energy was varied from 20 to 80 eV in synchrotron while we used the He αI line of an helium discharge lamp in the lab (21.2 eV). The angular resolution is better than 0.5° and the

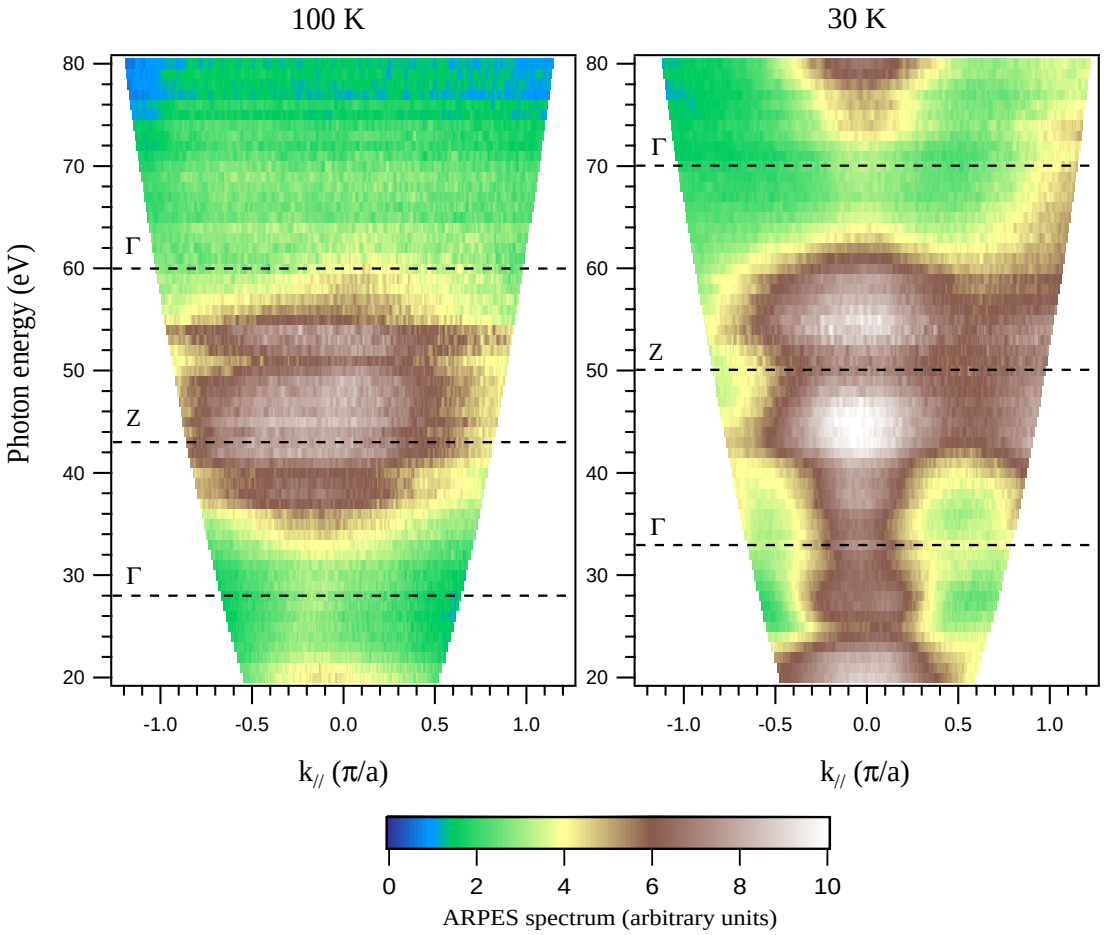

Figure 10.2.1: Photon energy dependence of the ARPES spectrum of $CaFe_2As_2$ in the tetragonal (T = 100 K) and collapsed tetragonal (T = 30 K) phases at the Fermi level around the Γ point.

energy resolution better than 10 meV.

Samples were measured at 200 K, 100 K, 80 K and 30 K. The tetragonal to collapsed tetragonal transition is shown to occur around 90 K by magnetic susceptibility measurements performed by Shaokui Su at the Institute of Physics, with a hysteresis smaller than 5 K, in agreement with [Saparov *et al.* (2014)]. Because of a quicker broadening of the signal with time in SOLEIL – possibly due to a worse working vacuum causing faster aging or to an intrinsic deterioration of measured samples – the measurement of a single sample at different temperatures presented below have only been done with a photon energy of 21.2 eV. Still, the Fermi surfaces obtained by a fast mapping in SOLEIL are similar to those obtained in the lab, showing that the measured samples are in the same phase. We use the synchrotron data mainly to obtain the value of the inner potential in order to deduce the k_z of our 21.2 eV measurements.

Figure 10.2.1 displays the photoemission spectra centered on the Γ point at the Fermi level for different photon energies, in the collapsed tetragonal and tetragonal phases. The loss of signal around 50 eV is probably not due to the structure of the Fermi surface but to small matrix elements. From the observed periodicity of the spectrum in the collapsed tetragonal phase we deduce an inner potential V_0 of about 15 eV. Using a nearly free-electron model for the final state:

$$k_\perp = \frac{\sqrt{2m}}{\hbar}\sqrt{E_{kin}cos^2\theta + V_0} \tag{10.2.1}$$

and the lattice parameters of [Saparov *et al.* (2014)], we find that it corresponds to a Γ point around 33 eV and 70 eV and a Z point around 50 eV and 18.5 eV in the collapsed tetragonal phase. This value of the inner potential also corresponds well to the data observed by [Dhaka *et al.* (2014)]. In the tetragonal phase data is less clear, but using the same value for V_0 we estimate the Γ point to be around 28 eV and 60 eV and the Z point around 43 eV. Though the agreement at 28 eV appears to be good, it seems that for higher energy there is a slight discrepancy with the observed spectrum. This might be due to a modification of the inner potential. Indeed, the surface will probably be different in the tetragonal phase, which could induce a small change of the work function.

Figure 10.2.2 shows the Fermi surface of our $CaFe_2As_2$ sample in tetragonal and collapsed tetragonal phases taken with a photon energy of 21.2 eV. We have lowered temperature from 200 K to 30 K and finished the measurement less than 30 hours after the cleave, such that the aging of the sample was not too important. Using the previously deduced inner potential and equation 10.2.1, we find that for the collapsed tetragonal phase the Γ point has a k_z close to 1.25 π/c' – with $c' = c/2$ the distance between two FeAs layers, close to the Z point of coordinates $(0, 0, \pi/c')$. k_z then decreases when $k_{\|}$ is increased, with a value of 0.89 π/c' at the M point and 1.01 π/c' at the X point. It is interesting to note that the point symmetric to Γ with respect to the X point would have for coordinates $(2\pi/a, 0, 0.5\pi/c')$, such that it would nearly correspond to the same high-symmetry point[2]. For the tetragonal phase, we find $k_z = 1.6\pi/c'$ at the Γ point and $k_z = 1.19\pi/c'$ at the M point.

For a more detailed analysis of the features of the Fermi surface, we also present three different cuts. We first show the ΓM direction for all temperatures (see Figure 10.2.3 and 10.2.4). We also display a cut near the M point on the direction perpendicular to ΓM (see Figure 10.2.5 left panel) and another one along the ΓX direction (Figure 10.2.5 right panel), for the collapsed tetragonal phase at 80 K only (similar results are obtained at 30 K). In the tetragonal phase, we can distinguish two hole-like bands forming circular hole pockets near the Γ point, although one may not cross the Fermi level. We also find two electron pockets around the M point. This is similar to what is found in many iron pnictides, and in particular in $BaFe_2As_2$. Below the transition temperature, the Fermi surface is reorganized. The circular hole pocket around the Γ point shrinks drastically – or even disappears – while a large square hole pocket develops (see the dashed lines on the 30 K Fermi surface of Figure 10.2.2). This shape of the hole-like bands is very characteristic of the collapsed structure and qualitatively different from what is seen in $BaFe_2As_2$. It is due to a stronger three-dimensional character, as can be observed from the photon-energy dependent data of Figure 10.2.1. Indeed, the k_z dispersion is enhanced by the strong As-As p_z interlayer hybridization in the collapsed phase. On the other hand, the electron pockets near M keep a similar size.

From the temperature-dependent photoemission spectra of Figure 10.2.2 and 10.2.3, it is interesting to see how the features become better defined as temperature is lowered. Notably, there is a clear difference before (at 100 K) and after (at 80 K) the collapse transition. However, because the quasiparticle dispersions are also changed through this transition, and because in overall the spectrum appears to be very sensitive to temperature, it is difficult to attribute this improvement to the transition only.

Finally, Figure 10.2.6 presents the superposition of bands extracted from LDA+DMFT calculations performed at 120 K (with a procedure similar to Chapter 9) with the ARPES

[2]Indeed, the point Z with coordinates $(0, 0, \pi/c')$ is equivalent to the point with coordinates $(2\pi/a, 0, 0)$ (see Figure 2.2.2).

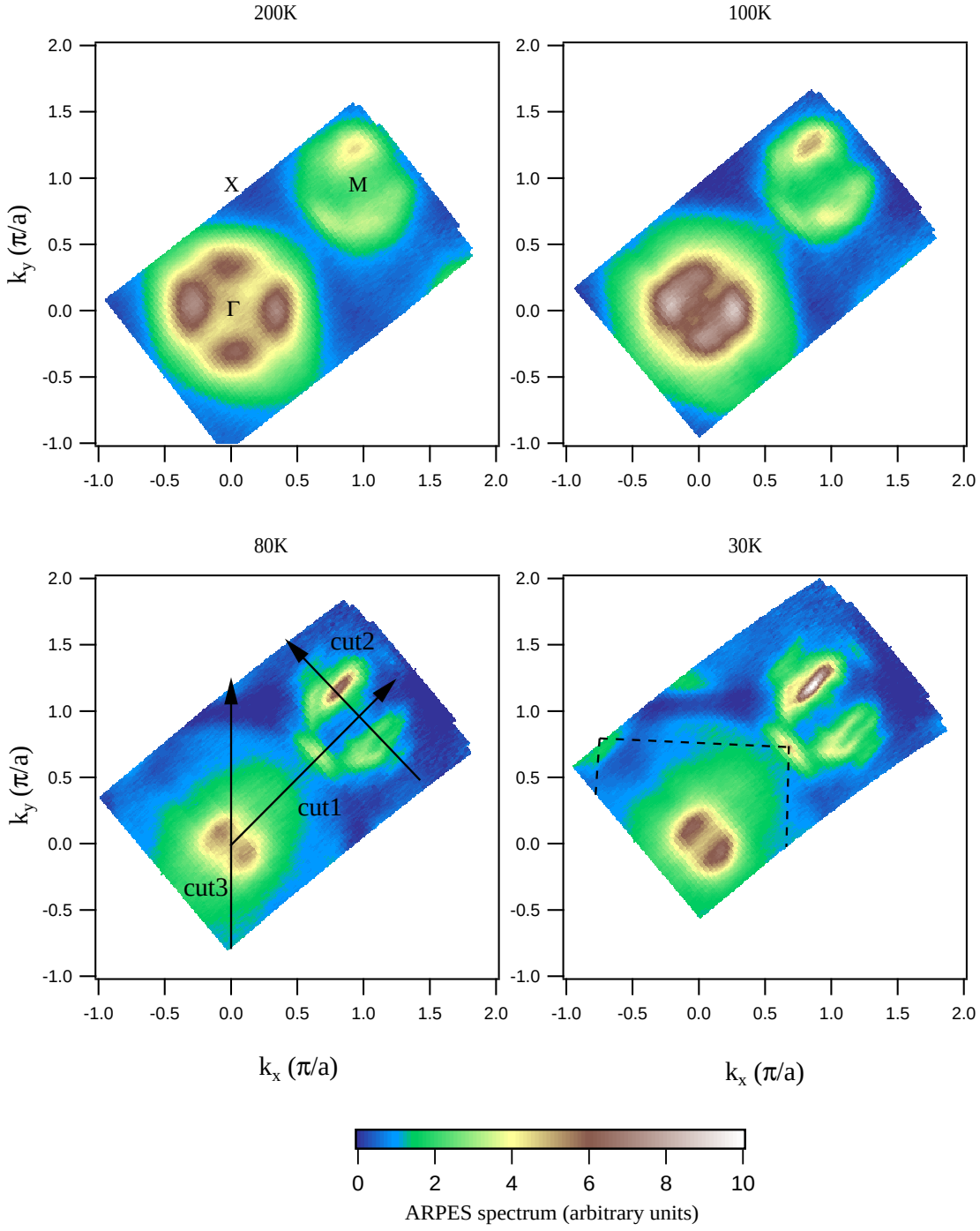

Figure 10.2.2: Fermi surface mapping of $CaFe_2As_2$ in the tetragonal (T > 90 K) and collapsed tetragonal (T < 90 K) phases.

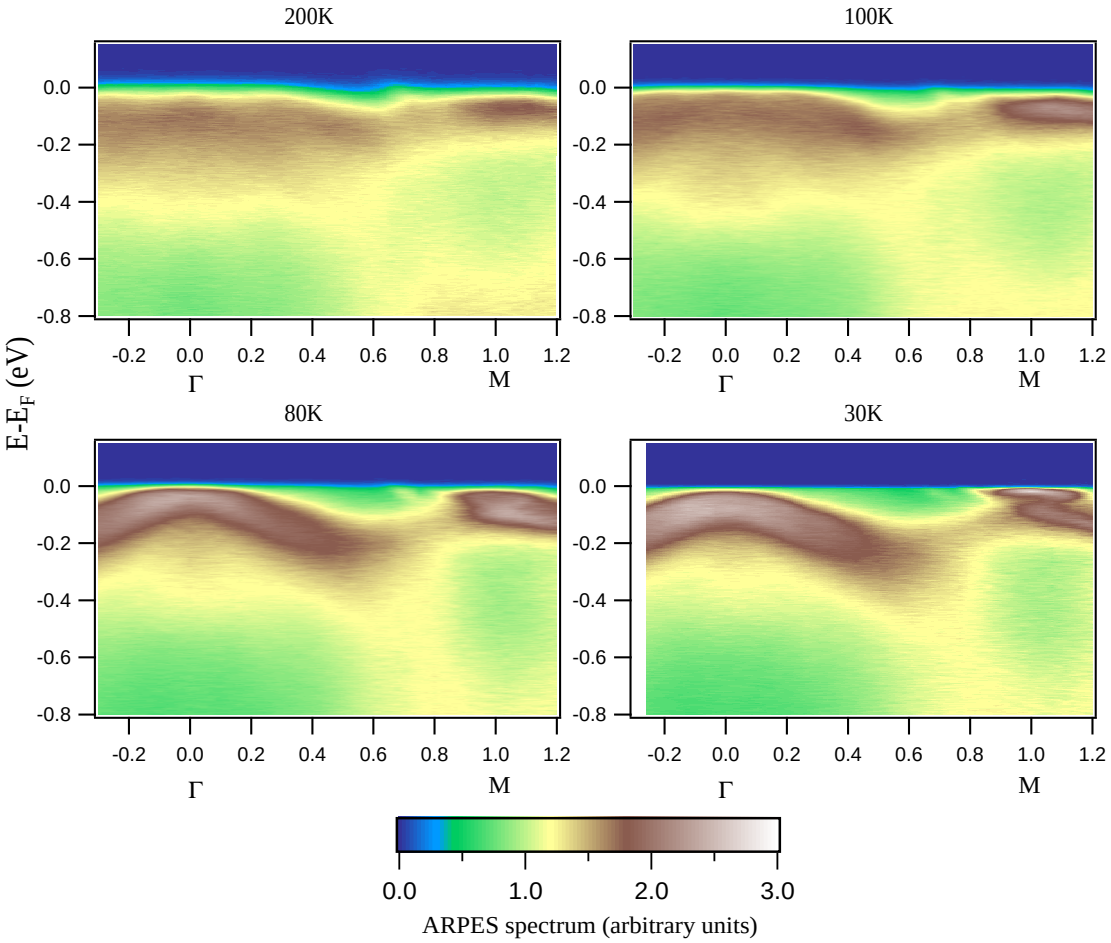

Figure 10.2.3: ARPES spectrum of $CaFe_2As_2$ in the tetragonal (T > 90 K) and collapsed tetragonal (T < 90 K) phases along the ΓM direction (cut 1 of Figure 10.2.2).

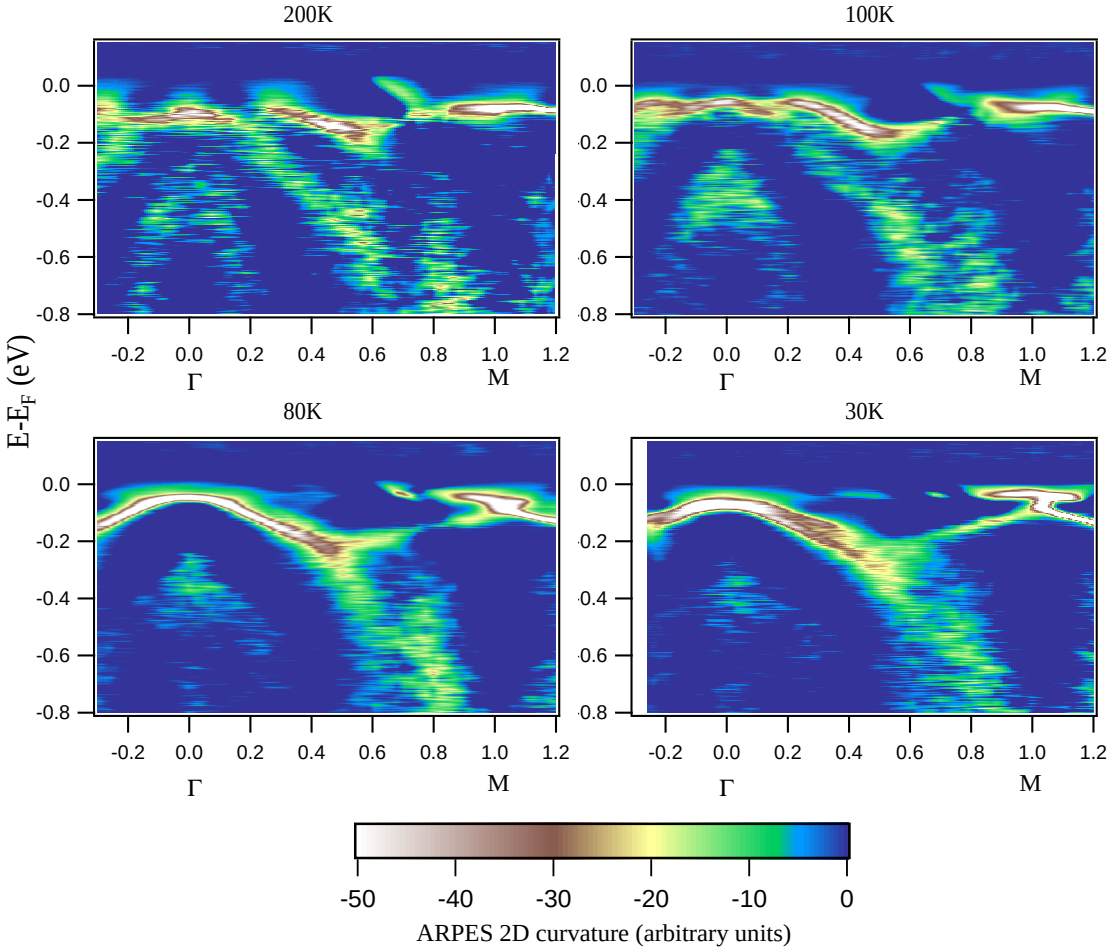

Figure 10.2.4: ARPES spectrum of $CaFe_2As_2$ in the tetragonal (T > 90 K) and collapsed tetragonal (T < 90 K) phases along the ΓM direction (cut 1 of Figure 10.2.2).

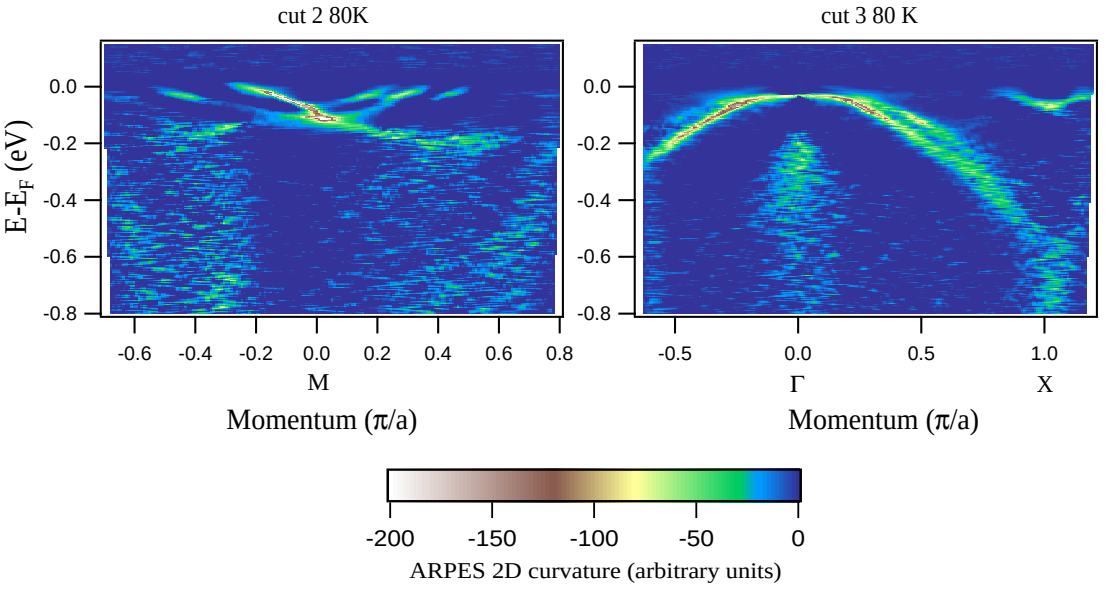

Figure 10.2.5: ARPES spectrum of $CaFe_2As_2$ in the tetragonal (T > 90 K) and collapsed tetragonal (T < 90 K) phases near the M point (left) along the direction perpendicular to ΓM and along the ΓX direction (right) (cut 2 and cut 3 of Figure 10.2.2 respectively).

spectrum along the ΓM direction. We have taken into account the variation of k_z as indicated previously. In overall, the band renormalization is correctly described by the LDA+DMFT calculations, similarly to what we have seen in Chapter 9. We can also see from the calculations that there may be three hole-like bands in total in the tetragonal phase but two are nearly degenerate near the Γ point. However, if we look at precise details of the low-energy states, we can find several discrepancies. In the tetragonal phase at the Fermi level, one of the bands near the Γ point is not well described. It is not clear if this is due to possible surface effects or to limitations of the calculations such as those described in Chapter 9. On the other hand the electron pockets are well described. In the collapsed tetragonal phase, the agreement is also disappointing. The two hole-like bands near the Γ point appear to be very close to each other from photoemission, as can be seen even more clearly on the 30 K data of Figure 10.2.4 and on the ΓX direction of Figure 10.2.5. This is not the case in the calculation. There is also a disagreement on the shape of the electron pockets. On the other hand, we consider the agreement for the Fermi vector of the large hole pocket relatively satisfying since this band is very sensitive to the precise value of k_z. If we suppose that the ARPES spectrum reflects the bulk features of the collapsed tetragonal phase, an important test for the future theoretical calculations would be the correct prediction of the dispersion of the two hole-like bands near Γ, and of the interesting topology found near the M point on Figure 10.2.5, which shows three bands crossing the Fermi level very close to each other – one of them being the large hole pocket. This last point is very peculiar in the iron pnictides family and due to the large k_z dispersion of the collapsed phase. We still have to apply our SEX+DMFT method on this material and expect that the dispersion of the low-energy states will be better predicted.

10.3 Decoupling interlayer and intralayer transitions within LDA+DMFT

The origin of the reduction of correlations in the collapsed tetragonal phase compared to the tetragonal phase is difficult to understand since both Fe-As and As-As bindings are modified. Indeed, in the collapsed structure the As-As interlayer binding is much stronger, which should increase the three dimensional character of the bandstructure dispersion. But the transition has also another effect on the Fe-As binding, for the c axis collapses so much that the As height to the Fe plane is reduced. The result is that the Fe-As distance is shortened, suggesting an enhancement of the hybridization between the As-4*p* and the Fe-3*d* orbitals – though the expansion of the a axis limits this enhancement.

To decouple these two effects we have performed LDA+DMFT calculations on two chimeric "hybrid" compounds. In the first one, we keep the same angle and distances between atoms within the FeAs layers as in the tetragonal phase, while the interlayer As-As distance is that of the collapsed tetragonal phase. In the other one, we do the opposite: the layer is that of the collapsed tetragonal phase and the interlayer distance is that of the tetragonal phase.

The imaginary part of the self-energy of the d_{xy} orbital in Matsubara frequencies is displayed on Figure 10.3.1. The effect on the $d_{xz} + d_{yz}$ orbital is similar, and since those orbitals have the highest density of states at the Fermi level we expect that they control the coherence properties of the compound[3]. We can first see that in the collapsed phase the imaginary part of the

[3] In contrast, there is no difference between the four structures for the $d_{x^2-y^2}$ orbital and a much smaller one for the d_{z^2} orbital.

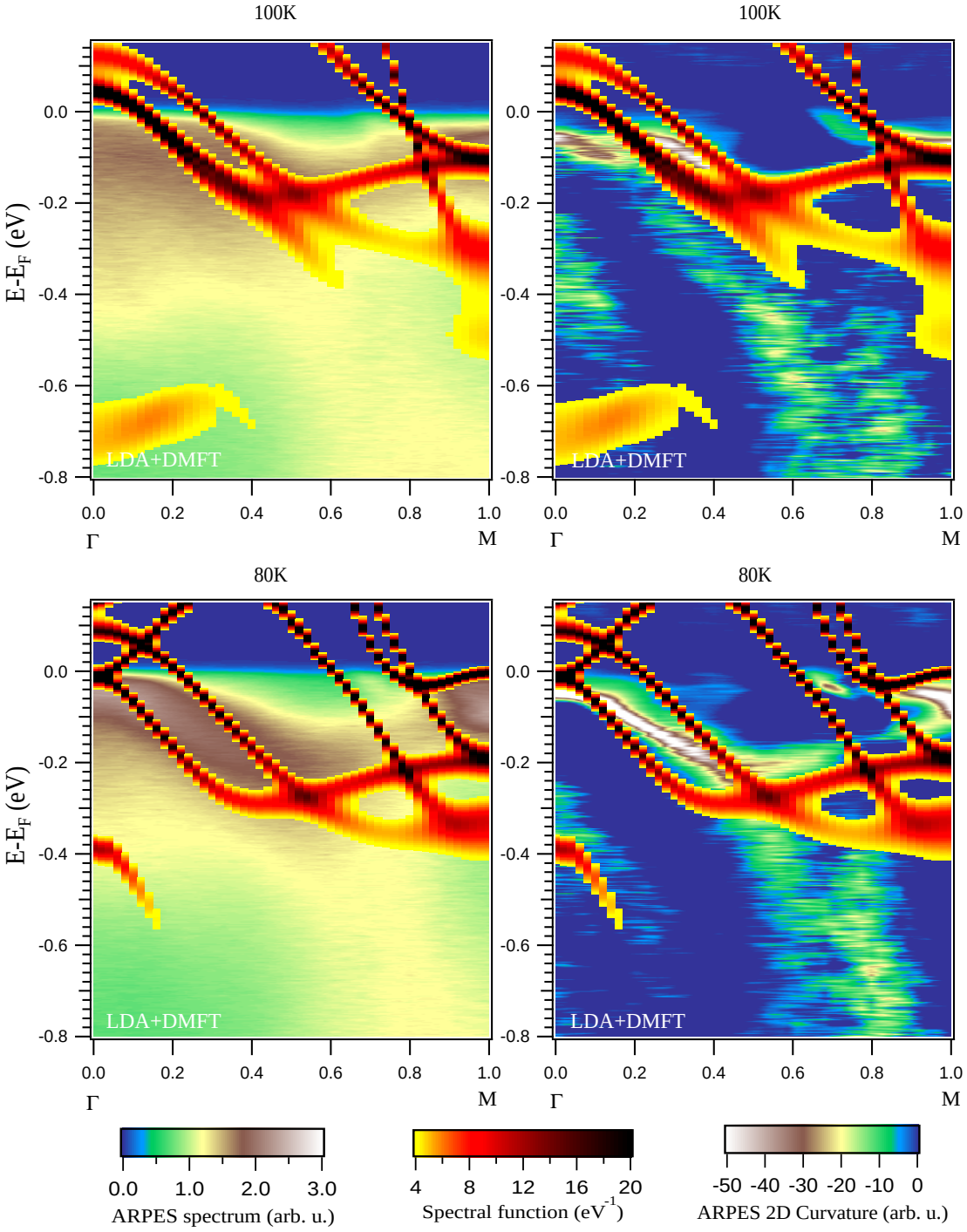

Figure 10.2.6: Comparison of LDA+DMFT spectral functions with ARPES spectra of $CaFe_2As_2$ in the tetragonal and collapsed tetragonal phases.
Left: bands extracted from the LDA+DMFT spectral function superposed on the ARPES spectra of $CaFe_2As_2$ in the tetragonal (100 K) and collapsed tetragonal (80 K) phases in the ΓM direction.
Right: bands extracted from the LDA+DMFT spectral function superposed on the 2D curvature of the ARPES spectra of $CaFe_2As_2$ in the tetragonal (100 K) and collapsed tetragonal (80 K) phases in the ΓM direction.

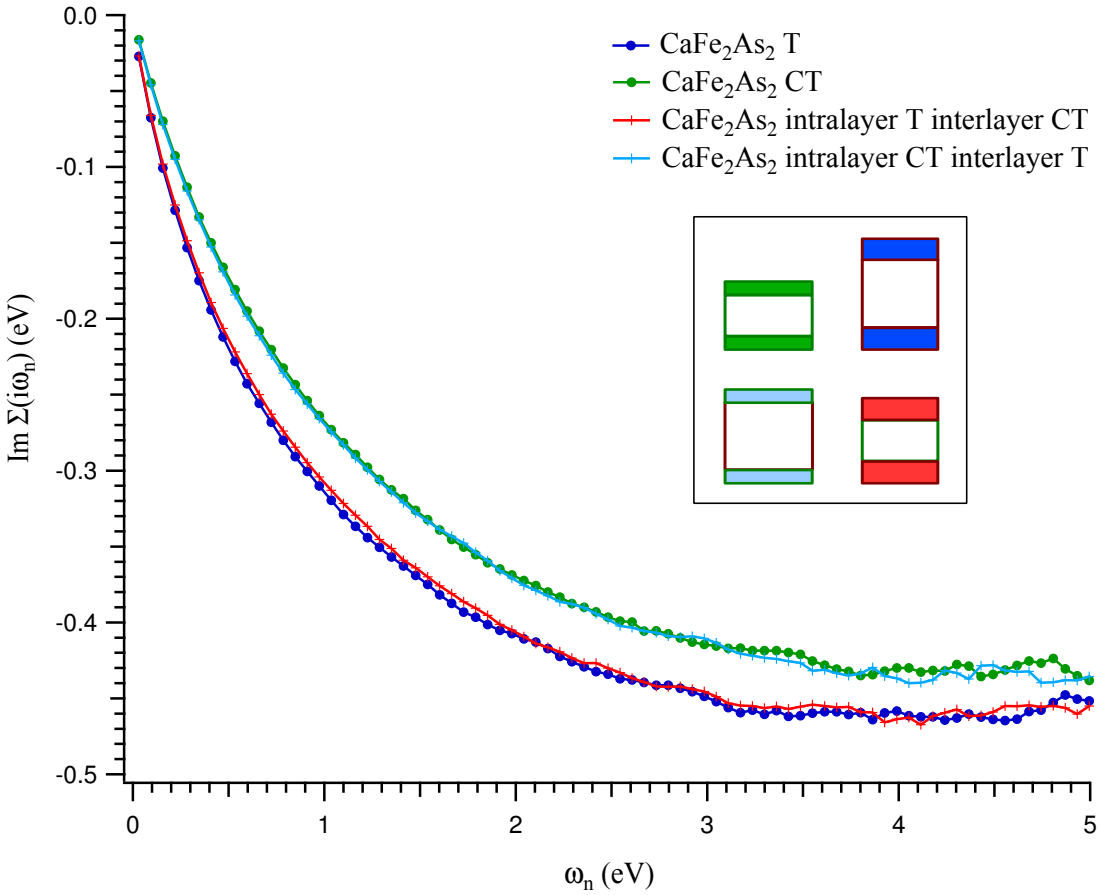

Figure 10.3.1: Imaginary part of the self energy in Matsubara frequencies of the d_{xy} orbital for $CaFe_2As_2$ in the tetragonal structure (T), collapsed tetragonal structure (CT) and in two chimeric structures mixing the interlayer (i.e. As-As interlayer distance) and intralayer (i.e. intralayer Fe and As angles and distances) of the tetragonal and collapsed tetragonal structures. The inset shows a schematic view of the different structures (colors correspond to the legend).

self-energy displays a more coherent behavior, which corresponds to the longer lifetime of quasiparticles displayed on Figure 10.2.6. Furthermore, the shape of the self-energy of the hybrid compounds depends on the structure of the FeAs layer, while it is nearly insensitive to the interlayer As-As distance. Naturally, in reality those two effects are linked with each other, since the deformation of the FeAs layer is caused by the formation of As-As bonds that make the c axis collapse. Still, this numerical experiment indicates that within LDA+DMFT the improvement of coherence properties is not due to the interlayer As-As bonding but to the increase of the Fe-As hybridization within one single layer.

10.4 Conclusion

At present, many questions have still to be solved and this conclusion should be taken with caution. In particular we do not obtain satisfactory agreement between the theoretical and experimental spectral functions. Still, our preliminary results support the picture that within DMFT, the collapsed tetragonal phase exhibits reduced correlations and higher coherence temperature due to the higher Fe-As hybridization, in agreement with other studies [Mandal *et al.* (2014), Diehl *et al.* (2014)]. However, it is unclear if such a reduction of correlations, that does not create a dramatic change in the electronic self-energy, can itself explain the behavior seen by resistivity measurements. This is confirmed by the ARPES results in the sense that the quasiparticles lifetimes away from the Γ point do not seem to be strongly impacted by the transition. Around the Γ point itself, it is difficult to make a statement since the electronic states found by photoemission appear more coherent but their dispersion has been largely reshaped by the collapse of the crystal. Furthermore, the reconstruction of the Fermi surface and of the low-energy electronic dispersion might also explain the modification of the resistivity via, e.g. the Fermi surface nesting. We should also mention the possible onset of phonons at this temperature range.

Chapter 11

Effective hole doping due to heterostructuring in $BaTi_2Fe_2As_4O$

In this chapter, in collaboration with the authors of [Ma et al. (2014)], we show that doping can be induced by electronic correlations in the iron-based superconductor $Ba_2Ti_2Fe_2As_4O$ (BTFAO, T_c ~ 21.5 K) due to the intercalation of metallic $BaTi_2As_2O$ layers. $Ba_2Ti_2Fe_2As_4O$ can be considered as a "heterostructure" of $BaFe_2As_2$ and $BaTi_2As_2O$. ARPES measurements performed and analyzed by Junzhang Ma, Pierre Richard, Hu Miao, Lingkun Zeng, Tian Qian and Hong Ding suggest that the low-energy band dispersions can be regarded as a superposition of the band structures of the FeAs and Ti_2As_2O layers. By counting the volumes of the Fermi surfaces, they find that about 0.25 electrons per unit cell are transferred from the FeAs layer to the Ti_2As_2O layer.

*Using the LDA+DMFT scheme described in Chapter 3, we identify electronic Coulomb correlations on the Fe-3*d *shell as the main cause for this self-doping effect. Our calculated spectral function is in good agreement with the experimental spectra. We find that the strength of correlations and the number of electrons in the Fe-3*d *orbitals is similar in $Ba_2Ti_2Fe_2As_4O$ and in optimally-doped $Ba_{0.6}K_{0.4}Fe_2As_2$. In passing, we benchmark the different possible choices for the double-counting term described in Section 3.3.*

11.1 Crystal structure and phase transition in $Ba_2Ti_2Fe_2As_4O$

$Ba_2Ti_2Fe_2As_4O$ can be regarded as a superlattice consisting of alternating stacking of $BaFe_2As_2$ and $BaTi_2As_2O$ layers (see Figure 11.2.1(a)) [Sun *et al.* (2012)]. A distinctive characteristic of $Ba_2Ti_2Fe_2As_4O$ is the metallic nature of the intercalated layers, which contributes to the density of states (DOS) at the Fermi level (E_F) [Jiang *et al.* (2012)]. We will focus on the high-temperature paramagnetic phase (T >125 K) [Sun *et al.* (2013)].

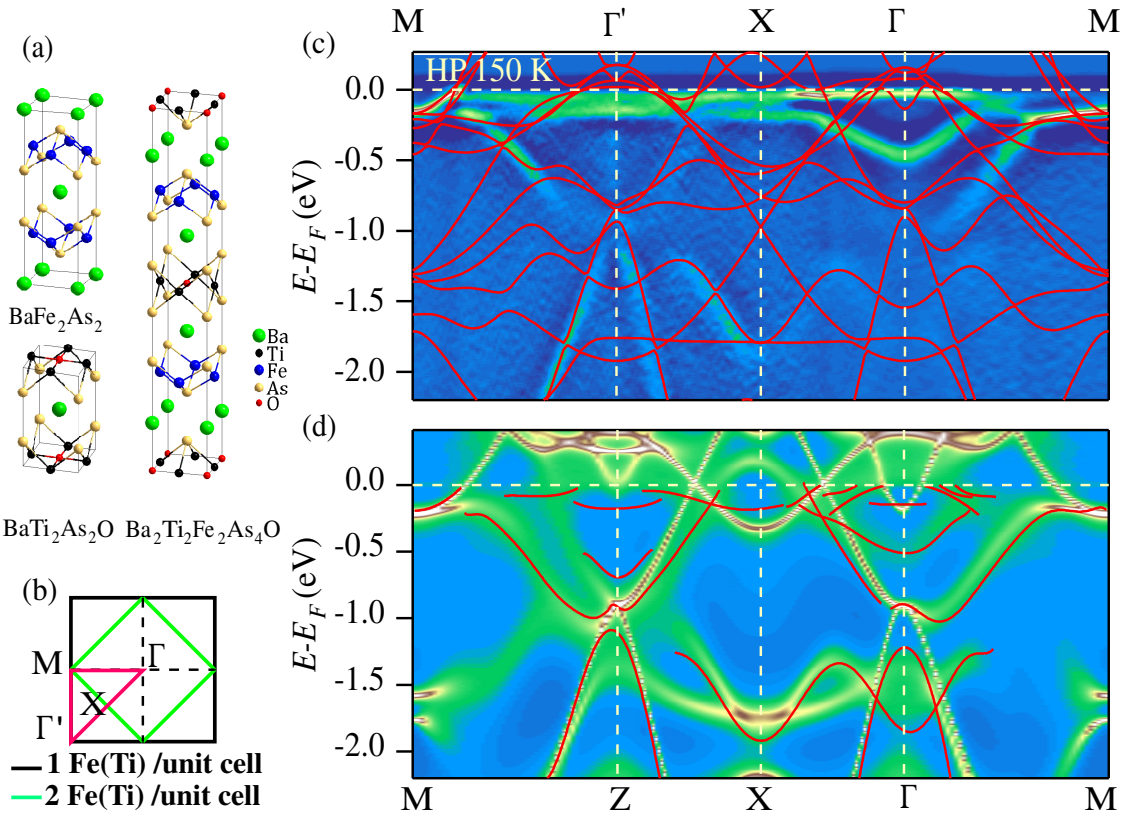

Figure 11.2.1: (a) Crystal structures of $BaFe_2As_2$, $BaTi_2As_2O$ and $Ba_2Ti_2Fe_2As_4O$. (b) Schematic Brillouin zones for one and two Fe (Ti) per unit cell. Red lines indicate the measurement locations in panel (c). (c) Two-dimension (2D) curvature intensity plot [Zhang *et al.* (2011a)] of the ARPES data along M-Γ'-X-Γ-M recorded at 150 K and photon energy $h\nu$ = 55 eV with Horizontal Polarization. The LDA bands are also plotted without renormalization for comparison. (d) Momentum-resolved spectral function calculated within LDA+DMFT at T = 145 K. Red curves represent the extracted experimental band dispersions.

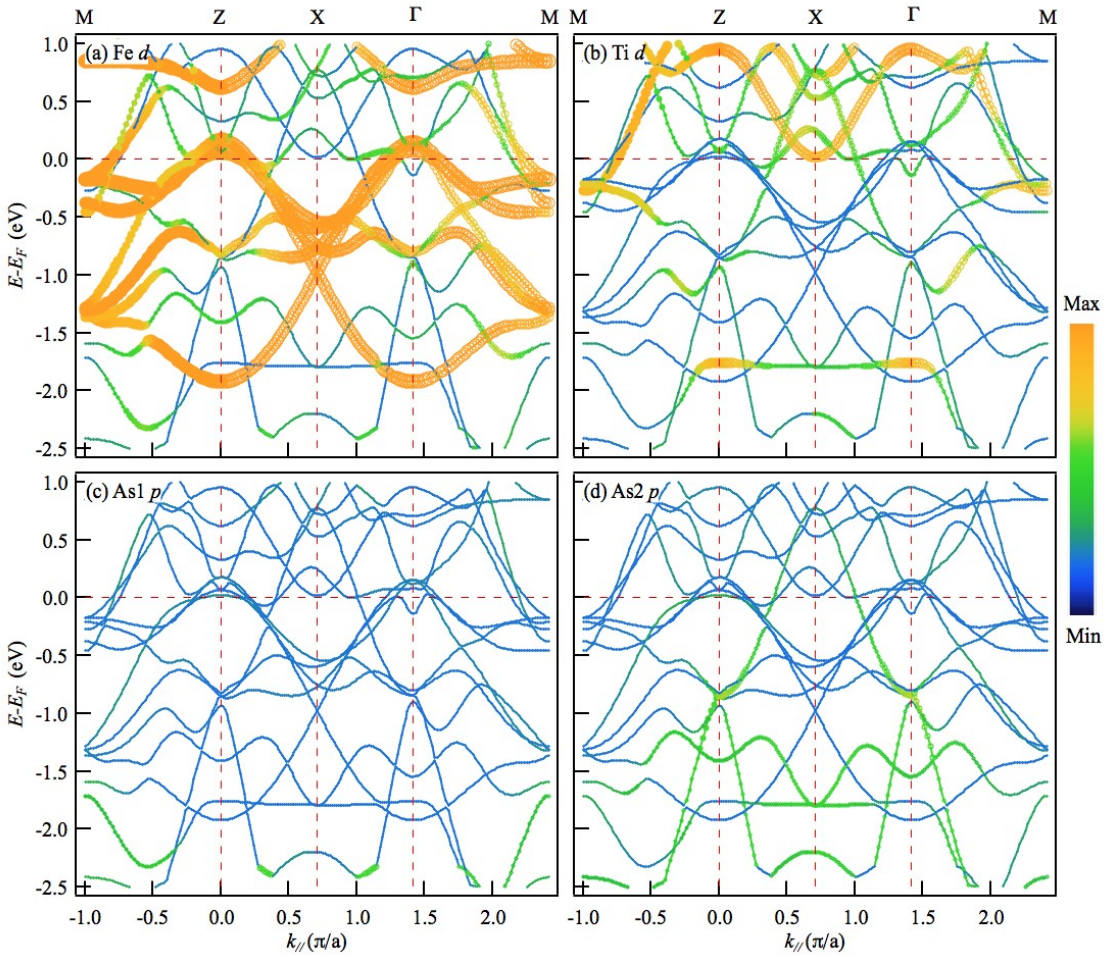

Figure 11.2.2: (a)-(d) Contributions of the Fe 3*d*, Ti 3*d*, As1 4*p* in the FeAs layers, and As2 4*p* in the Ti_2As_2O layers to the LDA calculated band structure of $Ba_2Ti_2Fe_2As_4O$, respectively. The contribution is represented by both the symbol size and the color scale.

11.2 ARPES measurements compared with LDA+DMFT spectral function

11.2.1 Comparison with LDA

Figure 11.2.1(c) shows the experimental band dispersions along the high-symmetry lines M-Γ'-X-Γ-M in an energy range within 2.2 eV below E_F (because of the nearly bidimensional nature of the compound we equivalently note Γ' the Z point). The band dispersions are much more complex than those of other iron pnictides due to the contribution of the Ti_2As_2O metallic layers. To understand the multiband electronic structure, we calculate the Kohn-Sham band structure of density functional theory within local density approximation (LDA), using the experimental crystal structure of [Sun *et al.* (2012)], and plot it on top of the experimental data in Figure 11.2.1(c). Figure 11.2.2 displays the different atomic characters of the calculated bands. The experimental band dispersions below -1 eV match well the LDA bands, which are mainly derived from As 4*p* of the Ti_2As_2O layers. In contrast, obvious discrepancies between the experimental results and the LDA calculations are observed within 1 eV below E_F, where the density of states is mainly of Fe 3*d* and Ti 3*d* characters. The deviation can be qualitatively attributed to non-negligible correlation effects between the 3*d* electrons, where the self-energy leads to strong band renormalizations near E_F, as observed in other iron pnictides.

11.2.2 Comparison with LDA+DMFT with static interactions

To analyze the effects of Coulomb correlations on the electronic structure, we have performed LDA+DMFT calculations of the momentum-resolved spectral function with a static interaction, starting from the above Kohn-Sham band structure. Since our target compound contains two different atomic species with partially filled narrow *d*-shells, we have generalized the usual LDA + DMFT scheme to include effective local Coulomb interactions on both the Fe-3*d* and the Ti-3*d* shells. We use U = 2.64 eV [3.50 eV] and J = 0.96 eV [0.74 eV] for the Hubbard interactions (monopole Slater integral F^0 and Hund's coupling on Fe [Ti]), and the multi-orbital around mean field double counting described in Section 3.3.5. The Hubbard interactions have been calculated by constrained-RPA in the separated compounds $BaFe_2As_2$ and $BaTi_2As_2O$ with the same distances and angles between atoms as in $Ba_2Ti_2Fe_2As_4O$, and using the shell-folding procedure described in Section 3.4.5. The resulting 10-orbital many-body problem was solved within a continuous-time Quantum Monte Carlo scheme, as implemented in the TRIQS suite [Ferrero and Parcollet(2011)]. The corresponding results are presented in Figure 11.2.1(d), which reproduces well the experimental band dispersions. The Fe 3*d* derived bands are strongly renormalized compared with the LDA results and their spectral intensities are very diffuse due to a large quasiparticle broadening encoded in the imaginary part of the DMFT self-energy.

11.2.3 Effect of double-counting

$Ba_2Ti_2Fe_2As_4O$ presents two very unique features that allows us to benchmark the different possible choices for double counting. First, there are two correlated shells (Fe 3*d* and Ti 3*d*) that interact with each other, making the DMFT calculation very sensitive to small changes in the double-counting expression that will shift the energy levels of those two shells with respect to each other, and thus change the hybridization. Second, the photoemission data of Figure

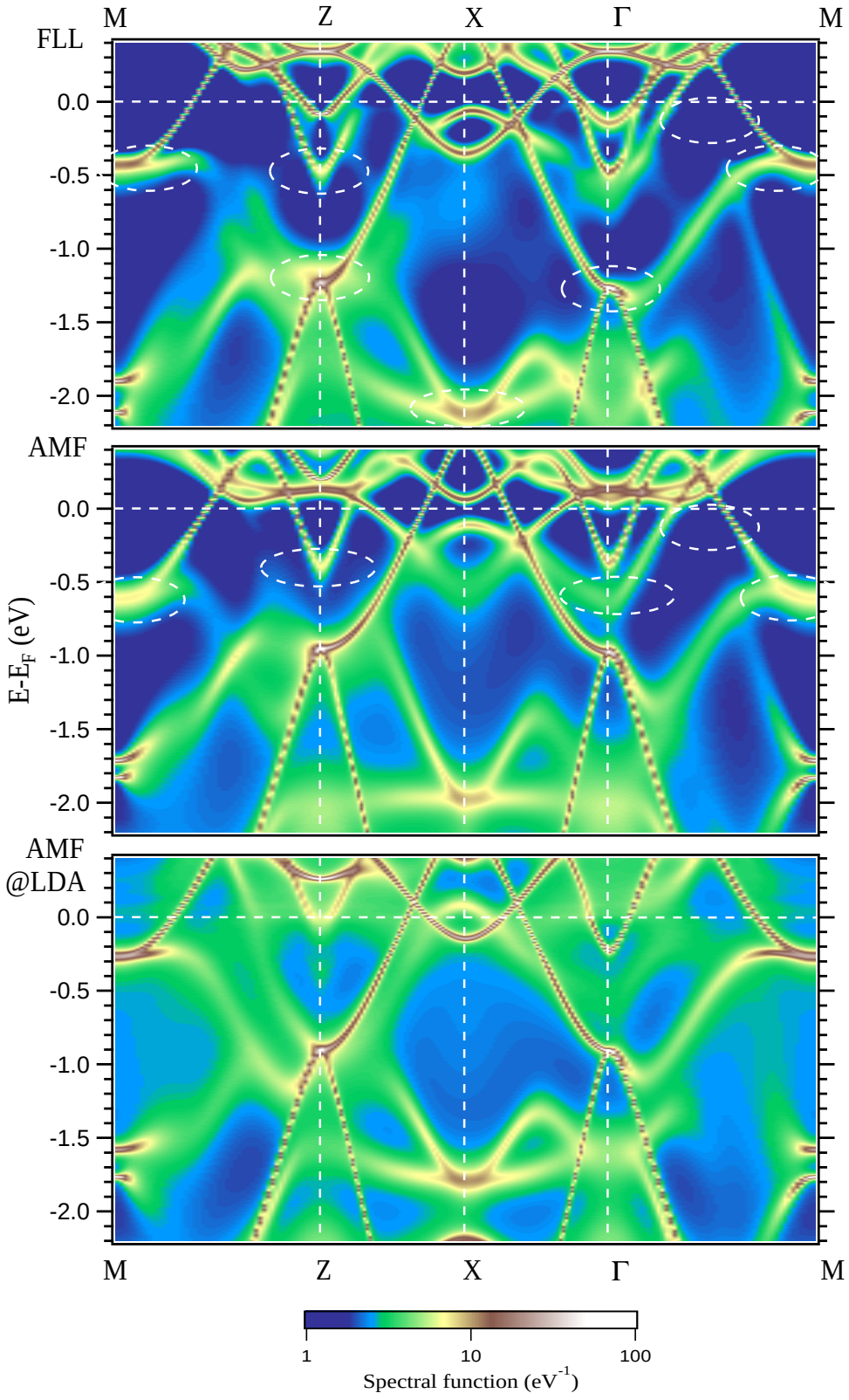

Figure 11.2.3: Spectral functions obtained with other possible choices for the LDA+DMFT double-counting term. Top: Fully Localized Limit double-counting using the DMFT electron count. Middle: Around Mean Field double-counting using the DMFT electron count and without orbital dependence. White ellipses indicate clear discrepancies with the photoemission data of Figure 11.2.1(c). Bottom: Around Mean Field double-counting using the LDA electron count and without orbital dependence.

11.2.1(c) captures clearly the position of the arsenic bands from the Ti_2As_2O layer. This position depends mainly on the values of the double-counting terms and of the chemical potential, and the fact that our multi-orbital AMF double-counting calculation predicts it correctly is a good indication that it describes well the physics of the system.

We have performed LDA+DMFT computations at T = 400 K using more usual double-counting terms, that is to say the Fully Localized Limit and Around Mean Field double-counting without orbital dependence (see Section 3.3 for details). Moreover, the mean number of electrons used in the calculation of the double-counting is taken from the solution of the impurity problem and enters the self-consistency loop, while in Figure 11.2.1(d) it is taken from the LDA solution as in Section 3.3.5. Figure 11.2.3 displays the momentum-resolved spectral functions obtained with these traditional choices for the double-counting term (top and middle panels). Several features – pointed out by white ellipses – are in contradiction with the experimental spectrum. In both calculations, the position of the Ti 3*d* electron pocket at the M point is too deep by 0.2 to 0.4 eV. They also predict a very coherent feature at the Z point around -0.5 eV, which is not observed in the spectrum. Finally, much of the washed out spectral weight from the Fe 3*d* electrons around the Fermi level is missing, and in the fully-localized limit calculation the arsenic bands are clearly too deep, especially around the X point. In overall, we can see that the number of Ti 3*d* electrons is overestimated in both calculations. Indeed, a small transfer of electrons from the Fe shell to the Ti shell will increase the Hartree energy in the Ti double-counting and decrease it in the Fe double-counting. If one uses the electron count from DMFT, the result is that the Ti energy levels are artificially lowered with respect to the Fe levels in order to keep the value of the Hartree energy calculated by LDA. In our one-shot procedure this is clearly not reasonable since the modification of the distribution of electrons between the two correlated shells will modify the density and thus the Hartree energy. It causes an even larger electron transfer that will keep feeding this phenomenon. Eventually, using the LDA electron count as in the spectral function of Figure 11.2.1 or of the bottom panel of Figure 11.2.3 gives a much better description of this compound. On the other hand, we can see that in this compound the spectral function does not really depend on the fact that we use or not an orbital-dependent double-counting.

11.3 Distribution of electrons between Fe and Ti layers

11.3.1 Fermi surface from ARPES measurements

To clarify the effects on the low-energy electronic states of the FeAs layers, we show the band dispersions near E_F in Figures 11.3.1 and 11.3.2. All the cuts are parallel to the ΓM direction, as schematically plotted in panel (f). ARPES measurements identify three hole-like bands near Γ (panels (a) and (b)), one hole-like band near X (panel (c)) and two electron-like bands near M (panels (d) and (e)), which cross E_F. The band dispersions can be regarded as a superposition of the band structures of the FeAs and Ti_2As_2O layers. Junzhang Ma and coauthors assign the three hole-like bands near Γ (panels (a) and (b)) and the shallow electron-like bands near M (panel (d)) to the Fe 3*d* orbitals, while the hole-like band near X (panel (c)) and the deep electron-like band near M (panel (e)) are attributed to the Ti 3*d* orbitals. The Fe-3*d* related band structure resembles those of other iron pnictides, which usually display two electron-like bands from Fe 3*d* near M. Only one electron-like band from Fe 3*d* is observed in their experiments (panel (d)), while another one from Fe 3*d* is not identified, most likely due to its extremely low spectral weight as it is folded from the adjacent M due to inequivalent As sites around Fe [Lin

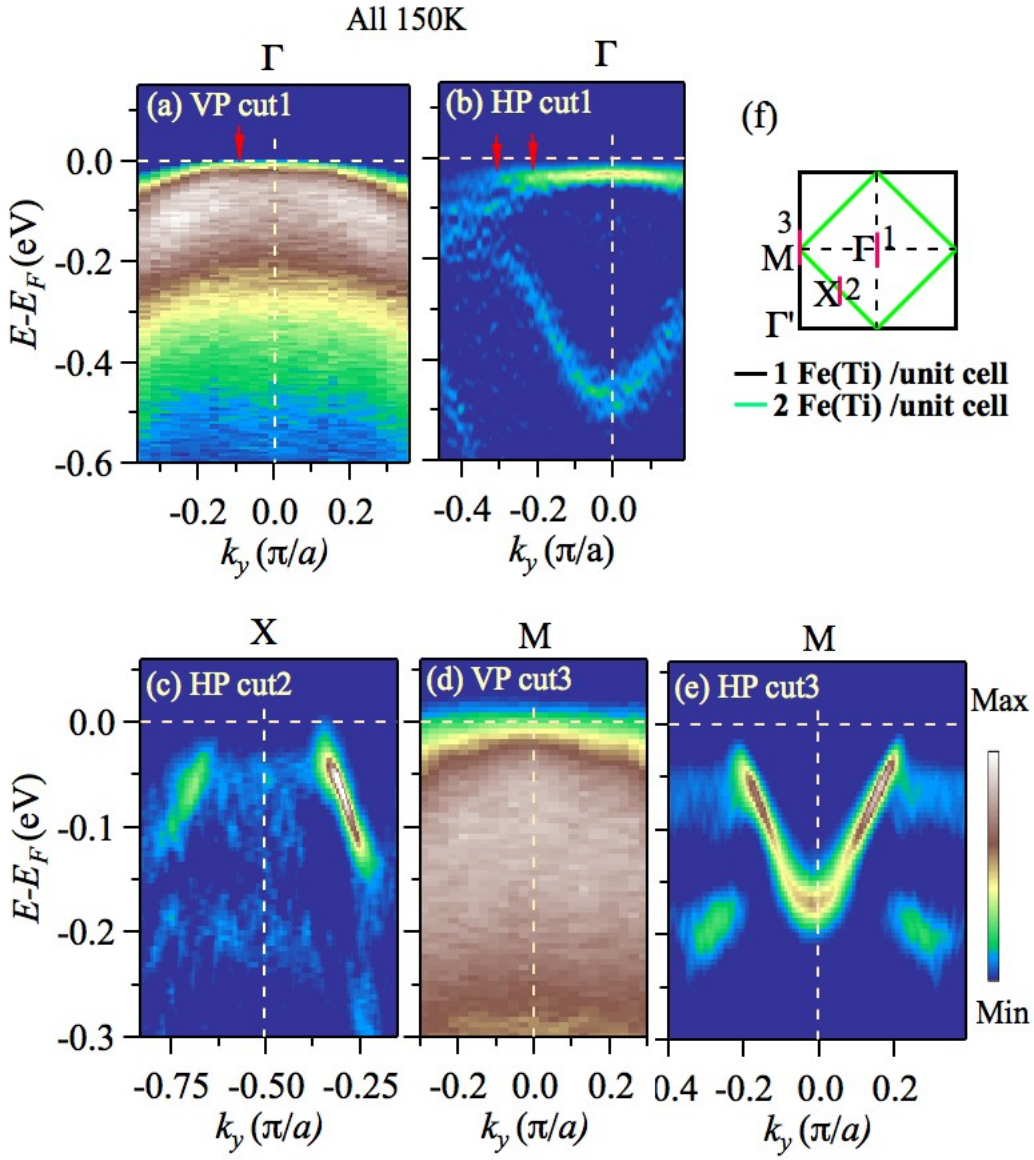

Figure 11.3.1: (a)-(e) ARPES data near the Fermi level recorded at hν = 55 eV and T = 150K. The momentum locations are indicated as red vertical lines in panel (f). In panels (b), (c) and (e) we plot the 2D curvature intensity plots, while in panel (a) and (d) the low coherence of the Fe 3*d* quasiparticles does not allow to extract it clearly at this temperature.

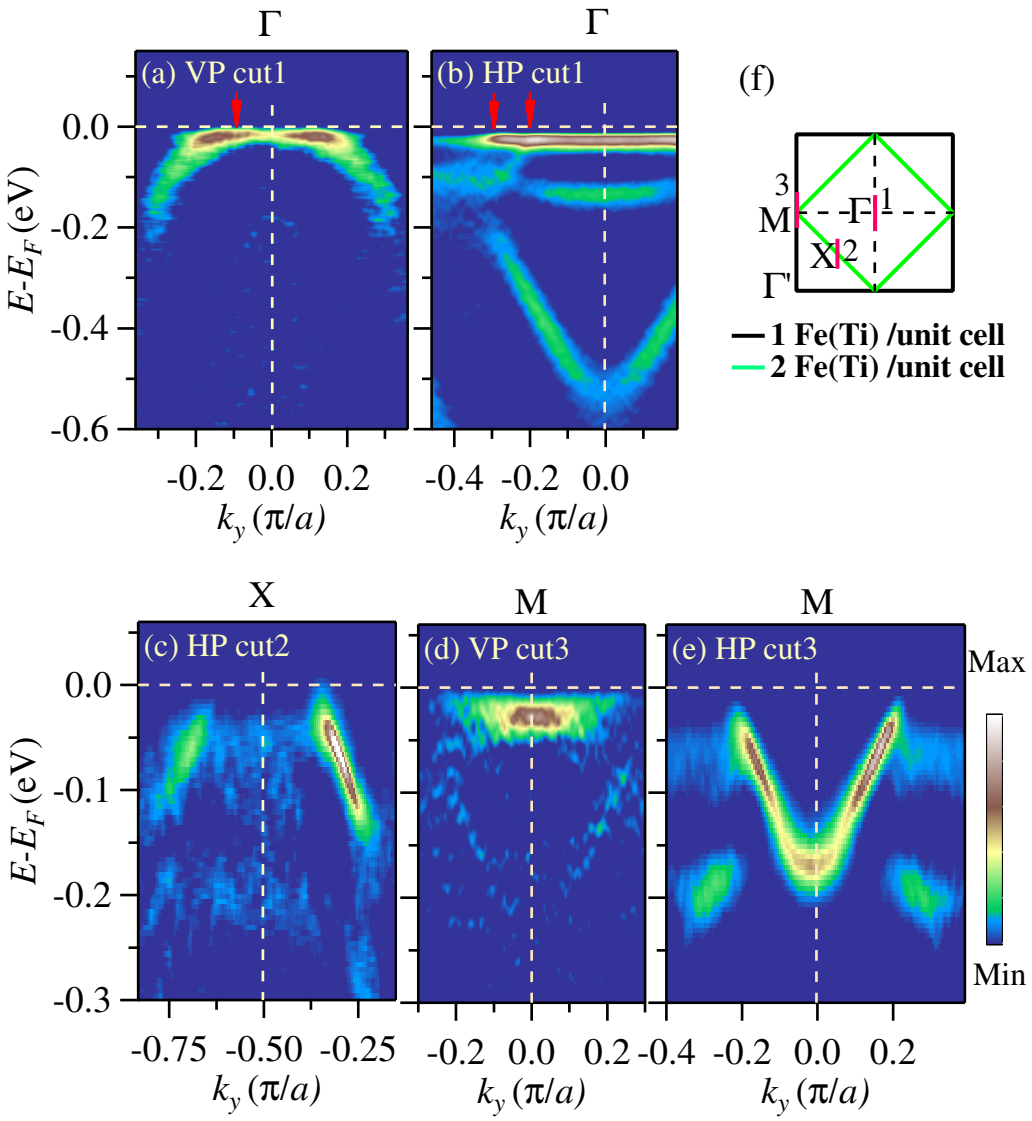

Figure 11.3.2: (a)-(e) 2D curvature intensity plots of the near-E_F ARPES data recorded at hν = 55 eV. The momentum locations are indicated as red vertical lines in panel (f). To illustrate the Fe-3d related band dispersions more clearly, the data taken at 30 K are shown in panels (a), (b) and (d). As the Ti-3d related band dispersions are dramatically changed across the transition at 125 K, the data taken at 150 K are shown in panels (c) and (e).

et al. (2011), Brouet *et al.* (2012)]. The Ti-3*d* related band structure is also similar to that of $BaTi_2As_2O$ [Xu *et al.* (2014)]. In $BaTi_2As_2O$, there are one electron-like band near Γ, one hole-like band near X and one electron-like band near M, which cross E_F. Junzhang Ma and coauthors do observe one electron-like band with a bottom of -0.5 eV at Γ (panel (b)) and their photon energy dependence measurements suggest it to originate mainly from Ti 3*d* states (see Figure 11.3.3), in agreement with the observation in $BaTi_2As_2O$ [Xu *et al.* (2014)]. The spectral intensity of this band is smeared out as dispersing towards E_F, and its wave vector is estimated to be close to 0.4 π/a along ΓM by extrapolating the band dispersion to E_F.

As seen in Figure 11.3.3 (panels (a) to (c)), the Fermi surface near the Brillouin zone center exhibits an obvious warping with a period of $2\pi/c'$, suggesting that the ARPES data reflect the bulk electronic structure. This Fermi surface is assigned to the hole-like Fe $3d_{xz+yz}$ band. This indicates that the interlayer coupling between the adjacent FeAs layers is not negligible, which can be attributed to the metallic nature of the intercalated $BaTi_2As_2O$ layer. In panel (d), the spectrum at the Brillouin zone center has two structures, which correspond to the shallow flat band and the bottom of the deep band, respectively, in panels (e) and (f). The spectral intensities of these shallow and deep bands are strongly suppressed at $h\nu$ = 53 eV and 34 eV, respectively, corresponding to the Fe 3*p*-3*d* and Ti 3*p*-3*d* antiresonances, respectively [Ding *et al.* (2011)].

With the identification of the near-E_F bands, Junzhang Ma and coauthors extract the corresponding Fermi surfaces and summarize them in Figure 11.3.4(c). The extracted Fermi surfaces related to the Fe 3*d* orbitals resemble those of other iron pnictides, indicating that the Fermi surface topology of the FeAs layers is not changed by the intercalated Ti_2As_2O layers. One prominent feature of the Fe-related Fermi surfaces is that the total enclosed area of the hole pockets near Γ is much larger than that of the electron pockets near M. The k_z dependent measurements suggest that the electronic structure of BTFAO is quasi-2D (see Figure 11.3.3). By counting the Luttinger volume of 2D Fermi surface sheets and assuming a purely 2D Fermi surface, they obtain a hole doping of ~ 0.25 per Fe site. The Fe-related Fermi surfaces look similar to those of the optimally-doped $Ba_{0.6}K_{0.4}Fe_2As_2$ with a hole doping of 0.2 per Fe site, as shown in Figure 11.3.4(d)[1]. By counting the volumes of the Ti-related Fermi surfaces sheets, they obtain an electron doping of ~ 0.25 per Ti site. Both the k_z and temperature dependent ARPES results reflect bulk features (see Figure 11.3.3), thus excluding the possibility of charge polarization on the surface. Therefore, the most significant effect of the intercalation of metallic $BaTi_2As_2O$ layers is that electrons are transferred from the FeAs layer to the Ti_2As_2O layer.

11.3.2 Electron count from dynamical mean-field theory

We analyze the electron transfer from Fe to Ti by comparing LDA and LDA+DMFT calculations for $Ba_2Ti_2Fe_2As_4O$ with the experimental crystal structure, $BaFe_2As_2$, $Ba_{0.63}K_{0.37}Fe_2As_2$ and the compounds derived by splitting BTFAO into $BaTi_2As_2O$ and $BaFe_2As_2$ while keeping the same distance and angle between atoms within one layer. We construct Wannier functions within the same window [-8.16 eV, 8.16 eV] for all the compounds and extract the number of electrons and the orbital-resolved electron counts for Fe-*d* and Ti-*d*, which are displayed on Table 11.3.1. For $Ba_{0.63}K_{0.37}Fe_2As_2$ we have taken the band structure of $BaFe_2As_2$ with the experimental crystal structure of optimally doped $BaFe_2As_2$ and calculated the chemical potential such as to obtain the correct total number of electrons. The number of electrons in the different orbitals of BTFAO obtained from LDA is independent of the particular stacking structure of this material, as we

[1] The inner hole pockets being almost doubly-degenerate at k_z ~ 0 for $Ba_{0.6}K_{0.4}Fe_2As_2$.

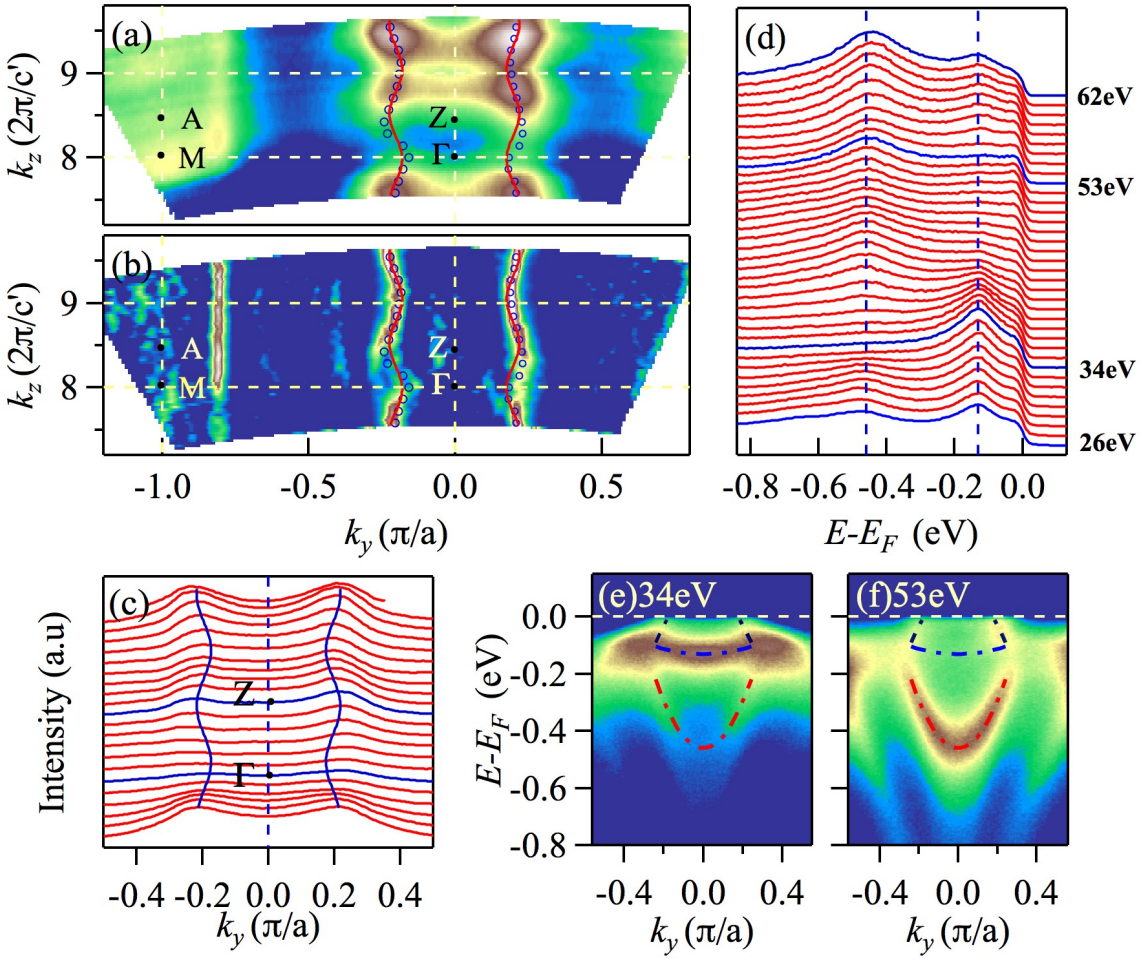

Figure 11.3.3: (a) ARPES intensity plot in the $k_y - k_z$ plane recorded at 25 K with different photon energies from 35 to 60 eV with horizontal polarization. The intensity is obtained by integrating the spectra within ±10 meV with respect to E_F. An inner potential of 14 eV is used to obtain k_z. $c' = c/2$, where c represents the lattice parameter perpendicular to the FeAs plane. (b) Curvature intensity plot of the ARPES intensity in panel (a). (c) Corresponding momentum distribution curves (MDCs) at E_F with different k_z. (d) Valence band spectra at the Brillouin zone center recorded with different photon energies from 26 to 62 eV. (e) and (f) ARPES intensity plots at $k_x = 0$ recorded with 34 and 53 eV photons, respectively.

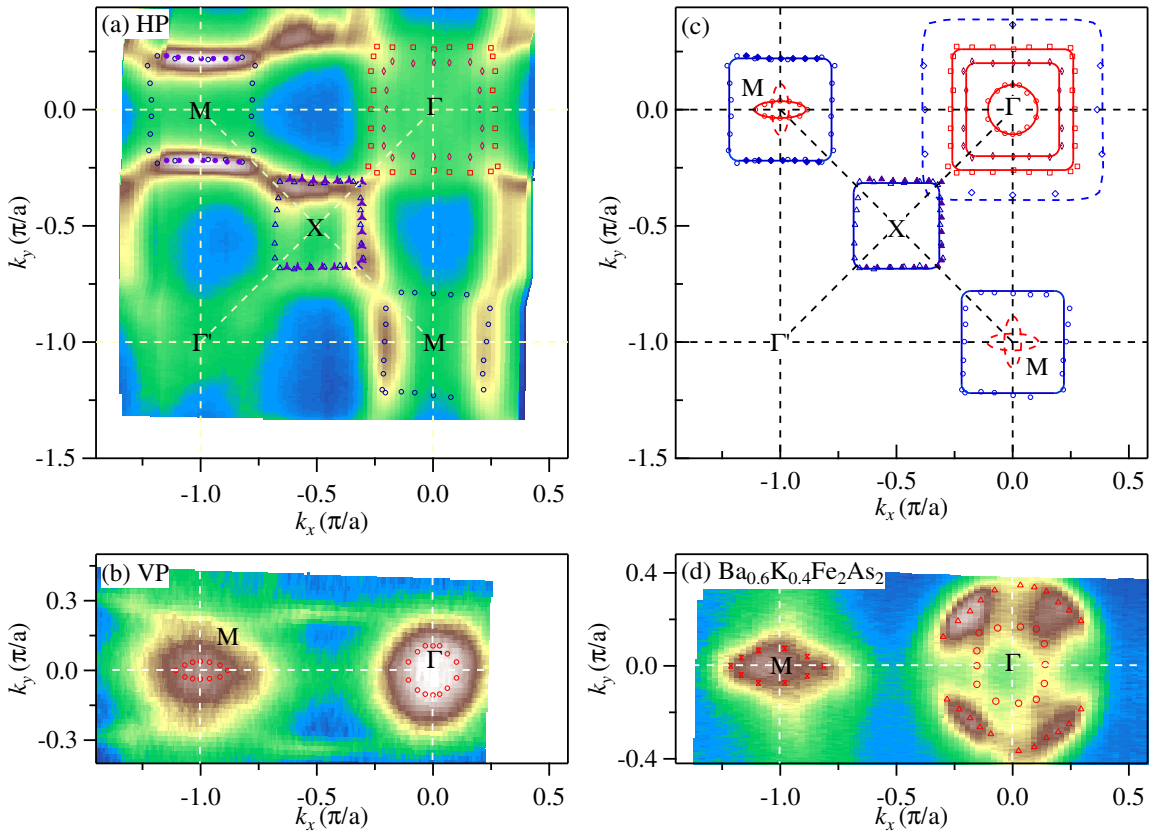

Figure 11.3.4: (a) Fermi surface intensity plot of $Ba_2Ti_2Fe_2As_4O$ recorded at 150 K and $h\nu$ = 55 eV with horizontal polarization. The intensity is obtained by integrating the spectra within ± 10 meV with respect to the Fermi level. a represents the nearest neighbor Fe(Ti)-Fe(Ti) distance. (b) Same as (a) but taken with vertical polarization. (c) Extracted Fermi surfaces of $Ba_2Ti_2Fe_2As_4O$. Red and blue symbols represent the extracted k_F points related to the FeAs and Ti_2As_2O layers, respectively. Solid and hollow symbols are extracted from the data taken at 150 K and 30 K, respectively. Solid curves are guides for eyes. (d) Fermi surface intensity plot of $Ba_{0.6}K_{0.4}Fe_2As_2$ recorded with the He Iα resonance line ($h\nu$ = 21.218 eV).

Table 11.3.1: Orbital-resolved electron count in Wannier functions calculated by LDA+DMFT (LDA) for $Ba_2Ti_2Fe_2As_4O$ (1st column), $BaFe_2As_2$ with the same structure than in BTFAO (2nd column), $BaTi_2As_2O$ with the same structure than in BTFAO (3rd column), $BaFe_2As_2$ (4th column) and optimally doped $BaFe_2As_2$ (5th column).

Orbital	$Ba_2Ti_2Fe_2As_4O$	$BaFe_2As_2$ @BTFAO	$BaTi_2As_2O$ @BTFAO	$BaFe_2As_2$	$Ba_{0.63}K_{0.37}Fe_2As_2$
Fe d_{z^2}	1.30 (1.41)	1.33 (1.42)		1.35 (1.43)	1.30 (1.43)
Fe $d_{x^2-y^2}$	1.33 (1.23)	1.34 (1.23)		1.32 (1.25)	1.32 (1.25)
Fe d_{xy}	1.20 (1.40)	1.23 (1.40)		1.26 (1.40)	1.20 (1.33)
Fe d_{xz+yz}	1.27 (1.35)	1.30 (1.34)		1.32 (1.34)	1.27 (1.29)
Total Fe d	6.38 (6.76)	6.50 (6.75)		6.56 (6.77)	6.36 (6.61)
Ti d_{z^2}	0.46 (0.43)		0.41 (0.42)		
Ti $d_{x^2-y^2}$	0.39 (0.39)		0.38 (0.38)		
Ti d_{xy}	0.63 (0.69)		0.60 (0.69)		
Ti d_{xz}	0.36 (0.15)		0.33 (0.15)		
Ti d_{yz}	0.45 (0.45)		0.48 (0.45)		
Total Ti d	2.29 (2.09)		2.20 (2.09)		

can see by comparing the calculation on BTFAO to calculations on $BaFe_2As_2$ and $BaTi_2As_2O$ crystals.

Two effects are contributing to the global hole-doping of the Fe-d orbitals when going from $BaFe_2As_2$ to $Ba_2Ti_2Fe_2As_4O$. The effect of correlations in $BaFe_2As_2$ is to reduce the number of electrons in the correlated shell. If the Fe-As hybridization is weaker, electrons are more localized and this effect is enhanced. In BTFAO, the Fe-As distance is about 1% larger than in $BaFe_2As_2$, thus lowering the hybridization with As. The consequence can be seen by comparing the number of electrons in the Fe-*d* Wannier orbitals in $BaFe_2As_2$ in the structure of BTFAO to $BaFe_2As_2$ in the experimental crystal structure: there is already a loss of 0.05 electrons per Fe in BTFAO. The second effect is a transfer of electrons from Fe to Ti due to correlations. In $BaTi_2As_2O$, correlations tend to increase the number of electrons in the Ti-*d* orbitals. This effect is enhanced when $BaTi_2As_2O$ and $BaFe_2As_2$ are put together, leading to a transfer of about 0.1 electrons from Fe to Ti. That transfer happens notably (but not exclusively) through the Fe-d_{z^2} – Ti-d_{z^2} hybridization, as Ti and Fe are on top of each other. We stress that the band with bottom around -0.5 eV at the Γ point is of mixed Ti d_{z^2} and Fe d_{z^2} characters, and wrongly predicted by LDA while correctly captured by our two-correlated shells LDA+DMFT.

The interlayer charge transfer creates an effective hole-doping of the Fe orbitals which places the compound in the regime of strong doping and temperature-dependent coherence properties induced by Hund's rule coupling (see [Werner *et al.* (2012)] and Chapter 9). As a result, the Fe-*d* states have a very low coherence scale and are observed by ARPES only close to the Fermi level – where the spectrum is still very broad. Figure 11.3.5 displays the many-body self-energies obtained within our DMFT calculations. In agreement with this previous discussion, we find qualitatively similar behavior for the Fe-3*d* states in $Ba_2Ti_2Fe_2As_4O$ and optimally hole-doped $BaFe_2As_2$, which are in a bad-coherence regime at the temperature of the calculation with very low lifetimes. In contrast, the Ti-3d states are in a Fermi-liquid regime with well defined quasi-particles. This corresponds very well to the ARPES spectra, in which

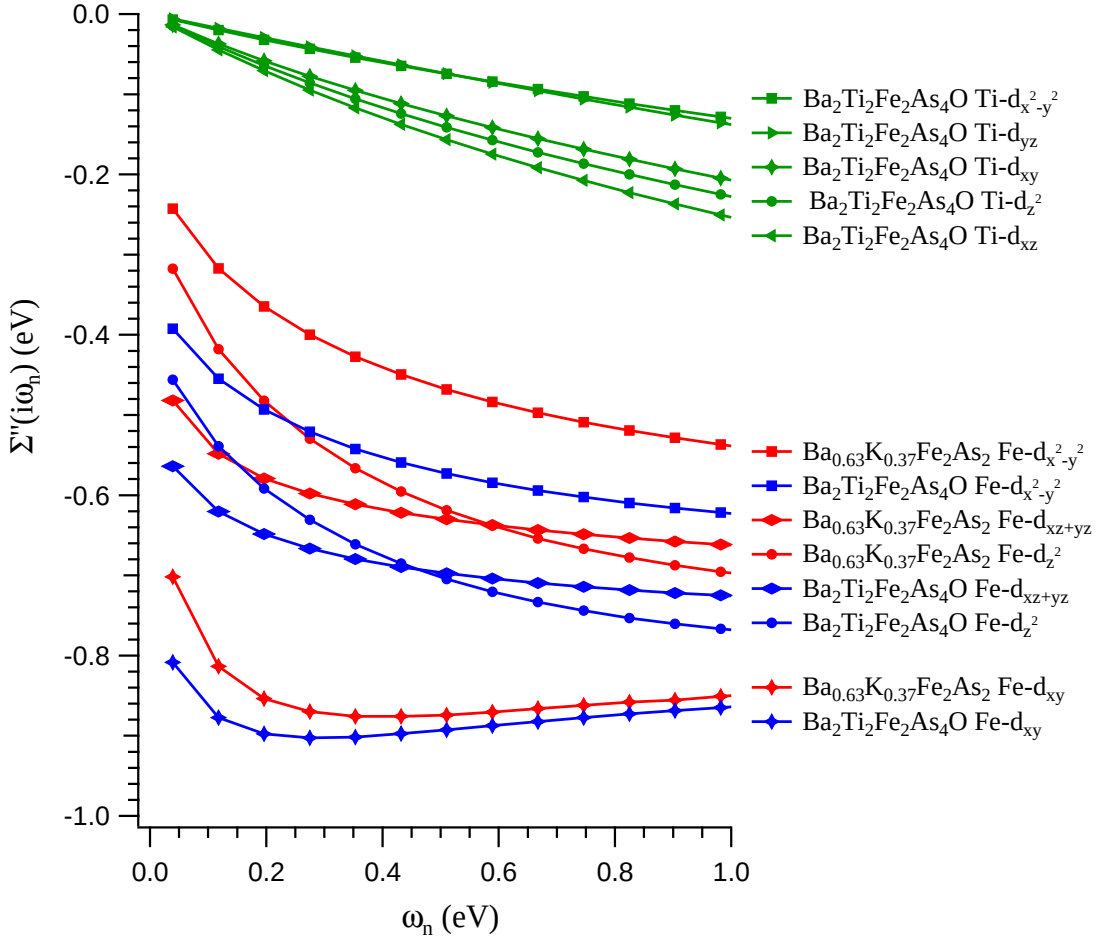

Figure 11.3.5: Imaginary part of the self-energy as a function of Matsubara frequencies from LDA+DMFT calculations of $Ba_2Ti_2Fe_2As_4O$ and optimally hole-doped $BaFe_2As_2$ at T = 150K.

the Ti bands are well observed up to -1 eV while the Fe bands are washed out.

11.3.3 Electron count in localized orbitals compared to the ARPES Fermi surface

We will now discuss the link between our findings and the Fermi surfaces captured by photoemission. Part of the diminution of the number of electrons in the Fe 3d localized orbitals with the onset of correlations comes from the reduced hybridization with the As ligand in the presence of correlations [Aichhorn *et al.* (2010)]. This kind of effect does not necessarily imply a modification of the Fermi surface, since it consists mostly in a reaffectation of orbitals characters of the bands below the Fermi level. We are able to quantify this reduction from our calculation of the number of electrons in $BaFe_2As_2$ with the crystal structure of $Ba_2Ti_2Fe_2As_4O$, and it is responsible for about 0.25 electron transfer per Fe (see Table 11.3.1). Indeed, the fact that the distribution of electrons in the different orbitals is the same for $BaFe_2As_2$ and $Ba_2Ti_2Fe_2As_4O$ in LDA reflects the fact that the Fe-As hybridization is similar in the construction of the localized orbitals. Moreover, we can see from the electron count of $Ba_{0.6}K_{0.4}Fe_2As_2$ that the electron transfer to As states is of the same magnitude even though this compounds is more correlated. As a consequence, the additional 0.12 electron transfer is mainly from Fe to Ti states, which

is confirmed by the fact that the Ti orbitals gain 0.09 electrons per Ti atom according to our calculations.

Since the Ti and Fe bands cross the Fermi level, this time the electron transfer will modify the Fermi surface. For instance, as we can see on Figure 11.2.1, at the M and X points the titanium electron pockets become larger than in LDA. To keep the neutrality of the compound, that implies that the iron Fermi surface will display larger hole pockets and smaller electron pockets, as in hole-doped $BaFe_2As_2$.

We stress that this effect is not due to the choice of the double-counting term. Our double-counting potential is kept constant, since it is calculated from the LDA electron count (see the discussion above). When electrons are transfered from Fe to Ti, the Hartree potential of the Hubbard model is reduced for Fe and increased for Ti. If one uses the electron count from DMFT, the result of the actualization of the double-counting is that the Fe energy level is pushed up with respect to the Ti one, increasing further the electron transfer. Our choice for double-counting actually quantitatively *limits* the electron transfer, and the spectral function we obtain is in much better agreement with the ARPES data – otherwise, the Ti electron pockets and As bands fall too far below the Fermi level, as shown on Figure 11.2.3.

11.4 Conclusion

In conclusion, the electronic structure of $Ba_2Ti_2Fe_2As_4O$ reveals a large charge transfer between the FeAs and intercalated Ti_2As_2O layers, which is identified as a consequence of electronic correlations in the 3*d* shells by our LDA+DMFT calculations. This provides an alternative route of effective doping without element substitution for the iron-based superconductors and thus without introducing disorder. Furthermore, our results prove the presence of strong interlayer coupling in $Ba_2Ti_2Fe_2As_4O$ arising from the Fe-d_{z^2} – Ti-d_{z^2} hybridization and the metallic nature of the intercalated Ti_2As_2O layer. These results and the technical choices we have presented may also have broader interest for the growing field of correlated oxides heterostructures.

Part VI

Conclusions

Chapter 12

Conclusions

In this thesis, we have studied the effects of many-body Coulomb interactions on the spectral properties of transition-metal pnictides. To this aim, we have pursued three main directions: the development of *ab-initio* techniques allowing to take into account the frequency-dependence of the Hubbard interactions, the computation of these interactions, and the analysis of the spectral properties of real materials. One of the main results is the development of a new method taking into account the non-local screened exchange in combination with Dynamical Mean Field Theory.

12.1 Methodological developments

We have proposed a new method including the Fock-like static screened exchange created by a Yukawa potential combined with Dynamical Mean Field Theory (DMFT). This allows us to get rid of the Local Density Approximation (LDA) exchange and correlation potential, which is not a well-controlled approximation. We have named this method SEX+DMFT, inspired by the so-called COHSEX approximation [Hedin(1965), Hedin(1999)] in which the self-energy is interpreted as a Coulomb hole plus screened exchange. This COHSEX self-energy is actually a static approximation to the GW self-energy, which itself corresponds to a first-order perturbation theory in the screened Coulomb interaction W. Thus, our SEX+DMFT method can also be understood as a simplified and extremely efficient version of the combined GW+DMFT method [Biermann *et al.* (2003)]. More precisely, it has been shown recently in the iron pnictides [Tomczak *et al.* (2012b)] and in the transition metal oxide $SrVO_3$ [Tomczak *et al.* (2014)] that the self-energy at the GW level can be roughly separated into a non-local static part and a local dynamical part at low-energy. The SEX+DMFT approximation then consists in interpreting the static term as screened-exchange and the dynamical term as correlations obtained within DMFT with a frequency-dependent Hubbard interaction $U(\omega)$.

The effects of the non-local screened exchange and of the high-frequency tail of the interaction are antagonistic: while the non-local exchange favors the delocalization of electrons and enlarges the bandwidth, the high-frequency tail reduces the hopping probability of correlated electrons and further localizes them. This is why it is important to take both into account. Moreover, to include the non-local term of the self-energy can be expected to give a better description of the low-energy properties of transition-metal pnictides, in particular of the Fermi surface. Furthermore and in contrast to perturbative schemes, we expect that this non-perturbative

SEX+DMFT method can be extended to regimes with arbitrarily strong correlations, making it a promising tool for probing the normal state of iron pnictides and chalcogenides superconductors.

In order to include the frequency-dependence of the Hubbard interaction in our *ab-initio* calculations, we have generalized the combination of DFT and DMFT described in [Aichhorn *et al.* (2009)] to dynamical interactions, using the dynamical solver implemented in the Toolbox for Research In Quantum Systems (TRIQS) [Ferrero and Parcollet(2011)]. Notably, we have proposed a new expression for the double-counting term, and participated in the development of an effective model which allows to take into account in an approximate way the intershell interaction between the atoms of ligand and metal – a procedure we call shell-folding [Seth *et al.* (2015)].

12.2 Dynamical Hubbard interactions in iron pnictides

We have presented a study of the frequency-dependent Coulomb interactions between different iron pnictide representatives of the 11, 111, 122 and 1111 families. The values of the Hubbard interactions have been computed using the constrained-random phase approximation (cRPA) approach using the recent implementation of [Vaugier *et al.* (2012b)]. Both Fe *d* and ligand As (and O in oxypnictides) *p* degrees of freedom were considered in the construction of the resulting parameter-free low-energy *dp-dp* Hamiltonian. An effective *d-dp* Hamiltonian where only the Fe-*d* orbitals are corrected by the Coulomb repulsion was then constructed via the shell-folding procedure.

In agreement with widespread ideas, we have found that the effective Coulomb interactions for Fe-3*d* shells, are larger in 11 chalcogenides than in 122 and 1111 pnictides, while the 111 are an intermediate case. The accuracy of an atomic-like parametrization of the two-index density-density interaction matrices has been further discussed. It is based on the calculation of an optimal set of three independent Slater integrals, assuming that the angular part of the Fe-*d* localized orbitals can be described within spherical harmonics as for isolated Fe atoms. We have found that this accuracy depends on the ligand-metal bonding character rather than on the dimensionality of the lattice: it is excellent for ionic-like Fe-Se (FeSe) chalcogenides and not as good for more covalent Fe-As (LaFeAsO, $BaFe_2As_2$) pnictides. This illustrates the differences in the sphericity of the Fe-3*d* Wannier orbitals and in the anisotropy of the screening. These results are very similar to the calculations performed in [Vaugier(2011)] in a *d-dp* model in which only the transitions from and to the *d*-like bands were cut within constrained-RPA.

We have also investigated the relative importance of the screening channels which reduce the on-site bare interaction to the fully screened one. We have shown that the screening channels are analogously structured in the pnictide and chalcogenide families, while this structure is very different in a benchmark oxide $SrVO_3$. The ligand channel does not appear to be responsible for the dominant screening effect in iron pnictides.

Finally, we have analyzed the frequency dependence of the interaction and its relation with the values of the free-electrons plasmon frequencies. We have shown that it cannot be simply modeled with a single plasmon, and that the effective model has a critical influence on the high-frequency tail and on the resulting bosonic renormalization of quasiparticle dispersions. Indeed, the spectral weight transfer due to plasmons excitations is reduced by about 20% in the shell-folded model compared to the *d-dp* model.

12.3 Spectral properties of iron pnictides

Eventually, we have calculated the spectral properties of $BaCo_2As_2$, $CaFe_2As_2$ and $Ba_2Ti_2Fe_2As_4O$ in the paramagnetic phase. For all three compounds, we have compared the obtained spectral functions with the angle-resolved photoemission spectroscopy (ARPES) experimental measurements (that we have taken in the case of $CaFe_2As_2$).

In $BaCo_2As_2$, this comparison shows that screened exchange combined with dynamical correlations (SEX+DMFT) provides an excellent description of the low-energy physics. Our study also indicates that $BaCo_2As_2$ is significantly less correlated than $BaFe_2As_2$, due to the larger filling of the *d* electron shell. Our results confirm the importance of local moments in the physics of the Fe-based superconductors, in agreement with [Werner *et al.* (2012)], and establish the *d*-shell filling as the most important tuning parameter for electronic correlations in the series of Mn, Fe, or Co pnictides.

We have presented preliminary results on the tetragonal to collapsed tetragonal transition in $CaFe_2As_2$. We have measured the Fermi surface and electronic dispersion for temperatures above and below the transition, which reveals a reorganization of the electronic states and a longer lifetime of the quasiparticles in the collapsed phase. Furthermore, we have performed LDA+DMFT calculations for $CaFe_2As_2$ in the tetragonal structure, collapsed tetragonal structure and in two chimeric structures mixing the interlayer and intralayer of the tetragonal and collapsed tetragonal structures. These calculations support the picture that within DMFT, the collapsed tetragonal phase exhibits reduced correlations and higher coherence temperature due to the higher Fe-As hybridization, in agreement with other studies [Mandal *et al.* (2014), Diehl *et al.* (2014)]. Yet, we do not obtain satisfactory agreement between the theoretical and experimental spectral functions and this conclusion should be taken with caution.

Finally, we have shown that doping can be induced by electronic correlations in the iron-based superconductor $Ba_2Ti_2Fe_2As_4O$ due to the intercalation of metallic $BaTi_2As_2O$ layers. Using LDA+DMFT calculations, we have identified electronic Coulomb correlations on the Fe-3*d* shell as the main cause for this self-doping effect. Indeed, we have found that the strength of correlations and the number of electrons in the Fe-3*d* orbitals is similar in $Ba_2Ti_2Fe_2As_4O$ and in optimally-doped $Ba_{0.6}K_{0.4}Fe_2As_2$. Because of the presence of two correlated shells, $Ba_2Ti_2Fe_2As_4O$ is an ideal benchmark compound for the different possible choices for the double-counting term. The spectral function calculated using an orbital-dependent around mean-field double-counting based on the LDA electron count, that we have proposed, was found in good agreement with the experimental spectra.

These three materials can all be considered as part of the 122 family of pnictides, for they crystallize in the $ThCr_2Si_2$-type crystal structure (*I4/mmm* space group). Because of the universality of the TM-As plane in the family of transition-metal pnictides, the conclusions presented above can be generalized, in particular:

- the control of the strength of correlations by the *d*-electron count
- the expression of the double-counting
- the tuning of coherence properties via the Fe-As hybridization
- and the importance of taking into account both the non-local screened exchange and the frequency-dependence of the Hubbard interactions to calculate the low-energy properties.

12.4 Future developments and perspectives

The development of our SEX+DMFT method has opened many questions. First of all, the relation between the screened-exchange based on the Thomas-Fermi screening length and the non-local GW self-energy has to be worked out. This point is crucial to know in which cases the SEX+DMFT method is reliable and to clarify the way of calculating the screening length. In particular, it should be kept in mind that the use of an orbital-independent screening length is probably unadapted for higher-energy degrees of freedom. Furthermore, the question of the level of self-consistency – for the calculation of the Thomas-Fermi screening length, of the ground-state density or of the Hubbard interactions – necessary to provide a good description of the low-energy properties is another fundamental issue. Additional investigations concerning the shell-folding procedure are also in order. Indeed, the construction of such an effective model is probably not adapted to all correlated materials. For instance, there should be a competition with the effects of the intersite Coulomb interaction.

At present, without even discussing the topic of superconductivity in iron pnictides, many issues concerning the normal state of these materials have still to be understood. In relation to what we have presented, a study of the spin-freezing phase within methods taking into account both the non-local exchange and the high-frequency tail of the Hubbard interaction in iron pnictides remains to be done from a quantitative point of view. Since these two effects have a strong impact on the low-energy properties of the self-energy, it appears necessary to consider them in order to identify precisely the temperature and doping range relevant to this exotic phase for a given material. An ARPES study of the evolution of the quasiparticle lifetimes with temperature or doping would also be a crucial step toward the understanding of the properties of transition metal pnictides in the paramagnetic state. In particular, it would help to discriminate between the effects of local electronic interactions and of the Fermi surface nesting that might impact other experimental probes such as resistivity or optical conductivity measurements.

Part VII

Appendices

Appendix A

Introduction to Green's functions

A.1 Green's functions of imaginary and real frequencies

To make things more formal, let us recall some definitions [Mahan(1990)]. We will focus on the finite temperature Green's functions, as real measurements are done at non-zero temperature and, practically speaking, because the corresponding Matsubara formalism is easier to handle than zero-temperature real time Green's functions. The Green's function in imaginary time is defined as:

$$G(k,\tau) = -<T_\tau C_k(\tau) C_k^\dagger(0)> = -Tr[e^{-\beta(K-\Omega)} T_\tau (e^{\tau K} C_k e^{-\tau K} C_k^\dagger)]$$

with $K = H - \mu N$ and $e^{-\beta\Omega}$ the normalization factor. Being antiperiodic of period β, this function can be expanded in a Fourier series with terms $G(k, i\omega_n)$, where ω_n are the Matsubara frequencies $\frac{(2n+1)\pi}{\beta}$.

In DMFT programs using Quantum Monte Carlo as the impurity solver, it is this imaginary frequency function that is computed. However, to evaluate physical quantities, usually we need real time (or equivalently real frequency) functions. In fact, those quantities often are retarded correlation functions, so we will define the retarded Green's function:

$$\begin{aligned} G_{ret}(k, t-t') &= -i\theta(t-t') < [C_k(t) C_k^\dagger(t') + C_k^\dagger(t') C_k(t)] > \\ &= -i\theta(t-t') Tr\{e^{-\beta(K-\Omega)} [C_k(t) C_k^\dagger(t') + C_k^\dagger(t') C_k(t)]\} \end{aligned}$$

How to pass from a Matsubara frequency function to a real frequency function? Formally, it is simple[1]: we just have to do an analytic continuation by changing every $i\omega_n$ to $\omega + i\delta$:

$$G(k, i\omega_n) \longleftrightarrow_{i\omega_n \longleftrightarrow \omega + i\delta} G_{ret}(k, \omega) \tag{A.1.1}$$

Both imaginary and real frequency functions verify Dyson's equations:

[1] However, when it comes to numerical analysis, it becomes more complex. In particular, two very different spectral functions can correspond to two nearly similar $G(\tau)$ [Tomczak(2007)]. The correspondence $G(\tau) \longrightarrow A(\omega)$ can be made using the maximum entropy algorithm [Jarrell and Gubernatic(1996)].

$$G(k, i\omega_n) = \frac{1}{i\omega_n - \epsilon_k - \Sigma(k, i\omega_n)} \quad (A.1.2)$$

$$G_{ret}(k, \omega) = \frac{1}{\omega + i\delta - \epsilon_k - \Sigma_{ret}(k, \omega)} \quad (A.1.3)$$

where we have made similarly the correspondence

$$\Sigma(k, i\omega_n) \longleftrightarrow_{i\omega_n \longleftrightarrow \omega + i\delta} \Sigma_{ret}(k, \omega) = Re\Sigma_{ret}(k, \omega) + iIm\Sigma_{ret}(k, \omega)$$

and defined the ϵ_k as the eigenvalues of an operator H_0 such that $H = H_0 + V$.

These equations thus define the self-energies Σ. We remark that they are equal to zero for an unperturbed system ($V = 0$).

A.2 Spectral density function

Let us suppose that we have a spectral function $A(k, \omega)$, which measures the probability that an electron of momentum k has energy ω [Mahan(1990)]. So, if there is only one energy associated to each momentum, such as for a free particle, $A(k_0, \omega) = \delta(\omega(k_0))$ (k_0 being fixed). However, in interacting systems, $A(k_0, \omega)$ often has a certain width. Still, by definition $A(k_0, \omega) \geq 0$ and

$$\int_{-\infty}^{+\infty} \frac{d\omega}{2\pi} A(k_0, \omega) = 1 \quad (A.2.1)$$

This probability allows us to compute physical quantities, as it codes the relation between momentum and energy. As a simple example, we can mention the total number of electrons with momentum k:

$$n_k = \int_{-\infty}^{+\infty} \frac{d\omega}{2\pi} n_F(\omega) A(k, \omega) \quad (A.2.2)$$

Summing $A(k, \omega)$ over momentum distribution gives the density of states of the interacting system, that is to say the density of electrons we can extract from the system by employing a certain energy.

Actually, this spectral function can be defined from the Green's function as:

$$A(k, \omega) = -2ImG_{ret}(k, \omega) \quad (A.2.3)$$

Symmetrically, we can also express Green's functions from that spectral function via Hilbert transforms:

$$G(k, i\omega) = \int_{-\infty}^{+\infty} \frac{d\omega'}{2\pi} \frac{A(k, \omega')}{i\omega - \omega'}$$

$$G_{ret}(k, \omega) = \int_{-\infty}^{+\infty} \frac{d\omega'}{2\pi} \frac{A(k, \omega')}{\omega - \omega' + i0^+ signe(\omega')}$$

Finally, here is a useful expression to understand the link between the self-energy and the spectral function:

$$A(k,\omega) = \frac{-2Im\Sigma_{ret}(k,\omega)}{[\omega - \epsilon_k - Re\Sigma_{ret}(k,\omega)]^2 + [Im\Sigma_{ret}(k,\omega)]^2} \tag{A.2.4}$$

A.3 ARPES data and other response functions

The density spectral function A is linked to ARPES data. Indeed, the photocurrent can be written [Damascelli(2004)]:

$$I(k,\omega) = I_0(k,\nu,\overrightarrow{A})A(k,\omega)f(\omega) * R(k,\omega) \tag{A.3.1}$$

R being the resolution function of our ARPES experiment, f the Fermi function, and I_0 depending on one-electron matrix elements.

From the Green's function of an interacting system, we can also define the self-energy Σ using the non-interacting Green's function G_0:

$$\Sigma(k,\omega) = G_0(k,\omega)^{-1} - G(k,\omega)$$

which allows us to compute the Fermi surface of a material by solving:

$$\mu - \epsilon_{k_F} - \Sigma(k_F,0) = 0$$

Finally, we can also calculate the response functions of a one-particle operator $O(R,\tau)$ (such as spin susceptibility or optical conductivity [Georges *et al.* (1996), Tomczak(2007)]), defined as:

$$\chi_O(q,i\omega_n) = \int_0^\beta d\tau e^{i\omega_n\tau} \sum_j e^{iqR_j} < O(R_j,\tau)O(0,0) > \tag{A.3.2}$$

Thus, we are able to predict much about the behavior of a solid only by knowing its Green's function, and we get not only information about the ground state – as is the case in DFT – but also about excitations, which makes the method so appealing.

Appendix B

Dynamical interactions

B.1 Lang-Firsov transformation of the Hubbard-Holstein model

We demonstrate in this section the expression of the Hamiltonian 4.1.5 as the result of a Lang-Firsov transformation of the Hubbard-Holstein Hamiltonian 4.1.2. We remind the expression of the Hubbard-Holstein Hamiltonian:

$$H_{loc} = V n_\uparrow n_\downarrow + \lambda(n_\uparrow + n_\downarrow)(b^\dagger + b) + \omega_0 \left(b^\dagger b + \frac{1}{2} \right) \tag{B.1.1}$$

and of the transformation matrix:

$$S = ipx_0 = \frac{\lambda}{\omega_0}(n_\uparrow + n_\downarrow)(b^\dagger - b) \tag{B.1.2}$$

Using the fact that for two matrices A and B that do not commute:

$$e^A B e^{-A} = \sum_{n=0}^{+\infty} \frac{1}{n!}[A,B]_n = B + [A,B] + \frac{1}{2}[A,[A,B]] + \frac{1}{6}[A,[A,[A,B]]] + ...$$

and the commutators:

$$\begin{aligned}
[S, c_\sigma] &= -\frac{\lambda(b^\dagger - b)}{\omega_0} c_\sigma \\
[S, c_\sigma^\dagger] &= \frac{\lambda(b^\dagger - b)}{\omega_0} c_\sigma^\dagger \\
[S, b] &= -\frac{\lambda(n_\uparrow + n_\downarrow)}{\omega_0} \\
[S, b^\dagger] &= -\frac{\lambda(n_\uparrow + n_\downarrow)}{\omega_0}
\end{aligned}$$

we can define new creation and annihilation operators $\tilde{o} = e^S o e^{-S}$:

$$\begin{aligned}
\tilde{c}_\sigma &= e^{(-\lambda/\omega_0)(b^\dagger - b)} c_\sigma \\
\tilde{c}^\dagger_\sigma &= e^{(\lambda/\omega_0)(b^\dagger - b)} c^\dagger_\sigma \\
\tilde{b} &= b - \frac{\lambda(n_\uparrow + n_\downarrow)}{\omega_0} \\
\tilde{b}^\dagger &= b^\dagger - \frac{\lambda(n_\uparrow + n_\downarrow)}{\omega_0}
\end{aligned}$$

and rewrite the hamiltonian $\tilde{H}_{loc} = e^S H_{loc} e^{-S}$ (noting that $\tilde{n}_\sigma = n_\sigma$ and that S is anti-Hermitian):

$$\begin{aligned}
\tilde{H}_{loc} &= V\tilde{n}_\uparrow\tilde{n}_\downarrow + \lambda(\tilde{n}_\uparrow + \tilde{n}_\downarrow)(\tilde{b} + \tilde{b}^\dagger) + \omega_0\left(\tilde{b}^\dagger\tilde{b} + \frac{1}{2}\right) \\
\tilde{H}_{loc} &= V\tilde{n}_\uparrow\tilde{n}_\downarrow + \lambda(\tilde{n}_\uparrow + \tilde{n}_\downarrow)\left(b + b^\dagger - \frac{2\lambda(n_\uparrow + n_\downarrow)}{\omega_0}\right) \\
&\quad + \omega_0\left(b^\dagger b - \frac{\lambda(n_\uparrow + n_\downarrow)}{\omega_0}(b + b^\dagger) + \frac{\lambda^2(n_\uparrow + n_\downarrow)^2}{\omega_0^2} + \frac{1}{2}\right) \\
\tilde{H}_{loc} &= V\tilde{n}_\uparrow\tilde{n}_\downarrow + \omega_0\left(b^\dagger b + \frac{1}{2}\right) - \frac{\lambda^2}{\omega_0}(n_\uparrow + n_\downarrow)^2
\end{aligned}$$

Finally, using the fact that $n_\sigma^2 = n_\sigma$, we find the Hamiltonian 4.1.5:

$$\tilde{H}_{loc} = (V - 2\frac{\lambda^2}{\omega_0})\tilde{n}_\uparrow\tilde{n}_\downarrow - \frac{\lambda^2}{\omega_0}(\tilde{n}_\uparrow + \tilde{n}_\downarrow) + \omega_0\left(b^\dagger b + \frac{1}{2}\right) \tag{B.1.3}$$

B.2 Correspondence between Hamiltonian and action in the Hubbard-Holstein model

The many-body physics of the system can be expressed in the form of an action S, such that the grand-canonical partition function $Z = \mathrm{Tr} e^{-\beta H}$ is now written $Z = \int D(c^\star, c) e^{-S}$. The instantaneous interaction part corresponding to $H_{Hubbard}$ becomes:

$$\begin{aligned}
S_{Hubbard}(c^\star, c) &= \int_0^\beta d\tau n_\uparrow(\tau) V n_\downarrow(\tau) \\
&= \frac{1}{2}\sum_{\sigma\sigma'}\int_0^\beta d\tau \int_0^\beta d\tau' n_\sigma(\tau) V \delta_{\tau\tau'}(1 - \delta_{\sigma\sigma'}) n_{\sigma'}(\tau')
\end{aligned} \tag{B.2.1}$$

As for the bosonic and coupling part of the Hamiltonian, using again equation 4.1.3:

$$H_B = H_{coupling} + H_{boson} = \lambda\sqrt{2} n x + \frac{\omega_0}{2}(x^2 + p^2)$$

and noting that

$$p^2(\tau) = -\frac{[\partial_\tau x(\tau)]^2}{\omega_0^2}$$

allows us to write an action:

$$S_B(c^\star, c, b^\star, b) = \frac{1}{\beta}\sum_n x(i\nu_n)\left(\frac{-(i\nu_n)^2+\omega_0^2}{2\omega_0}\right)x(-i\nu_n) + \lambda\sqrt{2}x(i\nu_n)n(-i\nu_n)$$

We then integrate out the bosonic degrees of freedom to obtain:

$$S_{ret}(c^\star, c) = \frac{1}{\beta}\sum_n n(i\nu_n)\left(-\lambda^2\frac{2\omega_0}{\nu_n^2+\omega_0^2}\right)n(-i\nu_n)$$

Now we define

$$U_{ret}(i\nu_n) = -2\frac{\lambda^2\omega_0}{\nu_n^2+\omega_0^2} \tag{B.2.2}$$

And the Fourier transformation gives us:

$$S_{ret}(c^\star, c) = \frac{1}{2}\int_0^\beta d\tau\int_0^\beta d\tau' n(\tau)U_{ret}(\tau-\tau')n(\tau')$$

At the end, we see that the full action of the system is written in the form (equation 4.2.3):

$$S_{loc}(c^\star, c) = \frac{1}{2}\sum_{\sigma\sigma'}\int_0^\beta d\tau\int_0^\beta d\tau' n_\sigma(\tau)U_{\sigma\sigma'}(\tau-\tau')n_{\sigma'}(\tau') \tag{B.2.3}$$

B.3 Some results for $K(\tau)$

We remind the definition of $K(\tau)$as in equation 4.3.1:

$$K(\tau) = -\frac{1}{\beta}\sum_{n\neq 0}\frac{U(i\omega_n)-V}{\omega_n^2}\left(e^{i\omega_n\tau}-1\right) + \frac{V-U_0}{2}\left(1-\frac{\tau}{\beta}\right)\tau \tag{B.3.1}$$

Differentiating K gives:

$$\begin{aligned} K'(\tau) &= -\frac{i}{\beta}\sum_{n\neq 0}\frac{U(i\omega_n)-V}{\omega_n}e^{i\omega_n\tau} + \frac{V-U_0}{2}\left(1-\frac{2\tau}{\beta}\right) \\ K'(0) &= \frac{V-U_0}{2} = -K'(\beta) \end{aligned} \tag{B.3.2}$$

There is a discontinuity in the derivative of K at 0, which will give, for $0 \leq \tau < \beta$:

$$\begin{aligned} K''(\tau) &= \frac{1}{\beta}\sum_{n\neq 0}\left(U(i\omega_n)-V\right)e^{i\omega_n\tau} + \frac{U_0-V}{\beta} + 2K'(0)\delta(\tau) \\ K''(\tau) &= \frac{1}{\beta}\sum_{n\in\mathbb{Z}}\left(U(i\omega_n)-V\right)e^{i\omega_n\tau} + \left(V-U_0\right)\delta(\tau) \\ K''(\tau) &= U_{ret}(\tau) + \left(V-U_0\right)\delta(\tau) \end{aligned} \tag{B.3.3}$$

As a consequence, we can write (equation 4.3.2):

$$\begin{aligned} S_{loc} &= \frac{1}{2}\sum_{\sigma,\sigma'}\int\int d\tau d\tau' n_\sigma(\tau)U_0(1-\delta_{\sigma,\sigma'})\delta(\tau-\tau')n_{\sigma'}(\tau') \\ &\quad -\frac{1}{2}\sum_{\sigma,\sigma'}\int\int d\tau d\tau' n_\sigma(\tau)(V-U_0)\delta_{\sigma\sigma'}\delta(\tau-\tau')n_{\sigma'}(\tau') \\ &\quad +\frac{1}{2}\sum_{\sigma,\sigma'}\int\int d\tau d\tau' n_\sigma(\tau)K''(\tau-\tau')n_{\sigma'}(\tau') \\ S_{loc} &= \frac{1}{2}\sum_{\sigma,\sigma'}\int\int d\tau d\tau' n_\sigma(\tau)U_0(1-\delta_{\sigma,\sigma'})\delta(\tau-\tau')n_{\sigma'}(\tau') \\ &\quad +\frac{1}{2}\sum_{\sigma,\sigma'}\int\int d\tau d\tau' n_\sigma(\tau)K''(\tau-\tau')n_{\sigma'}(\tau') - \frac{V-U_0}{2}\int n(\tau)d\tau \end{aligned} \quad \text{(B.3.4)}$$

We can also express $K(\tau)$ slightly differently. First, we remark that since $U(i\omega)$ is even and real, $K(\tau)$ is also real and:

$$K(\tau) = -\frac{2}{\beta}\sum_{n>0}\frac{U(i\omega_n)-V}{\omega_n^2}\left(\cos\left(\omega_n\tau\right)-1\right) + \frac{V-U_0}{2}\left(1-\frac{\tau}{\beta}\right)\tau \quad \text{(B.3.5)}$$

Now, let us define the β-periodic function $F(\tau)$ such that

$$\forall\tau\in[0,\beta] \quad F(\tau) = \frac{\tau}{2}\left(1-\frac{\tau}{\beta}\right)$$

This function is also even. We can calculate its Fourier coefficients related to the bosonic Matsubara frequencies $\omega_n = \frac{2n\pi}{\beta}$ for $n\in\mathbb{Z}^\star$:

$$\begin{aligned} F(i\omega_n) &= \int_0^\beta \cos\left(\omega_n\tau\right)F(\tau)d\tau \\ F(i\omega_n) &= \frac{1}{2}\int_0^\beta \cos\left(\omega_n\tau\right)\tau d\tau - \int_0^\beta \cos\left(\omega_n\tau\right)\frac{\tau^2}{2\beta}d\tau \end{aligned}$$

Noting that:

$$\int_0^\beta \cos\left(\omega_n\tau\right)\tau d\tau = \left[\frac{1}{\omega_n}\sin\left(\omega_n\tau\right)\tau\right]_0^\beta - \int_0^\beta \frac{1}{\omega_n}\sin\left(\omega_n\tau\right)d\tau = 0$$

We obtain:

$$\forall n\in\mathbb{Z}^\star \quad F(i\omega_n) = -\frac{1}{\omega_n^2}$$

Since $F(\tau=0)=0$ we also have:

$$F(i\omega_n=0) = \sum_{n\in\mathbb{Z}^\star}\frac{1}{\omega_n^2} = \int_0^\beta \frac{\tau}{2}\left(1-\frac{\tau}{\beta}\right)d\tau = \frac{\beta^2}{12}$$

Finally, we have shown that:

$$\forall \tau \in [0,\beta] \quad -\frac{2}{\beta}\sum_{n>0}\frac{1}{\omega_n^2}\left(\cos\left(\omega_n\tau\right)-1\right)=\frac{\tau}{2}\left(1-\frac{\tau}{\beta}\right)$$

Which allows us to write $K(\tau)$ as:

$$K(\tau)=\frac{-2}{\beta}\sum_{n>0}\frac{U(i\omega_n)-U_0}{\omega_n^2}\left(\cos\left(\omega_n\tau\right)-1\right) \tag{B.3.6}$$

We now express $K(\tau)$ as a function of U in real frequencies. We define:

$$f_\tau(z)=\frac{U(z)-U_0}{z^2}\left(e^{z\tau}-1\right)$$

Then if we look at $g(z)=f_\tau(z)n_B(z)$ we can see that

$$g(z)=\frac{U(z)-U_0}{z^2}\left(\frac{e^{z\tau}-1}{e^{\beta z}-1}\right)$$

around $z=0$ we have

$$g(z)\sim\left(\frac{z\tau}{\beta z}\right)\lim_{z\to 0}\frac{U(z)-U_0}{z^2}$$

which is finite so g has no pole at 0. Moreover, we can see that for all z such that $\Im(z)=\frac{(2n+1)\pi}{\beta}=R_n$:

$$\begin{aligned}
|g(z)| &< \frac{\max|U(z)-U_0|}{|z|^2}\left|\frac{e^{z\tau}-1}{-e^{\beta\Re(z)}-1}\right| \\
|g(z)| &< \frac{\max|U(z)-U_0|}{|z|^2}\left|\frac{1+e^{\tau\Re(z)}}{1+e^{\beta\Re(z)}}\right| \\
|g(z)| &< \frac{\max|U(z)-U_0|}{R_n^2}
\end{aligned}$$

Then for all z such that $\Re(z)=R_n$:

$$\begin{aligned}
|g(z)| &< \frac{\max|U(z)-U_0|}{|z|^2}\left(\frac{e^{\tau R_n}+1}{e^{\beta R_n}-1}\right) \\
|g(z)| &< \frac{\max|U(z)-U_0|}{R_n^2}\left(\frac{e^{\tau R_n}+1}{e^{\beta R_n}-1}\right)
\end{aligned}$$

In conclusion we see that integrating along the square path of cote R_n and taking the limit $n\longrightarrow+\infty$ gives the following result:

$$\begin{aligned}
\frac{2i\pi}{\beta}\sum_{n>0}f_\tau(i\omega_n) &= \int_{-\infty}^{+\infty}g(\omega)d\omega \\
-\frac{2i\pi}{\beta}\sum_{n>0}\frac{U(i\omega_n)-U_0}{\omega_n^2}\left(e^{i\omega_n\tau}-1\right) &= \int_{-\infty}^{+\infty}\frac{U(\omega)-U_0}{\omega^2}\left(\frac{e^{\omega\tau}-1}{e^{\beta\omega}-1}\right)d\omega
\end{aligned}$$

Taking the imaginary part of this expression we obtain:

$$K(\tau) = \int_{-\infty}^{+\infty} \frac{\Im\left(U(\omega) - U_0\right)}{\pi\omega^2} \left(\frac{e^{\omega\tau} - 1}{e^{\beta\omega} - 1}\right) d\omega$$

Now, considering that $\Im\left(U(\omega)\right)$ is an odd function and that:

$$\begin{aligned}
\frac{e^{\omega\tau} - 1}{e^{\beta\omega} - 1} - \frac{e^{-\omega\tau} - 1}{e^{-\beta\omega} - 1} &= 2\frac{e^{\omega\tau} - 1}{e^{\frac{\beta\omega}{2}} \sinh\left[\frac{\beta\omega}{2}\right]} + 2\frac{e^{-\omega\tau} - 1}{e^{-\frac{\beta\omega}{2}} \sinh\left[\frac{\beta\omega}{2}\right]} \\
&= 2\frac{e^{\omega(\tau - \frac{\beta}{2})} - e^{-\frac{\beta\omega}{2}} + e^{\omega(\frac{\beta}{2} - \tau)} - e^{\frac{\beta\omega}{2}}}{\sinh\left[\frac{\beta\omega}{2}\right]} \\
&= \frac{\cosh\left[\left(\tau - \frac{\beta}{2}\right)\omega\right] - \cosh\left[-\frac{\beta}{2}\omega\right]}{\sinh\left[\frac{\beta\omega}{2}\right]}
\end{aligned}$$

We finally get, defining the bosonic factor $b(\omega, \tau) = \cosh\left[\left(\tau - \frac{\beta}{2}\right)\omega\right] / \sinh\left[\frac{\beta\omega}{2}\right]$:

$$K(\tau) = \int_0^{+\infty} \frac{\Im\left(U(\omega)\right)}{\pi\omega^2} \left[b(\omega, \tau) - b(\omega, 0)\right] d\omega \tag{B.3.7}$$

Which is the same expression as in [Werner *et al.* (2012)] since $\Im\left(U(\omega = +\infty)\right) = 0$.

Another alternative (useful for numerical calculation) is to write it:

$$K(\tau) = \int_0^{+\infty} \frac{\Im\left(U(\omega)\right)}{\pi\omega^2} \left[\frac{e^{(\tau-\beta)\omega} + e^{-\tau\omega} - e^{-\beta\omega} - 1}{1 - e^{-\beta\omega}}\right] d\omega \tag{B.3.8}$$

B.4 Calculation of the bosonic factor Z_B

In practice, we rather use equation B.3.5 to calculate $K(\tau)$ since the approximation $\forall\, \omega_n > \omega_{n_0} \quad U(i\omega_n) = V$ naturally cuts the sum after frequency ω_{n_0}. Then the error for $K\left(\tau\right)$ with respect to this approximated function $\tilde{K}(\tau)$ can be evaluated:

$$\left|K\left(\tau\right) - \tilde{K}\left(\tau\right)\right| \leq \frac{4}{\beta} \sum_{n > n_0} \frac{|U(i\omega_n) - V|}{\omega_n^2} \tag{B.4.1}$$

$$\left|K\left(\tau\right) - \tilde{K}\left(\tau\right)\right| \leq \frac{\beta}{\pi^2} \sum_{n > n_0} \frac{V - U(i\omega_{n_0})}{n^2}$$

$$\left|K\left(\tau\right) - \tilde{K}\left(\tau\right)\right| \leq \beta\left(V - U(i\omega_{n_0})\right) \left(\frac{1}{6} - \frac{1}{\pi^2} \sum_{n \leq n_0} \frac{1}{n^2}\right) \tag{B.4.2}$$

For instance, if we take $\omega_{n_0} \geq 70$ eV and $\beta = 30$ eV^{-1} we obtain for $BaCo_2As_2$ in a *dp* effective model (see Section 3.4.5):

$$\frac{\left|K\left(\frac{\beta}{2}\right) - \tilde{K}\left(\frac{\beta}{2}\right)\right|}{\tilde{K}\left(\frac{\beta}{2}\right)} \leq 5\%$$

Which translates into about the same error on the estimation of Z_B. The upper bound is very sensitive to the choice of the cutoff frequency ω_{n_0}: the second factor in the right hand side of inequality B.4.2 scales roughly in $1/\omega_{n_0}^2$, as can be seen from equation 4.2.5 for the single plasmon case. It is nearly constant with β for the range of inverse temperatures we consider, since the last factor in B.4.2 is also reduced when β or ω_{n_0} is increased[1]. In practice we also recommend to have a good precision for $U(i\omega_n) - U_0 \sim \omega_n^2$ at low frequencies, since lowering temperature might make $K(\beta/2)$ diverge if this behavior is not correctly captured. For this reason it might be useful to use equation B.3.8 for temperatures lower than $\beta = 30$ eV^{-1}.

We can also find an upper bound for the difference between the zero-temperature value Z_B and a given temperature calculation:

$$\ln Z_B + K\left(\frac{\beta}{2}\right) \leq \ln Z_B \max_{\omega\in[A,+\infty]}\left[1 - \frac{1-\cosh\left(\frac{\omega\beta}{2}\right)}{\sinh\left(\frac{\omega\beta}{2}\right)}\right] + A \max_{\omega\in[0,A]}\left|\frac{\Im U_{ret}(\omega)}{\pi\omega^2}\right| \tag{B.4.3}$$

B.5 Analytic prolongation

We explain formula 4.6.4, which directly comes from the definition 4.6.2:

$$\tilde{G}(\tau) = \tilde{G}^{aux}(\tau)B(\tau)$$

A Fourier transformation gives:

$$\begin{aligned}
\tilde{G}(i\omega_n) &= \int_0^\beta \tilde{G}^{aux}(\tau)B(\tau)e^{i\omega_n\tau}d\tau \\
\tilde{G}(i\omega_n) &= \frac{1}{\beta^2}\int_0^\beta \left(\sum_{m=-\infty}^{+\infty}\tilde{G}^{aux}(i\omega_m)e^{-i\omega_m\tau}\right)\left(\sum_{p=-\infty}^{+\infty}B(i\omega_p)e^{-i\omega_p\tau}\right)e^{i\omega_n\tau}d\tau
\end{aligned}$$

where $\omega_m = \frac{(2m+1)\pi}{\beta}$ and $\omega_p = \frac{2p\pi}{\beta}$ since $\tilde{G}^{aux}$is fermionic and B is bosonic.

$$\begin{aligned}
\tilde{G}(i\omega_n) &= \frac{1}{\beta^2}\sum_{m=-\infty}^{+\infty}\sum_{p=-\infty}^{+\infty}\tilde{G}^{aux}(i\omega_m)B(i\omega_p)\int_0^\beta e^{i(\omega_n-\omega_m-\omega_p)\tau}d\tau \\
\tilde{G}(i\omega_n) &= \frac{1}{\beta}\sum_{m=-\infty}^{+\infty}\tilde{G}^{aux}(i\omega_m)B(i\omega_n - i\omega_m)
\end{aligned} \tag{B.5.1}$$

Using now the spectral representations of $\tilde{G}^{aux}$ and B:

$$\begin{aligned}
\tilde{G}(i\omega_n) &= \frac{1}{\beta}\sum_{m=-\infty}^{+\infty}\int_{-\infty}^{+\infty}\frac{\tilde{A}^{aux}(\nu)}{i\omega_m-\nu}d\nu\int_{-\infty}^{+\infty}\frac{\rho_B(\epsilon)}{i\omega_n - i\omega_m - \epsilon}d\epsilon \\
\tilde{G}(i\omega_n) &= \int_{-\infty}^{+\infty}\tilde{A}^{aux}(\nu)d\nu\int_{-\infty}^{+\infty}\rho_B(\epsilon)d\epsilon\left(\frac{1}{\beta}\sum_{m=-\infty}^{+\infty}\frac{1}{(i\omega_m-\nu)(i\omega_n-i\omega_m-\epsilon)}\right)
\end{aligned}$$

[1] For $\omega_{n_0} = 70eV$, $\left(\frac{1}{6} - \frac{1}{\pi^2}\sum_{n\leq n_0}\frac{1}{n^2}\right)$ has a value of $\sim 10^{-2}$ for $\beta = 1$ eV^{-1},$\sim 10^{-3}$ for $\beta = 10$ eV^{-1} and $\sim 10^{-4}$ for $\beta = 100$ eV^{-1}.

Let us examine the function:

$$f(z) = \frac{n_F(z)}{(z-\nu)(i\omega_n - \epsilon - z)}$$

$f(z)$ has poles at every Matsubara frequency (because of $n_F(z) = \frac{1}{1+e^{\beta z}}$), and at ν and $i\omega_n - \epsilon$. Moreover, it goes to zero faster than $\frac{1}{|z|^2}$ for $|z| \longrightarrow +\infty$. We can thus calculate the following integral using the residue theorem:

$$\begin{aligned}
\lim_{R\to+\infty} \int_{|z|=R} f(z)dz &= 0 \\
\lim_{R\to+\infty} \int_{|z|=R} f(z)dz &= 2i\pi \sum Res(f)
\end{aligned}$$

If those poles are all distinct, which does not happen only if $\epsilon = 0$, we can calculate the residues:

$$\begin{aligned}
Res_{i\omega_m} f &= \lim_{z\longrightarrow i\omega_m} \frac{z - i\omega_m}{1+e^{\beta z}} \frac{1}{(z-\nu)(i\omega_n - \epsilon - z)} \\
Res_{i\omega_m} f &= \lim_{\eta\longrightarrow 0} \frac{\eta}{1+e^{i\beta\omega_m}e^{\beta\eta}} \frac{1}{(i\omega_m - \nu)(i\omega_n - i\omega_m - \epsilon)} \\
Res_{i\omega_m} f &= -\frac{1}{\beta(i\omega_m - \nu)(i\omega_n - i\omega_m - \epsilon)}
\end{aligned}$$

$$Res_\nu f = \frac{1}{(1+e^{\beta\nu})(i\omega_n - \epsilon - \nu)}$$

$$\begin{aligned}
Res_{i\omega_n - \epsilon} f &= -\frac{1}{(1+e^{\beta(i\omega_n - \epsilon)})(i\omega_n - \epsilon - \nu)} \\
Res_{i\omega_n - \epsilon} f &= -\frac{1}{(1-e^{-\beta\epsilon})(i\omega_n - \epsilon - \nu)}
\end{aligned}$$

Thus if $\epsilon \neq 0$:

$$\frac{1}{\beta} \sum_{m=-\infty}^{+\infty} \frac{1}{(i\omega_m - \nu)(i\omega_n - i\omega_m - \epsilon)} = \frac{S(\nu,\epsilon)}{i\omega_n - \epsilon - \nu}$$

with

$$S(\nu,\epsilon) = \frac{1}{e^{\beta\nu}+1} + \frac{1}{e^{-\beta\epsilon}-1} = n_F(\nu) + n_B(-\epsilon)$$

If $\epsilon = 0$ the only difference is for the pole at $i\omega_n$ which is now double:

$$\begin{aligned}
Res_{i\omega_n} f &= \lim_{z\longrightarrow i\omega_n} \frac{\partial}{\partial z} \left[\frac{(z - i\omega_n)^2}{(1+e^{\beta z})(i\omega_n - z)(z-\nu)} \right] \\
Res_{i\omega_n} f &= \lim_{z\longrightarrow i\omega_n} -\frac{\partial}{\partial z} \left[\frac{z - i\omega_n}{(1+e^{\beta z})(z-\nu)} \right] \\
Res_{i\omega_n} f &= \lim_{\eta\longrightarrow 0} -\frac{1}{i\omega_n - \nu} \frac{\partial}{\partial \eta} \left[\frac{\eta}{1-e^{\beta\eta}} \right] \\
Res_{i\omega_n} f &= -\frac{1}{2(i\omega_n - \nu)}
\end{aligned}$$

So we can define

$$S(\nu,0) = n_F(\nu) - \frac{1}{2}$$

As $\rho_B(0) = 0$ though, we can just omit this case. We finally get (with $\omega' = \epsilon + \nu$):

$$\begin{aligned}
\tilde{G}(i\omega_n) &= \int_{-\infty}^{+\infty} d\epsilon \int_{-\infty}^{+\infty} d\nu \tilde{A}^{aux}(\nu)\rho_B(\epsilon)\left[n_F(\nu) + n_B(-\epsilon)\right] \frac{1}{i\omega_n - \epsilon - \nu} \\
G(i\omega_n) &= \int_{-\infty}^{+\infty} d\epsilon \int_{-\infty}^{+\infty} d\omega' \tilde{A}^{aux}(\omega' - \epsilon)\rho_B(\epsilon)\left[n_F(\omega' - \epsilon) + n_B(-\epsilon)\right] \frac{1}{i\omega_n - \omega'} \\
G(i\omega_n) &= \int_{-\infty}^{+\infty} d\omega' \frac{\tilde{A}(\omega')}{i\omega_n - \omega'}
\end{aligned} \tag{B.5.2}$$

with

$$\begin{aligned}
\tilde{A}(\omega) &= \int_{-\infty}^{+\infty} d\epsilon \tilde{A}^{aux}(\omega - \epsilon)\rho_B(\epsilon)\left[n_F(\omega - \epsilon) + n_B(-\epsilon)\right] \\
\tilde{A}(\omega) &= \int_{-\infty}^{+\infty} d\epsilon \tilde{A}^{aux}(\epsilon)\rho_B(\omega - \epsilon)\left[n_F(\epsilon) + n_B(\epsilon - \omega)\right]
\end{aligned} \tag{B.5.3}$$

We note in passing the identity:

$$\begin{aligned}
\frac{n_F(\epsilon) + n_B(\epsilon - \omega)}{n_F(-\epsilon) + n_B(\omega - \epsilon)} &= \frac{e^{\beta(\epsilon-\omega)} + e^{\beta\epsilon}}{(e^{\beta\epsilon} + 1)(e^{\beta(\epsilon-\omega)} - 1)} * \frac{(e^{-\beta\epsilon} + 1)(e^{\beta(\omega-\epsilon)} - 1)}{e^{-\beta\epsilon} + e^{\beta(\omega-\epsilon)}} \\
&= -e^{-\beta\epsilon+\beta(\omega-\epsilon)} \frac{e^{\beta(\epsilon-\omega)} + e^{\beta\epsilon}}{e^{-\beta\epsilon} + e^{\beta(\omega-\epsilon)}} \\
&= -1
\end{aligned}$$

One can thus verify that if $\omega - \epsilon > 0$ then $n_F(\epsilon) + n_B(\epsilon - \omega) < 0$ while $\rho_B(\omega - \epsilon) < 0$ and we add positive terms in the convolution integral. If $\omega - \epsilon < 0$ then $n_F(\epsilon) + n_B(\epsilon - \omega) > 0$: we still add positive terms.

The question is now how to obtain $\rho_B(\omega)$ from $B(\tau)$. Either we can make the analytic prolongation using Pade approximants, or calculate directly $K(t)$ in real time. For numerical reasons, we chose the second way.

Let us begin by the analytic prolongation of K ($\tau \longrightarrow it$):

$$
\begin{aligned}
K(t) &= \int_0^{+\infty} \frac{\Im U(\omega)}{\pi\omega^2} \left[b(\omega, it) - b(\omega, 0) \right] d\omega \\
K(t) &= \int_0^{+\infty} \frac{\Im U(\omega)}{\pi\omega^2} \left[\frac{e^{\left(it-\frac{\beta}{2}\right)\omega} + e^{-\left(it-\frac{\beta}{2}\right)\omega} - e^{\frac{\beta\omega}{2}} - e^{-\frac{\beta\omega}{2}}}{2\sinh\left(\frac{\beta\omega}{2}\right)} \right] d\omega \\
K(t) &= \int_0^{+\infty} \frac{\Im U(\omega)}{\pi\omega^2} \left[\frac{e^{-\frac{\beta\omega}{2}} \left(e^{it\omega} - 1\right) + e^{\frac{\beta\omega}{2}} \left(e^{-it\omega} - 1\right)}{2\sinh\left(\frac{\beta\omega}{2}\right)} \right] d\omega \\
K(t) &= \int_0^{+\infty} \frac{\Im U(\omega)}{\pi\omega^2} \left[\frac{\cosh\left(\frac{\beta\omega}{2}\right) \left(\cos(\omega t) - 1\right) - i \sinh\left(\frac{\beta\omega}{2}\right) \sin(\omega t)}{\sinh\left(\frac{\beta\omega}{2}\right)} \right] d\omega \\
K(t) &= \int_0^{+\infty} \frac{\Im U(\omega)}{\pi\omega^2} \left[\frac{\cos(\omega t) - 1}{\tanh\left(\frac{\beta\omega}{2}\right)} - i \sin(\omega t) \right] d\omega \\
K(t) &= \int_0^{+\infty} \frac{\Im U(\omega)}{\pi\omega^2} \left[\left(\cos(\omega t) - 1\right) \left(1 + 2n_B(\omega)\right) - i \sin(\omega t) \right] d\omega
\end{aligned}
\tag{B.5.4}
$$

To clean up every integration problem, we consider that $\Im U(\omega)$ is equal to zero at low frequency: indeed in cRPA calculations before the onset of transitions $\Im U(\omega)$ should be zero. It is important to keep the same function to build $B(\tau)$ and $B(t)$. In any case, we could take any function we want for $B(\tau)$ as long as this choice is still close to the physically justified atomic-like approximation.

Then, we remark that $B(t)$ does not go to zero at infinite frequency, thus causing a delta function to appear in $\rho_B(\omega)$. This function has a coefficient related to $B(i\omega_n = 0)$, indeed ρ_B is regular if $B(i\omega_n = 0) = 0$. Using equation B.5.1 we can see that it just modifies equation 4.6.4 to give:

$$
\tilde{A}(\omega) = \frac{B(i\omega_n = 0)}{\beta} \tilde{A}^{aux}(\omega) + \int_{-\infty}^{+\infty} d\epsilon \tilde{A}^{aux}(\epsilon) \rho_B^{regular}(\omega - \epsilon) \left[n_F(\epsilon) + n_B(\epsilon - \omega) \right] \tag{B.5.5}
$$

Thus we just have to substract $B(i\omega_n = 0)/\beta$ to $B(t)$ to get a regular function. We then calculate the regular part $\rho_B^{regular}(\omega)$ as a function of $B(t)$ by doing again the analytic continuation of $B(\tau)$:

$$
\begin{aligned}
B(i\omega_n) - B_0\delta(i\omega_n) &= \int_{-\infty}^{+\infty} \frac{\rho_B^{regular}(\omega)}{i\omega_n - \omega} d\omega \\
B(\tau) - \frac{B_0}{\beta} &= \tfrac{1}{\beta} \sum_{n=-\infty}^{+\infty} e^{-i\omega_n\tau} \int_{-\infty}^{+\infty} \frac{\rho_B^{regular}(\omega)}{i\omega_n - \omega} d\omega \\
B(\tau) - \frac{B_0}{\beta} &= \int_{-\infty}^{+\infty} d\omega \rho_B^{regular}(\omega) \frac{1}{\beta} \sum_{n=-\infty}^{+\infty} \frac{e^{-i\omega_n\tau}}{i\omega_n - \omega}
\end{aligned}
$$

and by contour integration of $n_B(-z)e^{-z\tau}/(z - \omega)$, since $\rho_B^{regular}(0) = 0$, we find:

$$
\begin{aligned}
B(\tau) - \frac{B_0}{\beta} &= \int_{-\infty}^{+\infty} d\omega \rho_B^{regular}(\omega) n_B(-\omega) e^{-\omega\tau} \\
B(t) - \frac{B_0}{\beta} &= \int_{-\infty}^{+\infty} d\omega \rho_B^{regular}(\omega) n_B(-\omega) e^{-i\omega t}
\end{aligned}
$$

Thus the Fourier transform of $B(t) - B_0/\beta$ gives the product of $\rho_B^{regular}(\omega)$ and of $n_B(-\omega)$.

We note that according to equation B.5.4 the real part of $K(t)$ is even and the imaginary part is odd. Since $B(t) = e^{-K_{real}(t)} \cos(K_{imag}(t)) - ie^{-K_{real}(t)} \sin(K_{imag}(t))$ we can see that it is the same for $B(t)$. Consequently the Fourier transform of $B(t) - B_0/\beta$ is real (which was expected for the product of $\rho_B^{regular}$ and of n_B) and:

$$
\begin{aligned}
\rho_B^{regular}(\omega) n_B(-\omega) &= \frac{1}{2\pi} \int_{-\infty}^{+\infty} \left[B(t) - \frac{B_0}{\beta} \right] e^{i\omega t} dt \\
\rho_B^{regular}(\omega) n_B(-\omega) &= \frac{1}{\pi} \int_{0}^{+\infty} \left[\left(B_{real}(t) - \frac{B_0}{\beta} \right) \cos(\omega t) - B_{imag}(t) \sin(\omega t) \right] dt
\end{aligned}
$$

Putting this into equation B.5.5 finally gives:

$$
\begin{aligned}
\tilde{A}(\omega) &= \frac{B_0}{\beta} \tilde{A}^{aux}(\omega) \\
&+ \frac{1}{2\pi} \int_{-\infty}^{+\infty} d\epsilon \tilde{A}^{aux}(\epsilon) \left[\frac{n_F(\epsilon)}{n_B(\epsilon - \omega)} + 1 \right] \int_{-\infty}^{+\infty} dt \left(B(t) - \frac{B_0}{\beta} \right) e^{i(\omega - \epsilon)t}
\end{aligned} \tag{B.5.6}
$$

List of Publications

[1] A. van Roekeghem, T. Ayral, J. M. Tomczak, M. Casula, N. Xu, H. Ding, M. Ferrero, O. Parcollet, H. Jiang, and S. Biermann. *Dynamical correlations and screened exchange on the experimental bench: spectral properties of the cobalt pnictide $BaCo_2As_2$*. *Phys. Rev. Lett.* **113** (2014): 266403.

[2] A. van Roekeghem and S. Biermann. *Screened exchange dynamical mean-field theory and its relation to density functional theory: $SrVO_3$ and $SrTiO_3$*. *EPL* **108** (2014): 75003.

[3] J.-Z. Ma, A. van Roekeghem (equal contribution), P. Richard, Z.-H. Liu, H. Miao, L.-K. Zeng, N. Xu, M. Shi, C. Cao, J.-B. He, G.-F. Chen, Y.-L. Sun, G.-H. Cao, S.-C. Wang, S. Biermann, T. Qian, and H. Ding. *Correlation-induced self-doping in the iron-pnictide superconductor $Ba_2Ti_2Fe_2As_4O$*. *Phys. Rev. Lett.* **113** (2014): 266407.

[4] Y.-B. Shi, Y.-B. Huang, X.-P. Wang, X. Shi, A. van Roekeghem, W.-L. Zhang, N. Xu, P. Richard, T. Qian, E. Rienks, S. Thirupathaiah, K. Zhao, C.-Q. Jin, M. Shi, and H. Ding. *Observation of Strong-Coupling Pairing with Weakened Fermi-Surface Nesting at Optimal Hole Doping in $Ca_{0.33}Na_{0.67}Fe_2As_2$*. *Chin. Phys. Lett.* **31** (2014)(6): 067403.

[5] N. Xu, P. Richard, A. van Roekeghem, P. Zhang, H. Miao, W.-L. Zhang, T. Qian, M. Ferrero, A. S. Sefat, S. Biermann, and H. Ding. *Electronic Band Structure of $BaCo_2As_2$: A Fully Doped Ferropnictide Analog with Reduced Electronic Correlations*. *Phys. Rev. X* **3** (2013): 011006.

[6] N. Xu, P. Richard, X. Shi, A. van Roekeghem, T. Qian, E. Razzoli, E. Rienks, G.-F. Chen, E. Ieki, K. Nakayama, T. Sato, T. Takahashi, M. Shi, and H. Ding. *Possible nodal superconducting gap and Lifshitz transition in heavily hole-doped $Ba_{0.1}K_{0.9}Fe_2As_2$*. *Phys. Rev. B* **88** (2013): 220508.

[7] N. Xu, P. Richard, X.-P. Wang, X. Shi, A. van Roekeghem, T. Qian, E. Ieki, K. Nakayama, T. Sato, E. Rienks, S. Thirupathaiah, J. Xing, H.-H. Wen, M. Shi, T. Takahashi, and H. Ding. *Angle-resolved photoemission observation of isotropic superconducting gaps in isovalent Ru-substituted $Ba(Fe_{0.75}Ru_{0.25})_2As_2$*. *Phys. Rev. B* **87** (2013): 094513.

[8] X.-P. Wang, P. Richard, X. Shi, A. van Roekeghem, Y.-B. Huang, E. Razzoli, T. Qian, E. Rienks, S. Thirupathaiah, H.-D. Wang, C.-H. Dong, M.-H. Fang, M. Shi, and H. Ding. *Observation of an isotropic superconducting gap at the Brillouin zone centre of $Tl_{0.63}K_{0.37}Fe_{1.78}Se_2$*. *EPL* **99** (2012): 67001.

[9] E. Papalazarou, J. Faure, J. Mauchain, M. Marsi, A. Taleb-Ibrahimi, I. Reshetnyak, A. van Roekeghem, I. Timrov, N. Vast, B. Arnaud, and L. Perfetti. *Coherent Phonon Coupling to Individual Bloch States in Photoexcited Bismuth*. *Phys. Rev. Lett.* **108** (2012): 256808.

In preparation

[10] N. Xu, C. E. Matt, P. Richard, A. van Roekeghem, S. Biermann, X. Shi, S.-F. Wu, H. W. Liu, D. Chen, T. Qian, N. C. Plumb, M. Radovic, M. H. Fang, J. Mesot, H. Ding, and M. Shi. *Camelback-shaped band reconciles heavy electron behavior with weak electronic Coulomb correlations in superconducting $TlNi_2Se_2$. arXiv: 1412.7016, submitted to Phys. Rev. Lett.* (2014).

[11] E. Razzoli, C. Matt, M. Kobayashi, A. van Roekeghem, S. Biermann, N. C. Plumb, M. Radovic, V. Strocov, C. Capan, P. Richard, H. Ding, P. Aebi, J. Mesot, and M. Shi. *Tuning electronic correlations in transition metal pnictides: chemistry beyond the valence count. arXiv:1502.04565* (2015).

[12] S.-F. Wu, P. Richard, A. van Roekeghem, S.-M. Nie, H. Miao, N. Xu, T. Qian, B. I. Saparov, Z. Fang, S. Biermann, A. Safa-Sefat, and H. Ding. *Direct spectroscopic evidence for completely filled Cu 3d shell in $BaCu_2As_2$ and α–$BaCu_2Sb_2$. arXiv: 1504.00437, submitted to Phys. Rev. B* (2015).

[13] W.-L. Zhang, P. Richard, A. van Roekeghem, S.-M. Nie, N. Xu, P. Zhang, H. Miao, S.-F. Wu, T. Qian, Z.-J. Wang, Z. Fang, S. Biermann, A. Safa-Sefat, and H. Ding. *ARPES observation of strong Mn-pnictide hybridization in $BaMn_2Pn_2$ (Pn = As, Sb). In preparation* (2015).

[14] A. van Roekeghem, L. Vaugier, H. Jiang, and S. Biermann. . *Hubbard interactions in iron-based pnictides and chalcogenides: Slater parametrization, screening channels and frequency dependence. In preparation* (2015).

[15] P. Seth, P. Hansmann, A. van Roekeghem, L. Vaugier, and S. Biermann. *Towards a first-principles determination of effective Coulomb interactions in correlated electron materials: Role of inter-shell interactions. In preparation* (2015).

[16] L.-K. Zeng, A. van Roekeghem, J.-X. Yin, P. Richard, Z.-G. Chen, N.-L. Wang, T. Qian, and H. Ding. *Angle-resolved photoemission spectroscopy study of the Ni-based superconductors $SrNi_2As_2$ and $SrNi_2P_2$. In preparation* (2015).

[17] A. van Roekeghem, P. Richard, X. Shi, S.-F. Wu, L.-K. Zeng, B. I. Saparov, Y. Ohtsubo, T. Qian, A. Safa-Sefat, S. Biermann, and H. Ding. *Tetragonal and collapsed-tetragonal phases of $CaFe_2As_2$ – a view from angle-resolved photoemission and dynamical mean field theory. In preparation* (2015).

Acknowledgments

Building a collaboration between two groups on different continents and with different specialties is not an easy task. Making this kind of collaboration fruitful is an even tougher challenge. Thanks to the help of all, these difficulties have been much easier to surmount.

First, I would like to thank my joint advisors, Silke Biermann and Hong Ding, for their exceptional open-mindedness, determination, availability and adaptability since the premises of this project, more than four years ago. Working with you has been a rich source of scientific and professional inspiration, and I hope that the links we have built will stay strong. I am also very grateful to the members of both groups and to close collaborators, some of them I have known for quite a long time and count as more than colleagues: Thomas Ayral, Florence Auger, Michele Casula, Sophie Chauvin, Fadila Debbou, Pascal Delange, Xiaoyu Deng, Dong Jing, Michel Ferrero, Charles Grenier, Antoine Georges, Philipp Hansmann, Huang Yaobo, Hong Jiang, Kong Wandong, Ma Jun, Ma Junzhang, Evgeny Kozik, Igor Krivenko, Malika Lang, Cyril Martins, Miao Hu, Jernej Mravlje, Pan Shuheng, Olivier Parcollet, Leonid Pourovskii, Elia Razzoli, Pierre Richard, Akiyuki Tokuno, Qian Tian, Shiro Sakai, Priyanka Seth, Shi Xun, Shi Yingbo, Jan Tomczak, Loïg Vaugier, Wang Xiaoping, Feng Wu, Xu Nan, Yang Shulei, Yin Jiaxin, Zeng Lingkun, Zhang Peng, and all those I certainly have forgotten in this list. Besides all the scientific and non-scientific help you have given to me, I am grateful for your ability to welcome me as a full member of the group though I was not present full-time, and for all the nice moments we have shared. I finally want to thank the members of the jury for helping me improve this manuscript and for joining the defense, sometimes after a long journey.

Pour finir, je souhaite remercier chaleureusement mes amis et ma famille, qui m'ont permis de devenir ce que je suis et m'ont soutenu tout au long de cette épreuve qu'est parfois le doctorat ; ainsi que mon épouse Sophie, qui m'a accompagné avec bonheur dans cette aventure en Chine et a enduré les fréquentes absences imposées par cette collaboration internationale.

Bibliography

[Aichhorn *et al.* (2010)] M. Aichhorn, S. Biermann, T. Miyake, A. Georges, and M. Imada. *Theoretical evidence for strong correlations and incoherent metallic state in FeSe*. *Phys. Rev. B* **82** (2010)(6): 064504. 8, 9, 13, 80, 81, 123, 153

[Aichhorn *et al.* (2011)] M. Aichhorn, L. Pourovskii, and A. Georges. *Importance of electronic correlations for structural and magnetic properties of the iron pnictide superconductor LaFeAsO*. *Phys. Rev. B* **84** (2011): 054529. 14, 37

[Aichhorn *et al.* (2009)] M. Aichhorn, L. Pourovskii, V. Vildosola, M. Ferrero, O. Parcollet, T. Miyake, A. Georges, and S. Biermann. *Dynamical mean-field theory within an augmented plane-wave framework: Assessing electronic correlations in the iron pnictide LaFeAsO*. *Phys. Rev. B* **80** (2009)(8): 085101. 9, 13, 36, 65, 79, 80, 158

[Anand *et al.* (2014)] V. K. Anand, R. S. Dhaka, Y. Lee, B. N. Harmon, A. Kaminski, and D. C. Johnston. *Physical Properties of Metallic Antiferromagnetic $CaCo_{1.86}As_2$ Single Crystals*. *arxiv:1402.6725* (2014). 106

[Andersen and Boeri(2011)] O. Andersen and L. Boeri. *On the multi-orbital band structure and itinerant magnetism of iron-based superconductors*. *Annalen der Physik* **523** (2011)(1-2): 8. 22

[Anisimov *et al.* (1997a)] V. I. Anisimov, F. Aryasetiawan, and A. I. Lichtenstein. *First-principles calculations of the electronic structure and spectra of strongly correlated systems: the LDA+U method*. *J. Phys.: Condens. Matter* **9** (1997a)(4): 767. 30, 43

[Anisimov *et al.* (2009)] V. I. Anisimov, D. Korotin, M. Korotin, A. V. Kozhevnikov, J. Kunes, S. A. O., S. L. Skornyakov, and S. V. Streltsov. *Coulomb repulsion and correlation strength in LaFeAsO from density functional and dynamical mean-field theories*. *J. Phys. Condens. Matter* **21** (2009): 075602. 9, 13

[Anisimov *et al.* (2008)] V. I. Anisimov, D. M. Korotin, S. V. Streltsov, A. V. Kozhevnikov, J. Kunes, S. A. O., and M. A. Korotin. *Density-functional calculation of the Coulomb repulsion and correlation strength in superconducting LaFeAsO*. *JETP Lett.* **88** (2008): 729. 9

[Anisimov *et al.* (1997b)] V. I. Anisimov, A. Poteryaev, M. Korotin, A. Anokhin, and G. Kotliar. *First-principles calculations of the electronic structure and spectra of strongly correlated systems : dynamical mean-field theory*. *J. Phys.: Condens. Matter* **9** (1997b): 943. 9, 34

[Anisimov *et al.* (1993)] V. I. Anisimov, I. V. Solovyev, M. A. Korotin, M. T. Czyżyk, and G. A. Sawatzky. *Density-functional theory and NiO photoemission spectra*. *Phys. Rev. B* **48** (1993)(23): 16929. 30, 36

[Anisimov *et al.* (1991)] V. I. Anisimov, J. Zaanen, and O. K. Andersen. *Band theory and Mott insulators: Hubbard U instead of Stoner I*. *Phys. Rev. B* **44** (1991)(3): 943. 36, 37, 39

[Antonides *et al.* (1977)] E. Antonides, E. C. Janse, and G. A. Sawatzky. *LMM Auger spectra of Cu, Zn, Ga, and Ge. I. Transition probabilities, term splittings, and effective Coulomb interaction*. *Phys. Rev. B* **15** (1977)(4): 1669. 44, 51, 60

[Aryasetiawan *et al.* (2004)] F. Aryasetiawan, M. Imada, A. Georges, G. Kotliar, S. Biermann, and A. I. Lichtenstein. *Frequency-dependent local interactions and low-energy effective models from electronic structure calculations*. *Phys. Rev. B* **70** (2004)(19): 195104. 9, 41

[Ayral *et al.* (2013)] T. Ayral, S. Biermann, and P. Werner. *Screening and nonlocal correlations in the extended Hubbard model from self-consistent combined GW and dynamical mean field theory*. *Phys. Rev. B* **87** (2013): 125149. 55, 63

[Ban and Sikirica(1965)] Z. Ban and M. Sikirica. *The crystal structure of ternary silicides $ThCr_2Si_2$ (M= Cr, Mn, Fe, Co, Ni and Cu)*. *Acta Crystallogr.* **18** (1965)(4): 594. 3

[Bednorz and Müller(1986)] J. Bednorz and K. Müller. *Possible high T_c superconductivity in the Ba-La-Cu-O system*. *Z. Phys. B Con. Mat.* **64** (1986)(2): 189. 3

[Biermann *et al.* (2003)] S. Biermann, F. Aryasetiawan, and A. Georges. *First-Principles Approach to the Electronic Structure of Strongly Correlated Systems: Combining the GW Approximation and Dynamical Mean-Field Theory*. *Phys. Rev. Lett.* **90** (2003)(8): 086402. 15, 49, 63, 64, 66, 157

[Biermann *et al.* (2001)] S. Biermann, A. Georges, A. Lichtenstein, and T. Giamarchi. *Deconfinement Transition and Luttinger to Fermi Liquid Crossover in Quasi-One-Dimensional Systems*. *Phys. Rev. Lett.* **87** (2001)(27): 276405. 63

[Biroli and Kotliar(2002)] G. Biroli and G. Kotliar. *Cluster methods for strongly correlated electron systems*. *Phys. Rev. B* **65** (2002)(15): 155112. 63

[Blaha *et al.* (2001)] P. Blaha, K. Schwarz, G. Madsen, D. Kvasnicka, and J. Luitz. *Wien2k, An Augmented Plane Wave+Local Orbitals Program for Calculating Crystal Properties*. Tech. Universität Wien, Austria (2001). 35, 39, 77, 79, 112

[Bondino *et al.* (2008)] F. Bondino, E. Magnano, M. Malvestuto, F. Parmigiani, M. A. McGuire, A. S. Sefat, B. C. Sales, R. Jin, D. Mandrus, E. W. Plummer, D. J. Singh, and N. Mannella. *Evidence for Strong Itinerant Spin Fluctuations in the Normal State of $CeFeAsO_{0.89}F_{0.11}$ Iron-Oxypnictide Superconductors*. *Phys. Rev. Lett.* **101** (2008): 267001. 126

[Borisenko *et al.* (2010)] S. V. Borisenko, V. B. Zabolotnyy, D. V. Evtushinsky, T. K. Kim, I. V. Morozov, A. N. Yaresko, A. A. Kordyuk, G. Behr, A. Vasiliev, R. Follath, and B. Büchner. *Superconductivity without Nesting in LiFeAs*. *Phys. Rev. Lett.* **105** (2010): 067002. 7, 8, 13, 14

[Borisenko *et al.* (2012)] S. V. Borisenko, V. B. Zabolotnyy, A. A. Kordyuk, D. V. Evtushinsky, T. K. Kim, I. V. Morozov, R. Follath, and B. Büchner. *One-Sign Order Parameter in Iron Based Superconductor*. *Symmetry* **4** (2012)(1): 251. 14

[Brouet *et al.* (2012)] V. Brouet, M. F. Jensen, P.-H. Lin, A. Taleb-Ibrahimi, P. Le Fèvre, F. Bertran, C.-H. Lin, W. Ku, A. Forget, and D. Colson. *Impact of the two Fe unit cell on the electronic structure measured by ARPES in iron pnictides*. *Phys. Rev. B* **86** (2012): 075123. 21, 24, 115, 146

[Brouet *et al.* (2011)] V. Brouet, M. F. Jensen, A. Nicolaou, A. Taleb-Ibrahimi, P. L. Fevre, F. Bertran, A. Forget, and D. Colson. *Orbitally resolved lifetimes in $Ba(Fe_{0.92}Co_{0.08})_2As_2$ measured by ARPES*. *arXiv:1105.5604* (2011). 7

[Brouet *et al.* (2013)] V. Brouet, P.-H. Lin, Y. Texier, J. Bobroff, A. Taleb-Ibrahimi, P. Le Fèvre, F. Bertran, M. Casula, P. Werner, S. Biermann, F. Rullier-Albenque, A. Forget, and D. Colson. *Large Temperature Dependence of the Number of Carriers in Co-Doped $BaFe_2As_2$*. *Phys. Rev. Lett.* **110** (2013): 167002. 8, 9, 13, 124

[Brouet *et al.* (2009)] V. Brouet, M. Marsi, B. Mansart, A. Nicolaou, A. Taleb-Ibrahimi, P. Le Fèvre, F. Bertran, F. Rullier-Albenque, A. Forget, and D. Colson. *Nesting between hole and electron pockets in $Ba(Fe_{1-x}Co_x)_2As_2$ (x = 0 - 0.3) observed with angle-resolved photoemission*. *Phys. Rev. B* **80** (2009): 165115. 7, 13

[Brouet *et al.* (2010)] V. Brouet, F. Rullier-Albenque, M. Marsi, B. Mansart, M. Aichhorn, S. Biermann, J. Faure, L. Perfetti, A. Taleb-Ibrahimi, P. Le Fèvre, F. Bertran, A. Forget, and D. Colson. *Significant Reduction of Electronic Correlations upon Isovalent Ru Substitution of $BaFe_2As_2$*. *Phys. Rev. Lett.* **105** (2010): 087001. 7, 8, 81, 124

[Bulla(2006)] R. Bulla. *Dynamical Mean-Field Theory - from Quantum Impurity Physics to Lattice Problems*. *Phil. Mag.* **86** (2006): 1877. 30

[Bylander and Kleinman(1990)] D. M. Bylander and L. Kleinman. *Good semiconductor band gaps with a modified local-density approximation*. *Phys. Rev. B* **41** (1990): 7868. 49

[Capone *et al.* (2004)] M. Capone, G. Sangiovanni, C. Castellani, C. Di Castro, and M. Grilli. *Phase Separation Close to the Density-Driven Mott Transition in the Hubbard-Holstein Model*. *Phys. Rev. Lett.* **92** (2004): 106401. 51

[Caruso *et al.* (2013)] F. Caruso, P. Rinke, X. Ren, A. Rubio, and M. Scheffler. *Self-consistent GW: All-electron implementation with localized basis functions*. *Phys. Rev. B* **88** (2013): 075105. 67

[Casula *et al.* (2012a)] M. Casula, A. Rubtsov, and S. Biermann. *Dynamical screening effects in correlated materials: Plasmon satellites and spectral weight transfers from a Green's function ansatz to extended dynamical mean field theory*. *Phys. Rev. B* **85** (2012a): 035115. 12, 44, 51, 60, 69, 106

[Casula *et al.* (2012b)] M. Casula, P. Werner, L. Vaugier, F. Aryasetiawan, T. Miyake, A. J. Millis, and S. Biermann. *Low-energy Models for Correlated Materials: Bandwidth Renormalization from Coulombic Screening*. *Phys. Rev. Lett.* **109** (2012b): 126408. 12, 44, 56, 95, 111, 121

[Ceperley and Alder(1980)] D. M. Ceperley and B. J. Alder. *Ground State of the Electron Gas by a Stochastic Method*. *Phys. Rev. Lett.* **45** (1980)(7): 566. 29

[Chauvière *et al.* (2010)] L. Chauvière, Y. Gallais, M. Cazayous, M. A. Méasson, A. Sacuto, D. Colson, and A. Forget. *Impact of the spin-density-wave order on the superconducting gap of Ba($Fe_{1-x}Co_x$)$_2As_2$. Phys. Rev. B* **82** (2010): 180521. 6

[Chen *et al.* (2008a)] G. F. Chen, Z. Li, D. Wu, G. Li, W. Z. Hu, J. Dong, P. Zheng, J. L. Luo, and N. L. Wang. *Superconductivity at 41 K and Its Competition with Spin-Density-Wave Instability in Layered $CeO_{1-x}F_xFeAs$. Phys. Rev. Lett.* **100** (2008a): 247002. 3

[Chen *et al.* (2008b)] X. H. Chen, T. Wu, G. Wu, R. H. Liu, H. Chen, and D. F. Fang. *Superconductivity at 43 K in $SmFeAsO_{1-x}F_x$. Nature* **453** (2008b): 761. 3

[Cheng *et al.* (2012)] B. Cheng, B. F. Hu, R. H. Yuan, T. Dong, A. F. Fang, Z. G. Chen, G. Xu, Y. G. Shi, P. Zheng, J. L. Luo, and N. L. Wang. *Field-induced spin-flop transitions in single-crystalline $CaCo_2As_2$. Phys. Rev. B* **85** (2012): 144426. 106

[Christianson *et al.* (2009)] A. D. Christianson, M. D. Lumsden, S. E. Nagler, G. J. MacDougall, M. A. McGuire, A. S. Sefat, R. Jin, B. C. Sales, and D. Mandrus. *Static and Dynamic Magnetism in Underdoped Superconductor $BaFe_{1.92}Co_{0.08}As_2$. Phys. Rev. Lett.* **103** (2009): 087002. 6

[Chubukov *et al.* (2008)] A. V. Chubukov, D. V. Efremov, and I. Eremin. *Magnetism, superconductivity, and pairing symmetry in iron-based superconductors. Phys. Rev. B* **78** (2008): 134512. 6

[Coldea *et al.* (2009)] A. I. Coldea, C. M. J. Andrew, J. G. Analytis, R. D. McDonald, A. F. Bangura, J.-H. Chu, I. R. Fisher, and A. Carrington. *Topological Change of the Fermi Surface in Ternary Iron Pnictides with Reduced c/a Ratio: A de Haas-van Alphen Study of $CaFe_2As_2$. Phys. Rev. Lett.* **103** (2009): 026404. 129

[Cui *et al.* (2012)] S. T. Cui, S. Y. Zhu, A. F. Wang, S. Kong, S. L. Ju, X. G. Luo, X. H. Chen, G. B. Zhang, and Z. Sun. *Evolution of the band structure of superconducting NaFeAs from optimally doped to heavily overdoped Co substitution using angle-resolved photoemission spectroscopy. Phys. Rev. B* **86** (2012): 155143. 7

[Czyżyk and Sawatzky(1994)] M. T. Czyżyk and G. A. Sawatzky. *Local-density functional and on-site correlations: The electronic structure of La_2Cu0_4 and $LaCu0_3$. Phys. Rev. B* **49** (1994)(20): 14211. 37

[Damascelli(2004)] A. Damascelli. *Probing the electronic structure of complex systems by ARPES. Physica Scripta* **2004** (2004)(T109): 61. 19, 23, 115, 165

[Danura *et al.* (2011)] M. Danura, K. Kudo, Y. Oshiro, S. Araki, T. C. Kobayashi, and M. Nohara. *Interplay of Superconductivity and Fermi-Liquid Transport in Rh-Doped CaFe2As2 with Lattice-Collapse Transition. J. Phys. Soc. Jpn.* **80** (2011)(10): 103701. 129, 130

[de Jong *et al.* (2009)] S. de Jong, Y. Huang, R. Huisman, F. Massee, S. Thirupathaiah, M. Gorgoi, F. Schaefers, R. Follath, J. B. Goedkoop, and M. S. Golden. *High-resolution, hard x-ray photoemission investigation of $BaFe_2As_2$: Moderate influence of the surface and evidence for a low degree of Fe $3d$˘As $4p$ hybridization of electronic states near the Fermi energy. Phys. Rev. B* **79** (2009): 115125. 13

[de La Cruz *et al.* (2008)] C. de La Cruz, Q. Huang, J. Lynn, J. Li, W. Ratcliff II, J. L. Zarestky, H. Mook, G. Chen, J. Luo, N. Wang, and P. Dai. *Magnetic order close to superconductivity in the iron-based layered LaO1-xFxFeAs systems*. *Nature* **453** (2008)(7197): 899. 6

[de' Medici(2011)] L. de' Medici. *Hund's coupling and its key role in tuning multiorbital correlations*. *Phys. Rev. B* **83** (2011): 205112. 10

[de' Medici *et al.* (2014)] L. de' Medici, G. Giovannetti, and M. Capone. *Selective Mott Physics as a Key to Iron Superconductors*. *Phys. Rev. Lett.* **112** (2014): 177001. 10, 126

[de' Medici *et al.* (2009)] L. de' Medici, S. R. Hassan, M. Capone, and X. Dai. *Orbital-Selective Mott Transition out of Band Degeneracy Lifting*. *Phys. Rev. Lett.* **102** (2009): 126401. 10

[de' Medici *et al.* (2011)] L. de' Medici, J. Mravlje, and A. Georges. *Janus-Faced Influence of Hund's Rule Coupling in Strongly Correlated Materials*. *Phys. Rev. Lett.* **107** (2011): 256401. 10

[Deppeler and Millis(2002)] A. Deppeler and A. J. Millis. *Electron-phonon interactions in correlated systems: Adiabatic expansion of the dynamical mean-field theory*. *Phys. Rev. B* **65** (2002): 100301. 51

[Dhaka *et al.* (2014)] R. S. Dhaka, R. Jiang, S. Ran, S. L. Bud'ko, P. C. Canfield, B. N. Harmon, A. Kaminski, M. Tomić, R. Valentí, and Y. Lee. *Dramatic changes in the electronic structure upon transition to the collapsed tetragonal phase in $CaFe_2As_2$*. *Phys. Rev. B* **89** (2014): 020511. 129, 132

[Dhaka *et al.* (2013)] R. S. Dhaka, Y. Lee, V. K. Anand, D. C. Johnston, B. N. Harmon, and A. Kaminski. *Angle-resolved photoemission spectroscopy study of $BaCo_2As_2$*. *Phys. Rev. B* **87** (2013): 214516. 7, 105, 106, 129

[Diallo *et al.* (2009)] S. O. Diallo, V. P. Antropov, T. G. Perring, C. Broholm, J. J. Pulikkotil, N. Ni, S. L. Bud'ko, P. C. Canfield, A. Kreyssig, A. I. Goldman, and R. J. McQueeney. *Itinerant Magnetic Excitations in Antiferromagnetic $CaFe_2As_2$*. *Phys. Rev. Lett.* **102** (2009): 187206. 129

[Diehl *et al.* (2014)] J. Diehl, S. Backes, D. Guterding, H. O. Jeschke, and R. Valentí. *Correlation effects in the tetragonal and collapsed-tetragonal phase of $CaFe_2As_2$*. *Phys. Rev. B* **90** (2014): 085110. 129, 139, 159

[Ding *et al.* (2011)] H. Ding, K. Nakayama, P. Richard, S. Souma, T. Sato, T. Takahashi, M. Neupane, Y.-M. Xu, Z.-H. Pan, A. V. Fedorov, Z. Wang, X. Dai, Z. Fang, G. F. Chen, J. L. Luo, and N. L. Wang. *Electronic structure of optimally doped pnictide $Ba_{0.6}K_{0.4}Fe_2As_2$: a comprehensive angle-resolved photoemission spectroscopy investigation*. *J. Phys. Condens. Matter* **23** (2011)(13): 135701. 7, 8, 14, 106, 107, 108, 123, 126, 149

[Ding *et al.* (2008)] H. Ding, P. Richard, K. Nakayama, K. Sugawara, T. Arakane, Y. Sekiba, A. Takayama, S. Souma, T. Sato, T. Takahashi, Z. Wang, X. Dai, Z. Fang, G. F. Chen, J. L. Luo, and N. L. Wang. *Observation of Fermi-surface–dependent nodeless superconducting gaps in $Ba_{0.6}K_{0.4}Fe_2As_2$*. *EPL* **83** (2008)(4): 47001. 7, 13

[Drew *et al.* (2009)] A. J. Drew, C. Niedermayer, P. Baker, F. Pratt, S. Blundell, T. Lancaster, R. Liu, G. Wu, X. Chen, I. Watanabe, V. Malik, A. Dubroka, K. Rössle, K. Kim, C. Baines, and C. Bernhard. *Coexistence of static magnetism and superconductivity in SmFeAsO$_{1-x}$F$_x$ as revealed by muon spin rotation*. *Nat. Mater.* **8** (2009)(4): 310. 6

[Eguchi *et al.* (2006)] R. Eguchi, T. Kiss, S. Tsuda, T. Shimojima, T. Mizokami, T. Yokoya, A. Chainani, S. Shin, I. H. Inoue, T. Togashi, S. Watanabe, C. Q. Zhang, C. T. Chen, M. Arita, K. Shimada, H. Namatame, and M. Taniguchi. *Bulk- and Surface-Sensitive High-Resolution Photoemission Study of Two Mott-Hubbard Systems: $SrVO3$ and $CaVO3$*. *Phys. Rev. Lett.* **96** (2006)(7): 076402. 68

[Fang *et al.* (2008)] M. H. Fang, H. M. Pham, B. Qian, T. J. Liu, E. K. Vehstedt, Y. Liu, L. Spinu, and Z. Q. Mao. *Superconductivity close to magnetic instability in Fe(Se$_{1-x}$Te$_x$)$_{0.82}$*. *Phys. Rev. B* **78** (2008): 224503. 8

[Ferber *et al.* (2012)] J. Ferber, K. Foyevtsova, R. Valentí, and H. O. Jeschke. *LDA + DMFT study of the effects of correlation in LiFeAs*. *Phys. Rev. B* **85** (2012): 094505. 9, 13, 14

[Ferrero and Parcollet(2011)] M. Ferrero and O. Parcollet. *TRIQS: A Toolbox for Research on Interacting Quantum Systems* (2011). 33, 51, 54, 65, 110, 144, 158

[Fink *et al.* (2009)] J. Fink, S. Thirupathaiah, R. Ovsyannikov, H. A. Dürr, R. Follath, Y. Huang, S. de Jong, M. S. Golden, Y.-Z. Zhang, H. O. Jeschke, R. Valentí, C. Felser, S. Dastjani Farahani, M. Rotter, and D. Johrendt. *Electronic structure studies of BaFe$_2$As$_2$ by angle-resolved photoemission spectroscopy*. *Phys. Rev. B* **79** (2009): 155118. 7, 8, 13

[Florens(2003)] S. Florens. *Continuous-Time Quantum Monte-Carlo Algorithms for Fermions*. Ph.D. thesis, Ecole Normale Supérieure (2003). 60

[Furukawa *et al.* (2014)] Y. Furukawa, B. Roy, S. Ran, S. L. Bud'ko, and P. C. Canfield. *Suppression of electron correlations in the collapsed tetragonal phase of CaFe$_2$As$_2$ under ambient pressure demonstrated by ^{75}As NMR/NQR measurements*. *Phys. Rev. B* **89** (2014): 121109. 130

[Georges(2004)] A. Georges. *Strongly Correlated Electron Materials : Dynamical Mean Field Theory and electronic structure*. *Lectures on the physics of highly correlated electron systems VIII* **715** (2004): 3. 30, 34

[Georges and Kotliar(1992)] A. Georges and G. Kotliar. *Hubbard model in infinite dimensions*. *Phys. Rev. B* **45** (1992)(12): 6479. 63

[Georges *et al.* (1996)] A. Georges, G. Kotliar, W. Krauth, and M. J. Rozenberg. *Dynamical mean-field theory of strongly correlated fermion systems and the limit of infinite dimensions*. *Rev. Mod. Phys.* **68** (1996)(1): 13. 9, 30, 165

[Georges *et al.* (2013)] A. Georges, L. d. Medici, and J. Mravlje. *Strong Correlations from Hund's Coupling*. *Annu. Rev. Condens. Matter Phys.* **4** (2013)(1): 137. 10, 123

[Gofryk *et al.* (2014)] K. Gofryk, B. Saparov, T. Durakiewicz, A. Chikina, S. Danzenbächer, D. V. Vyalikh, M. J. Graf, and A. S. Sefat. *Fermi-Surface Reconstruction and Complex Phase Equilibria in CaFe$_2$As$_2$*. *Phys. Rev. Lett.* **112** (2014): 186401. 129

[Goldman *et al.* (2008)] A. I. Goldman, D. N. Argyriou, B. Ouladdiaf, T. Chatterji, A. Kreyssig, S. Nandi, N. Ni, S. L. Bud'ko, P. C. Canfield, and R. J. McQueeney. *Lattice and magnetic instabilities in $CaFe_2As_2$: A single-crystal neutron diffraction study*. *Phys. Rev. B* **78** (2008): 100506. 6

[Hansmann *et al.* (2010)] P. Hansmann, R. Arita, A. Toschi, S. Sakai, G. Sangiovanni, and K. Held. *Dichotomy between Large Local and Small Ordered Magnetic Moments in Iron-Based Superconductors*. *Phys. Rev. Lett.* **104** (2010): 197002. 10, 12, 13, 123

[Hansmann *et al.* (2013)] P. Hansmann, T. Ayral, L. Vaugier, P. Werner, and S. Biermann. *Long-Range Coulomb Interactions in Surface Systems: A First-Principles Description within Self-Consistently Combined GW and Dynamical Mean-Field Theory*. *Phys. Rev. Lett.* **110** (2013): 166401. 51, 63

[Haule and Kotliar(2009)] K. Haule and G. Kotliar. *Coherence and incoherence crossover in the normal state of iron oxypnictides and importance of Hund's rule coupling*. *New J. Phys.* **11** (2009): 025021. 9, 10, 123

[Haule *et al.* (2008)] K. Haule, J. H. Shim, and G. Kotliar. *Correlated Electronic Structure of $LaO_{1-x}F_xFeAs$*. *Phys. Rev. Lett.* **100** (2008): 226402. 9, 13

[He *et al.* (2010)] C. He, Y. Zhang, B. P. Xie, X. F. Wang, L. X. Yang, B. Zhou, F. Chen, M. Arita, K. Shimada, H. Namatame, M. Taniguchi, X. H. Chen, J. P. Hu, and D. L. Feng. *Electronic-Structure-Driven Magnetic and Structure Transitions in Superconducting NaFeAs Single Crystals Measured by Angle-Resolved Photoemission Spectroscopy*. *Phys. Rev. Lett.* **105** (2010): 117002. 7

[Hedin(1965)] L. Hedin. *New Method for Calculating the One-Particle Green's Function with Application to the Electron-Gas Problem*. *Phys. Rev.* **139** (1965)(3A): A796. 14, 49, 63, 67, 112, 157

[Hedin(1999)] —. *On correlation effects in electron spectroscopies and the GW approximation*. *J. Phys. Condens. Matter* **11** (1999)(42): R489. 14, 157

[Held(2007)] K. Held. *Electronic structure calculations using dynamical mean-field theory*. *Advances in Physics* **56** (2007): 829. 37

[Hertz(1887)] H. Hertz. *Ueber einen Einfluss des ultravioletten Lichtes auf die electrische Entladung*. *Annalen der Physik* **267** (1887)(8): 983. 19

[Hettler *et al.* (1998)] M. H. Hettler, A. N. Tahvildar-Zadeh, M. Jarrell, T. Pruschke, and H. R. Krishnamurthy. *Nonlocal dynamical correlations of strongly interacting electron systems*. *Phys. Rev. B* **58** (1998): R7475. 63

[Hoffmann and Zheng(1985)] R. Hoffmann and C. Zheng. *Making and breaking bonds in the solid state: the thorium chromium silicide ($ThCr_2Si_2$) structure*. *J. Phys. Chem.* **89** (1985)(20): 4175. 3

[Hohenberg and Kohn(1964)] P. Hohenberg and W. Kohn. *Inhomogeneous Electron Gas*. *Phys. Rev.* **136** (1964)(3B): B864. 27, 60

[Holm and von Barth(1998)] B. Holm and U. von Barth. *Fully self-consistent* GW *self-energy of the electron gas*. *Phys. Rev. B* **57** (1998): 2108. 67

[Horigane *et al.* (2009)] K. Horigane, H. Hiraka, and K. Ohoyama. *Relationship between Structure and Superconductivity in FeSe1-xTex*. *Journal of the Physical Society of Japan* **78** (2009)(7): 074718. 5

[Hosono(2008)] H. Hosono. *Layered iron pnictide superconductors: discovery and current status*. *J. Phys. Soc. Jpn.* **77** (2008)(Suppl. C): 1. 4

[Hsieh *et al.* (2008)] D. Hsieh, Y. Xia, L. Wray, D. Qian, K. Gomes, A. Yazdani, G. Chen, J. Luo, N. Wang, and M. Hasan. *Experimental determination of the microscopic origin of magnetism in parent iron pnictides*. *arXiv:0812.2289* (2008). 7

[Hsu *et al.* (2008)] F.-C. Hsu, J.-Y. Luo, K.-W. Yeh, T.-K. Chen, T.-W. Huang, P. M. Wu, Y.-C. Lee, Y.-L. Huang, Y.-Y. Chu, D.-C. Yan, and M.-K. Wu. *Superconductivity in the PbO-type structure α-FeSe*. *Proc. Natl. Acad. Sci. U.S.A.* **105** (2008): 14262. 3

[Huang and Wang(2012)] L. Huang and Y. Wang. *Dynamical screening in strongly correlated metal $SrVO_3$*. *EPL* **99** (2012): 67003. 51, 69

[Huang *et al.* (2008a)] Q. Huang, Y. Qiu, W. Bao, M. A. Green, J. W. Lynn, Y. C. Gasparovic, T. Wu, G. Wu, and X. H. Chen. *Neutron-Diffraction Measurements of Magnetic Order and a Structural Transition in the Parent $BaFe_2As_2$ Compound of FeAs-Based High-Temperature Superconductors*. *Phys. Rev. Lett.* **101** (2008a): 257003. 6, 10

[Huang *et al.* (2008b)] Q. Huang, J. Zhao, J. W. Lynn, G. F. Chen, J. L. Luo, N. L. Wang, and P. Dai. *Doping evolution of antiferromagnetic order and structural distortion in $LaFeAsO_{1-x}F_x$*. *Phys. Rev. B* **78** (2008b): 054529. 6

[Huang *et al.* (2010)] S. X. Huang, C. L. Chien, V. Thampy, and C. Broholm. *Control of Tetrahedral Coordination and Superconductivity in $FeSe_{0.5}Te_{0.5}$ Thin Films*. *Phys. Rev. Lett.* **104** (2010): 217002. 5

[Hubbard(1963)] J. Hubbard. *Electron Correlations in Narrow Energy Bands*. *Proc. R. Soc. London A* **276** (1963)(1): 238. 30

[Hubbard(1964)] —. *Electron Correlations in Narrow Energy Bands. II. The Degenerate Band Case*. *Proc. R. Soc. London A* **277** (1964)(1369): 237. 30

[Hüfner(2003)] S. Hüfner. *Photoelectron spectroscopy: principles and applications*. Springer (2003). 19, 22

[Ieki *et al.* (2014)] E. Ieki, K. Nakayama, Y. Miyata, T. Sato, H. Miao, N. Xu, X.-P. Wang, P. Zhang, T. Qian, P. Richard, Z.-J. Xu, J. S. Wen, G. D. Gu, H. Q. Luo, H.-H. Wen, H. Ding, and T. Takahashi. *Evolution from incoherent to coherent electronic states and its implications for superconductivity in $FeTe_{1-x}Se_x$*. *Phys. Rev. B* **89** (2014): 140506. 8

[Ishida and Liebsch(2010)] H. Ishida and A. Liebsch. *Fermi-liquid, non-Fermi-liquid, and Mott phases in iron pnictides and cuprates*. *Phys. Rev. B* **81** (2010)(5): 054513. 123, 126

[Ishida *et al.* (2009)] K. Ishida, Y. Nakai, and H. Hosono. *To What Extent Iron-Pnictide New Superconductors Have Been Clarified: A Progress Report*. *J. Phys. Soc. Jpn.* **78** (2009): 062001. 10

[Jarrell and Gubernatic(1996)] M. Jarrell and J. Gubernatic. *Bayesian inference and the analytic continuation of imaginary-time quantum Monte Carlo data. Phys. Rep.* **269** (1996): 133. 61, 163

[Jayasekara *et al.* (2013)] W. Jayasekara, Y. Lee, A. Pandey, G. S. Tucker, A. Sapkota, J. Lamsal, S. Calder, D. L. Abernathy, J. L. Niedziela, B. N. Harmon, A. Kreyssig, D. Vaknin, D. C. Johnston, A. I. Goldman, and R. J. McQueeney. *Stripe Antiferromagnetic Spin Fluctuations in $SrCo_2As_2$. Phys. Rev. Lett* **111** (2013): 157001. 106

[Jiang *et al.* (2012)] H. Jiang, Y.-L. Sun, J. Dai, G.-H. Cao, and C. Cao. *Self-doping effect and possible antiferromagnetism at titanium-layers in the iron-based superconductor $Ba_2Ti_2Fe_2As_4O$. arXiv:1207.6705* (2012). 141

[Johnston(2010)] D. C. Johnston. *The puzzle of high temperature superconductivity in layered iron pnictides and chalcogenides. Adv. in Phys.* **59** (2010)(6): 803. 5

[Judd(1998)] B. R. Judd. *Operator Techniques in Atomic Spectroscopy*. Princeton University Press (1998). 42

[Kamerlingh Onnes(1911a)] H. Kamerlingh Onnes. *Further experiments with liquid helium. C. On the change of electric resistance of pure metals at very low temperatures etc. IV. The resistance of pure mercury at helium temperatures. Proc. K. Ned. Akad. Wet.* **13** (1911a)(II): 1274. 3

[Kamerlingh Onnes(1911b)] —. *Further experiments with Liquid Helium. D. On the change of Electrical Resistance of Pure Metals at very low Temperatures, etc. V. The Disappearance of the resistance of mercury. Proc. K. Ned. Akad. Wet.* **14** (1911b)(I): 113. 3

[Kamihara *et al.* (2006)] Y. Kamihara, H. Hiramatsu, M. Hirano, R. Kawamura, H. Yanagi, T. Kamiya, and H. Hosono. *Iron-Based Layered Superconductor:âĂL' LaOFeP. J. Am. Chem. Soc.* **128** (2006): 3296. 3

[Kamihara *et al.* (2008)] Y. Kamihara, T. Watanabe, M. Hirano, and H. Hosono. *Iron-Based Layered Superconductor $La[O_{1-x}F_x]FeAs$ (x = 0.05âĹŠ0.12) with Tc = 26 K. J. Am. Chem. Soc.* **130** (2008): 3296. 3

[Karolak *et al.* (2010)] M. Karolak, G. Ulm, T. Wehling, V. Mazurenko, A. Poteryaev, and A. Lichtenstein. *Double counting in LDA+DMFT - The example of NiO. Journal of Electron Spectroscopy and Related Phenomena : Proceedings of International Workshop on Strong Correlations and Angle-Resolved Photoemission Spectroscopy 2009* **181** (2010): 11. 37

[Kasahara *et al.* (2011)] S. Kasahara, T. Shibauchi, K. Hashimoto, Y. Nakai, H. Ikeda, T. Terashima, and Y. Matsuda. *Abrupt recovery of Fermi-liquid transport following the collapse of the c axis in $CaFe_2(As_{1-x}P_x)_2$ single crystals. Phys. Rev. B* **83** (2011): 060505. 129, 130

[Katase *et al.* (2011)] T. Katase, Y. Ishimaru, A. Tsukamoto, H. Hiramatsu, T. Kamiya, K. Tanabe, and H. Hosono. *Advantageous grain boundaries in iron pnictide superconductors. Nat. Commun.* **2** (2011): 409. 5

[Kihou *et al.* (2010)] K. Kihou, C. H. Lee, K. Miyazawa, P. M. Shirage, A. Iyo, and H. Eisaki. *Thermoelectric properties of $LaFeAsO_{1y}$ at low temperature*. *J. Appl. Phys* **108** (2010)(3): 033703. 5

[Kimber *et al.* (2009)] S. A. Kimber, A. Kreyssig, Y.-Z. Zhang, H. O. Jeschke, R. Valentí, F. Yokaichiya, E. Colombier, J. Yan, T. C. Hansen, T. Chatterji, R. McQueeney, P. Canfield, A. Goldman, and D. Argyriou. *Similarities between structural distortions under pressure and chemical doping in superconducting BaFe2As2*. *Nat. Mater.* **8** (2009)(6): 471. 5

[Kitagawa *et al.* (2009)] K. Kitagawa, N. Katayama, K. Ohgushi, and M. Takigawa. *Antiferromagnetism of SrFe2As2 Studied by Single-Crystal 75As-NMR*. *J. Phys. Soc. Jpn* **78** (2009)(6). 6

[Kitagawa *et al.* (2008)] K. Kitagawa, N. Katayama, K. Ohgushi, M. Yoshida, and M. Takigawa. *Commensurate itinerant antiferromagnetism in BaFe2As2: 75As-NMR studies on a self-flux grown single crystal*. *J. Phys. Soc. Jpn* **77** (2008)(11). 6

[Kohn(1999)] W. Kohn. *Nobel Lecture: Electronic structure of matter—wave functions and density functionals*. *Rev. Mod. Phys.* **71** (1999)(5): 1253. 30

[Kohn and Sham(1965)] W. Kohn and L. J. Sham. *Self-Consistent Equations Including Exchange and Correlation Effects*. *Phys. Rev.* **140** (1965)(4A): A1133. 28

[Koller *et al.* (2004)] W. Koller, D. Meyer, Y. Ōno, and A. Hewson. *First-and second-order phase transitions in the Holstein-Hubbard model*. *EPL* **66** (2004)(4): 559. 51

[Kondo *et al.* (2008)] T. Kondo, A. F. Santander-Syro, O. Copie, C. Liu, M. E. Tillman, E. D. Mun, J. Schmalian, S. L. Bud'ko, M. A. Tanatar, P. C. Canfield, and A. Kaminski. *Momentum Dependence of the Superconducting Gap in $NdFeAsO_{0.9}F_{0.1}$ Single Crystals Measured by Angle Resolved Photoemission Spectroscopy*. *Phys. Rev. Lett.* **101** (2008): 147003. 7

[Kordyuk *et al.* (2011)] A. A. Kordyuk, V. B. Zabolotnyy, D. V. Evtushinsky, T. K. Kim, I. V. Morozov, M. L. Kulić, R. Follath, G. Behr, B. Büchner, and S. V. Borisenko. *Angle-resolved photoemission spectroscopy of superconducting LiFeAs: Evidence for strong electron-phonon coupling*. *Phys. Rev. B* **83** (2011): 134513. 14

[Kotani *et al.* (2007)] T. Kotani, M. van Schilfgaarde, and S. V. Faleev. *Quasiparticle self-consistent GW method: A basis for the independent-particle approximation*. *Phys. Rev. B* **76** (2007): 165106. 112

[Kotliar *et al.* (2006)] G. Kotliar, S. Y. Savrasov, K. Haule, V. S. Oudovenko, O. Parcollet, and C. A. Marianetti. *Electronic structure calculations with dynamical mean-field theory*. *Rev. Mod. Phys.* **78** (2006)(3): 865. 9, 30

[Kotliar *et al.* (2001)] G. Kotliar, S. Y. Savrasov, G. Pálsson, and G. Biroli. *Cellular Dynamical Mean Field Approach to Strongly Correlated Systems*. *Phys. Rev. Lett.* **87** (2001)(18): 186401. 63

[Kreyssig *et al.* (2008)] A. Kreyssig, M. A. Green, Y. Lee, G. D. Samolyuk, P. Zajdel, J. W. Lynn, S. L. Bud'ko, M. S. Torikachvili, N. Ni, S. Nandi, J. B. Leão, S. J. Poulton, D. N.

Argyriou, B. N. Harmon, R. J. McQueeney, P. C. Canfield, and A. I. Goldman. *Pressure-induced volume-collapsed tetragonal phase of $CaFe_2As_2$ as seen via neutron scattering*. *Phys. Rev. B* **78** (2008): 184517. 129

[Krivenko and Biermann(2014)] I. S. Krivenko and S. Biermann. *A slave rotor approach to dynamically screened Coulomb interactions in solids*. *arxiv:1405.1263v1* (2014). 57

[Kuchinskii *et al.* (2005)] E. Z. Kuchinskii, I. A. Nekrasov, and M. V. Sadovskii. *Destruction of the Fermi surface due to pseudogap fluctuations in strongly correlated systems*. *JETP* **82** (2005)(4): 198. 63

[Kuroki *et al.* (2009)] K. Kuroki, H. Usui, S. Onari, R. Arita, and H. Aoki. *Pnictogen height as a possible switch between high-T_c nodeless and low-T_c nodal pairings in the iron-based superconductors*. *Phys. Rev. B* **79** (2009): 224511. 5

[Kutepov *et al.* (2010)] A. Kutepov, K. Haule, S. Y. Savrasov, and G. Kotliar. *Self-consistent GW determination of the interaction strength: Application to the iron arsenide superconductors*. *Phys. Rev. B* **82** (2010)(4): 045105. 43

[Lanatà *et al.* (2013)] N. Lanatà, H. U. R. Strand, G. Giovannetti, B. Hellsing, L. de' Medici, and M. Capone. *Orbital selectivity in Hund's metals: The iron chalcogenides*. *Phys. Rev. B* **87** (2013): 045122. 10

[Lang and Firsov(1962)] I. J. Lang and Y. A. Firsov. *Kinetic theory of small mobility semiconductors*. *Sov. Phys. JETP* **16** (1962): 1301. 52

[Lee *et al.* (2008)] C.-H. Lee, A. Iyo, H. Eisaki, H. Kito, M. Teresa Fernandez-Diaz, T. Ito, K. Kihou, H. Matsuhata, M. Braden, and K. Yamada. *Effect of Structural Parameters on Superconductivity in Fluorine-Free $LnFeAsO_{1-y}$ (Ln = La, Nd)*. *J. Phys. Soc. Jpn.* **77** (2008)(8): 083704. 5

[Lee *et al.* (2012)] G. Lee, H. S. Ji, Y. Kim, C. Kim, K. Haule, G. Kotliar, B. Lee, S. Khim, K. H. Kim, K. S. Kim, K.-S. Kim, and J. H. Shim. *Orbital Selective Fermi Surface Shifts and Mechanism of High T_c Superconductivity in Correlated AFeAs (A=Li, Na)*. *Phys. Rev. Lett.* **109** (2012): 177001. 14

[Lester *et al.* (2009)] C. Lester, J.-H. Chu, J. G. Analytis, S. C. Capelli, A. S. Erickson, C. L. Condron, M. F. Toney, I. R. Fisher, and S. M. Hayden. *Neutron scattering study of the interplay between structure and magnetism in $Ba(Fe_{1-x}Co_x)_2As_2$*. *Phys. Rev. B* **79** (2009): 144523. 6

[Li *et al.* (2009)] S. Li, C. de la Cruz, Q. Huang, Y. Chen, J. W. Lynn, J. Hu, Y.-L. Huang, F.-C. Hsu, K.-W. Yeh, M.-K. Wu, and P. Dai. *First-order magnetic and structural phase transitions in $Fe_{1+y}Se_xTe_{1-x}$*. *Phys. Rev. B* **79** (2009): 054503. 10

[Lichtenstein *et al.* (1995)] A. I. Lichtenstein, V. I. Anisimov, and J. Zaanen. *Density-functional theory and strong interactions: Orbital ordering in Mott-Hubbard insulators*. *Phys. Rev. B* **52** (1995)(8): R5467. 39

[Lichtenstein and Katsnelson(1998)] A. I. Lichtenstein and M. I. Katsnelson. *Ab initio calculations of quasiparticle band structure in correlated systems: LDA++ approach*. *Phys. Rev. B* **57** (1998)(12): 6884. 9, 34

[Lichtenstein and Katsnelson(2000)] —. *Antiferromagnetism and d-wave superconductivity in cuprates: A cluster dynamical mean-field theory*. *Phys. Rev. B* **62** (2000): R9283. 63

[Lichtenstein *et al.* (2001)] A. I. Lichtenstein, M. I. Katsnelson, and G. Kotliar. *Finite-Temperature Magnetism of Transition Metals: An ab initio Dynamical Mean-Field Theory*. *Phys. Rev. Lett.* **87** (2001)(6): 067205. 37

[Liebsch and Ishida(2010)] A. Liebsch and H. Ishida. *Correlation-induced spin freezing transition in FeSe: A dynamical mean field study*. *Phys. Rev. B* **82** (2010)(15): 155106. 123

[Lin *et al.* (2011)] C.-H. Lin, T. Berlijn, L. Wang, C.-C. Lee, W.-G. Yin, and W. Ku. *One-Fe versus Two-Fe Brillouin Zone of Fe-Based Superconductors: Creation of the Electron Pockets by Translational Symmetry Breaking*. *Phys. Rev. Lett.* **107** (2011): 257001. 21, 146

[Lin *et al.* (2013)] P.-H. Lin, Y. Texier, A. Taleb-Ibrahimi, P. Le Fèvre, F. Bertran, E. Giannini, M. Grioni, and V. Brouet. *Nature of the Bad Metallic Behavior of* $\mathrm{Fe_{1.06}Te}$ *Inferred from Its Evolution in the Magnetic State*. *Phys. Rev. Lett.* **111** (2013): 217002. 9

[Liu *et al.* (2009)] C. Liu, T. Kondo, A. Palczewski, G. Samolyuk, L. Y., M. Tillman, N. Ni, E. Mun, R. Gordon, A. Santander-Syro, S. Bud'ko, J. McChesney, E. Rotenberg, A. Fedorov, T. Valla, O. Copie, M. Tanatar, C. Martin, B. Harmon, P. Canfield, R. Prozorov, J. Schmalian, and A. Kaminski. *Electronic properties of iron arsenic high temperature superconductors revealed by angle resolved photoemission spectroscopy (ARPES)*. *Physica C* **469** (2009)(9-12): 491. 7, 14

[Liu *et al.* (2008)] C. Liu, G. D. Samolyuk, Y. Lee, N. Ni, T. Kondo, A. F. Santander-Syro, S. L. Bud'ko, J. L. McChesney, E. Rotenberg, T. Valla, A. V. Fedorov, P. C. Canfield, B. N. Harmon, and A. Kaminski. *K-Doping Dependence of the Fermi Surface of the Iron-Arsenic* $Ba_{1-x}K_xFe_2As_2$ *Superconductor Using Angle-Resolved Photoemission Spectroscopy*. *Phys. Rev. Lett.* **101** (2008): 177005. 13

[Liu *et al.* (2010)] T. Liu, J. Hu, B. Qian, D. Fobes, Z. Mao, W. Bao, M. Reehuis, S. Kimber, K. Prokeš, S. Matas, D. Argyriou, A. Hiess, A. Rotaru, H. Pham, L. Spinu, Y. Qiu, V. Thampy, A. Savici, J. Rodriguez, and C. Broholm. *From* $(\pi, 0)$ *magnetic order to superconductivity with* (π, π) *magnetic resonance in* $Fe_{1.02}Te_{1-x}Se_x$. *Nat. Mater.* **9** (2010)(9): 718. 8

[Liu *et al.* (2011)] Z.-H. Liu, P. Richard, K. Nakayama, G.-F. Chen, S. Dong, J.-B. He, D.-M. Wang, T.-L. Xia, K. Umezawa, T. Kawahara, S. Souma, T. Sato, T. Takahashi, T. Qian, Y. Huang, N. Xu, Y. Shi, H. Ding, and S.-C. Wang. *Unconventional superconducting gap in* $NaFe_{0.95}Co_{0.05}As$ *observed by angle-resolved photoemission spectroscopy*. *Phys. Rev. B* **84** (2011): 064519. 7

[Lu *et al.* (2009)] D. Lu, M. Yi, S.-K. Mo, J. Analytis, J.-H. Chu, A. Erickson, D. Singh, Z. Hussain, T. Geballe, I. Fisher, and Z.-X. Shen. *ARPES studies of the electronic structure of LaOFe(P,As)*. *Physica C* **469** (2009)(9-12): 452. 7, 8

[Lu *et al.* (2008)] D. Lu, M. Yi, S.-K. Mo, A. Erickson, J. Analytis, J.-H. Chu, D. Singh, Z. Hussain, T. Geballe, I. Fisher, and Z. Shen. *Electronic structure of the iron-based superconductor LaOFeP*. *Nature* **455** (2008)(7209): 81. 8

[Lynn and Dai(2009)] J. W. Lynn and P. Dai. *Neutron studies of the iron-based family of high T_c magnetic superconductors*. *Physica C* **469** (2009)(9-12): 469. Superconductivity in Iron-Pnictides. 4, 6

[Ma *et al.* (2014)] J.-Z. Ma, A. van Roekeghem, P. Richard, Z.-H. Liu, H. Miao, L.-K. Zeng, N. Xu, M. Shi, C. Cao, J.-B. He, G.-F. Chen, Y.-L. Sun, G.-H. Cao, S.-C. Wang, S. Biermann, T. Qian, and H. Ding. *Correlation-induced self-doping in the iron-pnictide superconductor $Ba_2Ti_2Fe_2As_4O$*. *Phys. Rev. Lett.* **113** (2014): 266407. 141

[Macridin *et al.* (2004)] A. Macridin, G. A. Sawatzky, and M. Jarrell. *Two-dimensional Hubbard-Holstein bipolaron*. *Phys. Rev. B* **69** (2004): 245111. 51

[Mahan(1990)] G. D. Mahan. *Many-Particle Physics*. Plenum Press, New York and London (1990). 68, 163, 164

[Maier *et al.* (2005)] T. Maier, M. Jarrell, T. Pruschke, and M. H. Hettler. *Quantum cluster theories*. *Rev. Mod. Phys.* **77** (2005): 1027. 63

[Malaeb *et al.* (2009)] W. Malaeb, T. Yoshida, A. Fujimori, M. Kubota, K. Ono, K. Kihou, P. M. Shirage, H. Kito, A. Iyo, H. Eisaki, Y. Nakajima, T. Tamegai, and R. Arita. *Three-Dimensional Electronic Structure of Superconducting Iron Pnictides Observed by Angle-Resolved Photoemission Spectroscopy*. *J. Phys. Soc. Jpn.* **78** (2009)(12): 123706. 13

[Malaeb *et al.* (2008)] W. Malaeb, T. Yoshida, A. Fujimori, M. Kubota, K. Ono, K. Kihou, P. M. Shirage, H. Kito, A. Iyo, H. Eisaki, Y. Nakajima, T. Tamegai, and R. Arita. *Three-Dimensional Electronic Structure of Superconducting Iron Pnictides Observed by Angle-Resolved Photoemission Spectroscopy*. *J. Phys. Soc. Jpn.* **78** (2008): 123706. 7, 107

[Mandal *et al.* (2014)] S. Mandal, R. E. Cohen, and K. Haule. *Pressure suppression of electron correlation in the collapsed tetragonal phase of $CaFe_2As_2$: A DFT-DMFT investigation*. *Phys. Rev. B* **90** (2014): 060501. 129, 139, 159

[Marchand and Jeitschko(1978)] R. Marchand and W. Jeitschko. *Ternary lanthanoid-transition metal pnictides with $ThCr_2Si_2$-type structure*. *J. Solid State Chem.* **24** (1978): 351. 3

[Mazin *et al.* (2008a)] I. I. Mazin, M. D. Johannes, L. Boeri, K. Koepernik, and D. J. Singh. *Problems with reconciling density functional theory calculations with experiment in ferropnictides*. *Phys. Rev. B* **78** (2008a): 085104. 10, 14

[Mazin *et al.* (2008b)] I. I. Mazin, D. J. Singh, M. D. Johannes, and M. H. Du. *Unconventional Superconductivity with a Sign Reversal in the Order Parameter of $LaFeAsO_{1-x}F_x$*. *Phys. Rev. Lett.* **101** (2008b): 057003. 13

[Mewis(1980)] A. Mewis. *Ternäre Phosphide mit $ThCr_2Si_2$-Struktur*. *Z. Naturforsch. B* **35 b** (1980): 141. 3

[Misawa *et al.* (2012)] T. Misawa, K. Nakamura, and M. Imada. *Ab Initio Evidence for Strong Correlation Associated with Mott Proximity in Iron-Based Superconductors*. *Phys. Rev. Lett.* **108** (2012): 177007. 126

[Miyake *et al.* (2010)] T. Miyake, K. Nakamura, R. Arita, and M. Imada. *Comparison of Ab initio Low-Energy Models for LaFePO, LaFeAsO, BaFe2As2, LiFeAs, FeSe and FeTe: Electron Correlation and Covalency*. *J. Phys. Soc. Jpn.* **79** (2010): 044705. 80, 81

[Miyake *et al.* (2008)] T. Miyake, L. Pourovskii, V. Vildosola, S. Biermann, and A. Georges. *d- and f-Orbital Correlations in the REFeAsO Compounds*. *J. Phys. Soc. Jpn. : Supplement C* **77** (2008): 99. 9

[Mizuguchi *et al.* (2010)] Y. Mizuguchi, Y. Hara, K. Deguchi, S. Tsuda, T. Yamaguchi, K. Takeda, H. Kotegawa, H. Tou, and Y. Takano. *Anion height dependence of T_c for the Fe-based superconductor*. *Superconductor Science and Technology* **23** (2010)(5): 054013. 5

[Mizuguchi and Takano(2010)] Y. Mizuguchi and Y. Takano. *Review of Fe Chalcogenides as the Simplest Fe-Based Superconductor*. *J. Phys. Soc. Jpn* **79** (2010)(10): 102001. 8

[Morikawa *et al.* (1995)] K. Morikawa, T. Mizokawa, K. Kobayashi, A. Fujimori, H. Eisaki, S. Uchida, F. Iga, and Y. Nishihara. *Spectral weight transfer and mass renormalization in Mott-Hubbard systems $SrVO_3$ and $CaVO_3$: Influence of long-range Coulomb interaction*. *Phys. Rev. B* **52** (1995)(19): 13711. 69

[Müller-Hartmann(1989)] E. Müller-Hartmann. *The Hubbard model at high dimensions : some exact results and weak coupling theory*. *Zeitschrift für Physik B Condensed Matter* **76** (1989)(2): 211. 63

[Nakayama *et al.* (2010)] K. Nakayama, T. Sato, P. Richard, T. Kawahara, Y. Sekiba, T. Qian, G. F. Chen, J. L. Luo, N. L. Wang, H. Ding, and T. Takahashi. *Angle-Resolved Photoemission Spectroscopy of the Iron-Chalcogenide Superconductor $Fe_{1.03}Te_{0.7}Se_{0.3}$: Strong Coupling Behavior and the Universality of Interband Scattering*. *Phys. Rev. Lett.* **105** (2010): 197001. 7

[Neupane *et al.* (2011)] M. Neupane, P. Richard, Y.-M. Xu, K. Nakayama, T. Sato, T. Takahashi, A. V. Federov, G. Xu, X. Dai, Z. Fang, Z. Wang, G.-F. Chen, N.-L. Wang, H.-H. Wen, and H. Ding. *Electron-hole asymmetry in the superconductivity of doped $BaFe_2As_2$ seen via the rigid chemical-potential shift in photoemission*. *Phys. Rev. B* **83** (2011): 094522. 6

[Ni *et al.* (2008)] N. Ni, S. Nandi, A. Kreyssig, A. I. Goldman, E. D. Mun, S. L. Bud'ko, and P. C. Canfield. *First-order structural phase transition in $CaFe_2As_2$*. *Phys. Rev. B* **78** (2008): 014523. 129

[Nomura *et al.* (2008)] T. Nomura, S. W. Kim, Y. Kamihara, M. Hirano, P. V. Sushko, K. Kato, M. Takata, A. L. Shluger, and H. Hosono. *Crystallographic phase transition and high-Tc superconductivity in LaFeAsO: F*. *Superconductor Science and Technology* **21** (2008)(12): 125028. 6

[Ogino *et al.* (2009)] H. Ogino, Y. Matsumura, Y. Katsura, K. Ushiyama, S. Horii, K. Kishio, and J.-i. Shimoyama. *Superconductivity at 17 K in $(Fe_2P_2)(Sr_4Sc_2O_6)$: a new superconducting layered pnictide oxide with a thick perovskite oxide layer*. *Superconductor Science and Technology* **22** (2009)(7): 075008. 4

[Okabe *et al.* (2010)] H. Okabe, N. Takeshita, K. Horigane, T. Muranaka, and J. Akimitsu. *Pressure-induced high-T_c superconducting phase in FeSe: Correlation between anion height and T_c*. *Phys. Rev. B* **81** (2010): 205119. 5

[Pandey *et al.* (2013)] A. Pandey, D. G. Quirinale, W. Jayasekara, A. Sapkota, M. G. Kim, R. S. Dhaka, Y. Lee, T. W. Heitmann, P. W. Stephens, V. Ogloblichev, A. Kreyssig, R. J. McQueeney, A. I. Goldman, A. Kaminski, B. N. Harmon, Y. Furukawa, and D. C. Johnston. *Crystallographic, electronic, thermal, and magnetic properties of single-crystal $SrCo_2As_2$. Phys. Rev. B* **88** (2013): 014526. 106

[Parcollet *et al.* (2004)] O. Parcollet, G. Biroli, and G. Kotliar. *Cluster Dynamical Mean Field Analysis of the Mott Transition. Phys. Rev. Lett.* **92** (2004)(22): 226402. 63

[Petukhov *et al.* (2003)] A. G. Petukhov, I. I. Mazin, L. Chioncel, and A. I. Lichtenstein. *Correlated metals and the LDA+U method. Phys. Rev. B* **67** (2003): 153106. 30, 36

[Pines(1964)] D. Pines. *Elementary excitations in solids : lectures on phonons, electrons, and plasmons*. W.A. Benjamin (1964). 60, 93

[Pinsard-Gaudart *et al.* (2008)] L. Pinsard-Gaudart, D. BÃl'rardan, J. Bobroff, and N. Dragoe. *Large Seebeck coefficients in iron-oxypnictides: a new route towards n-type thermoelectric materials. Phys. Stat. Sol. (RRL)* **2** (2008)(4): 185. 5

[Pinsard-Gaudart and Dragoe(2008)] L. Pinsard-Gaudart and N. Dragoe. *Large Thermoelectric Power Factor in Iron-Pnictide Derivatives. J. Phys. Soc. Jpn.* **77** (2008)(Suppl.C): 58. 5

[Pitcher *et al.* (2008)] M. J. Pitcher, D. R. Parker, P. Adamson, S. J. Herkelrath, A. T. Boothroyd, R. M. Ibberson, M. Brunelli, and S. J. Clarke. *Structure and superconductivity of LiFeAs. Chem. Commun.* (2008)(45): 5918. 3

[Pratt *et al.* (2009)] D. K. Pratt, W. Tian, A. Kreyssig, J. L. Zarestky, S. Nandi, N. Ni, S. L. Bud'ko, P. C. Canfield, A. I. Goldman, and R. J. McQueeney. *Coexistence of Competing Antiferromagnetic and Superconducting Phases in the Underdoped $Ba(Fe_{0.953}Co_{0.047})_2As_2$ Compound Using X-ray and Neutron Scattering Techniques. Phys. Rev. Lett.* **103** (2009): 087001. 6

[Prozorov *et al.* (2008)] R. Prozorov, N. Ni, M. A. Tanatar, V. G. Kogan, R. T. Gordon, C. Martin, E. C. Blomberg, P. Prommapan, J. Q. Yan, S. L. Bud'ko, and P. C. Canfield. *Vortex phase diagram of $Ba(Fe_{0.93}Co_{0.07})_2As_2$ single crystals. Phys. Rev. B* **78** (2008): 224506. 5

[Putti *et al.* (2010)] M. Putti, I. Pallecchi, E. Bellingeri, M. R. Cimberle, M. Tropeano, C. Ferdeghini, A. Palenzona, C. Tarantini, A. Yamamoto, J. Jiang, J. Jaroszynski, F. Kametani, D. Abraimov, A. Polyanskii, J. D. Weiss, E. E. Hellstrom, A. Gurevich, D. C. Larbalestier, R. Jin, B. C. Sales, A. S. Sefat, M. A. McGuire, D. Mandrus, P. Cheng, Y. Jia, H. H. Wen, S. Lee, and C. B. Eom. *New Fe-based superconductors: properties relevant for applications. Supercond. Sci. Technol.* **23** (2010)(3): 034003. 4, 5

[Qureshi *et al.* (2010)] N. Qureshi, Y. Drees, J. Werner, S. Wurmehl, C. Hess, R. Klingeler, B. Büchner, M. T. Fernandez-Diaz, and M. Braden. *Crystal and magnetic structure of the oxypnictide superconductor $LaFeAsO_{1-x}F_x$: A neutron-diffraction study. Phys. Rev. B* **82** (2010): 184521. 10

[Ran *et al.* (2011)] S. Ran, S. L. Bud'ko, D. K. Pratt, A. Kreyssig, M. G. Kim, M. J. Kramer, D. H. Ryan, W. N. Rowan-Weetaluktuk, Y. Furukawa, B. Roy, A. I. Goldman, and P. C. Canfield. *Stabilization of an ambient-pressure collapsed tetragonal phase in $CaFe_2As_2$*

and tuning of the orthorhombic-antiferromagnetic transition temperature by over 70 K via control of nanoscale precipitates. *Phys. Rev. B* **83** (2011): 144517. 129

[Ren *et al.* (2008)] Z.-A. Ren, L. Wei, Y. Jie, Y. Wei, S. Xiao-Li, Zheng-Cai, C. Guang-Can, D. Xiao-Li, S. Li-Ling, Z. Fang, and Z. Zhong-Xian. *Superconductivity at 55 K in Iron-Based F-Doped Layered Quaternary Compound Sm[$O_{1-x}F_x$]FeAs*. *Chin. Phys. Lett.* **25** (2008): 2215. 3

[Richard *et al.* (2010)] P. Richard, K. Nakayama, T. Sato, M. Neupane, Y.-M. Xu, J. H. Bowen, G. F. Chen, J. L. Luo, N. L. Wang, X. Dai, Z. Fang, H. Ding, and T. Takahashi. *Observation of Dirac Cone Electronic Dispersion in $BaFe_2As_2$*. *Phys. Rev. Lett.* **104** (2010): 137001. 123

[Richard *et al.* (2011)] P. Richard, T. Sato, K. Nakayama, T. Takahashi, and H. Ding. *Fe-based superconductors: an angle-resolved photoemission spectroscopy perspective*. *Rep. Prog. Phys.* **74** (2011)(12): 124512. 7, 19, 21

[Rieger and Parthé(1969)] W. Rieger and E. Parthé. *Ternäre Erdalkali-und Seltene Erdmetall-Silicide und-Germanide mit ThCr2Si2-Struktur*. *Monatsh. Chem.* **100** (1969)(2): 444. 3

[Ronning *et al.* (2008)] F. Ronning, T. Klimczuk, E. D. Bauer, H. Volz, and J. D. Thompson. *Synthesis and properties of $CaFe_2As_2$Âăsingle crystals*. *J. Phys.: Condens. Matter* **20** (2008)(32): 322201. 129

[Rotter *et al.* (2008a)] M. Rotter, M. Pangerl, M. Tegel, and D. Johrendt. *Superconductivity and Crystal Structures of (Ba1âĹŠxKx)Fe2As2 (x=0âĂŞ1)*. *Angew. Chem. Int. Edn.* **47** (2008a)(41): 7949. 6

[Rotter *et al.* (2008b)] M. Rotter, M. Tegel, and D. Johrendt. *Superconductivity at 38 K in the Iron Arsenide $Ba_{1-x}K_xFe_2As_2$*. *Phys. Rev. Lett.* **101** (2008b): 107006. 4

[Rotter *et al.* (2008c)] M. Rotter, M. Tegel, D. Johrendt, I. Schellenberg, W. Hermes, and R. Pöttgen. *Spin-density-wave anomaly at 140 K in the ternary iron arsenide $BaFe_2As_2$*. *Phys. Rev. B* **78** (2008c): 020503. 6

[Rózsa and Schuster(1981)] S. Rózsa and H.-U. Schuster. *Zur Struktur von KFe_2As_2, KCo_2As_2, KRh_2As_2 und KRh_2P_2*. *Z. Naturforsch. B* **86 b** (1981): 1668. 3

[Saha *et al.* (2012)] S. R. Saha, N. P. Butch, T. Drye, J. Magill, S. Ziemak, K. Kirshenbaum, P. Y. Zavalij, J. W. Lynn, and J. Paglione. *Structural collapse and superconductivity in rare-earth-doped $CaFe_2As_2$*. *Phys. Rev. B* **85** (2012): 024525. 129, 130

[Sakuma *et al.* (2013)] R. Sakuma, P. Werner, and F. Aryasetiawan. *Electronic structure of $SrVO_3$ within GW+DMFT*. *Phys. Rev. B* **88** (2013): 235110. 51, 64

[Saparov *et al.* (2014)] B. Saparov, C. Cantoni, M. Pan, T. C. Hogan, W. Ratcliff II, S. D. Wilson, K. Fritsch, B. D. Gaulin, and A. S. Sefat. *Complex structures of different $CaFe_2As_2$ samples*. *Sci. Rep.* **4** (2014). 129, 130, 131, 132

[Sato *et al.* (2009)] T. Sato, K. Nakayama, Y. Sekiba, P. Richard, Y.-M. Xu, S. Souma, T. Takahashi, G. F. Chen, J. L. Luo, N. L. Wang, and H. Ding. *Band Structure and Fermi Surface of an Extremely Overdoped Iron-Based Superconductor KFe_2As_2*. *Phys. Rev. Lett.* **103** (2009): 047002. 7, 8

[Satya *et al.* (2011)] A. T. Satya, A. Mani, A. Arulraj, N. V. C. Shekar, K. Vinod, C. S. Sundar, and A. Bharathi. *Pressure-induced metallization of $BaMn_2As_2$*. *Phys. Rev. B* **84** (2011): 180515. 126

[Sawatzky *et al.* (1975)] G. Sawatzky, P. Kuindersma, and J. Kommandeur. *Electronic polarization reduction of the on site electron-electron repulsion*. *Solid State Commun.* **17** (1975)(5): 569. 51

[Sawatzky and Allen(1984)] G. A. Sawatzky and J. W. Allen. *Magnitude and Origin of the Band Gap in NiO*. *Phys. Rev. Lett.* **53** (1984): 2339. 44

[Sawatzky *et al.* (2009)] G. A. Sawatzky, I. S. Elfimov, J. van den Brink, and J. Zaanen. *Heavy-anion solvation of polarity fluctuations in pnictides*. *Eur. Phys. Lett.* **86** (2009): 17006. 10

[Schiller and Ingersent(1995)] A. Schiller and K. Ingersent. *Systematic $1/d$ Corrections to the Infinite-Dimensional Limit of Correlated Lattice Electron Models*. *Phys. Rev. Lett.* **75** (1995)(1): 113. 63

[Seah and Dench(1979)] M. P. Seah and W. A. Dench. *Quantitative electron spectroscopy of surfaces: A standard data base for electron inelastic mean free paths in solids*. *Surface and Interface Analysis* **1** (1979)(1): 2. 19, 20

[Sefat *et al.* (2008a)] A. S. Sefat, R. Jin, M. A. McGuire, B. C. Sales, D. J. Singh, and D. Mandrus. *Superconductivity at 22 K in Co-Doped $BaFe_2As_2$ Crystals*. *Phys. Rev. Lett.* **101** (2008a): 117004. 4

[Sefat *et al.* (2008b)] A. S. Sefat, M. A. McGuire, B. C. Sales, R. Jin, J. Y. Howe, and D. Mandrus. *Electronic correlations in the superconductor $LaFeAsO_{0.89}F_{0.11}$ with low carrier density*. *Phys. Rev. B* **77** (2008b): 174503. 5

[Sefat *et al.* (2009)] A. S. Sefat, D. J. Singh, R. Jin, M. A. McGuire, B. C. Sales, and D. Mandrus. *Renormalized behavior and proximity of $BaCo_2As_2$ to a magnetic quantum critical point*. *Phys. Rev. B* **79** (2009): 024512. 106

[Seidl *et al.* (1996)] A. Seidl, A. Görling, P. Vogl, J. A. Majewski, and M. Levy. *Generalized Kohn-Sham schemes and the band-gap problem*. *Phys. Rev. B* **53** (1996): 3764. 49

[Sekiyama *et al.* (2004)] A. Sekiyama, H. Fujiwara, S. Imada, S. Suga, H. Eisaki, S. I. Uchida, K. Takegahara, H. Harima, Y. Saitoh, I. A. Nekrasov, G. Keller, D. E. Kondakov, A. V. Kozhevnikov, T. Pruschke, K. Held, D. Vollhardt, and V. I. Anisimov. *Mutual Experimental and Theoretical Validation of Bulk Photoemission Spectra of $Sr_{1-x}Ca_xVO_3$*. *Phys. Rev. Lett.* **93** (2004)(15): 156402. 69

[Seth *et al.* (2015)] P. Seth, P. Hansmann, A. van Roekeghem, L. Vaugier, and S. Biermann. *Towards a first-principles determination of effective Coulomb interactions in correlated electron materials: Role of inter-shell interactions*. *in preparation* (2015). 44, 93, 158

[Sharma *et al.* (2010)] S. Sharma, A. Bharathi, S. Chandra, V. R. Reddy, S. Paulraj, A. T. Satya, V. S. Sastry, A. Gupta, and C. S. Sundar. *Superconductivity in Ru-substituted polycrystalline $BaFe_{2-x}Ru_xAs_2$*. *Phys. Rev. B* **81** (2010): 174512. 4

[Shermadini *et al.* (2011)] Z. Shermadini, A. Krzton-Maziopa, M. Bendele, R. Khasanov, H. Luetkens, K. Conder, E. Pomjakushina, S. Weyeneth, V. Pomjakushin, O. Bossen, and A. Amato. *Coexistence of Magnetism and Superconductivity in the Iron-Based Compound $Cs_{0.8}(FeSe_{0.98})_2$*. *Phys. Rev. Lett.* **106** (2011): 117602. 6

[Shi *et al.* (2014)] Y.-B. Shi, Y.-B. Huang, X.-P. Wang, X. Shi, A. van Roekeghem, W.-L. Zhang, N. Xu, P. Richard, T. Qian, E. Rienks, S. Thirupathaiah, K. Zhao, C.-Q. Jin, M. Shi, and H. Ding. *Observation of Strong-Coupling Pairing with Weakened Fermi-Surface Nesting at Optimal Hole Doping in $Ca_{0.33}Na_{0.67}Fe_2As_2$*. *Chin. Phys. Lett.* **31** (2014)(6): 067403. 7

[Shimojima *et al.* (2010)] T. Shimojima, K. Ishizaka, Y. Ishida, N. Katayama, K. Ohgushi, T. Kiss, M. Okawa, T. Togashi, X.-Y. Wang, C.-T. Chen, S. Watanabe, R. Kadota, T. Oguchi, A. Chainani, and S. Shin. *Orbital-Dependent Modifications of Electronic Structure across the Magnetostructural Transition in $BaFe_2As_2$*. *Phys. Rev. Lett.* **104** (2010): 057002. 13

[Shorikov *et al.* (2009)] A. O. Shorikov, M. A. Korotin, S. V. Streltsov, S. L. Skornyakov, D. M. Korotin, and V. I. Anisimov. *Coulomb correlation effects in LaFeAsO: An LDA + DMFT(QMC) study*. *J. Exp. Theor. Phys.* **108** (2009): 121. 9

[Simonson *et al.* (2012)] J. Simonson, Z. Yin, M. Pezzoli, J. Guo, J. Liu, K. Post, A. Efimenko, N. Hollmann, Z. Hu, H.-J. Lin, *et al.* . *From antiferromagnetic insulator to correlated metal in pressurized and doped LaMnPO*. *Proc. Natl Acad. Sci. U.S.A.* **109** (2012)(27): E1815. 126

[Singh(2008)] D. J. Singh. *Electronic structure and doping in $BaFe_2As_2$ and LiFeAs: Density functional calculations*. *Phys. Rev. B* **78** (2008): 094511. 14

[Singh(2009)] —. *Electronic structure of Fe-based superconductors*. *Physica C* **469** (2009)(9): 418. 6, 13, 14

[Slater(1951)] J. C. Slater. *A simplification of the Hartree-Fock method*. *Phys. Rev.* **81** (1951)(3): 385. 66

[Slater(1960)] —. *Quantum Theory of Atomic Structure*, vol. 1. McGraw-Hill, New York (1960). 42

[Subedi *et al.* (2008)] A. Subedi, L. Zhang, D. J. Singh, and M. H. Du. *Density functional study of FeS, FeSe, and FeTe: Electronic structure, magnetism, phonons, and superconductivity*. *Phys. Rev. B* **78** (2008): 134514. 10

[Sugano *et al.* (1970)] S. Sugano, Y. Tanabe, and H. Kamimura. *Multiplets of transition-metal ions in crystal*, vol. 1. Academic Press, New York London (1970). 42

[Sun *et al.* (2013)] Y.-L. Sun, A. Ablimit, J.-K. Bao, H. Jiang, J. Zhou, and G.-H. Cao. *Growth and characterizations of $Ba_2Ti_2Fe_2As_4O$ single crystals*. *Sci. Technol. Adv. Mat.* **14** (2013)(5): 055008. 4, 141

[Sun *et al.* (2012)] Y.-L. Sun, H. Jiang, H.-F. Zhai, J.-K. Bao, W.-H. Jiao, Q. Tao, C.-Y. Shen, Y.-W. Zeng, Z.-A. Xu, and G.-H. Cao. *$Ba_2Ti_2Fe_2As_4O$: A New Superconductor Containing Fe_2As_2 Layers and Ti_2O Sheets*. *J. Am. Chem. Soc.* **134** (2012)(31): 12893. 141, 144

[Taen *et al.* (2009)] T. Taen, Y. Tsuchiya, Y. Nakajima, and T. Tamegai. *Superconductivity at T_c = 14 K in single-crystalline $FeTe_{0.61}Se_{0.39}$*. *Phys. Rev. B* **80** (2009): 092502. 5

[Takada and Chatterjee(2003)] Y. Takada and A. Chatterjee. *Possibility of a metallic phase in the charge-density-wave–spin-density-wave crossover region in the one-dimensional Hubbard-Holstein model at half filling*. *Phys. Rev. B* **67** (2003): 081102(R). 51

[Takeshita and Kadono(2009)] S. Takeshita and R. Kadono. *Competition/coexistence of magnetism and superconductivity in iron pnictides probed by muon spin rotation*. *New J. Phys.* **11** (2009)(3): 035006. 6

[Tamai *et al.* (2010)] A. Tamai, A. Y. Ganin, E. Rozbicki, J. Bacsa, W. Meevasana, P. D. C. King, M. Caffio, R. Schaub, S. Margadonna, K. Prassides, M. J. Rosseinsky, and F. Baumberger. *Strong Electron Correlations in the Normal State of the Iron-Based $FeSe_{0.42}Te_{0.58}$ Superconductor Observed by Angle-Resolved Photoemission Spectroscopy*. *Phys. Rev. Lett.* **104** (2010): 097002. 7, 8, 81

[Tapp *et al.* (2008)] J. H. Tapp, Z. Tang, B. Lv, K. Sasmal, B. Lorenz, P. C. W. Chu, and A. M. Guloy. *LiFeAs: An intrinsic FeAs-based superconductor with $T_c = 18$ K*. *Phys. Rev. B* **78** (2008): 060505. 3

[Taranto *et al.* (2013)] C. Taranto, M. Kaltak, N. Parragh, G. Sangiovanni, G. Kresse, A. Toschi, and K. Held. *Comparing quasiparticle GW+DMFT and LDA+DMFT for the test bed material $SrVO_3$*. *Phys. Rev. B* **88** (2013): 165119. 64

[Thirupathaiah *et al.* (2010)] S. Thirupathaiah, S. de Jong, R. Ovsyannikov, H. A. Dürr, A. Varykhalov, R. Follath, Y. Huang, R. Huisman, M. S. Golden, Y.-Z. Zhang, H. O. Jeschke, R. Valentí, A. Erb, A. Gloskovskii, and J. Fink. *Orbital character variation of the Fermi surface and doping dependent changes of the dimensionality in $BaFe_{2-x}Co_xAs_2$ from angle-resolved photoemission spectroscopy*. *Phys. Rev. B* **81** (2010): 104512. 7

[Tomczak(2007)] J. Tomczak. *Spectral and Optical Properties of Correlated Materials*. Ph.D. thesis, Ecole Polytechnique (2007). 163, 165

[Tomczak *et al.* (2012a)] J. M. Tomczak, M. Casula, T. Miyake, F. Aryasetiawan, and S. Biermann. *Combined GW and dynamical mean-field theory: Dynamical screening effects in transition metal oxides*. *EPL* **100** (2012a)(6): 67001. 51, 63, 69

[Tomczak *et al.* (2014)] J. M. Tomczak, M. Casula, T. Miyake, and S. Biermann. *Asymmetry in band widening and quasiparticle lifetimes in $SrVO_3$: Competition between screened exchange and local correlations from combined GW and dynamical mean-field theory GW + DMFT*. *Phys. Rev. B* **90** (2014): 165138. 51, 63, 64, 68, 69, 70, 111, 157

[Tomczak *et al.* (2012b)] J. M. Tomczak, M. van Schilfgaarde, and G. Kotliar. *Many-Body Effects in Iron Pnictides and Chalcogenides: Nonlocal Versus Dynamic Origin of Effective Masses*. *Phys. Rev. Lett.* **109** (2012b): 237010. 13, 14, 64, 68, 111, 157

[Tomić *et al.* (2012)] M. Tomić, R. Valentí, and H. O. Jeschke. *Uniaxial versus hydrostatic pressure-induced phase transitions in $CaFe_2As_2$ and $BaFe_2As_2$*. *Phys. Rev. B* **85** (2012): 094105. 129

[Torikachvili *et al.* (2008)] M. S. Torikachvili, S. L. Bud'ko, N. Ni, and P. C. Canfield. *Pressure Induced Superconductivity in $CaFe_2As_2$*. *Phys. Rev. Lett.* **101** (2008): 057006. 129

[Toschi *et al.* (2012)] A. Toschi, R. Arita, P. Hansmann, G. Sangiovanni, and K. Held. *Quantum dynamical screening of the local magnetic moment in Fe-based superconductors*. *Phys. Rev. B* **86** (2012): 064411. 12

[Tran and Blaha(2011)] F. O. Tran and P. Blaha. *Implementation of screened hybrid functionals based on the Yukawa potential within the LAPW basis set*. *Phys. Rev. B* **83** (2011)(23): 235118. 64, 112

[Tsubota *et al.* (2013)] K. Tsubota, T. Wakita, H. Nagao, C. Hiramatsu, T. Ishiga, M. Sunagawa, K. Ono, H. Kumigashira, M. Danura, K. Kudo, M. Nohara, Y. Muraoka, and T. Yokoya. *Collapsed Tetragonal Phase Transition of $Ca(Fe_{1-x}Rh_x)_2As_2$ Studied by Photoemission Spectroscopy*. *J. Phys. Soc. Jpn.* **82** (2013)(7): 073705. 129

[van der Marel *et al.* (1984)] D. van der Marel, G. A. Sawatzky, and F. U. Hillebrecht. *Direct Observation of the Exchange-Split Virtual Bound State in Dilute Mn Alloys*. *Phys. Rev. Lett.* **53** (1984)(2): 206. 44, 60

[van Roekeghem *et al.* (2014)] A. van Roekeghem, T. Ayral, J. M. Tomczak, M. Casula, N. Xu, H. Ding, M. Ferrero, O. Parcollet, H. Jiang, and S. Biermann. *Dynamical correlations and screened exchange on the experimental bench: spectral properties of the cobalt pnictide $BaCo_2As_2$*. *Phys. Rev. Lett.* **113** (2014): 266403. 105

[van Roekeghem and Biermann(2014)] A. van Roekeghem and S. Biermann. *Screened exchange dynamical mean-field theory and its relation to density functional theory: $SrVO_3$ and $SrTiO_3$*. *EPL* **108** (2014): 75003. 71

[van Schilfgaarde *et al.* (2006)] M. van Schilfgaarde, T. Kotani, and S. Faleev. *Quasiparticle Self-Consistent GW Theory*. *Phys. Rev. Lett.* **96** (2006)(22): 226402. 14

[Vaugier(2011)] L. Vaugier. *Electronic Structure of Correlated Materials from First Principles: Hubbard Interaction and Hund's Exchange*. Ph.D. thesis, Ecole Polytechnique, France (2011). 43, 77, 79, 81, 85, 107, 158

[Vaugier *et al.* (2012a)] L. Vaugier, H. Jiang, and S. Biermann. *Hubbard U and Hund exchange J in transition metal oxides: Screening versus localization trends from constrained random phase approximation*. *Phys. Rev. B* **86** (2012a)(16): 165105. 107

[Vaugier *et al.* (2012b)] —. *Hubbard U and Hund's Exchange J in Oxides : Screening vs. Localization Trends from Constrained Random Phase Approximation*. *Phys. Rev. B* **86** (2012b): 165105. 41, 42, 43, 77, 79, 158

[Vildosola *et al.* (2008)] V. Vildosola, L. Pourovskii, R. Arita, S. Biermann, and A. Georges. *Bandwidth and Fermi surface of iron oxypnictides: Covalency and sensitivity to structural changes*. *Phys. Rev. B* **78** (2008): 064518. 13, 14, 83

[Vilmercati *et al.* (2009)] P. Vilmercati, A. Fedorov, I. Vobornik, U. Manju, G. Panaccione, A. Goldoni, A. S. Sefat, M. A. McGuire, B. C. Sales, R. Jin, D. Mandrus, D. J. Singh, and N. Mannella. *Evidence for three-dimensional Fermi-surface topology of the layered electron-doped iron superconductor* $Ba(Fe_{1-x}Co_x)_2As_2$. *Phys. Rev. B* **79** (2009): 220503. 7, 14

[Vorontsov *et al.* (2009)] A. B. Vorontsov, M. G. Vavilov, and A. V. Chubukov. *Interplay between magnetism and superconductivity in the iron pnictides*. *Phys. Rev. B* **79** (2009): 060508. 6

[Wang *et al.* (2008a)] C. Wang, L. Li, S. Chi, Z. Zhu, Z. Ren, Y. Li, Y. Wang, X. Lin, Y. Luo, S. Jiang, X. Xu, G. Cao, and Z. Xu. *Thorium-doping–induced superconductivity up to 56 K in* $Gd_{1-x}Th_xFeAsO$. *EPL* **83** (2008a)(6): 67006. 4

[Wang *et al.* (2010)] G. Wang, Y. Qian, G. Xu, X. Dai, and Z. Fang. *Gutzwiller Density Functional Studies of FeAs-Based Superconductors: Structure Optimization and Evidence for a Three-Dimensional Fermi Surface*. *Phys. Rev. Lett.* **104** (2010): 047002. 10, 13

[Wang *et al.* (2008b)] X. Wang, Q. Liu, Y. Lv, W. Gao, L. Yang, R. Yu, F. Li, and C. Jin. *The superconductivity at 18 K in LiFeAs system*. *Solid State Commun.* **148** (2008b)(11): 538. 3

[Wang *et al.* (2012a)] X.-P. Wang, P. Richard, Y.-B. Huang, H. Miao, L. Cevey, N. Xu, Y.-J. Sun, T. Qian, Y.-M. Xu, M. Shi, J.-P. Hu, X. Dai, and H. Ding. *Orbital characters determined from Fermi surface intensity patterns using angle-resolved photoemission spectroscopy*. *Phys. Rev. B* **85** (2012a): 214518. 115

[Wang *et al.* (2012b)] X.-P. Wang, P. Richard, X. Shi, A. van Roekeghem, Y.-B. Huang, E. Razzoli, T. Qian, E. Rienks, S. Thirupathaiah, H.-D. Wang, C.-H. Dong, M.-H. Fang, M. Shi, and H. Ding. *Observation of an isotropic superconducting gap at the Brillouin zone centre of* $Tl_{0.63}K_{0.37}Fe_{1.78}Se_2$. *EPL* **99** (2012b)(6): 67001. 7

[Wen *et al.* (2008)] H.-H. Wen, G. Mu, L. Fang, H. Yang, and X. Zhu. *Superconductivity at 25 K in hole-doped* $(La_{1-x}Sr_x)OFeAs$. *Eur. Phys. Lett.* **82** (2008): 17009. 3

[Werner *et al.* (2012)] P. Werner, M. Casula, T. Miyake, F. Aryasetiawan, A. J. Millis, and S. Biermann. *Satellites and large doping- and temperature-dependence of electronic properties in hole-doped* $BaFe_2As_2$. *Nature Physics* **8** (2012): 331. 10, 11, 12, 13, 51, 80, 105, 106, 115, 123, 127, 128, 152, 159, 172

[Werner *et al.* (2006)] P. Werner, A. Comanac, L. de' Medici, M. Troyer, and A. J. Millis. *Continuous-Time Solver for Quantum Impurity Models*. *Phys. Rev. Lett.* **97** (2006)(7): 076405. 51, 54

[Werner *et al.* (2008)] P. Werner, E. Gull, M. Troyer, and A. J. Millis. *Spin freezing transition and non-Fermi-liquid self-energy in a three-orbital model*. *Phys. Rev. Lett.* **101** (2008)(16): 166405. 9, 123, 126, 127

[Werner and Millis(2007)] P. Werner and A. Millis. *Efficient dynamical mean field simulation of the holstein-hubbard model*. *Phys. Rev. Lett.* **99** (2007)(14): 146404. 51, 52

[Werner and Millis(2010)] P. Werner and A. J. Millis. *Dynamical Screening in Correlated Electron Materials*. *Phys. Rev. Lett.* **104** (2010): 146401. 49, 51, 54, 55, 110

[Wilson *et al.* (2009)] S. D. Wilson, Z. Yamani, C. R. Rotundu, B. Freelon, E. Bourret-Courchesne, and R. J. Birgeneau. *Neutron diffraction study of the magnetic and structural phase transitions in $BaFe_2As_2$*. *Phys. Rev. B* **79** (2009): 184519. 6

[Xu *et al.* (2014)] H. C. Xu, M. Xu, R. Peng, Y. Zhang, Q. Q. Ge, F. Qin, M. Xia, J. J. Ying, X. H. Chen, X. L. Yu, L. J. Zou, M. Arita, K. Shimada, M. Taniguchi, D. H. Lu, B. P. Xie, and D. L. Feng. *Electronic structure of the $BaTi_2As_2O$ parent compound of the titanium-based oxypnictide superconductor*. *Phys. Rev. B* **89** (2014): 155108. 149

[Xu *et al.* (2012)] N. Xu, T. Qian, P. Richard, Y.-B. Shi, X.-P. Wang, P. Zhang, Y.-B. Huang, Y.-M. Xu, H. Miao, G. Xu, G.-F. Xuan, W.-H. Jiao, Z.-A. Xu, G.-H. Cao, and H. Ding. *Effects of Ru substitution on electron correlations and Fermi-surface dimensionality in $Ba(Fe_{1-x}Ru_x)_2As_2$*. *Phys. Rev. B* **86** (2012): 064505. 7, 107, 124

[Xu *et al.* (2013a)] N. Xu, P. Richard, X. Shi, A. van Roekeghem, T. Qian, E. Razzoli, E. Rienks, G.-F. Chen, E. Ieki, K. Nakayama, T. Sato, T. Takahashi, M. Shi, and H. Ding. *Possible nodal superconducting gap and Lifshitz transition in heavily hole-doped $Ba_{0.1}K_{0.9}Fe_2As_2$*. *Phys. Rev. B* **88** (2013a): 220508. 7

[Xu *et al.* (2013b)] N. Xu, P. Richard, A. van Roekeghem, P. Zhang, H. Miao, W.-L. Zhang, T. Qian, M. Ferrero, A. S. Sefat, S. Biermann, and H. Ding. *Electronic Band Structure of $BaCo_2As_2$: A Fully Doped Ferropnictide Analog with Reduced Electronic Correlations*. *Phys. Rev. X* **3** (2013b): 011006. 7, 10, 105, 106, 110, 114

[Xu *et al.* (2013c)] N. Xu, P. Richard, X.-P. Wang, X. Shi, A. van Roekeghem, T. Qian, E. Ieki, K. Nakayama, T. Sato, E. Rienks, S. Thirupathaiah, J. Xing, H.-H. Wen, M. Shi, T. Takahashi, and H. Ding. *Angle-resolved photoemission observation of isotropic superconducting gaps in isovalent Ru-substituted $Ba(Fe_{0.75}Ru_{0.25})_2As_2$*. *Phys. Rev. B* **87** (2013c): 094513. 7

[Xu *et al.* (2011)] Y.-M. Xu, P. Richard, K. Nakayama, T. Kawahara, Y. Sekiba, T. Qian, M. Neupane, S. Souma, T. Sato, T. Takahashi, H.-Q. Luo, H.-H. Wen, G.-F. Chen, N.-L. Wang, Z. Wang, Z. Fang, X. Dai, and H. Ding. *Fermi surface dichotomy of the superconducting gap and pseudogap in underdoped pnictides*. *Nat. Commun.* **2** (2011): 394. 9

[Yamamoto *et al.* (2009)] A. Yamamoto, J. Jaroszynski, C. Tarantini, L. Balicas, J. Jiang, A. Gurevich, D. C. Larbalestier, R. Jin, A. S. Sefat, M. A. McGuire, B. C. Sales, D. K. Christen, and D. Mandrus. *Small anisotropy, weak thermal fluctuations, and high field superconductivity in Co-doped iron pnictide $Ba(Fe_{1x}Co_x)2As2$*. *Appl. Phys. Lett.* **94** (2009). 5

[Yamasaki *et al.* (2010)] A. Yamasaki, Y. Matsui, S. Imada, K. Takase, H. Azuma, T. Muro, Y. Kato, A. Higashiya, A. Sekiyama, S. Suga, M. Yabashi, K. Tamasaku, T. Ishikawa, K. Terashima, H. Kobori, A. Sugimura, N. Umeyama, H. Sato, Y. Hara, N. Miyagawa, and S. I. Ikeda. *Electron correlation in the FeSe superconductor studied by bulk-sensitive photoemission spectroscopy*. *Phys. Rev. B* **82** (2010): 184511. 7, 8

[Yang *et al.* (2008)] H. Yang, H. Luo, Z. Wang, and H.-H. Wen. *Fishtail effect and the vortex phase diagram of single crystal $Ba_{0.6}K_{0.4}Fe_2As_2$*. *Appl. Phys. Lett.* **93** (2008)(14): 142506. 5

[Yang *et al.* (2010)] L. X. Yang, B. P. Xie, Y. Zhang, C. He, Q. Q. Ge, X. F. Wang, X. H. Chen, M. Arita, J. Jiang, K. Shimada, M. Taniguchi, I. Vobornik, G. Rossi, J. P. Hu, D. H. Lu, Z. X. Shen, Z. Y. Lu, and D. L. Feng. *Surface and bulk electronic structures of LaFeAsO studied by angle-resolved photoemission spectroscopy*. *Phys. Rev. B* **82** (2010): 104519. 7

[Yeh *et al.* (2008)] K.-W. Yeh, T.-W. Huang, Y.-l. Huang, T.-K. Chen, F. Hsu, P. M. Wu, Y. C. Lee, Y.-Y. Chu, C.-L. Chen, J.-Y. Luo, D.-C. Yan, and M.-K. Wu. *Tellurium substitution effect on superconductivity of the Îś-phase iron selenide*. *Eur. Phys. Lett.* **84** (2008): 37002. 3

[Yi *et al.* (2009)] M. Yi, D. H. Lu, J. G. Analytis, J.-H. Chu, S.-K. Mo, R.-H. He, R. G. Moore, X. J. Zhou, G. F. Chen, J. L. Luo, N. L. Wang, Z. Hussain, D. J. Singh, I. R. Fisher, and Z.-X. Shen. *Electronic structure of the $BaFe_2As_2$ family of iron-pnictide superconductors*. *Phys. Rev. B* **80** (2009): 024515. 7, 8

[Yi *et al.* (2013)] M. Yi, D. H. Lu, R. Yu, S. C. Riggs, J.-H. Chu, B. Lv, Z. K. Liu, M. Lu, Y.-T. Cui, M. Hashimoto, S.-K. Mo, Z. Hussain, C. W. Chu, I. R. Fisher, Q. Si, and Z.-X. Shen. *Observation of Temperature-Induced Crossover to an Orbital-Selective Mott Phase in $A_xFe_{2-y}Se_2$ (A=K, Rb) Superconductors*. *Phys. Rev. Lett.* **110** (2013): 067003. 8, 9

[Yildirim(2008)] T. Yildirim. *Origin of the 150-K Anomaly in LaFeAsO: Competing Antiferromagnetic Interactions, Frustration, and a Structural Phase Transition*. *Phys. Rev. Lett.* **101** (2008): 057010. 6

[Yildirim(2009a)] —. *Frustrated magnetic interactions, giant magneto-elastic coupling, and magnetic phonons in iron-pnictides*. *Physica C* **469** (2009a)(9-12): 425. 6

[Yildirim(2009b)] —. *Strong Coupling of the Fe-Spin State and the As-As Hybridization in Iron-Pnictide Superconductors from First-Principle Calculations*. *Phys. Rev. Lett.* **102** (2009b): 037003. 5, 129, 130

[Yin *et al.* (2011)] Z. P. Yin, K. Haule, and G. Kotliar. *Kinetic frustration and the nature of the magnetic and paramagnetic states in iron pnictides and iron chalcogenides*. *Nature Materials* **10** (2011): 932. 10

[Ying *et al.* (2012)] J. J. Ying, Y. J. Yan, A. F. Wang, Z. J. Xiang, P. Cheng, G. J. Ye, and X. H. Chen. *Metamagnetic transition in $Ca_{1-x}Sr_xCo_2As_2$(x = 0 and 0.1) single crystals*. *Phys. Rev. B* **85** (2012): 214414. 106

[Ylvisaker *et al.* (2009)] E. R. Ylvisaker, W. E. Pickett, and K. Koepernik. *Anisotropy and magnetism in the LSDA+U method*. *Phys. Rev. B* **79** (2009): 035103. 37

[Yoshida *et al.* (2009)] R. Yoshida, T. Wakita, H. Okazaki, Y. Mizuguchi, S. Tsuda, Y. Takano, H. Takeya, K. Hirata, T. Muro, M. Okawa, K. Ishizaka, S. Shin, H. Harima, M. Hirai, Y. Muraoka, and T. Yokoya. *Electronic Structure of Superconducting FeSe Studied by High-Resolution Photoemission Spectroscopy*. *J. Phys. Soc. Jpn.* **78** (2009): 034708. 7, 8

[Yoshida *et al.* (2010)] T. Yoshida, M. Hashimoto, T. Takizawa, A. Fujimori, M. Kubota, K. Ono, and H. Eisaki. *Mass renormalization in the bandwidth-controlled Mott-Hubbard systems $SrVO_3$ and $CaVO_3$ studied by angle-resolved photoemission spectroscopy*. *Phys. Rev. B* **82** (2010): 085119. 68

[Yoshida *et al.* (2005)] T. Yoshida, K. Tanaka, H. Yagi, A. Ino, H. Eisaki, A. Fujimori, and Z.-X. Shen. *Direct Observation of the Mass Renormalization in $SrVO3$ by Angle Resolved Photoemission Spectroscopy*. *Phys. Rev. Lett.* **95** (2005)(14): 146404. 68

[Yuan *et al.* (2009)] H. Yuan, J. Singleton, F. Balakirev, S. Baily, G. Chen, J. Luo, and N. Wang. *Nearly isotropic superconductivity in (Ba,K)Fe_2As_2*. *Nature* **457** (2009)(7229): 565. 5

[Zeng *et al.* (2014)] L.-K. Zeng, A. van Roekeghem, J.-X. Yin, P. Richard, Z.-G. Chen, N.-L. Wang, T. Qian, and H. Ding. *Angle-resolved photoemission spectroscopy study of the Ni-based superconductors $SrNi_2As_2$ and $SrNi_2P_2$. in preparation* (2014). 39

[Zhang *et al.* (2011a)] P. Zhang, P. Richard, T. Qian, Y.-M. Xu, X. Dai, and H. Ding. *A Precise Method for Visualizing Dispersive Features in Image Plots*. *Rev. Sci. Instrum.* **82** (2011a): 043712. 118, 142

[Zhang *et al.* (2011b)] Y. Zhang, F. Chen, C. He, B. Zhou, B. P. Xie, C. Fang, W. F. Tsai, X. H. Chen, H. Hayashi, J. Jiang, H. Iwasawa, K. Shimada, H. Namatame, M. Taniguchi, J. P. Hu, and D. L. Feng. *Orbital characters of bands in the iron-based superconductor $BaFe_{1.85}Co_{0.15}As_2$*. *Phys. Rev. B* **83** (2011b): 054510. 7, 8

[Zhao *et al.* (2008a)] J. Zhao, Q. Huang, C. de La Cruz, S. Li, J. Lynn, Y. Chen, M. Green, G. Chen, G. Li, Z. Li, J. Luo, N. Wang, and P. Dai. *Structural and magnetic phase diagram of CeFeAsO1- xFx and its relation to high-temperature superconductivity*. *Nat. Mater.* **7** (2008a)(12): 953. 5, 6

[Zhao *et al.* (2008b)] L. Zhao, H.-Y. Liu, W.-T. Zhang, J.-Q. Meng, X.-W. Jia, G.-D. Liu, X.-L. Dong, G.-F. Chen, J.-L. Luo, N.-L. Wang, W. Lu, G.-L. Wang, Y. Zhou, Y. Zhu, X.-Y. Wang, Z.-Y. Xu, C.-T. Chen, and X.-J. Zhou. *Multiple nodeless superconducting gaps in $(Ba_{0.6}K_{0.4})Fe_2As_2$ superconductor from angle-resolved photoemission spectroscopy*. *Chin. Phys. Lett.* **25** (2008b)(12): 4402. 7

[Zhigadlo *et al.* (2008)] N. D. Zhigadlo, S. Katrych, Z. Bukowski, S. Weyeneth, R. Puzniak, and J. Karpinski. *Single crystals of superconducting $SmFeAsO_{1-x}F_y$ grown at high pressure*. *J. Phys.: Condens. Matter* **20** (2008)(34): 342202. 5

[Zhu *et al.* (2009)] X. Zhu, F. Han, G. Mu, P. Cheng, B. Shen, B. Zeng, and H.-H. Wen. *Transition of stoichiometric Sr_2VO_3FeAs to a superconducting state at 37.2 K*. *Phys. Rev. B* **79** (2009): 220512. 4